

TOWARDS PRECISION PHOTOMETRIC TYPE IA SUPERNOVA COSMOLOGY WITH  
MACHINE LEARNING

Helen Qu

A DISSERTATION

in

Physics and Astronomy

Presented to the Faculties of the University of Pennsylvania

in

Partial Fulfillment of the Requirements for the

Degree of Doctor of Philosophy

2024

Supervisor of Dissertation

Masao Sako, Professor, Physics and Astronomy

Graduate Group Chairperson

Ravi Sheth, Professor, Physics and Astronomy

Dissertation Committee

Bhuvnesh Jain, Professor, Physics and Astronomy

Gary Bernstein, Professor, Physics and Astronomy

Mariangela Bernardi, Professor, Physics and Astronomy

Dylan Rankin, Assistant Professor, Physics and Astronomy

TOWARDS PRECISION PHOTOMETRIC TYPE IA SUPERNOVA COSMOLOGY WITH  
MACHINE LEARNING

COPYRIGHT

2024

Helen Qu

*For my family, whose love and encouragement means the universe.*

## ACKNOWLEDGEMENT

It has been an incredible privilege to be supported by countless people during the course of my PhD and the completion of this work.

This thesis and my entire academic career was made possible by my advisor, Masao Sako. Masao taught my first year undergraduate physics class in 2013 and gave me the confidence to pursue a degree in engineering. When I was contemplating graduate school, he took me in with little to no advanced physics education on just a promise that I could figure things out. His unwavering trust in my potential has made an irreconcilable difference in my life, and for that I am immeasurably grateful.

My committee members deserve additional thanks: Bhuv Jain, Gary Bernstein, Dylan Rankin, and Mariangela Bernardi, who have all enriched my graduate school experience far beyond your committee roles. Thanks in particular to Bhuv Jain, who has been incredibly supportive both in my academic forays into machine learning and on-the-ground development of a machine learning community within the department. Finally, many thanks to our faculty and staff for providing the most welcoming environment a graduate student could ask for.

My path to graduate school was shaped by many important individuals. In my final year of college, Prof. Max Mintz first incepted the idea of returning to school for physics, and his tireless love for learning continues to inspire me every day. My colleagues and mentors at Academia.edu have taught me so much, from the ins-and-outs of vim to the importance of stepping out of my comfort zone. In particular, I am incredibly grateful to Yuri Niyazov, Alexei Chernikov, and Davis Vu, whose impacts on my life reach far beyond my time at Academia.edu and my software engineering career.

I have also been privileged to learn from and collaborate with a multitude of remarkable people over the years. Many thanks to wonderful friends, colleagues, and mentors in the DES-SN WG and LSST DESC - these have been the most welcoming communities to me and I always look forward

to our biannual in-person meetings. I feel particularly fortunate to have been a part of the final DES-SN analysis, the culmination of decades of hard work by many.

I am so grateful for the extraordinary researchers and human beings of Penn Physics and Astronomy. The support of my cohort of graduate students during our first year was invaluable: Justin Bracks, Yvonne Zagzag, Charlotte Slaughter, Eric Chong, Avi Kahn, Arpit Arora, Aaron Winn. I knew I could always ask for help, and I still think back to our long homework sessions together fondly. Since COVID reopening, I have been so lucky to find a community in the past and present residents of DRL 4N. Jason Lee, Qiuyue Liang, Minsu Park, Karen Perez Sarmiento, Julia Robe, Neha Joshi, Shivam Pandey, Guram Kartvelishvili, Tanvi Karwal, Cyrille Doux, Carles Sanchez, Marco Gatti, and Marco Raveri: our times together have been some of my fondest memories of graduate school, and I can't thank you all enough for your support in all aspects of my life.

My friends and family have been a vital source of unwavering love, encouragement, and support. Thank you to the residents of 1062 Oakridge for 1.5 years of unexpected time together: in the midst of a global pandemic, your companionship meant the world. Thank you to my mother, Hong, the most selfless person I know; and my father, Rongda, who sparked my interest in science from an early age. Their unconditional support has accompanied me every step of the way.

Finally, thank you to my partner Michael, who shows me daily that it is possible to strive for great things while giving selflessly to those you love.

## ABSTRACT

### TOWARDS PRECISION PHOTOMETRIC TYPE IA SUPERNOVA COSMOLOGY WITH MACHINE LEARNING

Helen Qu

Masao Sako

The revolutionary discovery of dark energy and accelerating cosmic expansion was made with just 42 type Ia supernovae (SNe Ia) in 1999. Since then, large synoptic surveys, e.g., Dark Energy Survey (DES), have observed thousands more SNe Ia and the upcoming Rubin Legacy Survey of Space and Time (LSST) and Roman Space Telescope promise to deliver millions in the next decade. This unprecedented data volume can produce the required precision to unambiguously test concordance cosmology which could represent a monumental shift in our understanding of dark energy and its role in cosmic history. However, extracting a pure SN Ia sample with accurate redshifts for such a large dataset will be a challenge. Specifically, spectroscopic classification will not be possible for the vast majority of discovered objects, and only  $\sim 25\%$  will have spectroscopic redshifts. This thesis presents a series of observational and methodological studies designed to address the questions associated with this new era of photometric SN Ia cosmology.

First, we present a machine learning method for photometric classification of SNe, Supernova Classification with a CONvolutional Neural Network (SCONE). Photometric classification enables SNe with no spectroscopic information to be confidently categorized, and is a critical component of current and future analysis pipelines. SCONE achieves  $> 99\%$  accuracy distinguishing simulated SNe Ia from non-Ia SNe, and has been integrated into DES, LSST, and Roman analysis pipelines. We also demonstrate the efficacy of SCONE on early-time photometric classification, which will be vital for optimal allocation of spectroscopic resources. We show that SCONE can distinguish between 6 SN types with 75% accuracy on the night of initial discovery, comparable to results in the literature for full-phase SNe.

Next, we study current methods for estimating SN Ia redshifts and propose a machine learning alternative that uses SN photometry alone to extract redshift information. Most SNe Ia inherit redshift information from their host galaxy, but the process of matching SNe to the correct host galaxy can be challenging. We systematically analyze the impact of incorrect redshifts from host galaxy mismatch on 5 years of DES SN data, and conclude that improved host matching or redshift estimation methods can reduce our systematic errors by  $\sim 10\%$ . In response to this finding, we present a SN photometry-only method for estimating redshifts independent of host galaxy information, Photo-zSNthesis. We show that Photo-zSNthesis redshift estimates are accurate to within 2% across the full redshift range of LSST, a first in the literature.

Finally, we focus on the robustness of machine learning (ML) algorithms for real-world and scientific applications. ML models generalize poorly beyond their training set and often experience severe performance degradation when deployed on new data. We demonstrate a general method for improving robustness that achieves new state-of-the-art results on astronomical object classification, wildlife identification, and tumor detection.

## TABLE OF CONTENTS

ACKNOWLEDGEMENT . . . . .	iv
ABSTRACT . . . . .	vi
LIST OF TABLES . . . . .	xi
LIST OF ILLUSTRATIONS . . . . .	xiii
CHAPTER 1: Introduction . . . . .	1
1.1 We live in an expanding universe! . . . . .	1
1.2 Cosmology with Type Ia Supernovae . . . . .	8
1.3 Cosmology in the Era of Big Data . . . . .	19
1.4 Motivation and Overview . . . . .	22
CHAPTER 2: SCONE: Supernova Classification with a Convolutional Neural Network . . . . .	24
2.1 Introduction . . . . .	24
2.2 Methods . . . . .	26
2.3 Results . . . . .	36
2.4 Discussion . . . . .	41
2.5 Conclusions . . . . .	43
2.6 Acknowledgments . . . . .	44
CHAPTER 3: Photometric Classification of Early-Time Supernova Lightcurves with SCONE . . . . .	45
3.1 Introduction . . . . .	45
3.2 Methods . . . . .	49
3.3 Results and Discussion . . . . .	55
3.4 Conclusions . . . . .	71
3.5 Acknowledgments . . . . .	72



CHAPTER 4 : The Dark Energy Survey Supernova Program: Cosmological Biases from Host Galaxy Mismatch of Type Ia Supernovae . . . . .	74
4.1 Introduction . . . . .	74
4.2 Host Galaxy Matching . . . . .	77
4.3 Data and host galaxy catalog . . . . .	79
4.4 Simulations and event selection . . . . .	86
4.5 Comparing Data with Simulations . . . . .	91
4.6 Cosmological Parameter Estimation . . . . .	95
4.7 Results and Discussion . . . . .	97
4.8 Conclusions . . . . .	109
CHAPTER 5 : Photo- $z$ SNthesis: Converting Type Ia Supernova Lightcurves to Redshift Es- timates via Deep Learning . . . . .	114
5.1 Introduction . . . . .	114
5.2 Data . . . . .	118
5.3 Model . . . . .	124
5.4 Results and Discussion . . . . .	129
5.5 Conclusions . . . . .	143
5.6 Redshift Prediction Outliers of the Real SDSS Dataset . . . . .	146
CHAPTER 6 : Connect Later: Improving Fine-tuning for Robustness with Targeted Aug- mentations . . . . .	147
6.1 Introduction . . . . .	147
6.2 Setup . . . . .	149
6.3 Pretraining may not improve OOD performance . . . . .	152
6.4 Connect Later: Pretrain First, Targeted Augmentations Later . . . . .	154
6.5 Experiments . . . . .	159
6.6 Discussion and Related Work . . . . .	164
6.7 Conclusion . . . . .	165

CHAPTER 7: Conclusions and Future Directions . . . . . 177

BIBLIOGRAPHY . . . . . 179

## LIST OF TABLES

TABLE 2.1	Makeup of the PLAsTiCC dataset by type. . . . .	27
TABLE 2.2	Makeup of the PLAsTiCC dataset by type after applying quality cuts. . . . .	29
TABLE 2.3	Central wavelength of each filter . . . . .	31
TABLE 2.4	Evaluation metrics for Ia vs. non-Ia classification on cut dataset . . . . .	38
TABLE 2.5	Evaluation metrics for out-of-distribution Ia vs. non-Ia classification . . . . .	39
TABLE 2.6	Misclassified test set heatmaps by true and predicted type for binary classification. . . . .	41
TABLE 2.7	Misclassified test set heatmaps by true and predicted type for categorical class-balanced classification. . . . .	42
TABLE 3.1	Training, validation, and test dataset sizes for the $t_{\text{trigger}} + N$ datasets. . . . .	50
TABLE 3.2	Training, validation, and test accuracies <i>without</i> redshift information for each early lightcurve dataset. These averages and standard deviations were computed from 5 independent runs of SCONE. . . . .	56
TABLE 3.3	Training, validation, and test accuracies <i>with</i> redshift information for each early lightcurve dataset. These averages and standard deviations were computed from 5 independent runs of SCONE. . . . .	57
TABLE 3.4	Test accuracies with and without redshift information for the bright datasets. . . . .	66
TABLE 4.1	Cuts applied to the host galaxy library and resulting galaxy counts. . . . .	84
TABLE 4.2	Summary of host galaxy matching for the DES Y5 sample. . . . .	85
TABLE 4.3	Summary of the mismatch rate averaged over 25 realizations after each selection cut on the SNIa+CC simulated dataset, split by Ia vs. non-Ia SNe. The non-Ia SNe include SNIax, SNIa-91bg, SNII, and SNIbc. All results using SNe Ia only are using the SN Ia subset of this dataset. . . . .	90
TABLE 4.4	$\Delta w$ and classification accuracies for each classifier. Accuracy change is only expected for the $\text{SNN}_{+Z}$ classifier, as it is the only classifier tested that requires redshift information. Accuracy change is defined as Accuracy (with mismatch) – Accuracy (no mismatch). . . . .	100
TABLE 4.5	$\Delta w$ and $\Delta\Omega_m$ values for the Ia-only SN population with and without a CMB prior. The values in the $\Delta w$ with CMB prior cell are reproduced from Table 4.4. . . . .	105
TABLE 4.6	$\Delta w$ values for the Ia-only and Ia+CC simulated SN populations with an alternative bias correction scheme (“bcor+mismatch”) that includes mismatched hosts in the bias correction simulations. The values in the $\Delta w$ , baseline column are reproduced from Table 4.4. . . . .	107
TABLE 4.7	$\Delta w$ values for the Ia-only and Ia+CC simulated SN populations with and without Sérsic scaling ( $k = 0.8$ and $k = 1$ ). The primary results presented in this work (Sections 4.7.1 and 4.7.2) use simulations scaled with $k = 0.8$ . The $\text{SNN}_{+Z}$ results with $k = 1$ have an inflated $\Delta w$ as well as $\sigma_{\Delta w}$ due to a realization with poor $\chi^2$ fit from <code>wfit</code> . . . . .	108
TABLE 5.1	Number of SDSS lightcurves remaining after each selection cut. We evaluate Photo- $z$ SNthesis on the remaining 489 SNe. . . . .	121
TABLE 5.2	Description of example layers in the model architecture. . . . .	127

TABLE 5.3	Evaluation metrics computed for the PLAsTiCC test dataset for both the mean(PDF) and max(PDF) point estimates for our model as well as LCFIT+Z. The best result for each metric is shown in bold. . . . .	134
TABLE 5.4	Evaluation metrics computed for the SDSS simulated and real test datasets for both the mean(PDF) and max(PDF) point estimates for our model as well as LCFIT+Z. The best result for each metric and dataset is shown in bold. . . . .	135
TABLE 5.5	Evaluation metrics computed for the SDSS observed photometric SNe Ia sample both with and without a host galaxy photo- $z$ prior. The best results for each metric and dataset are shown in bold. . . . .	142
TABLE 6.1	Contrastive pretraining with standard fine-tuning substantially improves OOD performance for CAMELYON17-WILDS but is not as effective for iWILDCAM-WILDS. Results are averaged over 15 trials for iWILDCAM-WILDS and 20 trials for CAMELYON17-WILDS, and we report the 95% confidence intervals on each mean estimate. . .	152
TABLE 6.2	Empirically estimated connectivity measures for iWILDCAM-WILDS and CAMELYON17-WILDS. From Shen et al. (2022), contrastive pretraining theoretically learns transferable representations for UDA when both across-domain ( $\alpha$ ) and across-class ( $\beta$ ) connectivity is greater than across-both ( $\gamma$ ), using notation from (Shen et al., 2022). In iWILDCAM-WILDS, across-both connectivity $>$ across-class, which violates the condition, while CAMELYON17-WILDS satisfies the condition. . . . .	153
TABLE 6.3	ID and OOD accuracy (%) for ASTROCLASSIFICATION and RMSE for REDSHIFTS of each method. Results are averaged over 5 trials and rows with means within 1 STD of the best mean are bolded. . . . .	160
TABLE 6.4	ID and OOD performance for each method on iWILDCAM-WILDS and CAMELYON17-WILDS. Results are averaged over 15 trials for iWILDCAM-WILDS and 20 trials for CAMELYON17-WILDS, and we report 95% confidence intervals on each mean estimate. Rows with means within 1 interval of the best mean are bolded. . . .	160
TABLE 6.5	Scaling up model size of Connect Later produces improvements in both ID and OOD performance on the ASTROCLASSIFICATION task. . . . .	162
TABLE 6.6	Linear probing (LP) in addition to fine-tuning (FT) hurts performance for the ERM+targeted augs model but improves performance for Connect Later (tested on the ASTROCLASSIFICATION task). . . . .	163
TABLE 6.7	Empirically estimated connectivity measures for iWILDCAM-WILDS, ASTROCLASSIFICATION, and CAMELYON17-WILDS. iWILDCAM-WILDS and ASTROCLASSIFICATION results are averaged over 15 randomly selected class-domain pairs, while CAMELYON17-WILDS results are averaged over all possible class-domain pairs. .	172

## LIST OF ILLUSTRATIONS

FIGURE 1.1	The near-linear velocity-distance relation discovered by Hubble through observations of “standard candle” Cepheid variable stars in 24 extragalactic nebulae (adapted from Hubble, 1929). . . . .	2
FIGURE 1.2	Evolution of radiation, matter, and dark energy (modeled as a cosmological constant) energy density as a function of the scale factor $a$ . . . . .	4
FIGURE 1.3	Constraints on $\Omega_m-w$ for the flat $w$ CDM model (68% and 95% confidence intervals). SN contours are shown with only statistical uncertainty (white-dashed) and with total uncertainty (green-shaded). Constraints from CMB (brown) and 3-year DES-SN+CMB combined (red) are also shown. Adapted from Abbott et al. (2019a). . . . .	8
FIGURE 1.4	$\chi^2$ contours representing constraints on the $\Lambda$ CDM model with a single observed SN Ia at different redshifts. . . . .	9
FIGURE 1.5	$\chi^2$ contours representing constraints on the $\Lambda$ CDM model with $N_{\text{Ia}}$ observed SNe Ia at uniformly sampled redshifts $z \in [0, 1]$ . . . . .	9
FIGURE 1.6	Results from Perlmutter et al. (1999): (top left) Hubble diagram of 42 high redshift SNe Ia from the Supernova Cosmology Project plotted over theoretical expectations for different choices of $(\Omega_\Lambda, \Omega_m)$ ; (top right) Constraints on $\Omega_\Lambda - \Omega_m$ for the $\Lambda$ CDM model; (bottom) constraints on $w - \Omega_m$ for the flat $w$ CDM model. . . . .	10
FIGURE 1.7	Results from DES Collaboration et al. (2024): (top) Hubble diagram of 1,635 high redshift SNe Ia from the DES 5-year (DES5YR) sample colored by the SN Ia probability assigned by the photometric classifier; (bottom left) Constraints on $\Omega_\Lambda - \Omega_m$ for the $\Lambda$ CDM model; (bottom right) constraints on $w - \Omega_m$ for the flat $w$ CDM model. . . . .	12
FIGURE 1.8	Projected redshift distribution of SNe Ia discovered by LSST and the Roman Space Telescope in one observing year. . . . .	13
FIGURE 1.9	<i>Upper panel:</i> Lightcurves of low-redshift supernovae discovered by the Calan/Tololo Supernova Survey. <i>Lower panel:</i> The same lightcurves after calibrating the supernova brightness using the “stretch” of the timescale of the lightcurve as an indicator of brightness and the color at peak as an indicator of dust absorption. Adapted from Perlmutter (2012). . . . .	15
FIGURE 2.1	Raw $ugrizY$ lightcurve data with the Gaussian process model at corresponding wavelengths and resulting heatmap and error heatmap for a type Ia SN. The shaded regions in the Gaussian process plots represent the Gaussian process error. . . . .	30
FIGURE 2.2	Example flux heatmaps for each supernova type. . . . .	31
FIGURE 2.3	SCONE architecture for binary and categorical classification. . . . .	35
FIGURE 2.4	Confusion matrix showing average and standard deviation over five runs for binary classification on the test set. . . . .	36
FIGURE 2.5	Semilog plot of the ROC curve for binary classification on the test set. . . . .	37
FIGURE 2.6	Test set accuracies for each choice of wavelength and time bins. . . . .	37

FIGURE 2.7	Confusion matrix showing average and standard deviation over five runs for categorical classification on the balanced test set. . . . .	40
FIGURE 2.8	Confusion matrix showing average and standard deviation over five runs for categorical classification on the PLAsTiCC (imbalanced) test set. . . . .	40
FIGURE 3.1	An SNII ( $z = 0.39$ ) shown in all five heatmap datasets along with the lightcurves and Gaussian process fits used to create each heatmap. The flux and flux error measurements from the raw photometry are shown as points with error bars, while the Gaussian process fits to each photometry band are shown as curves. The Gaussian process errors, which are used to create the heatmaps in the middle column, are not shown in the lightcurve plots. The $x$ -axis limit of the plots in each row are different, as the lightcurve is truncated according to the label on the left for each row in the figure. . . . .	51
FIGURE 3.2	SCONE architecture with redshift information for categorical early lightcurve classification. . . . .	54
FIGURE 3.3	Accuracy/efficiency over time for each supernova type without redshift (left) and with redshift (right) for the $t_{\text{trigger}} + N$ test datasets. The values used in this plot correspond with the diagonals on each normalized confusion matrix in Figure 3.4. . . . .	57
FIGURE 3.4	Normalized confusion matrices produced by SCONE without (left) and with (right) redshift for the $t_{\text{trigger}} + \{0, 5, 50\}$ test sets (heatmaps created from lightcurves truncated at 0, 5, and 50 days after the date of trigger). These matrices were made with test set classification performance from 5 independent runs of SCONE. . . . .	60
FIGURE 3.5	Receiver operating characteristic (ROC) curves produced by SCONE without (left) and with (right) redshift for the $t_{\text{trigger}} + \{0, 5, 50\}$ test sets (heatmaps created from lightcurves truncated at 0, 5, and 50 days after the date of trigger). . . . .	61
FIGURE 3.6	Area under the ROC curve (AUC) without (left) and with (right) redshift over time for each supernova type. . . . .	62
FIGURE 3.7	Distribution of $t_{\text{trigger}} - t_{\text{first detection}}$ in a SCONE test dataset of 4608 SNe. . . . .	63
FIGURE 3.8	Normalized confusion matrices produced by SCONE without (left) and with (right) redshift for the $t_{\text{trigger}} \leq t_{\text{first detection}} + 5$ subset of the $t_{\text{trigger}} + 0$ test set. This cut ensures that the lightcurves used for performance evaluation are not given substantially more information than those created with the first detection trigger definition. . . . .	63
FIGURE 3.9	Normalized confusion matrices produced by the baseline MLP model without (left) and with (right) redshift for the $t_{\text{trigger}} + 0$ test set (heatmaps created from lightcurves truncated at the date of trigger). . . . .	65
FIGURE 3.10	Early epoch confusion matrices with (right) and without (left) redshift for the bright supernovae ( $< 20$ magnitude) in each $t_{\text{trigger}} + N$ dataset. SCONE was trained with a class-balanced $t_{\text{trigger}} + N$ training set combined with 40% of $< 20$ magnitude supernovae. These confusion matrices were created by testing the trained SCONE model on the full $< 20$ magnitude supernovae dataset. The confusion matrices are colored according to normalized accuracies, as in Figure 3.4, and are overlaid with absolute (non-normalized) values since the dataset is imbalanced. . . . .	67

FIGURE 3.11	Test set accuracy/efficiency without (left) and with (right) redshift over time for SCONE trained on the mixed dataset and tested on each individual $t_{\text{trigger}} + N$ dataset. The values used in these plots correspond with the diagonals on a normalized confusion matrix. . . . .	68
FIGURE 3.12	Area under the ROC curve (AUC) without (left) and with (right) redshift over time for SCONE trained on the mixed dataset and tested on each individual $t_{\text{trigger}} + N$ dataset. . . . .	69
FIGURE 4.1	An illustration adapted from Gupta et al. (2016) showing an example of a challenging host galaxy matching problem. The supernova (labeled "SN") is closer in angular separation (red arrows) to the smaller galaxy on the right, but it is closer to the edge of the larger galaxy on the left. The directional light radius (DLR) of each galaxy is shown in the blue arrows. According to the DLR method, the most likely host galaxy is the one with minimal $d_{\text{DLR}}$ value, or ratio of the angular separation to the DLR, which would correctly identify the larger galaxy on the left as the more likely host. . . . .	77
FIGURE 4.2	$i$ -band MAG_MODEL magnitude distribution of all galaxies in our deep DES galaxy catalog with a spectroscopic or photometric redshift estimate. The catalog cuts off at $i \sim 26$ because photometric redshifts are unavailable for galaxies fainter than $i = 25.5$ mag. . . . .	81
FIGURE 4.3	Redshift distribution of matched host galaxies in one realization of the SNIa-only simulations. Since we find the mismatch rate resulting from the DLR method to be quite low (see Table 4.3), the true redshift distribution is not visibly different and was not included in this plot. . . . .	88
FIGURE 4.4	Parameter distributions of matched host galaxies in one realization of the SNIa-only simulations split into two populations: galaxies with spectroscopic redshifts and those with photometric redshift estimates only. Details and definitions of these parameters can be found in Section 4.5.2. Since we find the mismatch rate resulting from the DLR method to be quite low (see Table 4.3), the true distributions are not visibly different and were not included in this plot. . . . .	88
FIGURE 4.5	Redshift differences ( $\Delta z \equiv z_{\text{match}} - z_{\text{true}}$ ) for simulated SNe Ia with mismatched hosts. (left) $\Delta z$ as a function of $z_{\text{true}}$ for the full simulated sample prior to applying any selection cuts. (right) $\Delta z$ as a function of $z_{\text{true}}$ after all selection cuts (described in Section 4.4.2) and removal of SNe without a valid bias correction (described in Section 4.6.2). Our selection process not only reduces the mismatch rate (see Table 4.3) but also removes SNe with extremely biased redshift estimates from mismatched hosts, reducing the spread in $\Delta z$ . Quantitatively, the spread in $z_{\text{match}} - z_{\text{true}}$ characterized by the middle 90% of the distribution is reduced from 1.1 before cuts to 0.6 after cuts. . . . .	91

FIGURE 4.6	Histograms comparing our simulated SNe Ia against DES Y5 photometrically confirmed SNe Ia for angular SN-galaxy separation ( $\Delta\theta$ , arcsec), directional light radius (DLR), the DLR-normalized SN-galaxy separation ( $d_{\text{DLR}} = \frac{\Delta\theta}{\text{DLR}}$ ), and $r$ -band host galaxy magnitude ( $m_{r,\text{gal}}$ ) (see Section 4.5 for explanations of each). For ease of comparison, the simulation histograms are normalized to match the integral of the data histogram and the $x$ axis limits of each histogram are determined by the middle 90% of the data distribution to remove outliers. In both rows, points with error bars represent parameter distributions measured from the DES data and filled or unfilled histograms represent the analogous quantities for simulations. (top row) Histograms of parameter values for closest host galaxy match (HOSTGAL1) for SNe with only one host galaxy match. (bottom row) Histograms of parameter values for closest (HOSTGAL1) and second closest (HOSTGAL2) host galaxy match for SNe with 2 or more host galaxy matches. . . . .	93
FIGURE 4.7	Distributions of the ratio $r_{\text{DLR}} = \frac{d_{\text{DLR,HOSTGAL1}}}{d_{\text{DLR,HOSTGAL2}}}$ . . . . .	95
FIGURE 4.8	Biases in binned Hubble residuals for the SN Ia-only sample between samples with and without mismatched host galaxies, $\Delta\mu = \mu_{\text{match}} - \mu_{\text{truehost}}$ , as a function of redshift. Uncertainties are shown as the shaded region and calculated from the binned standard deviations of $\mu_{\text{match}}$ and $\mu_{\text{truehost}}$ . Lines showing $\Delta w = \pm 0.03$ are also plotted for reference. . . . .	99
FIGURE 4.9	Hubble diagram for a single realization of our SNIa-only simulation with matched hosts. This realization has 79 SNe matched to an incorrect host out of 5,811 total SNe, a 1.4% mismatch rate. The low- $z$ sample is omitted from this plot, since it is not part of the main DES sample. . . . .	99
FIGURE 4.10	Binned Hubble residuals ( $\mu_{\text{match}} - \mu_{\text{model}}$ ) for all 25 realizations of our SNIa-only simulation with mismatch. The percentages in the legend show the fraction of the sample represented by each population in the plot. . . . .	100
FIGURE 4.11	Visualization of the impact of incorrect redshifts on $\text{SNN}_{+Z}$ predictions. $\Delta P_{\text{Ia}} = P_{\text{Ia,wronghost}} - P_{\text{Ia,correcthost}}$ is the difference between $P_{\text{Ia}}$ values output by the $\text{SNN}_{+Z}$ classifier given the wrong host redshift ( $P_{\text{Ia,wronghost}}$ ) and the correct host redshift ( $P_{\text{Ia,correcthost}}$ ) for SNe with mismatched hosts. $\Delta P_{\text{Ia}}$ values are plotted against the difference between the distance modulus $\mu$ calculated at the wrong ( $\mu(z_{\text{match}})$ ) and correct host redshifts ( $\mu(z_{\text{true}})$ ). As $\mu(z_{\text{match}}) - \mu(z_{\text{true}})$ deviate from 0, we would expect larger deviations in $P_{\text{Ia}}$ values, i.e. $ \Delta P_{\text{Ia}}  > 0$ . Non-Ia SNe (orange points) more likely to be misclassified as Ia with the wrong redshift will appear in the upper half of the plot ( $\Delta P_{\text{Ia}} > 0$ ), whereas SNe Ia (blue points) more likely to be misclassified as non-Ia with the wrong redshift will appear in the lower half. 7% of mismatched SNe are incorrectly classified as a result of wrong host redshifts, leading to an overall 0.1% reduction in classification accuracy compared to a simulation with correct host redshifts. . . . .	102
FIGURE 4.12	Biases in binned Hubble residuals for all 4 photometric classifiers between samples with and without host galaxy mismatch. Uncertainties are shown as the shaded region and calculated from the binned standard deviations of $\mu_{\text{match}}$ and $\mu_{\text{truehost}}$ . Lines showing $\Delta w = \pm 0.03$ are also plotted for reference. . . . .	103



FIGURE 4.13	Binned Hubble residuals, $\Delta\mu = \mu_{\text{match}} - \mu_{\text{model}}$ , for the 4 photometric classifiers for our SNIa+CC simulation with mismatch. (top) SN populations classified as SNe Ia by each photometric classifier, including true SNe Ia with mismatched hosts as well as core collapse contamination. (bottom) SN populations classified as CC SNe, including SNe with mismatched hosts. . . . .	103
FIGURE 4.14	Cosmological contours computed with one realization of simulated DES Y5 SNe Ia with (red) and without host galaxy mismatch (gray). (top) SN+CMB contours, in which an approximate CMB prior $\Omega_m = 0.311 \pm 0.010$ prior is applied (see Section 4.6.3 for details). This results in good agreement between the two contours. (bottom) SN-only contours showing a substantial shift in best fit $w, \Omega_m$ between the two contours. . . . .	106
FIGURE 4.15	Distributions of $HC$ values for SNe with wrong and correct host matches. The dotted line is drawn at our chosen threshold of $HC = -2.5$ . . . . .	109
FIGURE 4.16	$\Delta w$ values from all tested variants of simulated DES SNe with CMB prior. Note that the total uncertainty on $w$ from the DES3YR analysis (Abbott et al., 2019b), $\delta w = 0.059$ , is much larger than the bounds of this plot. Details about each variant can be found in Section 4.7. . . . .	110
FIGURE 5.1	True redshift distribution of the 73,620 simulated SNe Ia in the LSST (PLAsTiCC) training dataset (left) and 4,057 simulated SNe Ia in the test dataset (right). . . . .	115
FIGURE 5.2	True redshift distribution of the 135,521 simulated SNe Ia in the SDSS training dataset (left) and the 5,274 simulated SNe Ia and 489 observed photometrically confirmed SNe Ia in the SDSS test sets (right). . . . .	117
FIGURE 5.3	Examples of a low (left), medium (middle), and high (right) redshift simulated PLAsTiCC SN. ( <b>top panel</b> ) The multi-band lightcurves are shown in colored points, with Gaussian process predictions and uncertainties for this lightcurve shown in colored lines and shaded regions, respectively. ( <b>bottom panel</b> ) The flux matrix created from the lightcurve in the top panel (see §5.2.2 for details). Large flux values are colored in yellow while lower flux values are in dark blue. The physical effects of redshifting, including longer wavelengths and longer transient durations, are observed in the flux matrices in the downward (towards higher wavelengths) shift of the yellow high flux region and the increased width of the yellow region with increasing redshift. . . . .	122
FIGURE 5.4	The model architecture developed for this work, described in the text in §5.3.3. A layer shown in the figure as " $h \times d$ conv, $n_{\text{filters}}$ " is a 2D convolutional layer with a kernel size of $h \times d$ and $n_{\text{filters}}$ filters. Similarly, " $h \times d, n_{\text{filters}}$ resid block" defines a residual block containing two $h \times d$ conv, $n_f$ convolutional layers. "fc $n_{\text{nodes}}$ " denotes a fully connected layer with $n_{\text{nodes}}$ nodes. The pooling layers apply max pooling, downsampling both the height and width by 2. The output softmax layer has $N_z$ nodes, $N_z = 50$ for SDSS and $N_z = 150$ for LSST. . . . .	126
FIGURE 5.5	Reliability diagram showing PLAsTiCC model calibration before and after temperature scaling. . . . .	129

FIGURE 5.6	Examples of a high accuracy ( $\Delta z < 0.005$ , top), medium accuracy ( $0.01 \leq \Delta z \leq 0.05$ , middle), and outlier ( $\Delta z > 0.05$ , bottom) lightcurve and Gaussian process fit from the SDSS spectroscopic sample and their predicted PDFs. The true (spectroscopic) redshift is shown in the black dotted line, while the predicted redshift (mean(PDF)) is shown in orange. The medium and poor accuracy lightcurves have larger errors and scatter than the high accuracy lightcurve, and the low accuracy lightcurve appears to have much fewer points.	130
FIGURE 5.7	Mean binned residuals $\Delta z$ as a function of true redshift $z_{\text{true}}$ for the PLAsTiCC simulated SNe Ia test set. Predictions from our model have much lower biases as well as scatter compared to predictions from LCFIT+Z. The max(PDF) and mean(PDF) point estimates for our model also agree quite well, resulting in similar $\Delta z$ values. Dotted lines are plotted at $\Delta z = \pm 0.02$ for reference.	132
FIGURE 5.8	Predicted vs. true redshifts for the PLAsTiCC simulated SNe Ia sample colored by the fraction of each sample represented by each point. <b>(left)</b> Predictions from Photo- $z$ SNthesis described in this work, <b>(right)</b> predictions from LCFIT+Z.	133
FIGURE 5.9	Mean binned residuals $\Delta z$ as a function of true redshift $z_{\text{true}}$ for the SDSS simulated and real SNe Ia samples. Predictions from this work have much lower biases as well as scatter compared to predictions from LCFIT+Z. We also show that two common methods of condensing redshift PDFs into point estimates, max(PDF) and mean(PDF), resulting in similar errors for our model. Dotted lines are plotted at $\Delta z = \pm 0.02$ for reference.	135
FIGURE 5.10	Predicted vs. true redshifts for the SDSS simulated and real SNe Ia samples colored by the fraction of each sample represented by each point. <b>(Top row)</b> Predictions from Photo- $z$ SNthesis described in this work, <b>(bottom row)</b> predictions from LCFIT+Z.	136
FIGURE 5.11	Predicted redshift error, $\Delta z$ , as a function of true redshift, $z_{\text{true}}$ , for the SDSS real SNe Ia sample with and without bias correction computed from the simulated results. The point estimates used in this figure are computed using the mean(PDF) method. Dotted lines are plotted at $\Delta z = \pm 0.02$ for reference.	137
FIGURE 5.12	An illustration of our estimated cosmological biases arising from photo- $z$ errors. <b>(top)</b> A Hubble diagram zoomed in to the neighborhood of $z_{\text{model}} = 1$ showing a fiducial cosmology (green: $w = -1, \Omega_m = 0.3$ ) and two biased cosmologies (pink: $\Delta w = -0.03$ , orange: $\Delta w = +0.03$ ). The dashed black line shows the distance modulus value at $z_{\text{model}} = 1$ for the fiducial cosmology, $\mu_{\text{model}}(z_{\text{model}} = 1)$ . The two dotted lines show the redshifts that correspond to the value of $\mu_{\text{model}}(z_{\text{model}} = 1)$ for the two biased cosmologies, i.e. $\mu_{\text{model}}(z_{\text{model}} = 1) = \mu_{\Delta w = -0.03}(z = 0.99528) = \mu_{\Delta w = +0.03}(z = 1.00486)$ . The values of these redshifts are labeled on the redshift axis. We approximate the redshift error required to create a bias of, e.g. $\Delta w = +0.03$ , as the difference between the biased and fiducial redshift values, $dz_{\text{bias}} = 1 - 1.00486 = -0.00486$ . <b>(bottom)</b> $\Delta z = dz/(1+z)$ values for various choices of $\Delta w$ , compared to the mean binned residuals $\Delta z$ produced by the mean point estimates of Photo- $z$ SNthesis PDFs (pink, reproduced from Figure 5.7).	139

FIGURE 5.13	Mean binned residuals, $\Delta z \equiv \frac{z_{\text{pred}} - z_{\text{true}}}{1 + z_{\text{true}}}$ , as a function of true redshift, $z_{\text{true}}$ , for the SDSS observed photometric SNe Ia sample. Errors from both Photo- $z$ SNthesis and LCFIT+Z are shown with (darker) and without (lighter) a prior on $z_{\text{pred}}$ from the host galaxy photometric redshift. The lighter (no prior) curves are identical to those in Figure 5.9, with the max(PDF) curves omitted for clarity. . . . .	143
FIGURE 5.14	Mean binned residuals, $\Delta z \equiv \frac{z_{\text{pred}} - z_{\text{true}}}{1 + z_{\text{true}}}$ , as a function of true redshift, $z_{\text{true}}$ , for the DES3YR SNe Ia sample produced by a model trained on the PLAS-TiCC dataset. The max(PDF) and mean(PDF) methods of obtaining point estimates from Photo- $z$ SNthesis PDFs are described in §5.4.1. . . . .	145
FIGURE 5.15	Mean binned SALT2 color, $c$ , as a function of predicted redshift, $z_{\text{pred}}$ , for the Photo- $z$ SNthesis prediction outliers and non-outliers in the SDSS observed photometric SN Ia sample. . . . .	146
FIGURE 6.1	Overview of the Connect Later framework for domain adaptation applied to a toy binary classification problem with two domains (filled and unfilled points), showing the representations from contrastive pretraining in $\mathbb{R}^2$ . <b>(Left)</b> After contrastive pretraining with generic augmentations, the classes within each domain are linearly separable in representation space. Since the domains are far apart in input space, generic augmentations may not connect the domains, resulting in misalignment in the pretrained representations. In this case, a classifier (with a linearly extrapolating decision boundary, dashed and solid line) learned on labeled source data will misclassify the target data. <b>(Right)</b> Connect Later employs targeted augmentations (filled points with black border), which are designed with knowledge of the distribution shift, to connect the domains better, resulting in a classifier that generalizes well to the target domain. . . . .	150
FIGURE 6.2	An example from the source dataset (left), an augmented version of the source example (middle), and an example from the target dataset (right) for our 3 tasks. <b>(Top row)</b> The target dataset in ASTROCLASSIFICATION and REDSHIFTS is much higher redshift than the source dataset. We apply the redshifting augmentation to simulate placing source objects at a higher redshift to better match the target dataset. The flux errors and flux values of the augmented example (middle) show much better resemblance of the target example. <b>(Bottom row)</b> The iWILDCAM-WILDS target dataset is composed of images from cameras unseen during fine-tuning, which are in potentially new habitats, so we randomize the habitat background by applying the Copy-Paste Same Y augmentation. This algorithm places source dataset animals into empty backgrounds from other cameras that have observed the same species. iWILDCAM-WILDS image examples shown here are from Gao et al. (2023). . . . .	155
FIGURE 6.3	On the ASTROCLASSIFICATION task, Connect Later is relatively robust to pre-training masking percentage both ID and OOD, but 60% masking performs best out of the percentages we tested. . . . .	163
FIGURE 6.4	Redshift distributions of source, augmented, and target datasets for the ASTROCLASSIFICATION and REDSHIFTS tasks. . . . .	168

FIGURE 6.5 Example distribution of data and augmentations for contrastive learning where Connect Later improves OOD performance over contrastive pretraining+standard fine-tuning and ERM+targeted augmentations. The augmentation graph is similar to Shen et al. (2022) except the edge weights connecting 1,2 and 3,4 are swapped. The shapes represent classes, while the labeled data is shaded in green. The generic augmentation probabilities are marked as edge weights, where we assume that  $\alpha > \gamma + \beta$ . Here, targeted augmentations which first swap inputs 1 and 2 before applying a generic augmentation help to align the source and target. However, some target inputs are not reachable via augmentations from source inputs. Standard fine-tuning can generalize throughout the target domain, but only in conjunction with targeted augmentations that align the source and target. The orange dotted lines on the far ends connect to each other (the graph wraps around). . . . . 174

# CHAPTER 1

## Introduction

### 1.1. We live in an expanding universe!

This year marks the 100<sup>th</sup> anniversary of Edwin Hubble’s monumental discovery that the universe doesn’t stop at the edge of our Milky Way – in fact, it contains “hundreds of thousands” of other stellar systems just like our own (New York Times, 1924). In other words, the universe is vast beyond imagination.

This marked the first of many notable discoveries made with *standard candle* distance measurements: a distance estimation technique using apparent brightness measurements of objects with known luminosity. Hubble used Cepheid variable stars, which had been established as standard candles following the discovery of the period-luminosity relation (Leavitt, 1908), enabling luminosity standardization for these stars. Estimated distances to 36 Cepheids in modern-day Andromeda and Triangulum galaxies revealed that these “nebulae” (now called galaxies) were far more distant than the edge of the Milky Way. Hubble concluded that these “extra-galactic nebulae [...] are now recognized as systems complete in themselves” (Hubble, 1926): that “spiral nebulae [...] are in reality distant stellar systems, or ‘island universes’” (New York Times, 1924).

That same year, Swedish astronomer Knut Lundmark became the first to measure distances to extragalactic nebulae, albeit using an unproven method of comparing apparent diameters to that of Andromeda, which he assumed had a “known” distance. He concluded that “more distant spirals have higher space-velocity” (Lundmark, 1925), a foreshadowing of Hubble’s next impactful discovery.

In the next five years, Hubble estimated distances to Cepheids in 24 extragalactic nebulae and combined these with radial velocities estimated from redshifts (Slipher, 1917) to discover that there was an approximately linear relationship between distance ( $d$ ) and radial velocity ( $v$ ) – nebulae are moving away from us at a rate proportional to their distance (Hubble, 1929). This simple

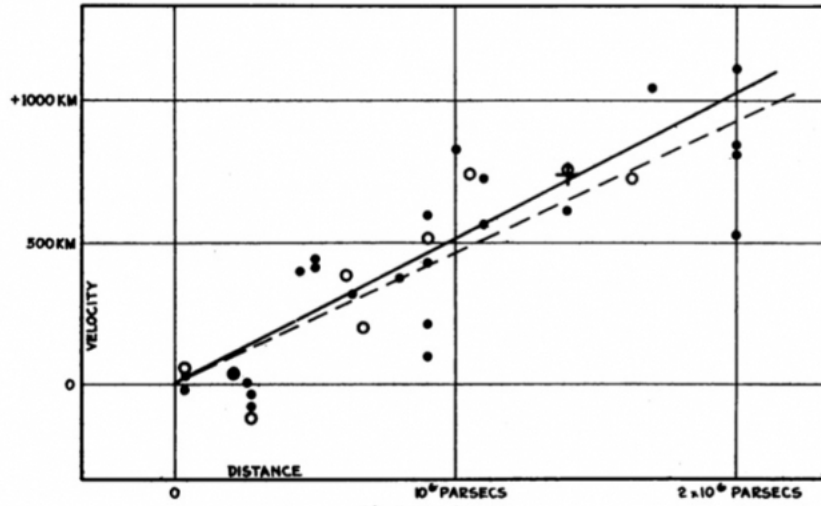


FIGURE 1  
Velocity-Distance Relation among Extra-Galactic Nebulae.

Figure 1.1: The near-linear velocity-distance relation discovered by Hubble through observations of “standard candle” Cepheid variable stars in 24 extragalactic nebulae (adapted from Hubble, 1929).

relationship,

$$v = H_0 d, \quad (1.1)$$

was theorized two years earlier by a Belgian priest named Georges Lemaître (Lemaître, 1927) and is known as the Hubble-Lemaître Law. These results provided the first observational proof for an expanding universe (Figure 1.1).

This conclusion was completely revolutionary for a scientific community, including Albert Einstein, that was convinced our universe was static. The theorized static universe consisted of gravitational attraction between massive bodies perfectly counterbalanced by a repulsive vacuum energy component, or “cosmological constant”, a mathematical trick introduced by Einstein in the equations of general relativity to allow for static solutions. In light of Hubble’s findings, Einstein abandoned his static universe and famously remarked in 1932 that the introduction of the cosmological constant was his “greatest blunder”.

The notion of a cosmological constant was largely dismissed for the ensuing 60 years as the sci-

entific consensus settled uneasily to that of a contracting universe, in which gravitational attraction above a critical matter density will eventually slow and reverse the expansion, causing the universe to collapse in on itself. However, measuring this deceleration parameter requires high-powered telescopes that can look further out and detect slight deviations to the linear velocity-distance relation found by Hubble. In the 1990s, when a combination of new technology (the 4-meter Victor Blanco telescope at Cerro Tololo) and new science (the replacement of Cepheids with their brighter cousins, type Ia supernovae, for distance measurement) finally made the first measurement of the deceleration parameter possible, scientists found the exact opposite of what they expected. Analyses by Riess (1998) and Perlmutter et al. (1999) showed that the deceleration parameter was negative, indicating that the expansion of the universe is, in fact, *accelerating*. This groundbreaking result once again revolutionized our understanding of the cosmos and was awarded the 2011 Nobel Prize in Physics. Today, this result has been bolstered by observations of thousands more type Ia supernovae as well as other cosmological probes, but the explanation for the accelerating expansion remains a mystery. A leading hypothesis is that of “dark energy”, an unknown form of energy that drives accelerated cosmic expansion and may be explained by the infamous cosmological constant postulated by Einstein more than a century ago.

### 1.1.1. Cosmological Framework

The theoretical groundwork for an expanding universe was laid in 1922, when Alexander Friedmann derived the now-famous Friedmann equations from general relativity. A universe that is homogeneous and isotropic on large scales can be described by the Friedmann-Lemaître-Robertson-Walker (FLRW) metric, in which the expansion (or contraction) of space is governed by a time-dependent scale factor,  $a(t)$ . Assuming the FLRW metric and a universe filled with a perfect fluid with energy density  $\rho$  and pressure  $p$ , Friedmann reduced Einstein’s field equations to two equations that model cosmic evolution:

$$\frac{\ddot{a}}{a} = \frac{-4\pi G}{3}(\rho(a) + 3p(a)) \quad (1.2)$$

$$\left(\frac{\dot{a}}{a}\right)^2 \equiv H(a)^2 = \frac{8\pi G}{3}\rho(a) - \frac{\kappa}{a^2}. \quad (1.3)$$

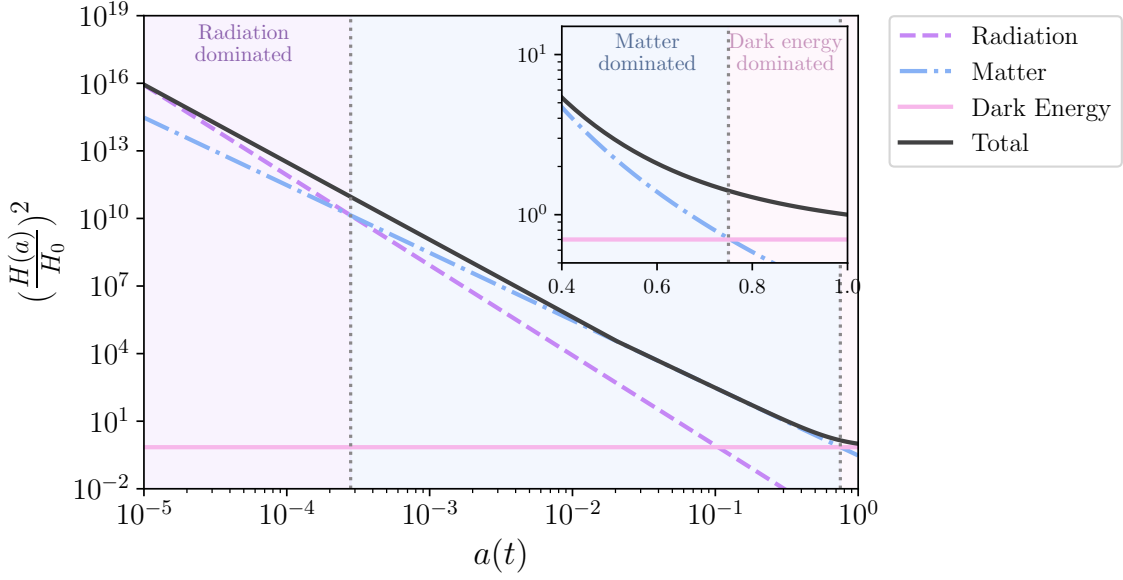


Figure 1.2: Evolution of radiation, matter, and dark energy (modeled as a cosmological constant) energy density as a function of the scale factor  $a$ .

Here, we set  $c = 1$ , we define the Hubble parameter as  $H(a) \equiv \frac{\dot{a}}{a}$ ,  $\kappa$  parameterizes the curvature of the universe, and  $G$  is Newton's gravitational constant.

Moreover, the perfect fluid assumption relates  $\rho$  and  $p$  via the equation of state  $p = w\rho$ , where  $w$  depends on the nature of the fluid. Then, the solution to the fluid equation for arbitrary  $w$  is

$$\rho(a) \propto \exp\left(3 \int_a^1 \frac{1 + w(a')}{a'} da'\right). \quad (1.4)$$

We know that the universe contains non-relativistic matter ( $w_m = 0$ ) which dilutes as  $\rho_m \propto a^{-3}$ , and radiation ( $w_r = 1/3$ ) which dilutes as  $\rho_r \propto a^{-4}$ . The current standard model of cosmology also postulates the presence of dark energy, which may be a cosmological constant ( $w_\Lambda = -1$ ) but the possibility of a time-varying  $w_\Lambda$  cannot be ruled out with the current data.

Finally, we introduce a convenient notation that expresses energy densities as a fraction of the critical energy density  $\rho_c$ , i.e. the total energy density for the universe to be flat ( $\kappa = 0$ ) given the



current value of the Hubble parameter  $H_0$ :

$$\Omega = \frac{\rho_0}{\rho_{c,0}} = \frac{8\pi G \rho_0}{3H_0^2} \quad (1.5)$$

The 0 subscripts denote present-day values of each parameter. We can now rewrite Equation 1.3 as

$$H(a)^2 = H_0^2 (\Omega_m a^{-3} + \Omega_r a^{-4} + \left\{ \begin{array}{ll} \Omega_\Lambda & \text{Cosmological Constant} \\ \Omega_\Lambda a^{-3(1+w_\Lambda)} & w_\Lambda \neq -1 \\ \Omega_\Lambda \exp\left(-3 \int_a^1 \frac{1+w(a')}{a'} da'\right) & \text{Time-varying } w_\Lambda \end{array} \right. ) \quad (1.6)$$

These 3 possibilities for  $w_\Lambda$  and the nature of dark energy correspond to 3 of the most widely-accepted cosmological models today:

- Flat  $\Lambda$ CDM: a flat universe consisting of non-relativistic matter, ultra-relativistic radiation, and a cosmological constant ( $w_\Lambda = -1$ )
- Flat  $w$ CDM: a flat universe consisting of non-relativistic matter, ultra-relativistic radiation, and dark energy described by a constant equation of state ( $w_\Lambda \neq -1$  but constant)
- Flat  $w_0 w_a$ CDM: a flat universe consisting of non-relativistic matter, ultra-relativistic radiation, and dark energy described by a time-varying equation of state, specifically of the form  $w_\Lambda(a) = w_0 + w_a(1 - a)$

This formulation of  $H(a)$  allows us to partition cosmic history into three discrete phases: a radiation-dominated phase at early times, followed by an extended matter-dominated phase, and finally, in the last  $\sim 5$  billion years we've entered a dark energy-dominated phase (Figure 1.2). Uncovering the nature and characteristics of dark energy, much of which remains a mystery today, is key to better understanding the future of our universe. A significant thrust of cosmology research today is towards increasingly precise measurements of  $w_\Lambda$  to constrain these possibilities.

### 1.1.2. Standard Candle Cosmology

Leavitt and Hubble pioneered the use of standard candles, celestial objects with a known luminosity, to measure distances at cosmological scales more than a century ago. This technique enabled the discoveries of cosmic expansion as well as its acceleration, and is still used today to make state-of-the-art measurements of cosmological parameters, such as  $\Omega_m$ ,  $w_0$ , and  $w_a$ .

We know that the comoving distance  $r$  traveled by light in an FLRW universe can be described by

$$r = -c \int_{a_e}^1 \frac{da}{a^2 H(a)}, \quad (1.7)$$

where  $a_e$  is the scale factor at emission and  $H(a)$  is defined as in Equation 1.6. After a change of variables to the cosmological redshift,  $z \equiv \frac{1}{a} - 1$ , we obtain

$$r = \frac{c}{H_0} \int_0^{z_e} \frac{dz}{E(z)}, \quad (1.8)$$

where  $E(z) \equiv H(z)/H_0$ .

Now that we have an expression relating cosmological parameters to distances, how does the standard candle method measure distance?

We know that the luminosity distance to an object is expressed by

$$d_L \equiv \sqrt{\frac{L}{4\pi f}}, \quad (1.9)$$

where  $L$  is an object's intrinsic luminosity and  $f$  is its observed flux. In a flat, expanding universe,

$$r = d_L(1 + z). \quad (1.10)$$

Since intrinsic luminosity is known for standard candles, we can leverage this machinery to constrain the cosmological parameters encoded in  $E(z)$ .

### 1.1.3. Complementary Cosmological Probes

While standard candles facilitated many groundbreaking cosmological discoveries, our understanding of cosmology today rests on the foundation of multiple independent cosmological probes.

#### **Cosmic Microwave Background**

The cosmic microwave background (CMB), discovered in 1965 by Arno Penzias and Robert Wilson, is the oldest light in the universe. It is a relic from the surface of last scattering, the moment when photons decoupled from the primordial plasma and the universe became transparent, around 370,000 years after the Big Bang or  $z \sim 1100$ . The CMB is one of the strongest pieces of observational evidence for the hot Big Bang theory and paved the way for further extensions (e.g. inflation) that explain the flatness, homogeneity, and isotropy of the universe.

Several decades later, it was discovered that the CMB was not perfectly isotropic, and the temperature anisotropies of order 0.1% are imprints of the primordial dark matter density distribution (Smoot et al., 1991). The first peak of the CMB temperature power spectrum carries information about curvature as well as baryon fraction of the universe, a complementary probe to standard candles, which are more sensitive to total matter density and dark energy. Figure 1.3 shows the complementary constraining power of CMB measurements compared with that of type Ia supernovae.

#### **Baryon Acoustic Oscillations**

Analogous to the standard candle distance measurement technique where distance information is extracted from comparing intrinsic vs. apparent luminosity, “standard rulers” are known intrinsic length scales that can be compared with observations of that length scale. An example of this is the size of the sound horizon at the epoch of recombination. Matter oscillations under the opposing effects of gravity and outward radiation pressure prior to photon decoupling created a universal clustering scale, imprinted as the first peak in the matter density power spectrum. A single BAO measurement requires surveying orders of magnitude more galaxies than are needed for standard candle measurements, but are much less affected by systematic uncertainties and can achieve higher precision (e.g., Bautista et al., 2020).

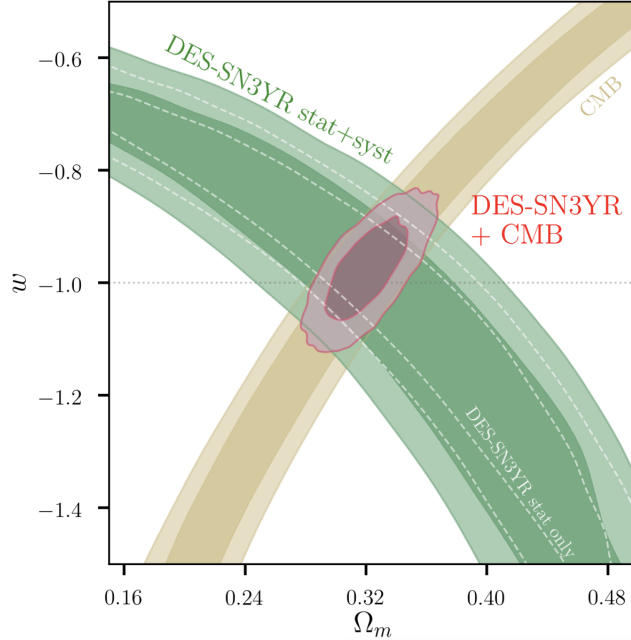


Figure 1.3: Constraints on  $\Omega_m$ - $w$  for the flat  $w$ CDM model (68% and 95% confidence intervals). SN contours are shown with only statistical uncertainty (white-dashed) and with total uncertainty (green-shaded). Constraints from CMB (brown) and 3-year DES-SN+CMB combined (red) are also shown. Adapted from Abbott et al. (2019a).

## 1.2. Cosmology with Type Ia Supernovae

Observations of type Ia supernovae (SNe Ia) led to the discovery of accelerating cosmic expansion (Riess, 1998; Perlmutter et al., 1999), and have become an established choice for cosmology with standard candles. They are standardizable ( $< 0.15$  mag scatter after standardization), bright and more easily visible at high redshifts ( $\sim -19$  mag in rest-frame  $B$  band), as well as frequent ( $\sim 1$  per galaxy per 2 centuries).

Astrophysically, they are thermonuclear explosions of white dwarfs and spectroscopically identified as SNe lacking hydrogen but showing strong silicon absorption lines. Little else can be firmly established about the SN Ia progenitor population or the physical mechanism of explosion. They are traditionally thought to arise from two possible progenitor scenarios: (1) “single degenerate”, in which a white dwarf accretes mass in a binary system and approaches the Chandrasekhar mass limit ( $M_\star \sim 1.4M_\odot$ ); and (2) “double degenerate”, in which two white dwarfs in a binary system

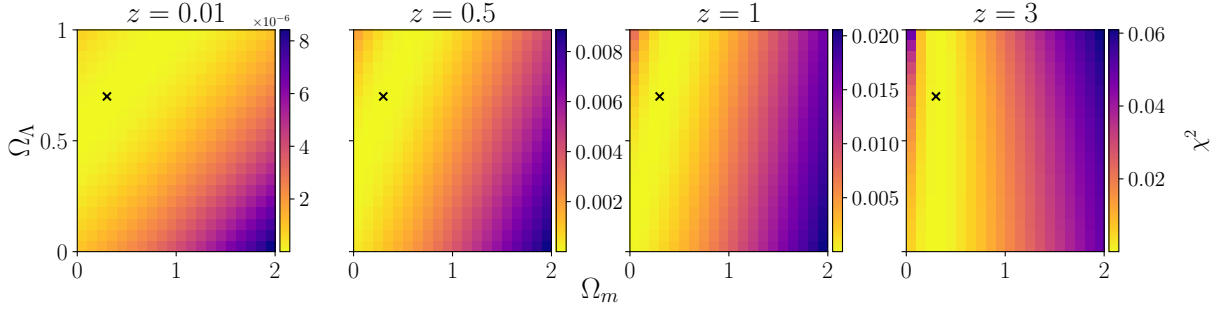


Figure 1.4:  $\chi^2$  contours representing constraints on the  $\Lambda$ CDM model with a single observed SN Ia at different redshifts.

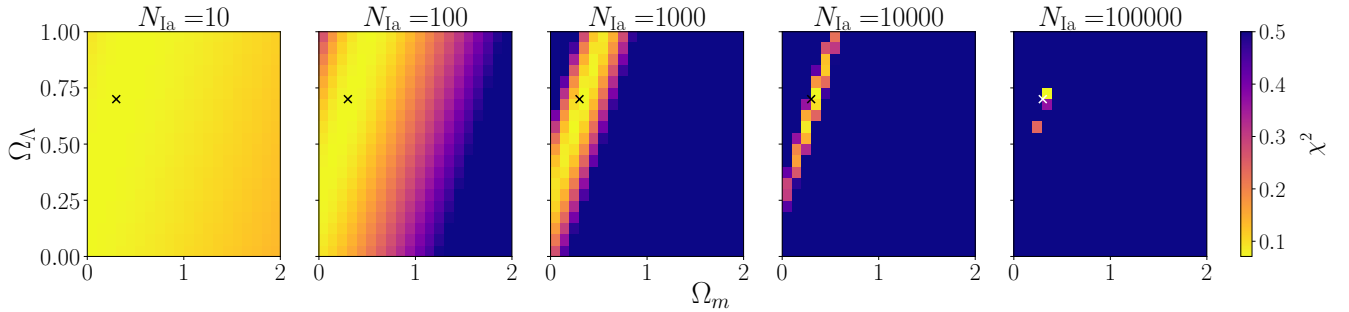


Figure 1.5:  $\chi^2$  contours representing constraints on the  $\Lambda$ CDM model with  $N_{\text{Ia}}$  observed SNe Ia at uniformly sampled redshifts  $z \in [0, 1]$ .

merge with combined mass greater than the Chandrasekhar limit. However, observations indicate a significant fraction of sub-Chandrasekhar mass explosions (see Wang and Han, 2012, for a review), clouding the picture.

### 1.2.1. Cosmological Parameter Constraints from SNe Ia

The constraining power of SNe Ia is explored in Figures 1.4 and 1.5. Figure 1.4 shows the cosmological constraining power of a single SN Ia observed at various redshifts. A single high redshift SN Ia is able to establish constraints on  $\Omega_m$ , but is not very effective at constraining  $\Omega_\Lambda$ . On the other hand, Figure 1.5 shows how the size of SNe Ia samples observed in the same redshift range affects their constraining power.

The initial discovery of dark energy and accelerating cosmic expansion was made with only 42 (Perlmutter et al., 1999) and 16 (Riess, 1998) high-redshift ( $0.18 < z < 0.82$ ) SNe Ia. The Hubble diagram made from the SNe Ia used in Perlmutter et al. (1999) is reproduced in Figure 1.6 (top

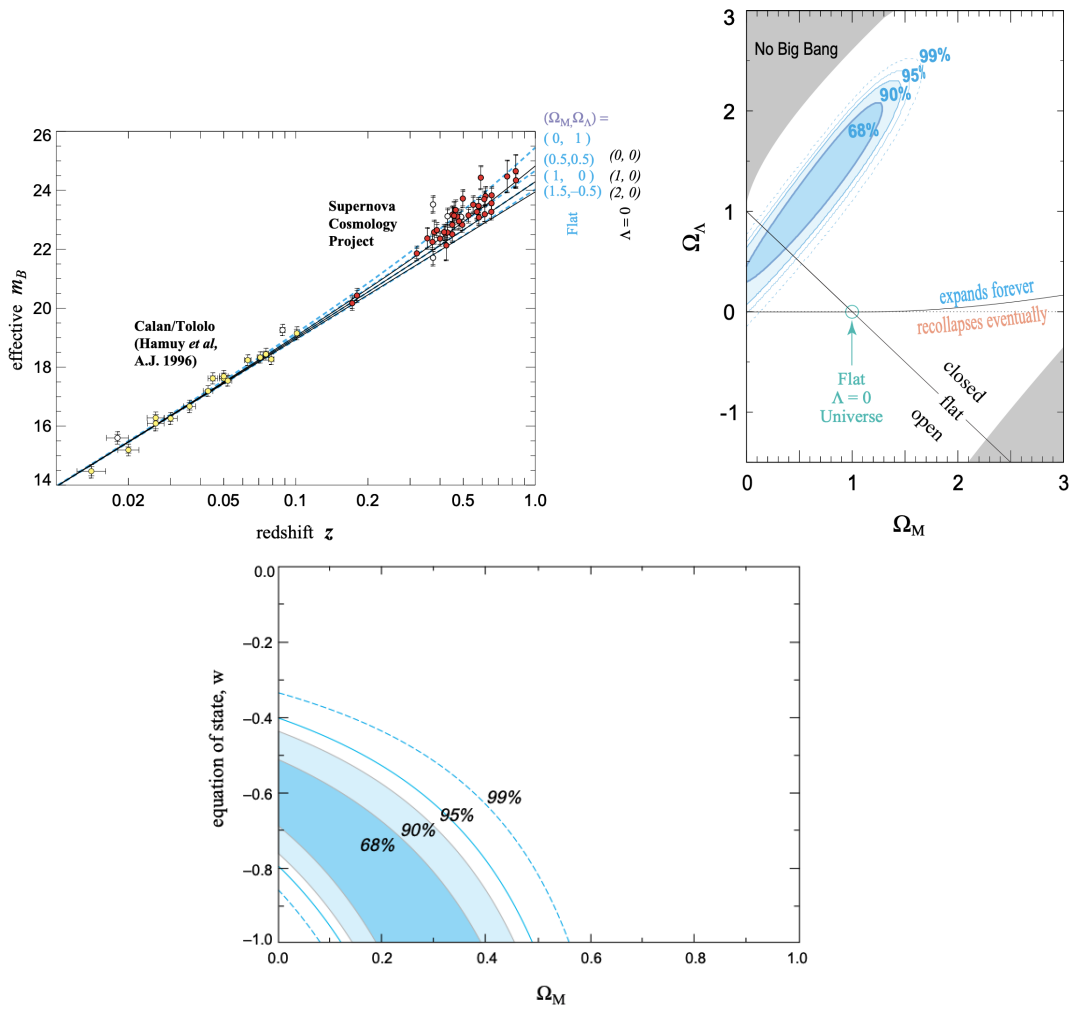


Figure 1.6: Results from Perlmutter et al. (1999): (top left) Hubble diagram of 42 high redshift SNe Ia from the Supernova Cosmology Project plotted over theoretical expectations for different choices of  $(\Omega_\Lambda, \Omega_m)$ ; (top right) Constraints on  $\Omega_\Lambda - \Omega_m$  for the  $\Lambda$ CDM model; (bottom) constraints on  $w - \Omega_m$  for the flat  $w$ CDM model.

left). These results confidently rejected the dark energy-free, flat  $\Lambda = 0$  universe model (Figure 1.6, top right) and found  $\Omega_m = 0.28^{+0.09}_{-0.08}$  assuming the flat  $\Lambda$ CDM model, but are not able to meaningfully constrain  $(\Omega_\Lambda, \Omega_m)$  for the  $\Lambda$ CDM model or  $(w, \Omega_m)$  for the flat  $w$ CDM model (Figure 1.6, bottom).

We have observed thousands of SNe Ia in the 25 years since through surveys such as the SuperNova Legacy Survey (SNLS, Guy et al., 2010a), Sloan Digital Sky Survey II (SDSS-II Kessler et al., 2009a), and Pan-STARRS (Rest et al., 2014). These SNe Ia samples from individual surveys have been combined by e.g., the Joint Lightcurve Analysis (Betoule et al., 2014) and Pantheon/Pantheon+ (Scolnic et al., 2018; Brout et al., 2022) to derive strong cosmological constraints by creating the largest SNe Ia samples to date.

However, though impressive SNe Ia discovery rates have steadily driven down statistical uncertainty, this unprecedented data volume as well as our improved understanding of SNe Ia continue to create new sources of systematic uncertainty. One example is the development and adoption of photometric classifiers for SN Ia type confirmation, replacing reliance on spectroscopic follow-up. However, classification error is significantly more likely with photometric data and has thus become an important systematic in recent analyses (e.g., DES Collaboration et al., 2024). A thorough description of spectroscopic vs. photometric samples is given in Section 1.2.4, and a review of photometric classification can be found in Section 1.3.2.

This month, the Dark Energy Survey collaboration published its final cosmology analysis with all 5 years of observed SNe Ia, representing the largest sample of SNe Ia from a single survey to date (DES Collaboration et al., 2024). This sample includes 1,635 photometrically classified SNe Ia in the range  $0.10 < z < 1.13$ , and reports  $\Omega_m = 0.352 \pm 0.017$  for flat  $\Lambda$ CDM and  $(w, \Omega_m) = (-0.80^{+0.14}_{-0.16}, 0.264^{+0.074}_{-0.096})$  for flat  $w$ CDM (Figure 1.7), representing  $> 5\times$  improvement over the Perlmutter et al. (1999); Riess (1998) results.

This is an exciting time for SN Ia cosmology, as two next-generation telescopes are scheduled to come online in the next 3 years: the Legacy Survey of Space and Time (LSST) at the Vera C. Ru-

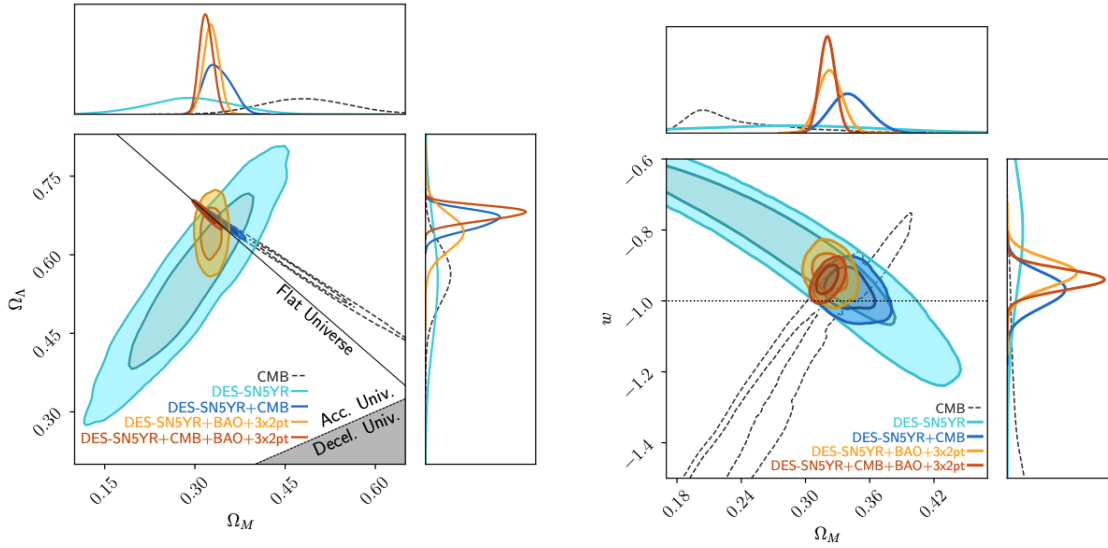
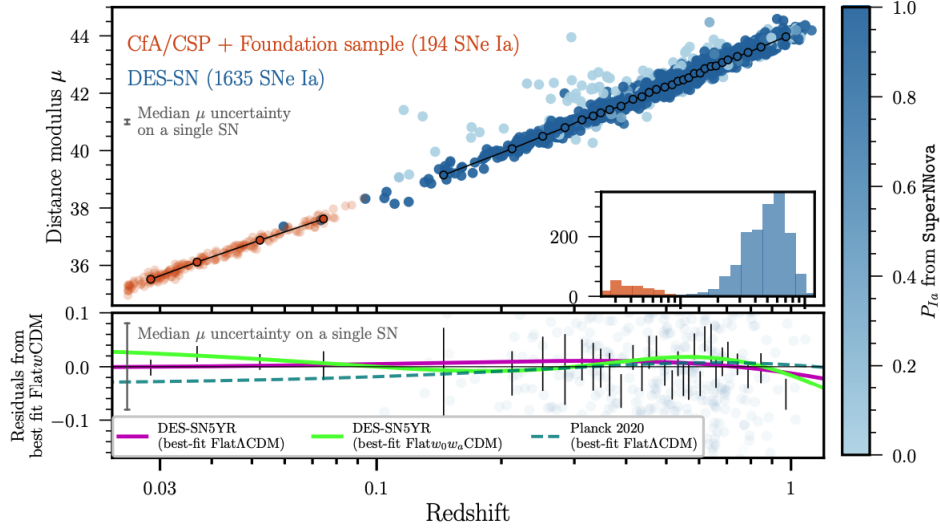


Figure 1.7: Results from DES Collaboration et al. (2024): (top) Hubble diagram of 1,635 high redshift SNe Ia from the DES 5-year (DES5YR) sample colored by the SN Ia probability assigned by the photometric classifier; (bottom left) Constraints on  $\Omega_\Lambda - \Omega_m$  for the  $\Lambda$ CDM model; (bottom right) constraints on  $w - \Omega_m$  for the flat  $w$ CDM model.



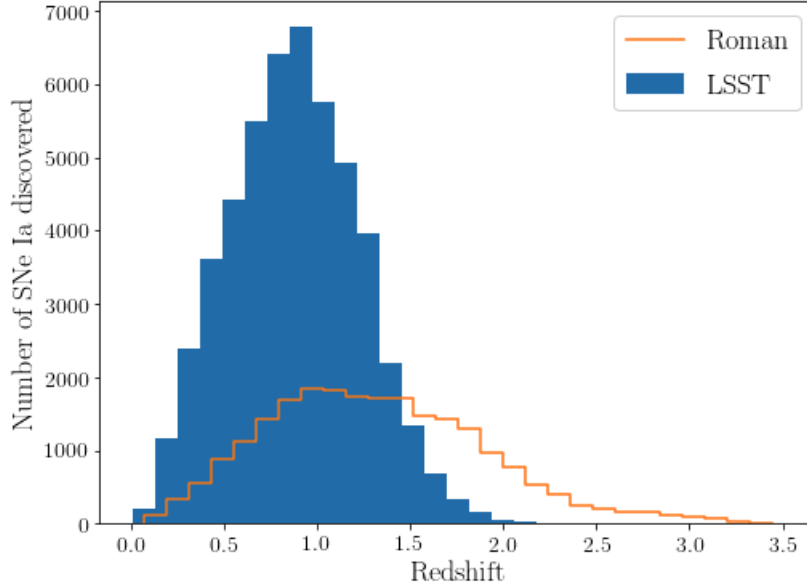


Figure 1.8: Projected redshift distribution of SNe Ia discovered by LSST and the Roman Space Telescope in one observing year.

bin Observatory and the Nancy Grace Roman Space Telescope. Expected redshift distributions for one observing year are shown in Figure 1.8. LSST is expected to observe 50,000 SNe Ia in a single year (one tenth of its planned observing lifetime), which is estimated to deliver better than 5% constraints on  $w$  (assumed constant) and constraints on  $w_0$  to 0.05,  $w_a$  to order unity for the  $w_0w_a$ CDM model (LSST Science Collaboration et al., 2009a). Roman will observe up to  $10^4$  SNe Ia, significantly fewer than expected from LSST, but Roman SNe Ia will cover an unprecedented redshift range of up to  $z \sim 3$ . Roman data alone is expected to produce 1% constraints on  $w_0$  and 10% constraints on  $w_a$  (Rose et al., 2021).

### 1.2.2. SN Ia Standardization

Given our limited knowledge about SN Ia progenitors and explosion mechanisms, our luminosity standardization machinery is largely empirically derived. Intrinsically, SNe Ia are a relatively diverse population with luminosity scatter  $\sim 0.8$  mag. However, two relations were observed that enabled standardization to within  $\sim 0.15$  mag and firmly established SNe Ia as standardizable candles.

**Stretch-luminosity correction.** Phillips (1993) observed that decline rate and lightcurve width (i.e. explosion duration) was well-correlated with SN Ia luminosity. Perlmutter et al. (1997) later showed that equivalently, fitting a “stretch” parameter representing the stretching of the timescale of an event could be used to effectively normalize SNe luminosities to within  $\sim 0.19$  mag (Figure 1.9).

**Color-luminosity correction.**  $B-V$  color was also found to correlate with SNe Ia luminosity, with bluer SNe appearing brighter than redder ones. This may be due to intrinsic physical properties of SNe Ia or to effects of dust in the host galaxy, but is able to be corrected with a simple linear relationship to decrease scatter to within  $\sim 0.15$  mag (Tripp, 1998).

While these corrections significantly improved the standardizability of SNe Ia, intrinsic scatter is still a sizable component of our modeling error budget today and an active area of study.

### 1.2.3. From Fluxes to Distances to Cosmology

We compute the standardized peak flux of a SN Ia by applying the stretch and color corrections described above, as well as a host galaxy correction:

$$m_B^{\text{standardized}} = m_B + \alpha x_1 - \beta c + \gamma G_{\text{host}}. \quad (1.11)$$

Here,  $m_B$  is the measured flux in magnitudes,  $x_1, c$  are the stretch and color parameters described above, and  $\alpha, \beta$  set the amplitude of these corrections.  $\gamma G_{\text{host}}$  is a further correction originating from observations that SNe Ia occurring in high-mass galaxies ( $M_\star > 10^{10} M_\odot$ ) are  $\sim 0.07$  mag fainter than SNe in lower mass galaxies (Kelly et al., 2010; Sullivan et al., 2011; Betoule et al., 2014; Smith et al., 2020b; Kelsey et al., 2021, 2023). We model this dependence as

$$\gamma G_{\text{host}} = \begin{cases} +1/2\gamma & M_\star > M_{\text{step}} \\ -1/2\gamma & \text{otherwise,} \end{cases} \quad (1.12)$$

where  $\gamma$  sets the size of the correction and  $M_{\text{step}}$  is generally fixed to  $10^{10} M_\odot$ .

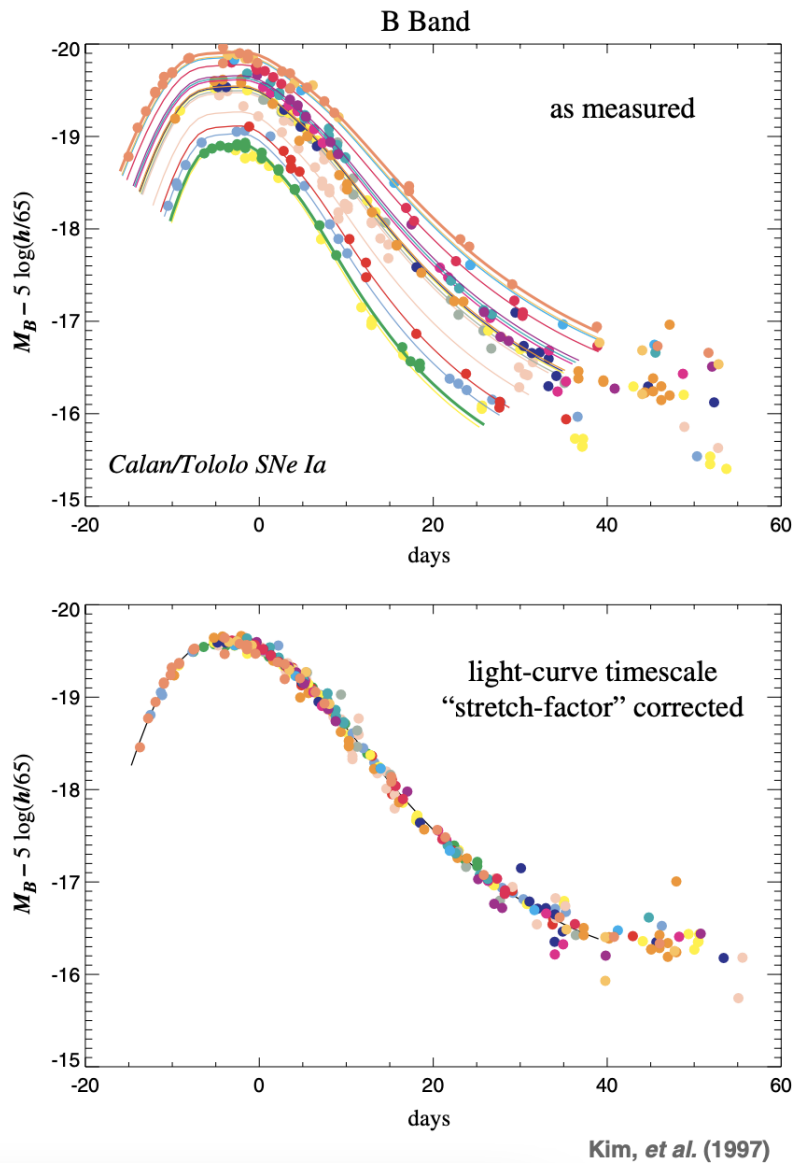


Figure 1.9: *Upper panel:* Lightcurves of low-redshift supernovae discovered by the Calan/Tololo Supernova Survey. *Lower panel:* The same lightcurves after calibrating the supernova brightness using the “stretch” of the timescale of the lightcurve as an indicator of brightness and the color at peak as an indicator of dust absorption. Adapted from Perlmutter (2012).

**Lightcurve Fitting.** Since we observe SNe Ia at various redshifts in fixed rest-frame wavelength bands and often miss the epoch of peak brightness, we leverage a lightcurve fitting approach to standardize these observations. An established lightcurve fitting method is SALT2 (Guy et al., 2007), which attempts to model SNe Ia spectral evolution with time by finding best-fit matrices  $F_0(t, \lambda), F_1(t, \lambda)$  of flux estimates on a grid of times  $t$  and wavelengths  $\lambda$ . Once trained, these matrices are combined with coefficients  $x_0, x_1$  that represent the overall scale of each component, and  $c$ , a coefficient to the fitted color correction relation. These fitted parameters are used in Equation 1.11 for luminosity standardization.

**Distance estimation.** To represent SN distances, we define the observed distance modulus as

$$\mu_{\text{obs}} = m^{\text{standardized}} - M + \Delta\mu_{\text{bias}}, \quad (1.13)$$

where  $m^{\text{standardized}}$  is the standardized SN peak magnitude described above,  $M$  is the absolute magnitude of a SN Ia with  $x_1 = 0, c = 0$ , and  $\Delta\mu_{\text{bias}}$  is a bias correction term applied to address survey selection effects (see e.g., Kessler and Scolnic, 2017, for a current approach).  $\mu_{\text{obs}}$  is simply defined for convenience and related to luminosity distance as  $\mu_{\text{obs}} \sim \log_{10} d_L$ .

**Cosmological parameter measurement.** To compare our observed distance moduli with theoretically predicted distance moduli  $\mu_{\text{theory}}(\Theta)$  computed from assumed cosmological parameters  $\Theta$ , we calculate

$$\Delta\mu_i = \mu_{\text{obs},i} - \mu_{\text{theory}}(\Theta, z_i). \quad (1.14)$$

for each  $i^{\text{th}}$  SN Ia. We then minimize

$$\chi^2 = \Delta\mu_i \mathcal{C}_{ij}^{-1} \Delta\mu_j^T, \quad (1.15)$$

where  $\mathcal{C}^{-1}$  is the inverse covariance matrix, to determine the best fit cosmological parameters. The covariance matrix accounts for all of our statistical and modeling-based (systematic) uncertainties (Conley et al., 2010).

Finally, we note that SN Ia absolute magnitude  $M$  is completely degenerate with the Hubble con-

stant  $H_0$ , leading SN Ia-only analyses to define  $\mathcal{M} \equiv M + 5\log_{10}(c/H_0)$  and marginalize over this term.

#### 1.2.4. Spectroscopic vs. Photometric Samples

Historically, spectroscopic follow-up observation has been crucial for determining a host of properties for any observed object. *Spectroscopy* provides a granular view of object flux as a function of wavelength, which can reveal chemical components of observed objects (e.g., emission/absorption lines), velocity (via broadening of emission lines), and redshift (via shifts in spectral features compared to a template spectrum). However, collecting enough light in each fine-grained wavelength bin requires long integration times [X min for Y mag object], which can be prohibitive for faint, distant objects. In contrast, broad-band *photometry* provides an inexpensive [Z min for Y mag object] but coarse-grained view. Most survey telescopes primarily collect data photometrically through 1-6 broad-band filters that cover complementary ranges of wavelengths. In this regime, information about specific spectral features is difficult to extract, rendering redshift estimation and object typing a challenge.

Traditional SN Ia cosmology analyses relied on spectroscopic follow-up for two reasons: (1) confirmation that an object is in fact a SN Ia, and (2) a precise redshift measurement for either the SN or its host galaxy. However, as time domain surveys become wider, faster, and deeper, our ability to photometrically discover new SNe Ia as well as other time domain events is far outpacing our spectroscopic resource availability. < 0.1% of SNe Ia observed by the upcoming Rubin Legacy Survey of Space and Time (LSST) will be followed up spectroscopically. This has led to two distinct types of SN samples:

- Spectroscopic SN Ia samples, composed of spectroscopically confirmed SNe Ia;
- Photometric SN samples, composed of SNe that do not have spectroscopic type confirmation but generally have a spectroscopic redshift from its likely host galaxy.

Spectroscopic samples have high guaranteed purity but a severely limited sample size, driving up statistical uncertainty of parameter estimates. Photometric samples, on the other hand, are much

larger but may contain objects that are not SNe Ia. These non-Ia “contaminants” are not standard candles and will bias cosmological parameter estimates, impacting our systematic uncertainty.

The past decade has seen a significant effort to develop accurate photometric SN classification methods, ranging from template matching (Sako et al., 2011) to deep learning (Möller and de Boissière, 2019) (see Section 1.3.2 for further details). In conjunction with new statistical methods for marginalizing over non-Ia contamination in the cosmological parameter fitting process (Kessler and Scolnic, 2017), these classifiers have made precision cosmology with photometric samples possible.

### 1.2.5. Host Galaxy Correlations

The type and properties of SNe have been shown to depend heavily on its host galaxy environment. Broadly, since core-collapse SNe have massive ( $> 8M_{\odot}$ ) progenitors, they are almost exclusively hosted by gas-rich, star-forming galaxies. In contrast, SNe Ia arise from white dwarfs and have been observed to occur in a variety of host galaxy environments. In fact, Foley and Mandel (2013) and Gagliano et al. (2021) found that host galaxy information alone is sufficient to perform accurate classification of supernova types.

In the context of SN Ia standardization, host galaxy correlations have played an important role. Numerous studies have observed that higher stellar mass, passive galaxies tend to host brighter/slower declining SNe Ia, whereas SNe Ia found in star-forming galaxies are dimmer/fast declining (e.g., Lampeitl et al., 2010; Sullivan et al., 2010). This so-called “mass step” has persisted over a decade of study though its physical origins remain mysterious, and has become enshrined in the canon of SN Ia standardization (Equation 1.12).

Host galaxies are also the primary source of accurate redshifts for photometrically classified SNe Ia, which is vital for determining the distance-redshift relation that we use to estimate cosmological parameters. Procuring spectroscopic redshift measurements for large numbers of SN host galaxies has been tractable so far, since spectroscopic follow-up of galaxies is not time-sensitive and large (and growing) catalogs of galaxy redshifts are available in the literature.

Finally, identifying the correct host galaxy for each SN Ia is crucial to ensuring accurate host galaxy

correlations and redshifts. Host galaxy matching is nontrivial, however, since SNe can occur in crowded fields or in faint galaxies that are below the detection limit. In certain cases, host galaxy mismatch can even lead to nontrivial biases in estimated cosmological parameters. I provide an overview of current host matching methods as well as the impact of mismatch on cosmology in Chapter 4.

### 1.3. Cosmology in the Era of Big Data

In the next three years, both the Rubin Legacy Survey of Space and Time (LSST) and the Roman Space Telescope will be streaming science-grade data. This is an exciting time for time domain studies and SN Ia cosmology: these surveys promise to deliver millions of time domain objects, including hundreds of thousands of SNe Ia, over their observing lifetimes. This data deluge represents  $100\times$  the number of time domain objects ever observed, and presents immense promise as well as new challenges. Machine learning has a unique ability to derive insights from massive amounts of data, and may be the key to maximizing science returns from future survey data.

#### 1.3.1. The Role of Machine Learning

Machine learning is a non-parametric, data-driven approach to function approximation. Specifically, a machine learning algorithm defines a transformation  $\hat{f}(x, \theta)$  to approximate the true function  $f(x)$ . The objective of the learning process is to learn parameters  $\theta$  that minimize a loss function  $L(f(x), \hat{f}(x, \theta))$ . Traditional machine learning techniques generally operate on tabular data, where an input (e.g., an SN Ia event) is summarized by a collection of expert-designed *features* (e.g., peak magnitude, stretch, color, etc.). On the other hand, *deep learning* provides the additional benefit of learning the best features for a particular task, allowing raw data (e.g., supernova time-series, galaxy image) to act as the input with minimal expert guidance. Deep learning models can generally be thought of as a composition of functions, e.g.,  $\hat{f} = \hat{f}^{(n)} \circ \dots \circ \hat{f}^{(2)} \circ \hat{f}^{(1)}$ , where  $\hat{f}^{(1)}$  defines the first *layer* of the model, etc. This deep, layered architecture allows intermediate layers to build off of previous layer outputs and learn more abstract or complicated concepts.

The power and flexibility of deep learning approaches has led to a proliferation of architectures tailored to diverse data types. For example, convolutional neural networks (LeCun et al., 1989a;

Krizhevsky et al., 2012a; He et al., 2016b) are designed to leverage the spatial hierarchy and local patterns inherent in images, while transformers (Vaswani et al., 2017) are well-suited for sequential data due to their ability to capture long-range dependencies and relationships within sequences.

**Robust Machine Learning.** In real-world scenarios, machine learning models are often deployed on data that differ from the training data. Machine learning is well known to generalize poorly outside of its training data distribution, and performance on these out-of-distribution (OOD) datasets can drop dramatically (Quiñonero-Candela et al., 2009; Koh et al., 2021). This is of utmost importance to scientific applications – we often have large unlabeled datasets (e.g., real data from telescopes) that we use machine learning models to sort through (e.g., photometric SN classification). However, these machine learning models are traditionally trained on a different data distribution (e.g., simulated or a labeled subset of telescope data), with no means of precisely measuring model performance on the real data. In astronomy, the Photometric LSST Astronomical Time-Series Classification Challenge (PLAsTiCC, team et al., 2018) dataset attempts to simulate this by creating a training set modeled after a spectroscopically confirmed dataset of time-varying objects (lower redshift, brighter), while the test set represents the full photometric dataset of these objects (higher redshift, fainter). Improving robustness to OOD inputs is an active area of study in the machine learning community and is the subject of Chapter 6.

### 1.3.2. Machine Learning in Observational Cosmology

In recent years, the unprecedented data volume of wide-field sky surveys has highlighted the need for fast, automated, and accurate algorithms at every stage of the pipeline, from object detection in telescope images to cosmological parameter inference.

**Transient detection.** The current technique to detect time-varying objects in astronomical survey images, difference imaging, involves subtracting pixel values of each telescope image from a “template” image of only constant light sources (e.g., galaxies) (Kessler et al., 2015). This process requires precise alignment of the image coordinates and point spread functions, which is extremely computationally expensive and prone to failure. A class of machine learning-based “real-bogus” detection algorithms emerged to distinguish difference imaging artifacts (bogus detections) from



actual time-varying object detections (e.g., Goldstein et al., 2015). Recent work has focused on real-bogus detection with the search and template images only (Acero-Cuellar et al., 2023), opening the door to potential future approaches that can perform transient detection without difference imaging altogether.

**Transient classification.** After detection, objects must be classified by type for further analysis. In Section 1.2.4, I described the importance of spectroscopic follow-up for determining SN type information, and the limitations of scaling spectroscopic resources to modern photometric data volumes. In the absence of spectroscopic information for the vast majority of discovered objects, attention has turned in recent years to the role of computational methods and machine learning to extract that information from photometry. Early methods used a template fitting approach that compares an input against known SN Ia and core-collapse SN templates to find the best match (e.g., Sako et al., 2011). Recent years have seen significant interest in machine learning-based photometric classifiers with increasingly impressive reported performance (Möller and de Boissière, 2019; Muthukrishna et al., 2019; Boone, 2019b; Villar et al., 2020; Boone, 2021; Villar et al., 2023). Some of these models (e.g., Sako et al., 2011; Möller and de Boissière, 2019) have been successfully incorporated into SN Ia cosmology analysis pipelines to extract a photometrically classified SN Ia sample (Campbell et al., 2013; Jones et al., 2017; Sako et al., 2018; DES Collaboration et al., 2024). However, practical concerns such as long training times/large training sets, ease of use, and generalizability from simulated to real data are still common issues plaguing these approaches.

**Host Galaxy Matching.** Information about an event’s host galaxy environment can be very useful for understanding its properties and physical progenitor scenarios. Host galaxy matching can be a nontrivial problem, however, and traditional methods, such as the directional light radius method (DLR, Sullivan et al., 2006), are prone to occasional catastrophic failure. Gupta et al. (2016) showed that adding a random forest classifier to detect incorrect matches on top of DLR-identified host galaxies can improve host matching accuracy. A few recent studies introduce novel machine learning-based solutions to host galaxy matching, (e.g., Gagliano et al., 2021; Förster et al., 2022), and could be an interesting avenue for future work.

**Distance/Redshift Estimation for SNe Ia.** Redshifts for SNe Ia have traditionally come from either live spectra of the SNe themselves or spectroscopic redshifts from their matched host galaxies. In parallel with improving host galaxy matching, another line of work has emerged on photometric redshift estimation from SNe themselves. An extension to the SALT2 lightcurve fitting model is a popular and well-studied approach (Kessler et al., 2010b), but degeneracies between redshift and other fitted properties (e.g., color) can lead to poor fits. de Oliveira et al. (2022) explored applying machine learning to this problem, but most redshift estimation techniques in the literature suffer heavily from redshift-dependent bias (i.e., predictions tend toward the mean). Estimation of a joint posterior over distance and redshift using machine learning techniques (e.g. neural density estimators) is a potential direction for future work.

**Cosmological Parameter Estimation.** As described in Section 1.2.3, traditional parameter estimation uses  $\chi^2$  minimization to determine a posterior distribution over best-fit cosmological parameters given the data. However, this makes the strong assumption that our likelihood is Gaussian. An alternative approach known as *simulation-based inference* (SBI) does not require such assumptions (see Cranmer et al. (2020) for a review). This method was explored for SN Ia cosmology by Jennings et al. (2016), an approximate Bayesian computation approach that requires a “distance metric” over the simulated vs. observed raw data, which is nontrivial to define. Exploring modern machine learning-based SBI techniques for principled posterior inference is a promising direction for future work.

#### 1.4. Motivation and Overview

In the preceding sections, I presented a brief overview of SN Ia cosmology today and my view of the opportunities and challenges ahead. In summary, I believe that the data deluge of LSST and the Roman Space Telescope will pose substantial challenges for our statistical frameworks and infrastructure, especially our heavy reliance on spectroscopy to elucidate SN properties. Machine learning techniques offer a way forward by learning spectroscopic properties from photometric data, and have already enabled the shift away from spectroscopic confirmation of supernova type (DES Collaboration et al., 2024). Photometric SN cosmology in the LSST era, however, will also require an optimized spectroscopic targeting program and accurate redshift estimates for SNe Ia.

Further gains in cosmological constraints could come from further emphasis on robust machine learning, e.g., for photometric classification; and improved statistical methodology for parameter inference, such as with machine learning-accelerated simulation-based inference. The development of the photometric supernova cosmology toolkit will rely on harnessing the power of machine learning and other cutting-edge technologies. My research, outlined in this thesis, has focused on developing practical, impactful machine learning tools to accelerate this transition:

1. I developed SCONE, a quick-to-train, lightweight convolutional neural network approach to photometric SN classification (Chapter 2);
2. I demonstrated SCONE's classification performance on early epoch SN photometry for use cases in spectroscopic targeting and allocation (Chapter 3);
3. I analyzed the impact of incorrect SN redshifts from mismatched host galaxies on inferred cosmological parameters in the DES 5-year SN analysis (Chapter 4);
4. I developed Photo-zSNthesis, a novel photometric redshift estimation algorithm for SNe Ia (Chapter 5);
5. I developed Connect Later, a general framework for improving model robustness under distribution shift (Chapter 6).

## CHAPTER 2

### SCONE: Supernova Classification with a Convolutional Neural Network

#### Abstract

We present a novel method of classifying Type Ia supernovae using convolutional neural networks, a neural network framework typically used for image recognition. Our model is trained on photometric information only, eliminating the need for accurate redshift data. Photometric data is pre-processed via 2D Gaussian process regression into two-dimensional images created from flux values at each location in wavelength-time space. These “flux heatmaps” of each supernova detection, along with “uncertainty heatmaps” of the Gaussian process uncertainty, constitute the dataset for our model. This preprocessing step not only smooths over irregular sampling rates between filters but also allows SCONE to be independent of the filter set on which it was trained. Our model has achieved impressive performance without redshift on the in-distribution SNIa classification problem:  $99.73 \pm 0.26\%$  test accuracy with no over/underfitting on a subset of supernovae from PLAsTiCC’s unblinded test dataset. We have also achieved  $98.18 \pm 0.3\%$  test accuracy performing 6-way classification of supernovae by type. The out-of-distribution performance does not fully match the in-distribution results, suggesting that the detailed characteristics of the training sample in comparison to the test sample have a big impact on the performance. We discuss the implication and directions for future work. All of the data processing and model code developed for this paper can be found in the SCONE software package located at [github.com/helenqu/scone](https://github.com/helenqu/scone) (Qu, 2021a).

#### 2.1. Introduction

The discovery of the accelerating expansion of the universe (Perlmutter et al., 1999; Riess, 1998) has led to an era of sky surveys designed to probe the nature of dark energy. Type Ia supernovae (SNe Ia) have been instrumental to this effort due to their standard brightness and light curve profiles. Building a robust dataset of SNe Ia across a wide range of redshifts will allow for the construction of an accurate Hubble diagram that will enrich our understanding of the expansion history of the universe as well as place constraints on the dark energy equation of state.

Modern-scale sky surveys, including SDSS, Pan-STARRS, and the Dark Energy Survey, have identified thousands of supernovae throughout their operational lifetimes (Frieman et al., 2008; Chambers et al., 2016; Smith et al., 2020a). However, it has been logistically challenging to follow up on most of these detections spectroscopically. The result is a low number of spectroscopically confirmed SNe Ia and a large photometric dataset of SNe Ia candidates. The upcoming Rubin Observatory Legacy Survey of Space and Time (LSST) is projected to discover  $10^7$  supernovae (LSST Science Collaboration et al., 2009a), with millions of transient alerts each observing night. As spectroscopic resources are not expected to scale with the size of these surveys, the ratio of spectroscopically confirmed SNe to total detections will continue to shrink. With only photometric data, distinguishing between SNe Ia and other types can be difficult. A reliable photometric SNe Ia classification algorithm will allow us to tap into the vast potential of the photometric dataset and pave the way for confident classification and analysis of the ever-growing library of transients from current and future sky surveys.

Significant progress has been made in the past decade in the development of such an algorithm. Most approaches involve lightcurve template matching (Sako et al., 2011a), or feature extraction paired with either sequential cuts (Bazin et al., 2011; Campbell et al., 2013) or machine learning algorithms (Möller et al., 2016; Lochner et al., 2016; Dai et al., 2018; Boone, 2019a). Most recently, the spotlight has been on deep learning techniques since it has been shown that classification based on handcrafted features is not only more time-intensive for the researcher but is outperformed by neural networks trained on raw data (Charnock and Moss, 2017; Moss, 2018; Kimura et al., 2017). Since then, many neural network architectures have been explored for SN photometric classification, such as PELICAN's CNN architecture (Pasquet et al., 2019a) and SuperNNova's deep recurrent network (Möller and de Boissière, 2020b).

Several photometric classification competitions have been hosted, including the Supernova Photometric Classification Challenge (SPCC) (Kessler et al., 2010a) and the Photometric LSST Astronomical Time Series Classification Challenge (PLAsTiCC) (The PLAsTiCC team et al., 2018a). These have not only resulted in the development of new techniques, such as PSNID (Sako et al., 2011a) and Avocado (Boone, 2019a), but have also provided representative datasets available to

researchers during and after the competition, such as the PLAsTiCC unblinded dataset used in this paper.

In this paper we present SCONE, a novel application of deep learning to the photometric classification problem. SCONE is a convolutional neural network (CNN), an architecture prized in the deep learning community for its state-of-the-art image recognition capabilities (LeCun et al., 1989b, 1998; Krizhevsky et al., 2012a; Zeiler and Fergus, 2014; Simonyan and Zisserman, 2014b). Our model requires raw photometric data only, precluding the necessity for accurate redshift approximations. The dataset is preprocessed using a lightcurve modeling technique via Gaussian processes described in Boone (2019a), which alleviates the issue of irregular sampling between filters but also allows the CNN to learn from information in all filters simultaneously. The model also has relatively low computational and dataset size requirements without compromising on performance – 400 epochs of training on our  $\sim 10^4$  dataset requires around 15 minutes on a GPU.

We will introduce the datasets used to train and evaluate SCONE its computational requirements, as well as the algorithm itself in Section 2. Section 3 will focus on the performance of SCONE on both binary and categorical classification, and Section 4 presents an analysis of misclassified lightcurves and heatmaps for both modes of classification.

## 2.2. Methods

### 2.2.1. Datasets

The PLAsTiCC training and test datasets were originally created for the 2018 Photometric LSST Astronomical Time Series Classification Challenge.

The PLAsTiCC training set includes  $\sim 8000$  simulated observations of low-redshift, bright astronomical sources, representing objects that are good candidates for spectroscopic follow-up observation. This dataset will be referred to in future sections as the “spectroscopic dataset”. We use this dataset to evaluate the out-of-distribution performance of SCONE in section 3.1.2.

The PLAsTiCC test set consists of 453 million simulated observations of 3.5 million transient and

Table 2.1: Makeup of the PLAsTiCC dataset by type.

SN type	number of sources	
	spectroscopic	main
SNIa	2,313	12,640
SNIIf	1,193	15,986
SNIbc	484	2,194
SNIa-91bg	208	362
SNIax	183	807
SLSN-1	175	98

variable sources, representing 3 years of expected LSST output (Kessler et al., 2019b). The objects in this dataset are generally fainter, higher redshift, and do not have associated spectroscopy. Note that most of the results presented in this paper are produced from this dataset alone and will be referred to as “the dataset”, “the main dataset”, or “the PLAsTiCC dataset” in future sections.

All observations in both datasets were made in LSST’s *ugrizY* bands and realistic observing conditions were simulated using the LSST Operations Simulator (Delgado and Schumacher, 2014). While PLAsTiCC includes data from many other transient sources, we are using only the supernovae in the datasets. We selected all of the type II, Iax, Ibc, Ia-91bg, Ia, and SLSN-1 sources (corresponding to `true_target` values of 42, 52, 62, 67, 90, and 95) from this dataset and chose only well-sampled lightcurves by restricting ourselves to observations simulating LSST’s deep drilling fields (`ddf=1`). `peak_mjd` values, the modified Julian date of peak flux for each object, were calculated for both the main dataset and the spectroscopic dataset by taking the signal-to-noise weighted average of all observation dates. `peak_mjd` is referred to as  $t_{\text{peak}}$  in future sections. The total source count for the spectroscopic set is 4,556, and the total source count for the main dataset is 32,087. A detailed breakdown by type is provided in Table 2.1.

The categorical dataset was created using SNANA (Kessler et al., 2009c) with the same models and redshift distribution as the main dataset in order to perform categorical classification with balanced classes. 2,000 examples of each type were randomly selected to constitute a class-balanced dataset of 12,000 examples.

### 2.2.2. Quality Cuts

In order to ensure that the model is learning only from high-quality information, we have instituted some additional quality-based cuts on all datasets. These cuts are based on lightcurve quality, so all metrics are defined for a single source. The metrics evaluated for these cuts are as follows:

- **number of detection datapoints** ( $n_{\text{detected}}$ ): number of observations where the source was detected. We chose a detection threshold of  $S/N > 5$ , based on Fig. 8 of Kessler et al. (2015)
- **cumulative signal-to-noise ratio** ( $CSNR$ ): cumulative S/N for all points in the lightcurve

$$CSNR = \sqrt{\sum \frac{f^2}{\sigma_f^2}}$$

- **duration**: timespan of detection datapoints

$$t_{\text{active}} = t_{\text{last}} - t_{\text{first}}$$

where  $f$  represents the flux measurements from all observations of a given source,  $\sigma_f$  represents the corresponding uncertainties,  $t$  represents the timestamps of all observations of a given source,  $t_{\text{first}}$  is the time of initial detection, and  $t_{\text{last}}$  is the time of final detection. Our established quality thresholds require that:

- $n_{\text{detected}} \geq 5$
- $CSNR > 10$
- $t_{\text{active}} \geq 30$  days

for lightcurve points in the range  $t_{\text{peak}} - 50 \leq t \leq t_{\text{peak}} + 130$ . 1,150 out of 4,556 sources passed these cuts in the spectroscopic dataset and 12,611 out of 32,087 sources passed these cuts in the main dataset. The makeup of these datasets is detailed in Table 2.2. The categorical dataset was



Table 2.2: Makeup of the PLAsTiCC dataset by type after applying quality cuts.

SN type	number of sources	
	spectroscopic	main
SNIa	654	6,128
SNI	262	5,252
SNIbc	97	779
SNIa-91bg	41	113
SNIax	59	281
SLSN-1	37	58

created from sources that already passed the cuts, so the makeup is unchanged.

### 2.2.3. Class Balancing

Maintaining an equal number of examples of each class, or a balanced class distribution, is important for machine learning datasets. Balanced datasets allow for an intuitive interpretation of the accuracy metric as well as provide ample examples of each class for the machine learning model to learn from.

As shown in Table 2.2, the natural distribution of the spectroscopic dataset is more abundant in Ia sources than non-Ia sources. Thus, all non-Ia sources were retained in the class balancing process for binary classification and an equivalent number of Ia sources were randomly chosen. SNIax and SNIa-91bg sources were labeled as non-Ia sources for binary classification. The class-balanced spectroscopic dataset has 496 sources of each class for a total of 992 sources.

In contrast, the natural distribution of the main dataset is more abundant in non-Ia sources than Ia sources. Thus, all Ia sources were retained in the class balancing process for binary classification and an equivalent number of non-Ia sources were randomly chosen. The random selection process does not necessarily preserve the original distribution of non-Ia types. The class-balanced dataset has 6,128 sources of each class for a total of 12,256 sources.

The categorical dataset of 2,000 sources for each of the 6 types was created explicitly for the purpose of retaining balanced classes in categorical classification, as mentioned in Section 2.1.

All datasets were split by class into 80% training, 10% validation, and 10% testing. Splitting by

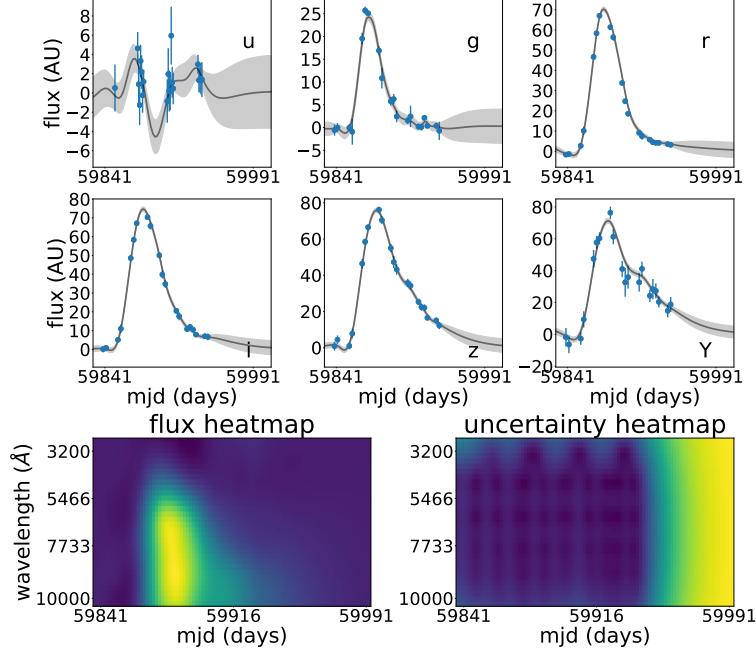


Figure 2.1: Raw *ugrizY* lightcurve data with the Gaussian process model at corresponding wavelengths and resulting heatmap and error heatmap for a type Ia SN. The shaded regions in the Gaussian process plots represent the Gaussian process error.

class ensures balanced classes in each of the training, validation, and test sets.

#### 2.2.4. Heatmap Creation

Prior to training, we preprocess our lightcurve data into heatmap form. First, all observations are labeled with the central wavelength of the observing filter according to Table 2.3, which was calculated from the filter functions used by The PLAsTiCC team et al. (2018a). We then use the approach described by Boone (2019a) to apply 2-dimensional Gaussian process regression to the raw lightcurve data to model the event in the wavelength ( $\lambda$ ) and time ( $t$ ) dimensions. We use the Matern 32 kernel with a fixed  $6000 \text{ \AA}$  characteristic length scale in  $\lambda$  and fit for the length scale in  $t$ . Once the Gaussian process model has been trained, we obtain its predictions on a  $\lambda, t$  grid and call this our “heatmap”. Our choice for the  $\lambda, t$  grid was  $t_{\text{peak}} - 50 \leq t \leq t_{\text{peak}} + 130$  with a 1-day interval and  $3000 < \lambda < 10,100 \text{ \AA}$  with a  $221.875 \text{ \AA}$  interval. The significance of this choice is explored further in Section 3.

The result of this is a  $n_\lambda \times n_t$  image-like matrix, where  $n_\lambda$  and  $n_t$  are the lengths of the wavelengths

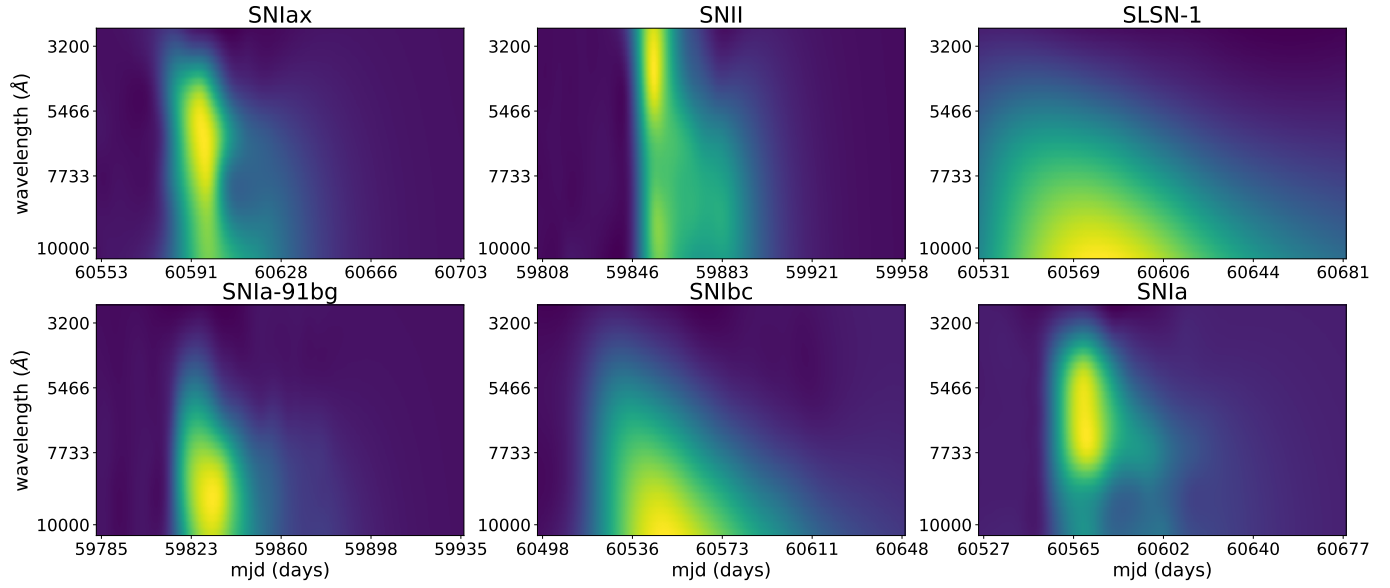


Figure 2.2: Example flux heatmaps for each supernova type.

Table 2.3: Central wavelength of each filter

Filter	Central Wavelength (Å)
u	3670.69
g	4826.85
r	6223.24
i	7545.98
z	8590.90
Y	9710.28

array and times array, respectively, given to the Gaussian process. We also take into account the uncertainties on the Gaussian process predictions at each time and wavelength, producing a second image-like matrix. We stack these two matrices depthwise and divide by the maximum flux value to constrain all entries to  $[0,1]$ . This matrix is our input to the convolutional neural network.

Figure 2.1 shows the raw lightcurve data in the  $t_{\text{peak}} - 50 \leq t \leq t_{\text{peak}} + 130$  range for each filter in blue, the Gaussian process model in gray, and the resulting flux and uncertainty heatmaps at the bottom. Figure 2.2 shows a representative example of a heatmap for each supernova type.

### 2.2.5. Convolutional Neural Networks

Convolutional neural networks (CNNs) are a type of artificial neural network that makes use of the convolution operation to learn local, small-scale structures in an image. This is paired with an averaging or sub-sampling layer, often called a *pooling layer*, that reduces the resolution of the image and allows the subsequent convolutional layers to learn hierarchically more complex and less localized structures.

In a *convolutional layer*, each unit receives input from only a small neighborhood of the input image. This use of a restricted receptive field, or *kernel size*, resembles the neural architecture of the animal visual cortex and allows for extraction of local, elementary features such as edges, endpoints, or corners. All units, each corresponding to a different small neighborhood of the image, share the same set of learned weights. This allows them to detect the presence of the same feature in each neighborhood of the image. Each convolutional layer often has several layers of these units, each of which is called a *filter* and extracts a different feature. The output of a convolutional layer is called a *feature map*.

Pooling layers reduce the local precision of a detected feature by sub-sampling the each unit's receptive field, often  $2 \times 2$  pixels, based on some rule. Average-pooling, for example, extracts the average of the 4 pixels, and max-pooling extracts the maximum value. Assuming no overlap in the receptive fields, the spatial dimensions of the resulting feature maps will be reduced by half.

Dropout (Hinton et al., 2012) is a commonly used regularization technique in fully connected lay-

ers. A *dropout layer* chooses a random user-defined percentage of the input weights to set to zero, improving the robustness of the learning process.

A convolutional neural network typically consists of alternating convolutional layers and pooling layers, followed by a series of fully-connected layers that learn a mapping between the result of the convolutions and the desired output.

### 2.2.6. SCONE Architecture

The relatively simple architecture of SCONE, shown in Figure 2.3, allows for a minimal number of trainable parameters, speeding up the training process significantly without compromising on performance. It has a total of 22,606 trainable parameters for categorical classification and 22,441 trainable parameters for binary classification when trained on heatmaps of size  $32 \times 180 \times 2$  ( $h \times w \times d$ ).

As mentioned in Section 2.4, each heatmap is divided by its maximum flux value for normalization. After receiving the normalized heatmap as input, the network pads the heatmap with a column of zeros on both sides, bringing the heatmap size to  $32 \times 182 \times 2$ . Then, a convolutional layer is applied with  $h$  filters and a kernel size of  $h \times 3$ , which in this case is 32 filters and a  $32 \times 3$  kernel, resulting in a feature map of size  $1 \times 180 \times 32$ . We reshape this feature map to be  $32 \times 180 \times 1$ , apply batch normalization, and repeat the above process one more time. We have now processed our heatmap through two “convolutional blocks” with an output feature map of size  $32 \times 180 \times 1$ .

We apply  $2 \times 2$  max pooling to our output, reducing its dimensions to  $16 \times 90 \times 1$ , and pass it through two more convolutional blocks, but this time  $h = 16$ .

We pass our output through a final  $2 \times 2$  max pooling layer, resulting in a  $8 \times 45 \times 1$  feature map. This is subsequently flattened into a 360-element array and passed through a 50% dropout layer. A 32-unit fully connected layer followed by a 30% dropout layer feeds into the final layer. For binary classification, this is a node with a sigmoid activation that returns the model’s predicted Ia probability. For categorical classification, the final layer contains 6 nodes with softmax activations that return the respective probabilities of each of the 6 SN types. Both of these versions of SCONE

are shown in Figure 2.3.

The model is trained with the binary crossentropy loss function for binary classification and the sparse categorical crossentropy loss function for categorical classification. Both classification modes use the Adam optimizer (Kingma and Ba, 2017) at a constant 1e-3 learning rate for 400 epochs.

### 2.2.7. Evaluation Metrics

*Accuracy* is defined as the number of correct predictions divided by the number of total predictions. We also evaluated the model on a number of other performance metrics: purity, efficiency, and AUC.

*Purity* and *efficiency* are defined as:

$$\text{purity} = \frac{\text{TP}}{\text{TP} + \text{FP}}; \text{efficiency} = \frac{\text{TP}}{\text{TP} + \text{FN}}$$

where TP is true positive, FP is false positive, and FN is false negative.

*AUC*, or *area under the receiver operating characteristic (ROC) curve*, is a common metric used to evaluate binary classifiers. The ROC curve is created by plotting the false positive rate against the true positive rate at various discrimination thresholds, showing the sensitivity of the classifier to the chosen threshold. A perfect classifier would score a 1.0 AUC value while a random classifier would score a 0.5.

### 2.2.8. Computational Requirements

Due to the minimal number of trainable parameters and dataset size, the time and hardware requirements for training and evaluating with SCONE are relatively low. The first training epoch on one NVIDIA V100 Volta GPU takes approximately 2 seconds, and subsequent training epochs take approximately 1 second each with TensorFlow's dataset caching. Training epochs on one Haswell node (with Intel Xeon Processor E5-2698 v3), which has 32 cores, take approximately 26 seconds each.

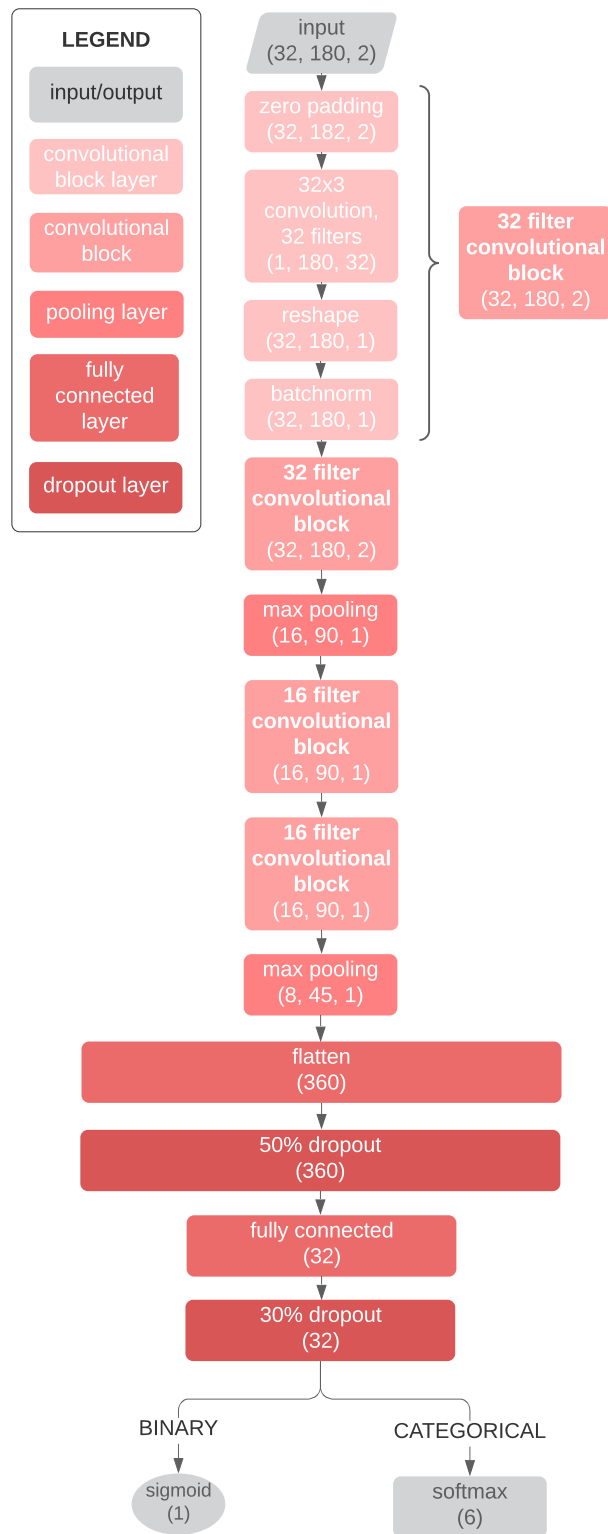


Figure 2.3: SCONE architecture for binary and categorical classification.

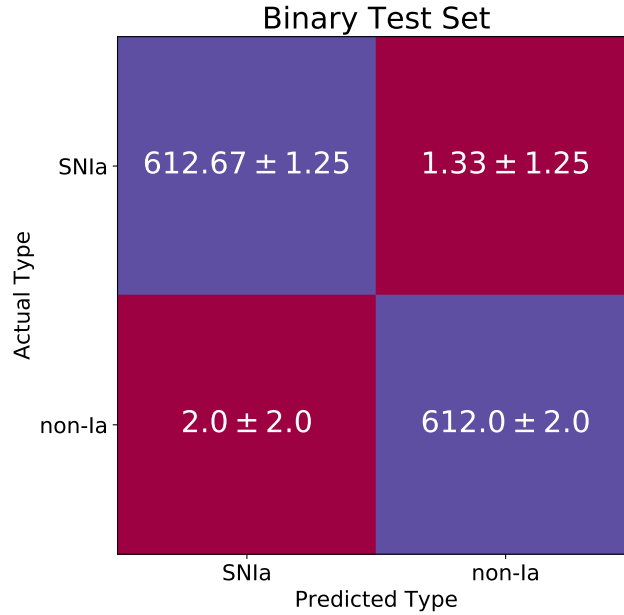


Figure 2.4: Confusion matrix showing average and standard deviation over five runs for binary classification on the test set.

## 2.3. Results

### 2.3.1. Binary Classification

Our model achieved  $99.93 \pm 0.06\%$  training accuracy,  $99.71 \pm 0.2\%$  validation accuracy, and  $99.73 \pm 0.26\%$  test accuracy on the Ia vs. non-Ia binary classification problem performed on the class-balanced dataset of 12,256 sources.

Figure 2.4 shows the confusion matrices for binary classification, and Table 2.4 shows the model’s performance on all the evaluation metrics described in Section 2.7. Both Figure 2.4 and Table 2.4 were created with data from five independent training, validation, and test runs of the classifier. Unless otherwise noted, the default threshold for binary classification is 0.5, where classifier confidence equal to or exceeding 0.5 counts as an SNIa classification, and vice versa. Altering this threshold produces Figure 2.5, the ROC curve of one of these test runs.



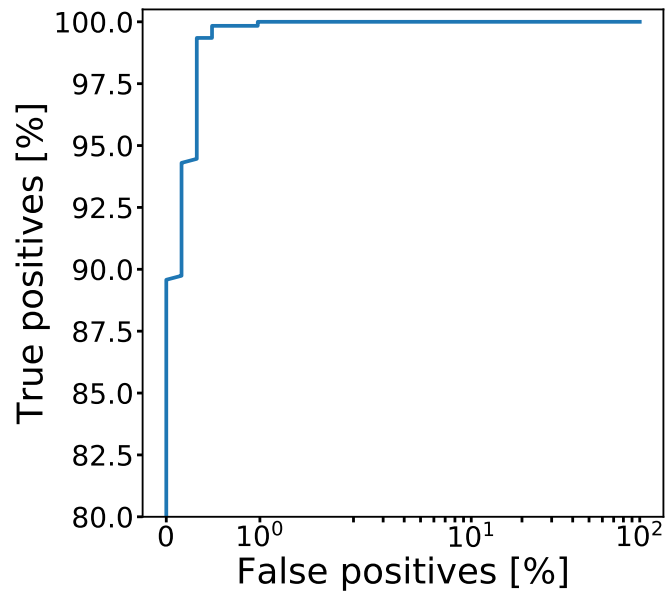


Figure 2.5: Semilog plot of the ROC curve for binary classification on the test set.

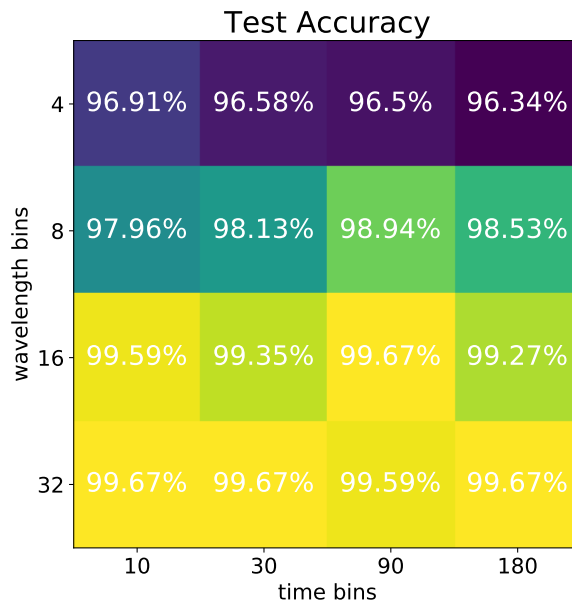


Figure 2.6: Test set accuracies for each choice of wavelength and time bins.

Table 2.4: Evaluation metrics for Ia vs. non-Ia classification on cut dataset

Metric	Training	Validation	Test
Accuracy	$99.93 \pm 0.06\%$	$99.71 \pm 0.2\%$	$99.73 \pm 0.26\%$
Purity	$99.93 \pm 0.06\%$	$99.76 \pm 0.25\%$	$99.68 \pm 0.35\%$
Efficiency	$99.93 \pm 0.05\%$	$99.67 \pm 0.23\%$	$99.78 \pm 0.22\%$
AUC	$1.0 \pm 4.1e-5$	$0.9991 \pm 1.6e-3$	$0.9994 \pm 1e-3$

### Heatmap Dimensions

We explored the binary classification performance of different heatmap dimensions in both the time (width) and wavelength (height) axes. For our 7100 Å wavelength range ( $3000 \text{ Å} < \lambda < 10,100 \text{ Å}$ ), we chose intervals of 221.875 Å, 443.8 Å, 887.5 Å, and 1775 Å, resulting in heatmaps with 32, 16, 8, and 4 wavelength "bins", respectively. For our 180 day range ( $t_{\text{peak}} - 50 \leq t \leq t_{\text{peak}} + 130$ ), we chose intervals of 1, 2, 6, and 18 days, resulting in heatmaps with 180, 90, 30, and 10 time bins.

Figure 2.6 shows the training, validation, and test accuracies for each choice of wavelength and time dimensions. Our classifier seems relatively robust to these changes, showing minimal performance impacts for wavelength bins  $\geq 16$  and impressive performance for the smaller sizes as well. Test accuracy drops a maximum of 2.67% between the best- and worst-performing variants,  $32 \times 180$  and  $4 \times 10$ . This is noteworthy as the  $32 \times 180$  heatmaps contain 144 times the number of pixels of the  $4 \times 10$  heatmaps.

The performance seems to unilaterally improve as expected as the number of wavelength bins increase, but increasing the number of time bins seems to yield varying, though likely not statistically significant, results.

We have reported all of our SCONE results using one of the best performing variants, the  $32 \times 180$  heatmaps.

### Out-of-Distribution Results

Preliminary exploration into the out-of-distribution task of training on the spectroscopic dataset and testing on the main dataset yielded 80.6% test accuracy. The full results of training on 85% of

the spectroscopic dataset, validating on the remaining 15%, and testing on the full main dataset are shown in Table 2.5. Since the redshift distribution of the spectroscopic dataset is skewed toward lower redshifts, testing on class-balanced low-redshift subsets of the main dataset yielded 83% test accuracy for  $z < 0.4$  and 87% test accuracy for  $z < 0.3$ . Boone (2019a) introduced redshift augmentation to mitigate this effect. The mismatch between the test and training sets, however, comes in other forms. For example, if the training data is generated using models rather than real data, differences in the characteristics of the spectral surfaces can have an impact on classification. The unknown relative rates of each type of event also affect the overall performance. Since out-of-distribution robustness is an integral part of the challenge of photometric SNe classification, improving the performance of SCONE on these metrics will be the topic of a future paper.

Table 2.5: Evaluation metrics for out-of-distribution Ia vs. non-Ia classification

Metric	Training	Validation	Test
Accuracy	$99.65 \pm 0.36\%$	$98.84 \pm 1.1\%$	$80.61 \pm 1.75\%$
Purity	$99.86 \pm 0.31\%$	$98.74 \pm 1.31\%$	$81.86 \pm 2.22\%$
Efficiency	$99.67 \pm 0.46\%$	$98.75 \pm 1.27\%$	$80.06 \pm 1.31\%$
AUC	$1.0 \pm 8.9e-5$	$0.9939 \pm 9.5e-3$	$0.8552 \pm 1.4e-2$

### 2.3.2. Categorical Classification

In addition to binary classification, SCONE is able to perform categorical classification and discriminate between different types of SNe. We performed 6-way categorical classification with the same PLAsTiCC dataset used for binary classification as well as the class-balanced dataset described in Section 2.1. Our model differentiated between SN types Ia, II, Ibc, Iax, SN-91bg, and SLSN-1. On the PLAsTiCC dataset (not class-balanced), it achieved  $99.26 \pm 0.18\%$  training accuracy,  $99.13 \pm 0.34\%$  validation accuracy, and  $99.18 \pm 0.18\%$  test accuracy. The confusion matrices in Figure 2.8 show the average by-type breakdown for five independent runs.

On the balanced dataset, it achieved  $97.8 \pm 0.32\%$  training accuracy,  $98.52 \pm 0.28\%$  validation accuracy, and  $98.18 \pm 0.3\%$  test accuracy. The confusion matrices in Figure 2.7 show the average and standard deviations of the by-type breakdown for 5 independent runs.

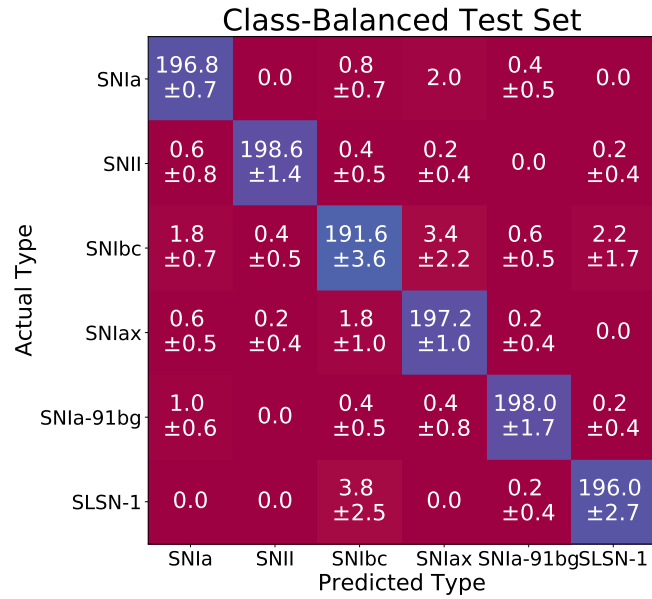


Figure 2.7: Confusion matrix showing average and standard deviation over five runs for categorical classification on the balanced test set.

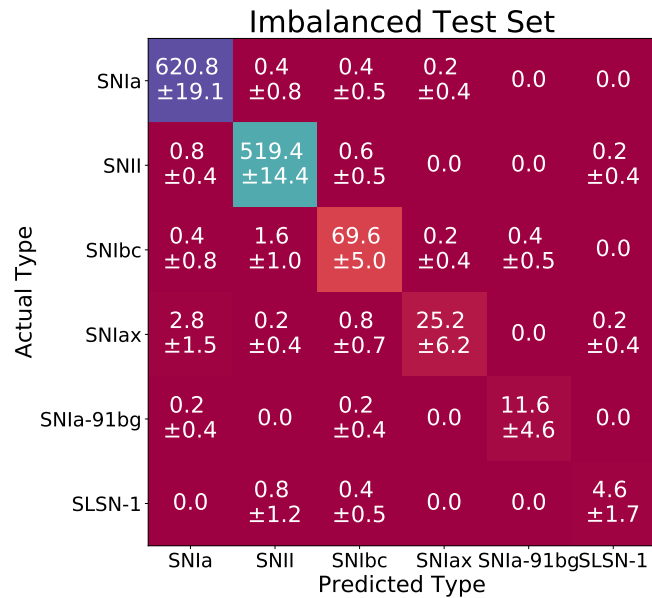


Figure 2.8: Confusion matrix showing average and standard deviation over five runs for categorical classification on the PLAsTiCC (imbalanced) test set.

Table 2.6: Misclassified test set heatmaps by true and predicted type for binary classification.

True Type	Predicted Type	Confidence			Total	Percentage
		> 90%	90-70%	70-50%		
SNIa	non-Ia	1	0	0	1	25%
SNIa	SNIa	2	0	0	2	50%
SNIax	SNIa	1	0	0	1	25%

It is worth noting that we trained and tested with the PLAsTiCC dataset even though it is not class-balanced for this task to try to evaluate the model’s performance on a dataset emulating the relative frequencies of these events in nature.

## 2.4. Discussion

Analysis of misclassified heatmaps was performed for both binary and class-balanced categorical classification. No clear evidence of the effect of redshift on accuracy was found for either mode of classification. The quantity of misclassified SNIa examples per run is not sufficient for us to draw conclusions about the accuracy evolution as a function of redshift.

### 2.4.1. Binary Classification

According to the data presented in Figure 2.4, the model seems to mispredict about the same number of Ia’s as non-Ia’s. An average of 3.33 Ia’s are mispredicted in the training set compared with 3.5 non-Ia’s. For the validation set, 2 Ia’s are mispredicted compared to 1.5, and 1.33 Ia’s and 2 non-Ia’s are mislabeled for the test set.

The misclassified set summarized in Table 2.6 is the result of one of the five runs represented by the data in Figure 2.4. In this example, the model missed 5 examples total during testing – 1 SNIa, 2 SNIa, and 1 SNIax. It was > 90% confident about all of these misclassifications, which is certainly not the case for categorical classification. This could be due to the fact that there are more examples of each type for binary classification than categorical ( $\sim 6,000$  and  $1,200$  per type for training, respectively).

Table 2.7: Misclassified test set heatmaps by true and predicted type for categorical class-balanced classification.

True Type	Predicted Type	Confidence			Total	Percentage
		> 90%	90-70%	70-50%		
SN Ia	SN Iax	1	0	0	1	4.8%
SN II	SN Ia	1	0	0	1	4.8%
	SN Ibc	0	0	1	1	4.8%
SN Ibc	SN Ia	0	0	1	1	4.8%
	SN Iax	1	0	0	1	4.8%
	SLSN-1	0	0	1	1	4.8%
SN Iax	SN Ia	1	2	0	3	14.3%
	SN Ibc	1	2	0	3	14.3%
	SN Ia-91bg	1	0	0	1	4.9%
SLSN-1	SN Ibc	3	1	3	7	33.3%
SN Ia-91bg	SN Ibc	0	1	0	1	4.8%

#### 2.4.2. Categorical Classification

The data in Figures 2.7 and 2.8 show some level of symmetry between misclassifications. SN Iax and SLSN-1 seem to be easily distinguishable across the board, for example, with 0's in all relevant cells in both figures except one. In Figure 2.7, SN Ibc and SLSN-1 are seemingly very similar, as they are misclassified as one another at similarly high rates.

There are notable differences between Figures 2.7 and 2.8, however. In Figure 2.7, representing the classifier's performance on class-balanced categorical classification, the model mispredicts SN Ia's as other types at a similar rate as non-Ia's mispredicted as Ia's. An average of 3.2 Ia's are mispredicted, whereas an average of 4 non-Ia's are misclassified as Ia. In the confusion matrix shown in Figure 2.8, significantly more non-Ia's were mispredicted as Ia. An average of 1 Ia was mispredicted compared to an average of 4.2 non-Ia's misclassified as Ia. The rate of SN Ibc's mispredicted as SLSN-1 is also significantly lower for the PLAsTiCC dataset than for the balanced dataset. These observations further reinforce the impact of imbalanced classes in classification tasks.

The misclassified set summarized in Table 2.7 is the result of one of the five class-balanced categorical classification runs represented by the data in Figure 2.7.

One point of interest is the lack of symmetry between misclassifications, in contrast with the analysis of Figures 2.7 and 2.8. This is clear in the significantly larger number of SLSN-1 misclassified as SNIbc (7) compared with the number of SNIbc misclassified as SLSN-1 (1). SNIax is also more often misclassified as other types (3 as SNIa, 3 as SNIbc, and 1 as SNIa-91bg) than non-Iax misclassified as Iax (1 SNIa and 1 SNIbc). The more symmetric Figure 2.7 suggests that the asymmetry of this table is due to randomness and would be corrected with data from other runs.

The distribution of misclassified examples across the confidence spectrum is non-uniform. In this table, *confidence* refers to the probability assigned to the predicted type by the classifier. Confidence near 100% for a misclassified example is potentially more insightful than one near 50%. 9 out of the 21 misclassified heatmaps were misclassified at > 90% confidence, 6 at 90-70% confidence, and 6 at 70-50%. Surprisingly, the classifier is confidently wrong almost half the time. One particularly interesting example is a SNIbc "misclassified" as SLSN-1, but the classification probabilities for both SLSN-1 and SNIbc were 50%.

#### 2.4.3. Limitations and Future Work

As stated in section 2.1, it is important to note that the metrics reported in this paper are in-distribution results since the training, validation, and test sets are mutually exclusive segments of the main dataset. The out-of-distribution performance of SCONE, as evaluated in section 3.1.2, is noticeably diminished from the > 99% in-distribution test accuracy. The high in-distribution test accuracy shows that SCONE is robust to previously unseen data, but the lower out-of-distribution test accuracy demonstrates SCONE's sensitivity to variations in the parameters of the dataset, such as the redshift distribution, relative rates of different types of SNe, small variations in the SN Ia model, as well as telescope characteristics. Generalizing SCONE to become robust to these variations will be the subject of a future paper.

## 2.5. Conclusions

In this paper we have presented SCONE, a novel application of deep learning to the photometric supernova classification problem. We have shown that SCONE has achieved unprecedented performance on the in-distribution Ia vs. non-Ia classification problem and impressive performance

on classifying SNe by type without the need for accurate redshift approximations or handcrafted features.

Using the wavelength-time flux and error heatmaps from the Gaussian process for image recognition also allows the convolutional neural network to learn about the development of the supernova over time in all filter bands simultaneously. This provides the network with far more information than a photograph taken at one moment in time. Our choice of an  $h \times 3$  convolutional kernel, where  $h$  is the number of wavelength bins, supplements these benefits by allowing the network to learn from data on the full spectrum of wavelengths in a sliding window of 3 days.

As future large-scale sky surveys continue to add to our ever-expanding transients library, we will need an accurate and computationally inexpensive photometric classification algorithm. Such a model can inform the best choice for allocation of our limited spectroscopic resources as well as allow researchers to further cosmological science using minimally contaminated SNIa datasets. SCONE can be trained on tens of thousands of lightcurves in minutes and confidently classify thousands of lightcurves every second at  $> 99\%$  accuracy.

Although SCONE was formulated with supernovae in mind, it can easily be applied to classification problems with other transient sources. The documented source code has been released on Github ([github.com/helenqu/scone](https://github.com/helenqu/scone)) to ensure reproducibility and encourage the discovery of new applications.

## 2.6. Acknowledgments

The authors would like to thank Rick Kessler for his help with SNANA simulations and Michael Xie for his guidance on the model architecture. This research used resources of the National Energy Research Scientific Computing Center (NERSC), a U.S. Department of Energy Office of Science User Facility located at Lawrence Berkeley National Laboratory, operated under Contract No. DE-AC02-05CH11231. This work was supported by DOE grant DE-FOA-0001781 and NASA grant NNH15ZDA001N-WFIRST.



## CHAPTER 3

### Photometric Classification of Early-Time Supernova Lightcurves with SCONE

#### Abstract

In this work, we present classification results on early supernova lightcurves from SCONE, a photometric classifier that uses convolutional neural networks to categorize supernovae (SNe) by type using lightcurve data. SCONE is able to identify SN types from lightcurves at any stage, from the night of initial alert to the end of their lifetimes. Simulated LSST SNe lightcurves were truncated at 0, 5, 15, 25, and 50 days after the trigger date and used to train Gaussian processes in wavelength and time space to produce wavelength-time heatmaps. SCONE uses these heatmaps to perform 6-way classification between SN types Ia, II, Ibc, Ia-91bg, Iax, and SLSN-I. SCONE is able to perform classification with or without redshift, but we show that incorporating redshift information improves performance at each epoch. SCONE achieved 75% overall accuracy at the date of trigger (60% without redshift), and 89% accuracy 50 days after trigger (82% without redshift). SCONE was also tested on bright subsets of SNe ( $r < 20$  mag) and produced 91% accuracy at the date of trigger (83% without redshift) and 95% 5 days after trigger (94.7% without redshift). SCONE is the first application of convolutional neural networks to the early-time photometric transient classification problem. All of the data processing and model code developed for this paper can be found in the SCONE software package located at [github.com/helenqu/scone](https://github.com/helenqu/scone) (Qu, 2021b).

#### 3.1. Introduction

Observations of transient and supernova phenomena have informed fundamental discoveries about our universe, ranging from its expansion history and current expansion rate (Riess, 1998; Perlmutter et al., 1999; Freedman et al., 2019; Riess et al., 2019) to the progenitor physics of rare and interesting events (Pursiainen et al., 2018; Armstrong et al., 2021). In the near future, next generation wide-field sky surveys such as the Vera C. Rubin Observatory Legacy Survey of Space and Time (LSST, Ivezić et al., 2019a) will have the ability to observe larger swaths of sky with higher resolution and certainly uncover even more new and exciting astrophysical phenomena.

These surveys promise to generate ever larger volumes of photometric data at unprecedented rates. However, the availability of spectroscopic resources is not expected to scale nearly as quickly. Thus, the challenge of effectively allocating these limited resources is more important than ever. For type Ia SN cosmology, spectroscopic information is used to minimize contamination in constructing pure and representative samples of SNe Ia to continue to constrain the dark energy equation of state. For supernova physicists, spectra uncover important information about an event’s potential progenitor processes (Filippenko, 2005; Perets et al., 2010; Modjaz et al., 2014; Sollerman et al., 2021). Spectra taken near peak brightness of an event are optimal as they include mostly transient information and are not dominated by host galaxy features.

With millions of alerts each night, fast and accurate automatic classification mechanisms will be needed to replace the time-consuming process of manual inspection. More specifically, the ability to perform classification early on in the lifetime of a transient would allow for ample time to take spectra at the peak luminosity of the event or at multiple points over the course of the event’s lifetime.

### 3.1.1. Photometric Supernova Classification

An impressive body of work has emerged over the past decade on photometric classification of supernovae. Since only a small percentage of discovered supernovae have ever been followed up spectroscopically, a reliable photometric classifier is indispensable to the advancement of supernova science.

The Supernova Photometric Classification Challenge (SNPhotCC, Kessler et al., 2010b,c) created not only an incentive to invest in photometric SN classification, but also a dataset that would be used to train and evaluate classifiers for years to come. Successful approaches range from empirical template-fitting (Sako et al., 2008a) to making classification decisions based on manually extracted features (Richards et al., 2012; Karpenka et al., 2013). The more recent Photometric LSST Astronomical Time-series Classification Challenge (PLAsTiCC, The PLAsTiCC team et al., 2018a) diversified the dataset by asking participants to differentiate between 14 different transient and variable object classes, including the 6 common supernova types included in this work. The top

entries made use of feature extraction paired with various machine learning classification methods, such as boosted decision trees and neural networks (Hložek et al., 2020). Ensemble methods, in which the results of multiple classifiers are combined to create the final classification probability, were widely used as well.

Deep learning is a branch of machine learning that seeks to eliminate the necessity of human-designed features, decreasing the computational cost as well as avoiding the introduction of potential biases (Charnock and Moss, 2017; Moss, 2018; Naul et al., 2018; Aguirre et al., 2019). In recent years, many deep learning techniques have been applied to the challenge of photometric SN classification.

Recurrent neural networks (RNNs) are designed to learn from sequential information, such as time-series data, and have been used with great success on this problem. Charnock and Moss (2017) applies a variant of RNNs known as Long Short Term Memory networks (LSTMs, Hochreiter and Schmidhuber, 1997) to achieve impressive performance distinguishing SNIa from core collapse (CC) SNe. Muthukrishna et al. (2019) uses a gated recurrent unit (GRU) RNN architecture to be able to perform real-time and early lightcurve classification. Möller and de Boissière (2020a) performs both binary classification and classification by type with full and partial lightcurves using Bayesian RNNs. Villar et al. (2020) uses a GRU RNN as an autoencoder to smooth out irregularities in lightcurve data that is then fed into a random forest classifier.

Convolutional neural networks (CNNs), which are used in this work, are a state-of-the-art image recognition architecture (LeCun et al., 1989b, 1998; Krizhevsky et al., 2012a; Zeiler and Fergus, 2014). Pasquet et al. (2019b) addresses the issue of non-representative training sets by using a CNN as an autoencoder to learn from unlabeled test data. Carrasco-Davis et al. (2021) developed an image time-series classifier as part of the ALERCE alert broker, using a CNN to differentiate between various transient types as well as bogus alerts.

Outside of these traditional models, deep learning is still providing new and creative solutions to the photometric transient classification problem. Convolutional recurrent neural networks are

used to classify a time series of image stamps by Kodi Ramanah et al. (2021) to detect gravitationally lensed supernovae. A newer type of deep learning architecture, known as a transformer, achieves a very impressive result when applied to the PLAsTiCC dataset by Allam and McEwen (2021). A variational autoencoder was used by ParSNIP (Boone, 2021) to develop a low-dimensional representation of transient lightcurves that uses redshift-annotated photometric data to perform full lightcurve photometric classification and generate time-varying spectra, among other tasks.

### 3.1.2. Early Photometric Supernova Classification

Though much progress has been made on the photometric supernova classification problem, most of the solutions tackle classification of full supernova lightcurves retrospectively. However, the earlier an object can be classified, the more opportunities there are for the community to perform follow-up observation. Spectroscopic or photometric follow-up at early stages not only reveals insights into progenitor physics, but can also serve as a benchmark for further observations at later epochs. SN type IIb, for example, exhibit hydrogen features in early spectra that quickly disappear over time (Woosley et al., 1987). Shock breakout physics is another use case of follow-up observation. Armstrong et al. (2021) was the first to report capturing the complete evolution of a shock cooling lightcurve, a short-lived event preceding peak luminosity that reveals properties of the shock breakout and progenitor star for stripped-envelope supernovae such as the IIb.

Despite the general focus on full lightcurve classification, several notable works have addressed the challenge of early photometric classification. Sullivan et al. (2006a) was able to not only differentiate between SNIa and CC SN, but also predict redshift, phase, and lightcurve parameters for SNIa using only two or three epochs of multiband photometry data. Poznanski et al. (2007) also performed binary Ia vs. CC SNe classification, but using a Bayesian template-fitting technique on only single epoch photometry and photometric redshift estimates. PSNID (Sako et al., 2008a, 2011b), the algorithm that produced the highest overall figure of merit in SNPhotCC, was used by the Sloan Digital Sky Survey (Frieman et al., 2008) and the Dark Energy Survey (Smith et al., 2020a) to classify early-time and full supernova lightcurves.

Muthukrishna et al. (2019) is a recent application of deep learning techniques specifically to early-

time transient classification. A GRU RNN is trained and tested on a PLAsTiCC-derived dataset of 12 transients, including 7 supernova types, that are labeled at each epoch with “pre-explosion” prior to the date of explosion and the correct transient type after explosion. Thus, the model is able to produce a classification at each epoch of observation. Möller and de Boissière (2020a) has also produced an RNN-based photometric classifier that is capable of classifying partial supernova lightcurves, but primarily achieves good results for Ia vs. CC SN classification. Villar et al. (2020) uses a recurrent variational autoencoder architecture to perform early-time anomaly detection for exotic astrophysical events within the PLAsTiCC dataset, such as active galactic nuclei and super-luminous SNe. Finally, LSST alert brokers such as ALERCE (Sánchez-Sáez et al., 2021) specialize in accurate early-time classification of transient alerts.

### 3.1.3. Overview

Originally introduced in Qu et al. (2021), hereafter Q21, as a full lightcurve photometric classification algorithm, SCONE was able to retrospectively differentiate Ia vs. CC SN with  $> 99\%$  accuracy and categorize SNe into 6 types with  $> 98\%$  accuracy without redshift information. Our approach centers on producing heatmaps from 2-dimensional Gaussian processes fit on each lightcurve in both wavelength and time dimensions. These “flux heatmaps” of each supernova detection, along with “uncertainty heatmaps” of the Gaussian process uncertainty, constitute the dataset for our model. This preprocessing step smooths over irregular sampling rates between filters, mitigates the effect of flux outliers, and allows the CNN to learn from information in all filters simultaneously.

Section 2 outlines the details of the datasets and models used in this work and we discuss the classifier’s performance on the various dataset types in Section 3, including a comparison with existing literature. We state our conclusions and goals for future work in Section 4.

## 3.2. Methods

### 3.2.1. Simulations

For this work, SCONE was trained and tested on a set of LSST deep drilling field (DDF) simulations. The dataset was created with SNANA (Kessler et al., 2009c) using the PLAsTiCC transient

Table 3.1: Training, validation, and test dataset sizes for the  $t_{\text{trigger}} + N$  datasets.

Dataset	Number of Each Type	Total Size
Training	6148	36888
Validation	769	4614
Test	768	4608
Full	7685	46110

class models for supernovae types Ia, II, Ibc, Ia-91bg, Iax, and SLSN (The PLAsTiCC team et al., 2018b; Kessler et al., 2019c; Guy et al., 2010b; Kessler et al., 2013a; Pierel et al., 2018b; Jha, 2017; Kessler et al., 2010a; Pierel et al., 2018a; Guillochon et al., 2018b; Villar et al., 2017a; Kessler et al., 2010b; Pierel et al., 2018c; Guillochon et al., 2018c; Villar et al., 2017b; Guillochon et al., 2018a; Nicholl et al., 2017; Kasen and Bildsten, 2010). The relative rates and redshift distribution are identical to those of the data produced for the PLAsTiCC challenge. This is the same dataset used to evaluate SCONE’s categorical classification performance in Q21. No cuts on individual low S/N lightcurve points were made, but lightcurves with fewer than two  $5\sigma$  detections were removed, as  $t_{\text{trigger}}$  would be ill-defined in those cases. We note that in observed data, transient light curve samples will contain SNe contaminated by other galactic astrophysical sources, but methods such as Sánchez-Sáez et al. (2021) are reliably able to distinguish extragalactic and galactic events. Thus, we can assume the feasibility of creating a pure sample of SN lightcurves such as the one used in this work.

### 3.2.2. Trigger Definition

We define a *detection* as any observation exceeding the  $5\sigma$  signal-to-noise (S/N) threshold. We define the *trigger* as the next detection that occurs at least one night after the first. In this work, the dataset with the least photometric information includes observations up to (and including) the date of trigger. Thus, all SNe in our datasets have at least two epochs of observation. As the date of first detection is also a common choice of trigger date in other transient surveys, the implications of this discrepancy are explored further in Section 3.3. We present results on a dataset where the distinction between these two definitions is small, i.e.  $t_{\text{trigger}} \leq t_{\text{first detection}} + 5$ .

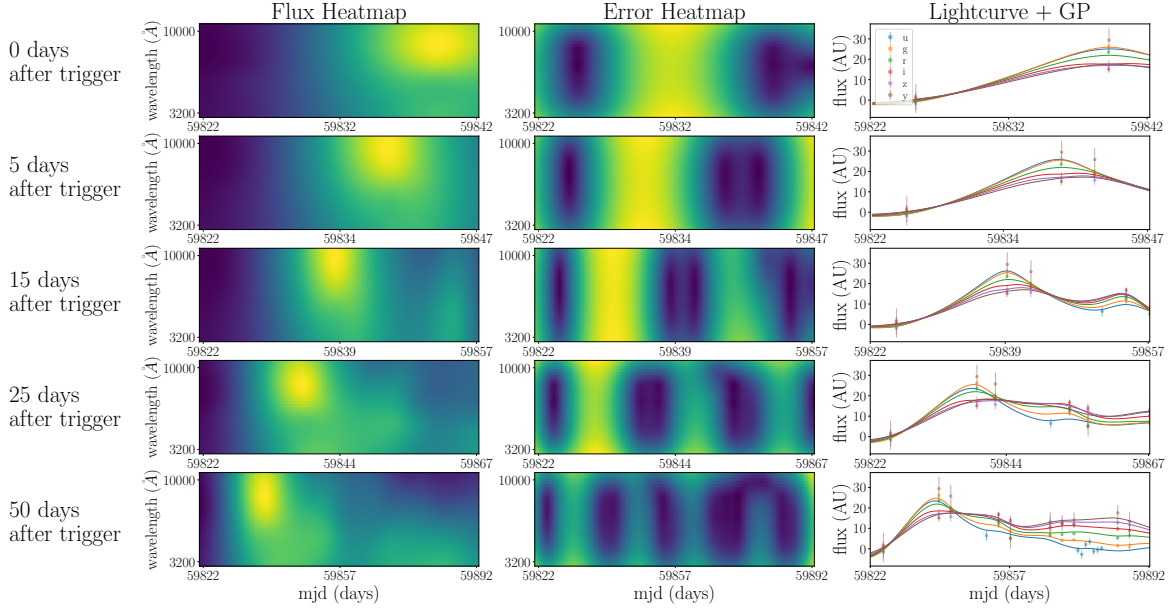


Figure 3.1: An SNIi ( $z = 0.39$ ) shown in all five heatmap datasets along with the lightcurves and Gaussian process fits used to create each heatmap. The flux and flux error measurements from the raw photometry are shown as points with error bars, while the Gaussian process fits to each photometry band are shown as curves. The Gaussian process errors, which are used to create the heatmaps in the middle column, are not shown in the lightcurve plots. The  $x$ -axis limit of the plots in each row are different, as the lightcurve is truncated according to the label on the left for each row in the figure.

### 3.2.3. Datasets and Heatmap Creation

#### $t_{\text{trigger}} + N$ Datasets

To evaluate SCONE’s classification performance on lightcurves at different stages of the supernova lifetime, five sets of heatmaps were created from the simulations described in Section 2.1. All sets of heatmaps take data starting 20 nights prior to the date of trigger ( $t_{\text{trigger}}$ ) and end at  $N = 0, 5, 15, 25,$  and  $50$  days after the date of trigger, respectively. Hereafter, these are collectively referred to as “ $t_{\text{trigger}} + N$  datasets”.

Prior to training, the lightcurve data is processed into heatmaps. We use the approach described by Boone (2019b) to apply 2-dimensional Gaussian process regression to the raw lightcurve data to model the event in the wavelength ( $\lambda$ ) and time ( $t$ ) dimensions. We use the Matérn kernel

( $\nu = \frac{3}{2}$ ) with a fixed 6000 Å characteristic length scale in  $\lambda$  and fit for the length scale in  $t$ . Once the Gaussian process regression model has been trained, we obtain its predictions on a  $\lambda, t$  grid and call this our “flux heatmap”.

It is important to note that the Gaussian processes are fit on lightcurves truncated at  $N$  days after trigger in each dataset and not given access to lightcurve information past the cutoff date. Thus, though the  $\lambda$  axis is not affected by the different choices of  $N$ , the  $t$  range of the input lightcurve data varies for each  $t_{\text{trigger}} + N$  dataset. For the datasets in this work, the  $\lambda, t$  grids were chosen to preserve the shape of the resulting heatmap despite the fact that the number of nights of lightcurve data varies between the  $t_{\text{trigger}} + N$  datasets.  $\lambda$  is chosen to be  $3000 < \lambda < 10,100$  Å with a 221.875 Å interval for all datasets, while the  $t$  interval depends on the number of nights of data:  $t_{\text{trigger}} - 20 \leq t \leq t_{\text{trigger}} + N$  with a  $\frac{N+20}{180}$  day interval, where  $N = 0, 5, 15, 25, 50$ . This ensures that all heatmaps have size  $32 \times 180$ .

In addition to the flux heatmap, we also take into account the uncertainties on these predictions at each  $\lambda_i, t_j$ , producing an “error heatmap”. We stack these two heatmaps depthwise for each SN lightcurve and divide by the maximum flux value to constrain all entries to  $[0,1]$ . This  $32 \times 180 \times 2$  tensor is our input to the convolutional neural network.

An example of the heatmaps and associated lightcurves of a single SN in all 5 datasets is shown in Figure 3.1. Results on the  $t_{\text{trigger}} + N$  datasets are described in Section 3.2.

### Bright Supernovae

Our model was also evaluated on the subset of particularly bright supernovae from the  $t_{\text{trigger}} + 0$  and  $t_{\text{trigger}} + 5$  datasets to emulate a real-world use case of SCONE for spectroscopic targeting, as bright supernovae are better candidates for spectroscopic follow-up. “Bright SNe” included in these datasets were chosen to be SNe with last included detection  $r < 20$  mag. With this threshold, there were 907 SNe in the  $t_{\text{trigger}} + 0$  bright dataset and 5,088 SNe in the  $t_{\text{trigger}} + 5$  bright dataset. As described in more detail in Section 2.4, SCONE was trained with a standard  $t_{\text{trigger}} + N$  training set combined with 40% of the  $t_{\text{trigger}} + N$  bright dataset, and tested on the  $t_{\text{trigger}} + N$  bright dataset.



Results on these datasets are described in Section 3.5.

### Mixed Dataset

In order to evaluate SCONE’s ability to classify SNe with any number of nights of photometry, a sixth dataset (the “mixed” dataset) was created from the same PLAsTiCC simulations. Data is taken starting 20 nights prior to the date of trigger (as with the  $t_{\text{trigger}} + N$  datasets) but truncated at a random night between 0 and 50 days after trigger. Due to the choice of the  $t$  interval described in Section 2.3.1, heatmaps with any number of nights of photometry data are all the same size and can thus be mixed in a single dataset in this manner. We train SCONE on this mixed dataset and evaluate its performance on each of the  $t_{\text{trigger}} + N$  datasets in Section 3.6.

#### 3.2.4. Dataset Train/Test Split

Due to the importance of class balancing in machine learning datasets, the same quantity of SNe from each SN type was selected to create the  $t_{\text{trigger}} + N$  and mixed datasets used to train, validate, and test SCONE. 7685 SNe of each of the 6 types were randomly chosen, as this was the quantity of the least abundant type. Thus, the size of each full dataset was 46,110. An 80/10/10 training/validation/test split was used for all results in this work. The sizes of the training, validation, and test subsets of each dataset can be found in Table 3.1.

For evaluation on the bright datasets, SCONE was trained on a hybrid training set of 40% of the  $t_{\text{trigger}} + N$  bright dataset combined with a  $t_{\text{trigger}} + N$  training set, prepared as described in Section 2.3.1. Thus, the training set was not quite class-balanced, as the bright dataset is not class-balanced but the  $t_{\text{trigger}} + N$  training set is. The trained model was then evaluated on the full bright dataset to produce the results shown in Figure 3.10. Due to the imbalanced nature of the bright datasets, the confusion matrices in this figure take the place of an accuracy metric, which could be misleading. We chose to include 40% of the bright dataset in the training process to ensure that the model has seen enough of these particularly bright objects to make reasonable predictions.

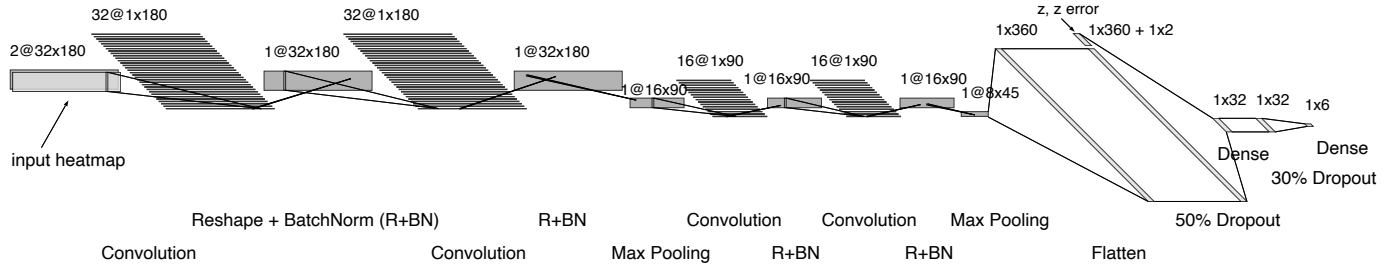


Figure 3.2: SCONE architecture with redshift information for categorical early lightcurve classification.

### 3.2.5. Model

In this work, we report early lightcurve classification results using the vanilla SCONE model developed in Q21 as well as a variant of SCONE that incorporates redshift information. The architecture of SCONE with redshift is shown in Figure 3.2. Both redshift and redshift error are concatenated with the output of the first dropout layer and used as inputs to the fully connected classifier. The model uses spectroscopic redshift information when available and photometric redshift estimates if not.

Prior to training and testing, the input flux and error heatmaps are divided by the maximum flux value of each heatmap for normalization. This means that absolute brightness information is not used for classification. All results in this work, with and without redshift, used the sparse categorical crossentropy loss function, the Adam optimizer (Kingma and Ba, 2014), and trained for 400 epochs with a batch size of 32. SCONE without redshift used a constant  $1e-3$  learning rate, whereas SCONE with redshift used a constant  $5e-4$  learning rate.

### 3.2.6. Computational Performance

The time required for the heatmap creation process was measured using a sample of 100 heatmaps on a single 32-core NERSC Cori Haswell compute node (with Intel Xeon Processor E5-2698 v3). The time required to create one heatmap was  $0.03 \pm 0.01$  seconds. When producing larger-scale datasets, this process is also easily parallelizable over multiple cores or nodes to further decrease heatmap creation time.

SCONE without redshift has 22,606 trainable parameters and SCONE with redshift has 22,670 trainable parameters, while other photometric classification models require at least hundreds of thousands. The performance gains of this simple but effective model compounded with a small training set make SCONE lightweight and fast to train. The first training epoch on a NVIDIA V100 Volta GPU takes approximately 17 seconds (4 milliseconds per batch with a batch size of 32), and subsequent training epochs take approximately 5 seconds each with TensorFlow’s dataset caching. The first training epoch on a Haswell node takes approximately 12 minutes (625 milliseconds per batch), and subsequent epochs take approximately 6 minutes each. Test time per batch of 32 examples is 3 milliseconds on GPU and 10 milliseconds on a Haswell CPU.

### 3.3. Results and Discussion

#### 3.3.1. Evaluation Metrics

The *accuracy* of a set of predictions describes the frequency with which the predictions match the true labels. In this case, we define our prediction for each SN example as the class with highest probability output by the model, and compare this to the true label to obtain an accuracy.

The *confusion matrix* is a convenient visualization of the correct and missed predictions by class, providing a bit more insight into the model’s performance. The confusion matrices shown in Figure 3.4 are normalized such that the  $(i, j)$  entry describes the fraction of the true class,  $i$ , classified as class  $j$ . The confusion matrices in Figure 3.10 are colored by the normalized values, just like Figure 3.4, but overlaid with absolute (non-normalized) values. For both figures, the  $(i, i)$  entries, or those on the diagonal, describe correct classifications.

The *receiver operating characteristic (ROC) curve* makes use of the output probabilities for each class rather than simply taking the highest probability class, as the previous two metrics have done. We consider an example to be classified as class  $i$  if the output probability for class  $i$ , or  $p_i$ , exceeds some threshold  $p$  ( $p_i > p$ ). The ROC curve sweeps values of  $p$  between 0 and 1 and plots the true positive rate (TPR) at each value of  $p$  against the false positive rate (FPR).

TPR is the percentage of correctly classified objects in a particular class, or true positives (TP), as

Table 3.2: Training, validation, and test accuracies *without* redshift information for each early lightcurve dataset. These averages and standard deviations were computed from 5 independent runs of SCONE.

Accuracy	Days After Trigger				
	0 days	5 days	15 days	25 days	50 days
Training	$58.36 \pm 0.14\%$	$68.92 \pm 0.21\%$	$73.99 \pm 0.14\%$	$76.89 \pm 0.29\%$	$80.93 \pm 0.14\%$
Validation	$59.57 \pm 0.51\%$	$70.74 \pm 0.59\%$	$73.31 \pm 3.01\%$	$79 \pm 0.84\%$	$82.5 \pm 2.35\%$
Test	$59.66 \pm 0.43\%$	$70.05 \pm 0.63\%$	$73.66 \pm 2.36\%$	$79 \pm 0.86\%$	$82.2 \pm 1.8\%$

a fraction of all examples in that class, true positives and false negatives (TP+FN). Other names for TPR include *recall* and *efficiency*. The values along the diagonal of the normalized confusion matrices in Figure 3.4 are efficiency values.

$$\text{Efficiency} = \text{TPR} = \frac{\text{TP}}{\text{TP} + \text{FN}}$$

FPR is the percentage of objects incorrectly classified as a particular class, or false positives (FP), as a fraction of all examples not in that class, false positives and true negatives (FP+TN).

$$\text{FPR} = \frac{\text{FP}}{\text{FP} + \text{TN}}$$

The *area under the ROC curve*, or *AUC*, is used to evaluate the classifier from its ROC curve. A perfect classifier would have an AUC of 1, while a random classifier would score (on average) a 0.5.

The *precision* or *purity* of a set of predictions is the percentage of correctly classified objects in a particular predicted class.

$$\text{Precision} = \frac{\text{TP}}{\text{TP} + \text{FP}}$$

### 3.3.2. $t_{\text{trigger}} + N$ Datasets

The accuracies our model achieved without redshift on each  $t_{\text{trigger}} + N$  dataset are described in Table 3.2, and the accuracies with redshift are described in Table 3.3. These tables show that redshift unequivocally improves classification performance, especially at early times when there is little photometric data to learn from. The inclusion of redshift information not only increases the

Table 3.3: Training, validation, and test accuracies *with* redshift information for each early lightcurve dataset. These averages and standard deviations were computed from 5 independent runs of SCONE.

Accuracy	Days After Trigger				
	0 days	5 days	15 days	25 days	50 days
Training	$72.73 \pm 0.27\%$	$79.61 \pm 0.3\%$	$83.07 \pm 0.2\%$	$84.68 \pm 0.2\%$	$87.17 \pm 0.26\%$
Validation	$74.78 \pm 0.18\%$	$80.52 \pm 1.42\%$	$83.98 \pm 1.15\%$	$86.75 \pm 0.5\%$	$89.2 \pm 0.85\%$
Test	$74.27 \pm 0.51\%$	$80.2 \pm 0.93\%$	$84.14 \pm 1.37\%$	$86.71 \pm 1\%$	$89.04 \pm 0.39\%$

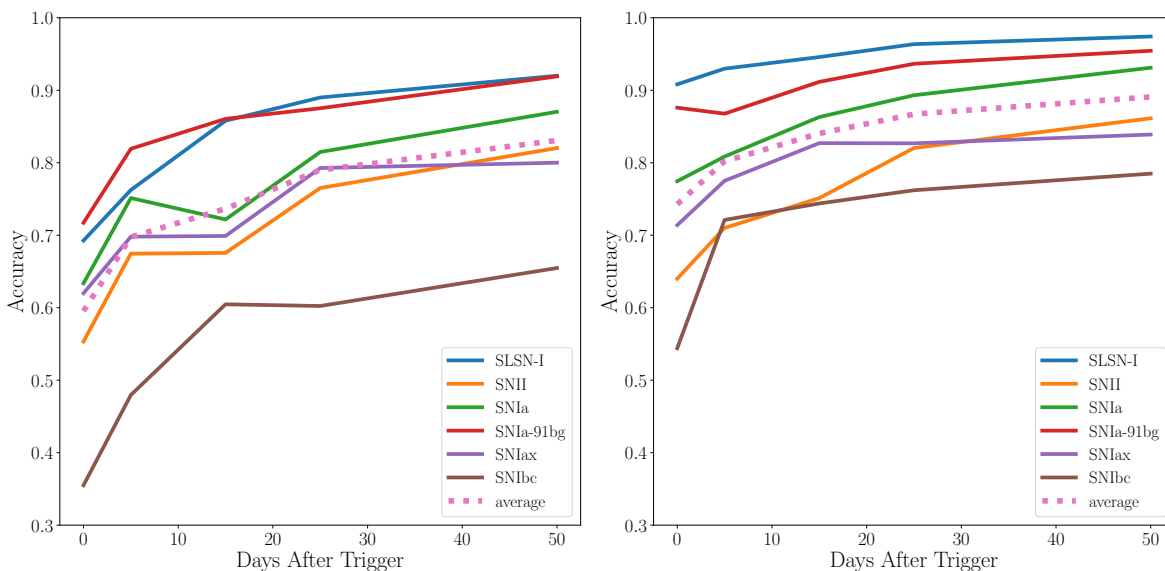


Figure 3.3: Accuracy/efficiency over time for each supernova type without redshift (left) and with redshift (right) for the  $t_{\text{trigger}} + N$  test datasets. The values used in this plot correspond with the diagonals on each normalized confusion matrix in Figure 3.4.

average accuracies for each dataset but also improves the model’s generalizability, as the standard deviations for the validation and test accuracies are lower overall in Table 3.3.

The largest improvement in accuracy between  $t_{\text{trigger}} + N$  datasets occurred between 0 and 5 days after trigger for all datasets. Since the explosion likely reached peak brightness during this period, the lightcurves truncated at 5 days after trigger includes much more information necessary for differentiating between the SN types.

Figure 3.3 shows the accuracy evolution over time for each supernova type in the test sets. From the test sets with redshift plot on the right, it is clear that the jump in overall accuracy between 0 and 5 days after trigger can be attributed to the sharp accuracy boost experienced by SNIbc at 5 days after trigger. Overall, SNIbc benefited the most from the inclusion of redshift, though classification performance on all types saw improvement. Note that, as described in Section 2.3, all heatmaps are normalized to values between 0 and 1 so absolute flux values are not used to differentiate between types. Thus, the model cannot rely on relative luminosity information.

The confusion matrices for  $t_{\text{trigger}} + \{0, 5, 50\}$  test sets with and without redshift information are shown in Figure 3.4. The top two panels are early epoch classification results (0 and 5 days after trigger) and the bottom panel shows late epoch results. The confusion matrices from intermediate epochs (15 and 25 days after trigger) were omitted for brevity.

At the date of trigger (top panel of Figure 3.4), the incorporation of redshift information primarily prevents confusion between SLSN-I and SNIbc. True SLSN-I events misclassified as SNIbc decreased from 11% on average to 2% with redshift. True SNIbc misclassified as SLSN-I decreased from 16% on average to 2% with redshift. Overall, SLSN-I were classified with 91% accuracy with redshift compared to 69% without redshift, and SNIbc were classified with 54% accuracy with redshift compared to 36% without redshift. All types saw marked improvement in classification performance without redshift from 0 to 5 days after trigger, while classification with redshift saw drastic improvement in SNIbc accuracy but only minor improvement for other types. Finally, the effect of added redshift becomes less noticeable by late epochs, where classification accuracy (along

the diagonal) is only mildly improved in the bottom panel of Figure 3.4.

The confusion matrices in Figure 3.4 are normalized by true type, meaning that the values in each row sum to 1. Thus, the values along the diagonal are *efficiency* scores. Normalizing by predicted type, such that the values in each column sum to 1, would result in *purity* scores along the diagonal. However, since all datasets used in Figure 3.4 are class-balanced, the purity scores can be reconstructed from these confusion matrices by dividing each main diagonal value by the sum of the values in its column.

The datasets used for the confusion matrices in Figure 3.4 were also used to create ROC curves for each SN type. ROC curves for test sets without redshift are shown on the left side of Figure 3.5 and ROC curves for test sets with redshift are shown on the right. The addition of redshift information seems to most notably improve the model’s ability to classify SLSN-I – all three panels on the right show SLSN-I as the highest AUC curve whereas all three panels on the left show SNIa-91bg with a higher AUC curve than SLSN-I. This is consistent with our earlier observations from the confusion matrices and accuracy plots.

The information in the ROC curves for all  $t_{\text{trigger}} + N$  datasets is summarized in Figure 3.6, AUC over time plots with and without redshift. The performance looks quite impressive, starting at an average AUC of above 0.9 with redshift at the date of trigger and increasing to 0.975 by 50 days after trigger. Without redshift, average AUC is still respectable, starting at 0.88 and increasing to 0.97.

### 3.3.3. Approximating a First-Detection Trigger Definition

Another common trigger definition used in transient surveys places the trigger at the date of the first detection ( $t_{\text{first detection}}$ ) rather than the second, which is the definition followed in this work. In order to more directly compare SCONE’s results with those of other classifiers following the first detection trigger definition, the distribution of  $t_{\text{trigger}} - t_{\text{first detection}}$  was examined as well as SCONE’s performance on the subset of the  $t_{\text{trigger}} + 0$  dataset with date of second detection ( $t_{\text{trigger}}$ ) at most 5 days after the date of first detection (i.e.  $t_{\text{trigger}} \leq t_{\text{first detection}} + 5$ ).

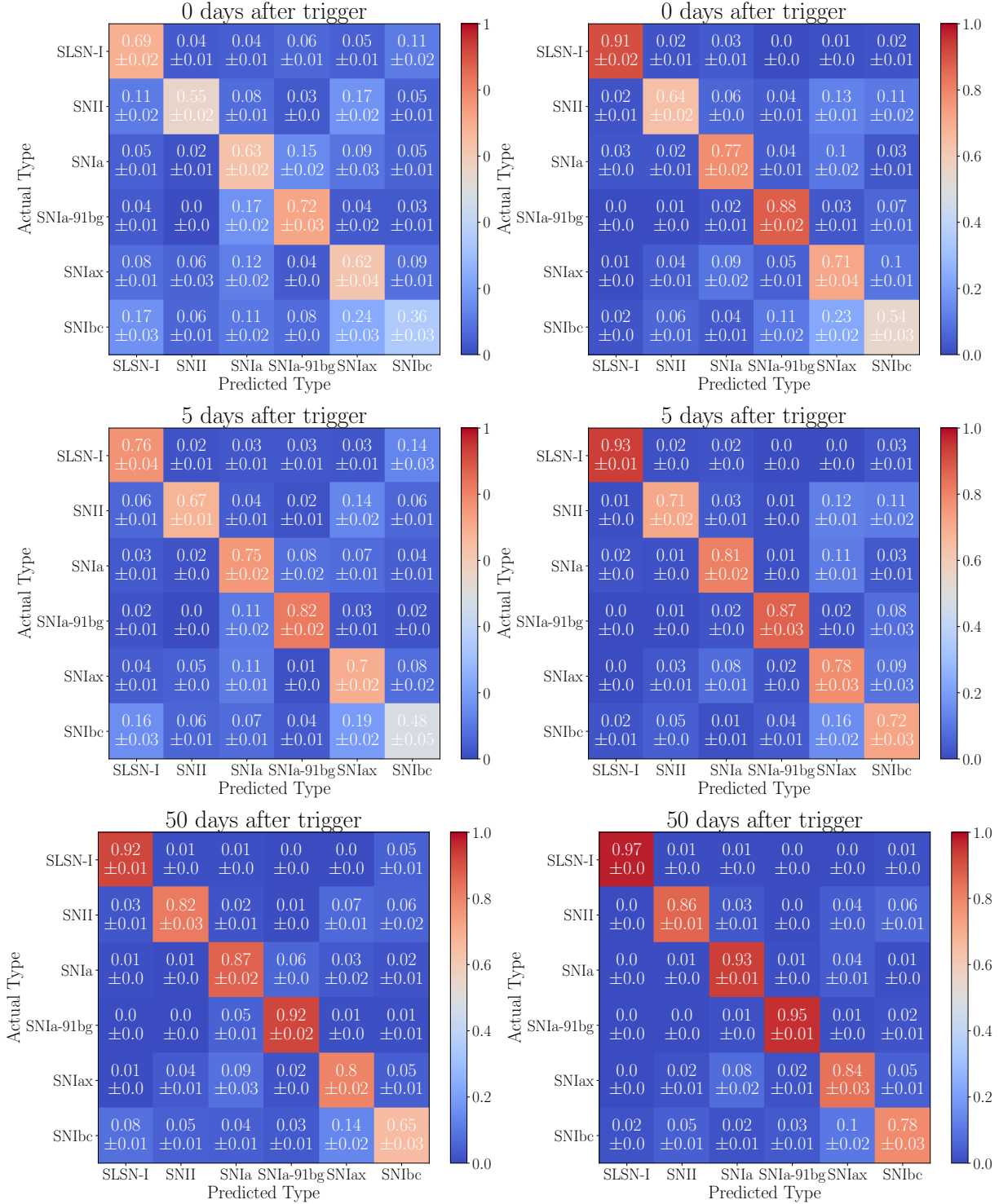


Figure 3.4: Normalized confusion matrices produced by SCONE without (left) and with (right) redshift for the  $t_{\text{trigger}} + \{0, 5, 50\}$  test sets (heatmaps created from lightcurves truncated at 0, 5, and 50 days after the date of trigger). These matrices were made with test set classification performance from 5 independent runs of SCONE.



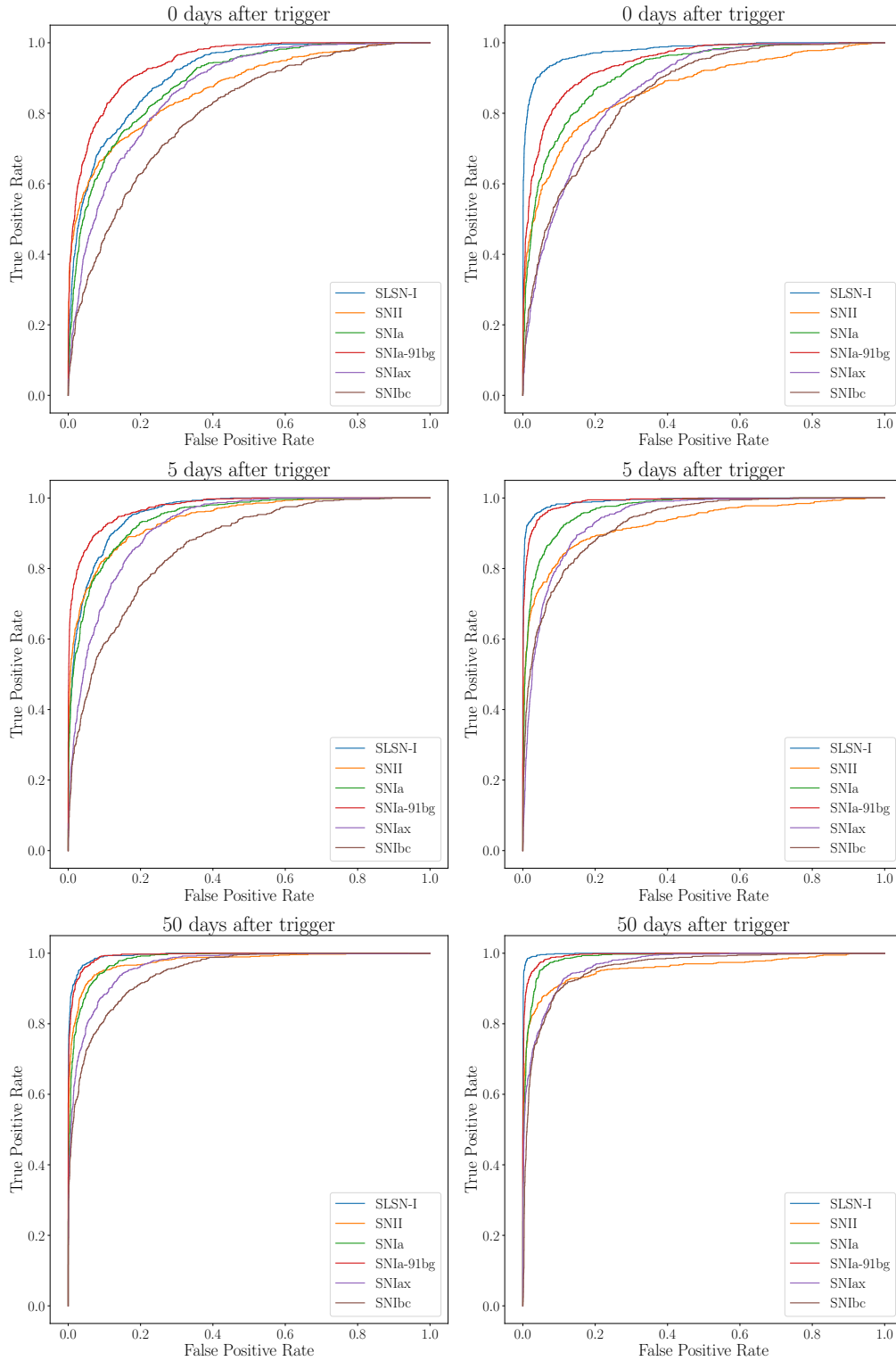


Figure 3.5: Receiver operating characteristic (ROC) curves produced by SCONE without (left) and with (right) redshift for the  $t_{\text{trigger}} + \{0, 5, 50\}$  test sets (heatmaps created from lightcurves truncated at 0, 5, and 50 days after the date of trigger).

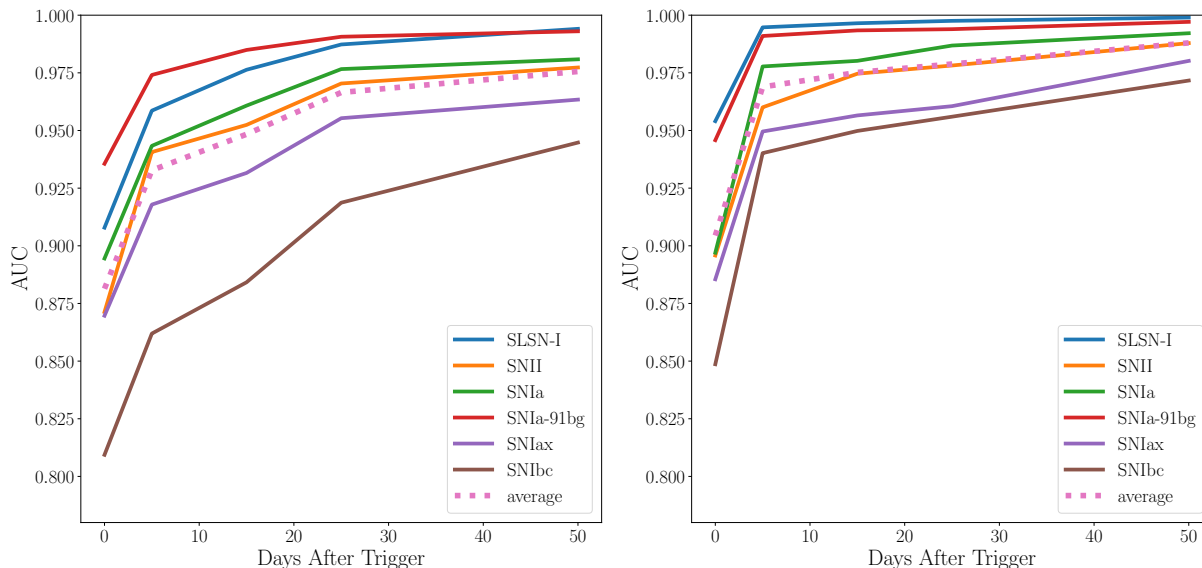


Figure 3.6: Area under the ROC curve (AUC) without (left) and with (right) redshift over time for each supernova type.

Figure 3.7 shows that  $> 65\%$  of  $t_{\text{trigger}}$  dates are no more than 5 days after the date of first detection. To further understand the direct impact of this choice of trigger definition, SCONE was tested on the subset of the  $t_{\text{trigger}} + 0$  dataset with date of second detection ( $t_{\text{trigger}}$ ) at most 5 days after the date of first detection. This cut ensures that the lightcurves used for classification are not given substantially more information than those created with the first detection trigger definition. The normalized confusion matrices for the  $t_{\text{trigger}} \leq t_{\text{first detection}} + 5$  dataset are shown with and without redshift in Figure 3.8.

With redshift, SCONE's performance primarily suffers on SLSN-I and SNIa classification. SLSN-I appears to more strongly resemble SNIax and SNIbc at early times, as the SNIax confusion rose to 8% from 1% and the SNIbc confusion rose to 11% from 2%. SNIa were commonly misclassified as SNIa-91bg at early times, which is not reflected in the  $t_{\text{trigger}} + 0$  confusion matrices in Figure 3.4. Surprisingly, true SNIa-91bg were not misclassified as SNIa despite the prevalence of SNIa misclassified as SNIa-91bg. Without redshift, however, SCONE's performance on the  $t_{\text{trigger}} \leq t_{\text{first detection}} + 5$  subset very closely resembles the  $t_{\text{trigger}} + 0$  results shown in Figure 3.4.

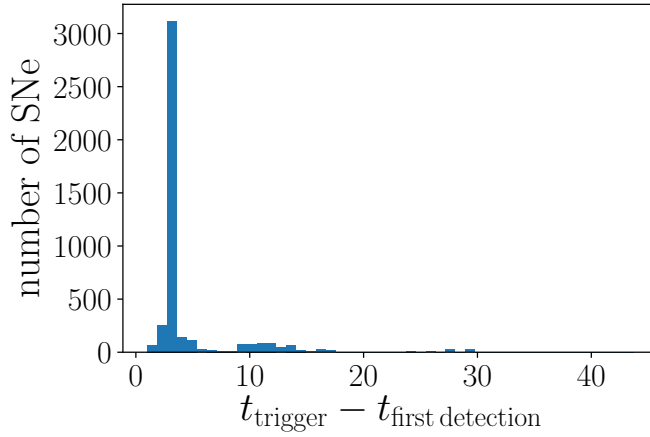


Figure 3.7: Distribution of  $t_{\text{trigger}} - t_{\text{first detection}}$  in a SCONE test dataset of 4608 SNe.

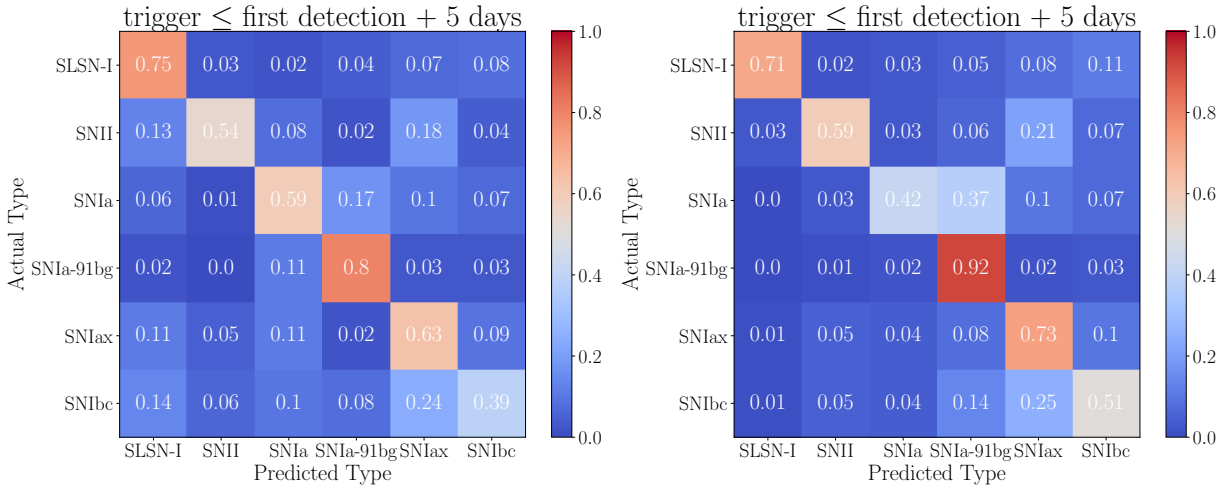


Figure 3.8: Normalized confusion matrices produced by SCONE without (left) and with (right) redshift for the  $t_{\text{trigger}} \leq t_{\text{first detection}} + 5$  subset of the  $t_{\text{trigger}} + 0$  test set. This cut ensures that the lightcurves used for performance evaluation are not given substantially more information than those created with the first detection trigger definition.

### 3.3.4. Baseline Model

A multi-layer perceptron model (MLP, Hornik et al., 1989) was developed as a baseline for direct comparison to SCONE. MLP architectures are a simple type of feedforward neural network with at least 3 layers (input, hidden, output) in which each node in a particular layer is connected to every node in the subsequent layer. They have been successfully used in many general as well as image classification tasks (Tolstikhin et al., 2021; Liu et al., 2021).

The  $32 \times 180 \times 2$  input heatmap is split into 180 non-overlapping “patches” of size  $32 \times 1$ . The patches were chosen to be full height in the wavelength dimension to remain consistent with the full height convolutional kernels used in SCONE. A  $180 \times 64$ -dimensional hidden layer is then computed via  $h_{1,ij} = \text{relu}(x_i^j W_{1,ji} + b_{1,j})$ , where  $\text{relu}(x) = \max(0, x)$  is the rectified linear unit,  $x^j$  is the  $j^{\text{th}}$  input heatmap patch,  $W_1$  is the weight matrix learned by the network, and  $b_1$  is the learned bias vector. The dimensionality of the hidden layer is then squashed to a single 64-dimensional vector with global average pooling:  $h_{2,i} = \text{average}(h_{1,ij})$ . Finally, the output class is computed via  $y_k = \sigma(h_{2,i} W_{2,ji} + b_{2,j})_k$ , where  $\sigma(\vec{x})_k = \frac{e^{x_k}}{\sum_j e^{x_j}}$  is the softmax function,  $W_2$  is the learned weight matrix, and  $b_2$  is the learned bias vector.

Without redshift, our model achieved a test accuracy of 56%. With redshift, the test accuracy improved to 67.19%. The performance of the MLP on the  $t_{\text{trigger}} + 0$  dataset with and without redshift is summarized in the confusion matrices in Figure 3.9. Compared to the performance of SCONE on the  $t_{\text{trigger}} + 0$  dataset in the top panel of Figure 3.4, the MLP is less accurate at classifying most SN types, most noticeably with redshift. The degraded but still respectable performance of the MLP on classification both with and without redshift shows that these supernova types can indeed be differentiated in some hyperdimensional space by a neural network, and that SCONE in particular possesses the required discriminatory power for this task.

### 3.3.5. Bright Supernovae

Bright supernovae, defined as supernovae with last included  $r$ -band observation  $r < 20$  mag, were identified from both the  $t_{\text{trigger}} + 0$  and  $t_{\text{trigger}} + 5$  datasets. Since fewer (and likely dimmer)

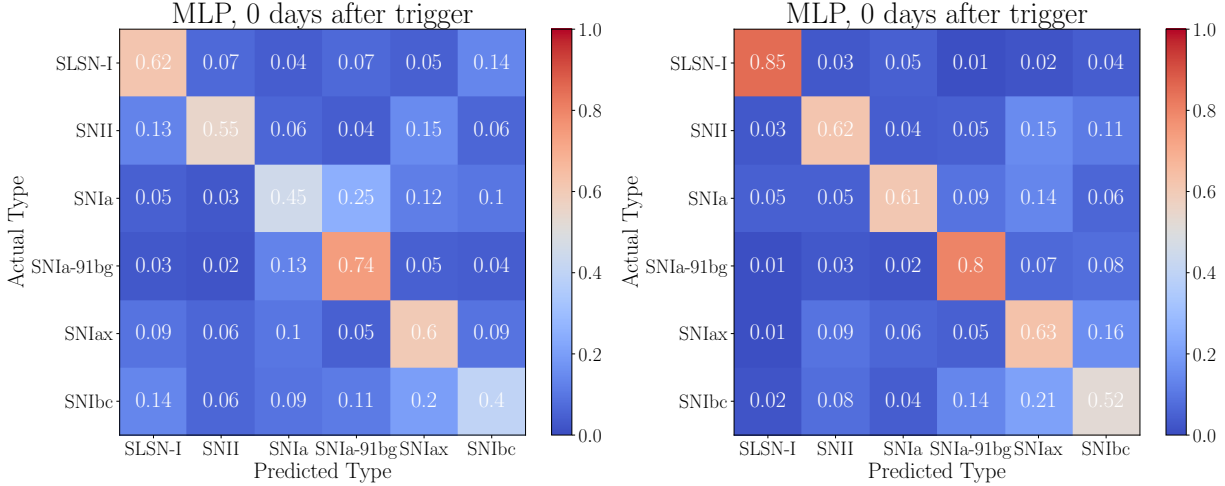


Figure 3.9: Normalized confusion matrices produced by the baseline MLP model without (left) and with (right) redshift for the  $t_{\text{trigger}} + 0$  test set (heatmaps created from lightcurves truncated at the date of trigger).

observations were included for each supernova in the  $t_{\text{trigger}} + 0$  dataset, there are much fewer examples of bright supernovae than in the  $t_{\text{trigger}} + 5$  dataset. The bright supernovae subsets of these datasets are referred to as the “bright  $t_{\text{trigger}} + N$  datasets”.

To evaluate the performance of SCONE on identifying bright supernovae at early epochs, the model was trained on a regular class-balanced  $t_{\text{trigger}} + N$  training set, prepared as described in Section 2.4, combined with 40% of the bright  $t_{\text{trigger}} + N$  dataset. The results of testing the trained SCONE model on the bright  $t_{\text{trigger}} + N$  datasets are shown in Figure 3.10. These confusion matrices, like the ones in Figure 3.4, are colored by efficiency score. However, since the dataset is not class-balanced, the overlaid values are absolute (non-normalized) to preserve information on the relative abundance of each type. Thus, an efficiency (purity) score for each type can be calculated by dividing each main diagonal value by the sum of the values in its row (column). The overall accuracies as well as the total number of SNe in each dataset are summarized in Table 3.4.

The benefits of redshift information are much more pronounced for certain types than others. As also noted in analyses of Figures 3.4 and 3.6, the quantity of SNIbc misclassified as SLSN-I was significantly reduced in results from SCONE with redshift information. At the date of trigger, 44.4% of SNIbc were misclassified as SLSN-I without redshift. This contamination rate was reduced to only

Table 3.4: Test accuracies with and without redshift information for the bright datasets.

	Total	Accuracy no $z$	Accuracy with $z$
bright $t_{\text{trigger}} + 0$	907	82.91%	91.18%
bright $t_{\text{trigger}} + 5$	5088	94.65%	95.2%

3.7% with redshift. However, classification of bright SNIa seems relatively unaffected by the presence of redshift information. 5 days after trigger, SNIa were classified with an efficiency/accuracy of 98.6% and a purity score of 98.1% without redshift, and 97.4% efficiency/accuracy and 99.1% purity with redshift.

### 3.3.6. Mixed Dataset

Training on the  $t_{\text{trigger}} + N$  datasets represents one way of deploying SCONE for real-world transient alert applications, while training on a mixed dataset is a much less computationally expensive alternative. On one hand, testing a  $t_{\text{trigger}} + N$ -trained model on a  $t_{\text{trigger}} + N$  test set yields the best classification accuracies. However, this approach requires the creation of separate datasets for each choice of  $N$ , which could be an expensive initial time investment depending on the number of datasets and size of each dataset (see Section 2.6 for computational requirements for heatmap creation). In this work, only five datasets ( $N = 0, 5, 15, 25, 50$ ) were created, but perhaps  $N = 0, 1, \dots, 50$  will be needed to accurately classify real-world transient alerts with any number of nights of photometry. Training on a mixed dataset, where each heatmap is created with a random number of nights of photometry after trigger, is a viable alternative for resource- or time-constrained applications.

To directly compare the performance of SCONE trained on the mixed dataset and the  $t_{\text{trigger}} + N$  datasets, the mixed-dataset-trained model was tested on each individual  $t_{\text{trigger}} + N$  dataset. The accuracies over time split by SN type are summarized in Figure 3.11. Compared to the results of SCONE trained and tested on each individual  $t_{\text{trigger}} + N$  dataset (Figure 3.3), the accuracies are lower but still respectable. The performance at the date of trigger is the most dissimilar, with average accuracy 74% with  $z$  for a model trained on  $t_{\text{trigger}} + 0$  and 64% with mixed. The performance of the mixed-trained model performs similarly to the  $t_{\text{trigger}} + N$ -trained model by 5 days after

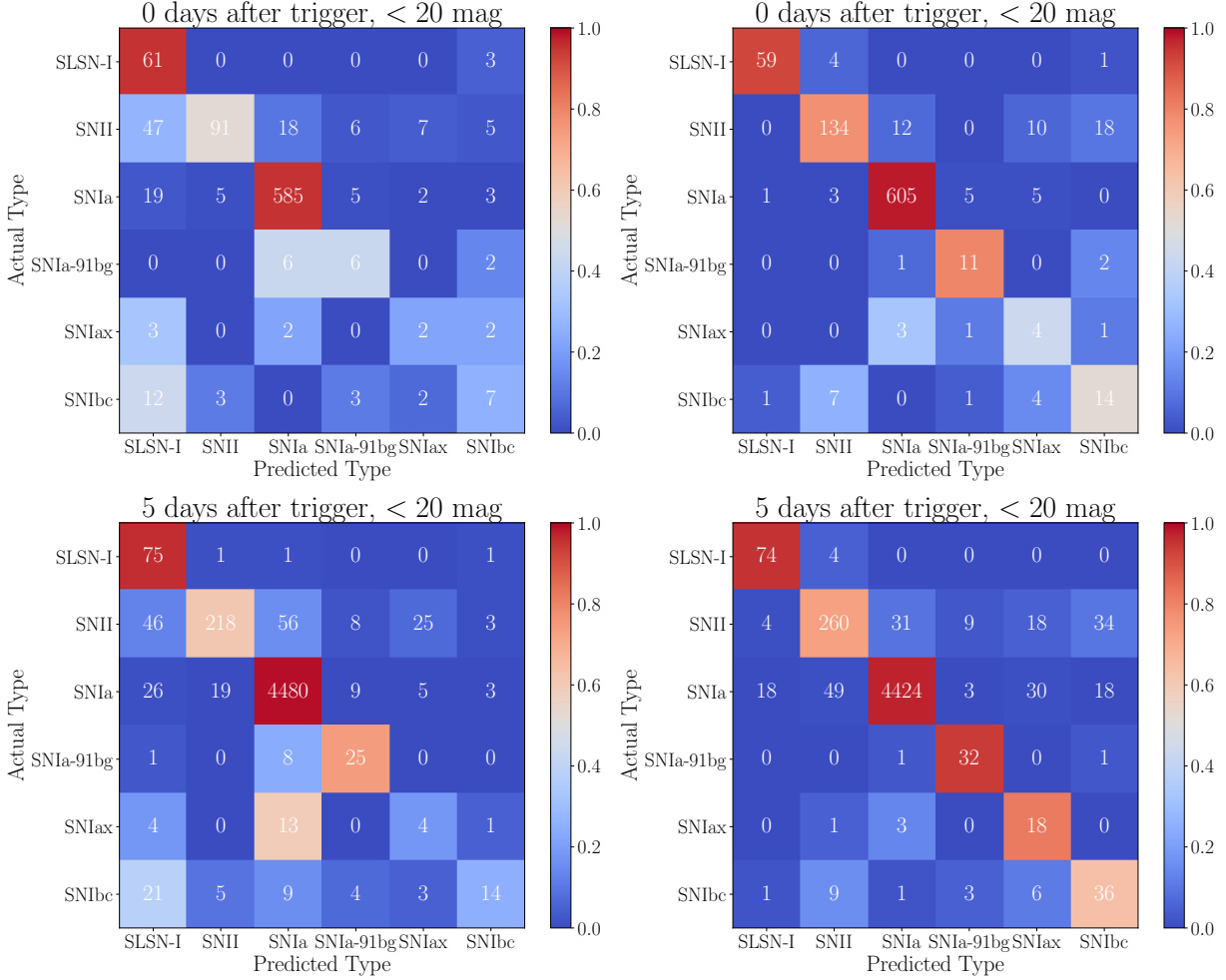


Figure 3.10: Early epoch confusion matrices with (right) and without (left) redshift for the bright supernovae (< 20 magnitude) in each  $t_{\text{trigger}} + N$  dataset. SCONE was trained with a class-balanced  $t_{\text{trigger}} + N$  training set combined with 40% of < 20 magnitude supernovae. These confusion matrices were created by testing the trained SCONE model on the full < 20 magnitude supernovae dataset. The confusion matrices are colored according to normalized accuracies, as in Figure 3.4, and are overlaid with absolute (non-normalized) values since the dataset is imbalanced.

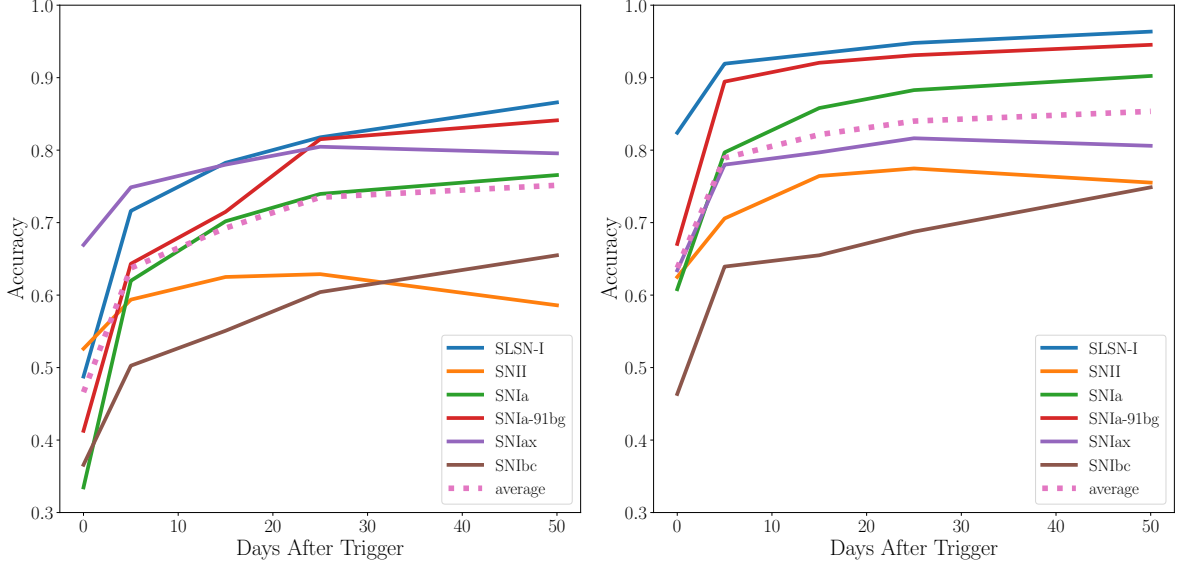


Figure 3.11: Test set accuracy/efficiency without (left) and with (right) redshift over time for SCONe trained on the mixed dataset and tested on each individual  $t_{\text{trigger}} + N$  dataset. The values used in these plots correspond with the diagonals on a normalized confusion matrix.

trigger, however, both averaging just under 80% with  $z$ . The AUCs over time split by SN type are shown in Figure 3.12. These AUC plots are comparable to the  $t_{\text{trigger}} + N$  AUCs in Figure 3.6, indicating that the performances of both models are comparable when averaged over all values of the prediction threshold  $p$ . However, the predicted class for categorical classification is not typically calculated with respect to a threshold; rather, it is defined as the class with the highest prediction confidence for each example. Thus, the AUCs are analogous to analyzing the performance on each type as its own binary classification problem, resulting in slight discrepancies from the accuracies.

### 3.3.7. Comparison with Existing Literature

At the time of this writing, the only work in existing literature with a similarly strong focus on early photometric classification of supernovae is RAPID (Muthukrishna et al., 2019, hereafter M19), a GRU RNN approach to photometric transient classification that differentiates between 12 transient types, including 7 supernova types. RAPID differs in several significant ways from the data, model, and results presented in this work. We highlight some of the differences in these two works below.



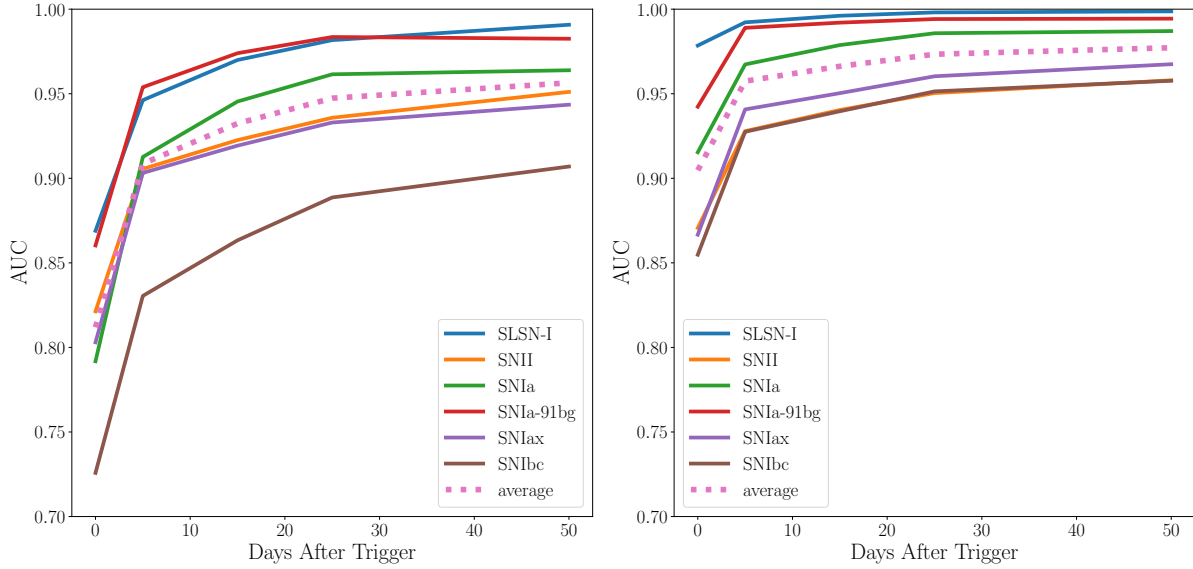


Figure 3.12: Area under the ROC curve (AUC) without (left) and with (right) redshift over time for SCONE trained on the mixed dataset and tested on each individual  $t_{\text{trigger}} + N$  dataset.

### Comparison of Methods

The most obvious difference is in the type of neural network architecture used for classification. RAPID uses a uni-directional RNN architecture, which is designed to learn from time-series data chronologically. SCONE employs a convolutional neural network architecture, which is most commonly used for image recognition tasks. In this instance, however, SCONE is designed to read in data chronologically. Convolutional layers in a CNN work by computing functions on a “sliding window” of the input image, thereby allowing the model to learn small-scale structures in the image. These windows, or the convolutional kernel, is typically a small square chosen to match the characteristic length scale of structures in the images. SCONE’s convolutional kernel, however, is chosen to span the full height of the input heatmap, resulting in a window that slides chronologically along the horizontal, or time, axis.

M19 trained and tested on a dataset of simulated Zwicky Transient Facility (ZTF) lightcurves, which have  $g$ - and  $r$ - band photometry, compared to the LSST lightcurves used in this work, with  $ugrizY$  photometry bands. In addition to the 6 supernova types that this work focuses on, M19 includes 4 rare transient classes (pair instability supernovae (PISN), intermediate luminosity tran-

sients (ILOT), calcium-rich gap transients (CART), tidal disruption events (TDE)) as well as point-Ia and KN.

Other differences include the addition of a “pre-explosion” class, rest- vs. observer-frame time intervals, and the choice of trigger definition. M19 chooses to include an additional class, “pre-explosion”, to describe examples at time-steps prior to the occurrence of the transient event. M19 also converts time intervals out of observer-frame by dividing by  $1 + z$ , which is not done in this work to ensure that mistakes in redshift estimates will not be propagated to affect the lightcurve data. Finally, M19 uses the first-detection trigger date definition, while this work defines  $t_{\text{trigger}}$  to be the date of the second detection.

### Comparison of Results

The results of SCONE classification with redshift (right side panels of Figures 3.4-3.6) is used to compare with RAPID’s results, as RAPID also incorporates redshift information. As described in the previous section, this work differs in many ways from M19 and the following comparison does not account for these differences; a rigorous comparison of the two models against a single dataset is left to a future work.

Most notably, SCONE improves upon RAPID’s SNIbc and SNII classification accuracy, while RAPID performs very well at classifying early-time SNIa. From Figure 7 of M19, 12% of SNIbc are correctly classified 2 days after detection, compared to SCONE’s 54% accuracy at the date of trigger. In RAPID’s results, 30% of true SNIbc are misclassified as CART, which is not included in the datasets in this work. The second and third largest contaminants (SNIax at 19%, then SNIa and SNIa-91bg at 8% each), are both part of this analysis. From Figure 3.4, we find that SNIax and SNIa-91bg are also major contaminants for SCONE at 23% and 11%, respectively, at the date of trigger and 16% and 4%, respectively, 5 days after trigger. However, there is no significant contamination from SNIa, with contamination rates at 4% on the date of trigger and 1% 5 days after trigger.

2 days after detection, SNII is classified at 7% accuracy by RAPID compared to 64% accuracy at the date of trigger by SCONE. The primary contaminant of SNII for RAPID 2 days after detection

is SNIa at 21%, which is not reflected in SCONE’s results, where the contamination rate is 6% at the date of trigger and 3% 5 days after trigger. The second largest contaminant, SLSN-I, is also not an issue in SCONE’s SNII classification. Surprisingly, the improvement over time of RAPID’s SNII classification accuracy outpaces its SNIbc classification accuracy, as it is able to achieve 49% accuracy on SNII 40 days after detection compared to 31% accuracy on SNIbc.

While SCONE’s SNIa classification accuracy slowly climbs from 77% at the date of trigger to 93% 50 days after trigger, RAPID is able to classify SNIa at 88% accuracy almost immediately after detection. A future direct comparison will aid in concluding whether this discrepancy is due to differences in the datasets, such as M19’s exclusion of  $z \geq 0.5$  objects, or something more fundamental to the model architectures.

### 3.4. Conclusions

Our ability to observe the universe has improved in leaps and bounds over the past century, allowing us to find new and rare transient phenomena, enrich our understanding of transient physics, and even make cosmological discoveries aided by observational data. Our photometric observing capabilities greatly outpace the rate at which we can gather the associated spectroscopic information, resulting in a vast trove of photometric data sparsely annotated by spectroscopy. In the era of large-scale sky surveys, with millions of transient alerts per night, an accurate and efficient photometric classifier is essential not only to make use of the photometric data for science analysis, but also to determine the most effective spectroscopic follow-up program early on in the life of the transient.

In this work, we presented SCONE’s performance classifying simulated LSST early-time supernova lightcurves for SN types Ia, II, Ibc, Ia-91bg, Iax, and SLSN-I. As a neural network-based approach, SCONE avoids the time-intensive manual process of feature selection and engineering, and requires only raw photometric data as input. We showed that the incorporation of redshift estimates as well as errors on those estimates significantly improved classification accuracy across the board, and was especially noticeable at very early times. Notably, this is the first application of convolutional neural networks to this problem.

SCONE was tested on 3 types of datasets: datasets of lightcurves that were truncated at 0, 5, 15, 25, and 50 days after trigger ( $t_{\text{trigger}} + N$  datasets); bright ( $< 20$  magnitude) subsets of the  $t_{\text{trigger}} + \{0, 5\}$  datasets; and a dataset of lightcurves truncated at a random number of nights between 0 and 50 ("mixed"). Without redshift, SCONE was able to classify  $t_{\text{trigger}} + 0$  lightcurves with 60% overall accuracy, which increases to 82% at 50 days after trigger. SCONE with redshift information starts at 74% overall accuracy at the date of trigger and improves to 89% 50 days after trigger. Confusion matrices, ROC plots, and accuracy over time as well as AUC over time plots of results with and without redshift were presented to better understand classification performance and identify areas of improvement. For the bright subsets, overall accuracy is  $> 90\%$  at the date of trigger with redshift and over 80% without. These results improve to around 95% accuracy both with and without redshift by 5 days after trigger. The overall accuracy over time of a mixed-dataset-trained model tested on the  $t_{\text{trigger}} + N$  datasets shows some degradation in accuracy at very early epochs, but may be a worthwhile lightweight alternative to the more resource-intensive process of creating many  $t_{\text{trigger}} + N$  datasets.

We showed that SCONE's performance with redshift is competitive with existing work on early classification, such as M19, while improving on computational time requirements. SCONE has a lightweight pre-processing step and can achieve impressive performance with a small training set. It requires only hundredths of a second to preprocess each lightcurve into a heatmap and seconds for each training epoch on GPU. This makes SCONE a great candidate for incorporation into alert brokers for LSST and future wide-field sky surveys.

In future work, we plan to apply this model to real data to further validate the approach. We also plan to extend SCONE to classify both full-duration and early lightcurves for more transient and variable classes in the PLAsTiCC simulations.

### 3.5. Acknowledgments

This work was supported by DOE grant DE-FOA-0002424, NASA Grant NNN15ZDA001N-WFIRST, and NSF grant AST-2108094. This research used resources of the National Energy Research Scientific Computing Center (NERSC), a U.S. Department of Energy Office of Science User Facil-

ity located at Lawrence Berkeley National Laboratory, operated under Contract No. DE-AC02-05CH11231.

## CHAPTER 4

### The Dark Energy Survey Supernova Program: Cosmological Biases from Host Galaxy Mismatch of Type Ia Supernovae

#### Abstract

Redshift measurements, primarily obtained from host galaxies, are essential for inferring cosmological parameters from type Ia supernovae (SNe Ia). Matching SNe to host galaxies using images is non-trivial, resulting in a subset of SNe with mismatched hosts and thus incorrect redshifts. We evaluate the host galaxy mismatch rate and resulting biases on cosmological parameters from simulations modeled after the Dark Energy Survey 5-Year (DES-SN5YR) photometric sample. For both DES-SN5YR data and simulations, we employ the directional light radius method for host galaxy matching. In our SN Ia simulations, we find that 1.7% of SNe are matched to the wrong host galaxy, with redshift difference between the true and matched host of up to 0.6. Using our analysis pipeline, we determine the shift in the dark energy equation of state parameter ( $\Delta w$ ) due to including SNe with incorrect host galaxy matches. For SN Ia-only simulations, we find  $\Delta w = 0.0013 \pm 0.0026$  with constraints from the cosmic microwave background (CMB). Including core-collapse SNe and peculiar SNe Ia in the simulation, we find that  $\Delta w$  ranges from 0.0009 to 0.0032 depending on the photometric classifier used. This bias is an order of magnitude smaller than the expected total uncertainty on  $w$  from the DES-SN5YR sample of  $\sim 0.03$ . We conclude that the bias on  $w$  from host galaxy mismatch is much smaller than the uncertainties expected from the DES-SN5YR sample, but we encourage further studies to reduce this bias through better host-matching algorithms or selection cuts.

#### 4.1. Introduction

Type Ia supernovae (SNe Ia) enabled the discovery of accelerating cosmic expansion (Perlmutter et al., 1999; Riess, 1998) and have since been an important probe of the dark energy thought to cause it. To constrain cosmology, each SN Ia must have an accurate estimate of cosmological redshift as well as physical distance. Distance estimates are obtained from the standardized luminosities of

SNe Ia, earning them the title of *standardizable candles*, but redshift is difficult to determine without spectroscopy. The depth of modern photometric surveys has resulted in orders of magnitude more photometrically observed SNe than can be followed up spectroscopically. Thus, the vast majority of SNe Ia used for estimation of cosmological parameters are assigned the redshift of their matched host galaxies. Moreover, galaxy redshifts are more precise than redshifts measured from SN spectroscopy due to the broadened features and phase-dependent nature of SN spectra.

This work investigates the impact of mismatched host galaxies and the resulting incorrect SN redshifts on the measurement of cosmological parameters. Using images alone, host galaxy matching is a nontrivial problem when there are multiple galaxies near the SN location. Two-dimensional images have little distance information, and galaxies in a crowded field can be difficult to disentangle without distance measurements to each. In addition, the large scale structure of the universe dictates that many galaxies occur in pairs, groups, or clusters, making it difficult to determine which galaxy is the host. Finally, some “hostless” SNe explode in extremely faint or distant galaxies that fall below the threshold of detection, even in the deep coadded images created for this work described in Section 4.3.2. These SNe could be incorrectly matched to brighter, nearby galaxies that are close in projected distance and thus assigned an incorrect redshift. Figure 4.1 illustrates a challenging example of host galaxy matching, where the larger and more likely host galaxy is further in terms of SN-galaxy separation than the smaller galaxy on the right.

Though automated methods for host galaxy matching have been in use since the SuperNova Legacy Survey (SNLS) analysis (Sullivan et al., 2006b, S06), accurate characterization of systematic uncertainties such as the effect of mismatched host galaxies has become more pressing with the advent of wider and deeper SN surveys. Future surveys such as the Legacy Survey of Space and Time (LSST) at the Vera Rubin Observatory will observe hundreds of thousands more SNe in the coming decade (LSST Science Collaboration et al., 2009b), further shrinking statistical uncertainties and necessitating accurate measurements of systematic uncertainties. This work represents the first thorough exploration of systematics related to the host galaxy mismatch problem and its effect on cosmological parameter estimates as part of an ongoing cosmology analysis.

A commonly used method for matching SNe with a host galaxy is the directional light radius (DLR) method, initially developed to characterize host properties for the SNLS survey by S06 and tested extensively on simulations by Gupta et al. (2016). More details about the DLR method can be found in Section 4.2.1. Recently, Popovic et al. (2020, P20) performed the first retrospective estimate of cosmological biases resulting from host galaxy mismatches by applying the DLR method on simulations based on SDSS data. P20 found a mismatch rate of 0.6% with a resulting bias on  $w$  of  $\Delta w = 0.0007$ .

Recently, a number of promising alternative approaches for host matching have emerged, including DELIGHT (Förster et al., 2022) and GHOST (Gagliano et al., 2021). DELIGHT introduces a deep learning-based approach to host galaxy identification in which a convolutional neural network is trained on transient images to predict a 2-dimensional vector connecting the transient position with the position of its host galaxy center. GHOST uses a novel gradient ascent method for host galaxy identification that was shown to produce accurate matches in situations where DLR was unable to identify a match. Though this work did not explore these novel approaches, they certainly merit consideration for future SNe Ia cosmological analyses.

In this work, we focus on understanding the cosmological biases arising from host galaxy mismatch using the DLR method on the full Dark Energy Survey 5-Year photometric SNe Ia sample (DES-SN5YR; Vincenzi et al., 2021; Möller et al., 2022). Section 4.2 details the DLR host matching algorithm and an overview of our analysis strategy. Section 4.3 describes the DES-SN5YR data sample along with the host galaxy catalog used in this analysis. Section 4.4 reviews the simulations used to model the host mismatch rate and characterize its effects on the cosmological parameters, and Section 4.5 describes the methods and results used to ensure consistency between the DES-SN5YR data and our simulations. Section 4.6 reviews the framework used for cosmological parameter estimation in this work, and Section 4.7 describes the cosmological biases resulting from host galaxy mismatch.



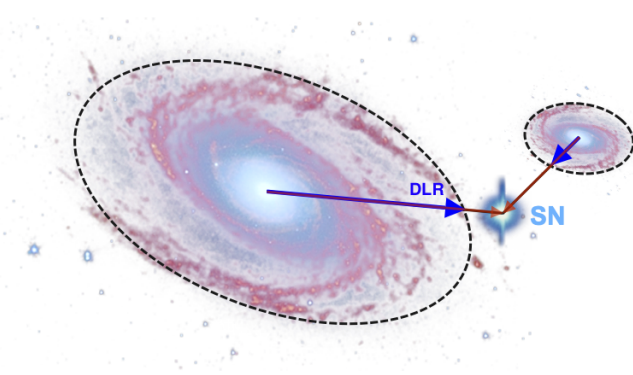


Figure 4.1: An illustration adapted from Gupta et al. (2016) showing an example of a challenging host galaxy matching problem. The supernova (labeled “SN”) is closer in angular separation (red arrows) to the smaller galaxy on the right, but it is closer to the edge of the larger galaxy on the left. The directional light radius (DLR) of each galaxy is shown in the blue arrows. According to the DLR method, the most likely host galaxy is the one with minimal  $d_{\text{DLR}}$  value, or ratio of the angular separation to the DLR, which would correctly identify the larger galaxy on the left as the more likely host.

## 4.2. Host Galaxy Matching

### 4.2.1. The DLR Method

The directional light radius (DLR) method for host galaxy matching, developed in S06, involves computing a dimensionless distance ( $d_{\text{DLR}}$ ) for each potential host galaxy measured between the SN position and the centroid of the galaxy normalized by the galaxy size in the direction of the SN. Explicitly,  $d_{\text{DLR}}$  is defined as

$$d_{\text{DLR}} = \frac{\Delta\theta}{\text{DLR}} \quad (4.1)$$

where  $\Delta\theta$  is the angular separation (arcsec) between the galaxy centroid and the SN, and DLR (arcsec) is the radius of the galaxy in the direction of the SN. We require all galaxies in our catalog (see Section 4.3.2) to be well modeled by ellipses parameterized by a semi-major axis  $a$ , a semi-minor axis  $b$ , and a position angle  $\phi$ , which is defined relative to the positive RA axis. Thus, the DLR value for each SN-galaxy pair is computed as follows:

$$\text{DLR} = \frac{ab}{\sqrt{(a \sin \phi)^2 + (b \cos \phi)^2}}. \quad (4.2)$$

For our DLR calculations, the values for the  $a, b, \phi$  parameters are the `A_IMAGE`, `B_IMAGE` (converted into arcsec), and `THETA_IMAGE` parameters output by Source Extractor (Bertin, 2011, `sExtractor`) using the coadded  $r + i + z$  detection image. The galaxy with the lowest  $d_{\text{DLR}}$  value is chosen as the host galaxy.

#### 4.2.2. Analysis Overview

We quantify the cosmological biases resulting from host galaxy mismatch by generating two sets of simulated SNe, one with and one without host galaxy mismatches, and comparing the fitted cosmological parameters. Details about the DES data can be found in Section 4.3 and the simulations are described in Section 4.4.

To ensure that our results from simulations are applicable to real DES data, we show consistency between simulations and data across relevant parameter distributions, following Popovic et al. (2020):

- angular SN-galaxy separation ( $\Delta\theta$ ),
- directional light radius (DLR),
- the DLR-normalized SN-galaxy separation,  $d_{\text{DLR}} = \frac{\Delta\theta}{\text{DLR}}$
- $r$ -band host galaxy magnitude ( $m_{r,\text{gal}}$ ),
- the ratio between smallest and second smallest  $d_{\text{DLR}}$  values,  $r_{\text{DLR}} = \frac{d_{\text{DLR,HOSTGAL1}}}{d_{\text{DLR,HOSTGAL2}}}$ , where  $d_{\text{DLR,HOSTGAL}\{i\}}$  is the  $i^{\text{th}}$  smallest  $d_{\text{DLR}}$  value, i.e. the  $d_{\text{DLR}}$  value of the  $i^{\text{th}}$  most likely host galaxy.

Further description of these parameters and the results of our consistency checks can be found in Section 4.5. Host matching is performed on one set of simulated SNe to model mismatches as

well as the DES-SN5YR data with the DLR method using the catalog of galaxies generated from deep DES imaging stacks, as described in Section 4.3.2. Finally, we estimate biases by comparing the fitted cosmological parameters from simulations with matched hosts and an identical set of simulations with true hosts, i.e. those assigned by the simulation.

### 4.3. Data and host galaxy catalog

#### 4.3.1. Dark Energy Survey 5-Year Photometric Sample

DES is an optical imaging survey designed to deliver precision cosmological results and constraints on dark energy by combining the probing power of weak gravitational lensing, baryon acoustic oscillations, galaxy clusters, and SNe Ia (Abbott et al., 2019). DES imaged  $5000 \text{ deg}^2$  of the southern sky for 6 years using the Dark Energy Camera (Flaugher et al., 2015) mounted on the 4m Blanco Telescope at the Cerro Tololo Inter-American Observatory. The time-domain survey component of the DES survey strategy covers a smaller area on the sky (10 supernova fields covering  $27 \text{ deg}^2$ ), but exposures were repeated approximately weekly over the course of the survey. Eight of the ten fields were surveyed to a depth of  $\sim 23.5 \text{ mag}$  per visit (‘shallow fields’), and the remaining two to a deeper limit of  $\sim 24.5 \text{ mag}$  per visit (‘deep fields’), thus extending the SN detection limit to  $z \sim 1.2$ . Transient identification from images was performed using difference imaging (DiffImg; Kessler et al., 2015, hereafter K15). Spectroscopic follow-up of SN Ia candidates as well as their host galaxies was performed as described in Smith et al. (2020b); Lidman et al. (2020).

#### 4.3.2. Host Galaxy Catalog

To ensure sufficient depth and density of potential host galaxies as well as consistency between the galaxy catalogs used for real data matching and simulation, we produce a deep galaxy catalog by coadding DES images, identifying sources, and estimating photometric redshifts and galaxy parameters for each source.

The coadd procedure is similar to those described in Wiseman et al. (2020) with several updates. First, we apply stricter selection requirements (cuts) on the quality of the single-epoch images.

Images with effective exposure time ratio <sup>1</sup>

$\tau_{\text{eff}} \leq 0.3$  and those with point spread function full width at half maximum (PSF FWHM)  $\geq 1.3''$ ,  $1.2''$ ,  $1.1''$ ,  $1.0''$  in *griz*, respectively, are excluded to ensure higher quality images across the focal plane and to mitigate source confusion. Second, each image is scaled to a common zeropoint using the same framework adopted in *DiffImg* (see K15). Third, rather than excluding images from the season in which the supernova candidate was discovered, we instead use all images from the 5-year survey and perform a median coaddition with *swarp* (Bertin, 2011). Although median coaddition is not statistically optimal, it loses only  $\sim 0.1$  mag in depth compared to other weighted average methods and is a more robust way to exclude light from transients and image artifacts when adding hundreds of images. Finally, we determine the PSF model of the coadded images with *psfex* (Bertin, 2011) using our tertiary standard stars. The PSFs are used by *sExtractor* (Bertin, 2011) to fit for the true (unblurred) Sérsic profiles and derive their parameters, which are necessary for the placement of simulated SNe in their host galaxies.

Sources from all 10 DES SN fields are identified using *sExtractor*. Magnitudes are corrected for Milky Way dust using  $E(B - V)$  values from Schlegel et al. (1998) and extinction coefficients for DECam filters from Schlafly and Finkbeiner (2011) and assuming  $R_V = 3.1$ . These coefficients are  $A/E(B - V) = 3.237, 2.176, 1.595,$  and  $1.217$  in DECam *griz*, respectively.

The galaxies were matched to a spectroscopic redshift catalog compiled from multiple surveys including OzDES (Lidman et al., 2020), SDSS (Sako et al., 2008b), 6dF (Jones et al., 2004), ATLAS (Cappellari et al., 2011), GAMA (Driver et al., 2009), VVDS (Le Fèvre, O. et al., 2005), VIPERS (Guzzo et al., 2014), ACES (Cooper et al., 2012), DEEP2 (Newman et al., 2013), 2dFGRS (Colless et al., 2001), UDS/VANDELS (McLure et al., 2018), and PRIMUS (Coil et al., 2011). Among the 7.8 million galaxies, a total of 124,824 have secure spectroscopic redshifts. Although we require a spectroscopic redshift for the DES data, the simulation needs a complete galaxy catalog to accurately model mis-matches. We therefore use photometric redshifts when spectroscopic redshifts are not

---

<sup>1</sup> $\tau_{\text{eff}} = \left(\frac{FWHM_{fid}}{FWHM}\right)^2 \left(\frac{B_{fid}}{B}\right) F_{trans}$ , where  $FWHM$  and  $FWHM_{fid}$  are the measured and fiducial PSF full width half max, respectively;  $B$  and  $B_{fid}$  are the measured and fiducial sky background;  $F_{trans}$  is the atmospheric transmission relative to a nearly clear night. See Morganson et al. (2018) for details.

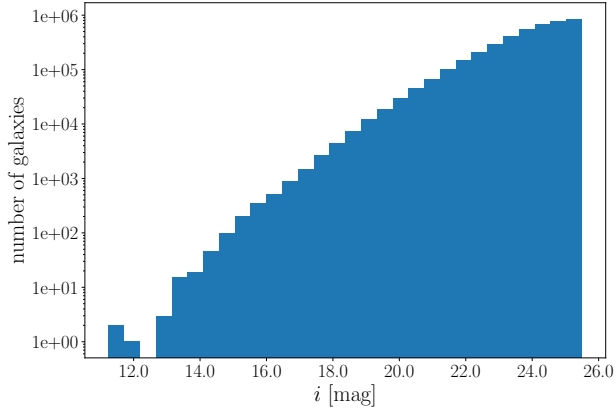


Figure 4.2:  $i$ -band `MAG_MODEL` magnitude distribution of all galaxies in our deep DES galaxy catalog with a spectroscopic or photometric redshift estimate. The catalog cuts off at  $i \sim 26$  because photometric redshifts are unavailable for galaxies fainter than  $i = 25.5$  mag.

available.

For the vast majority of galaxies without a spectroscopic redshift, we estimate photometric redshifts of galaxies that are brighter than  $i = 25.5$  mag using the method described in Section 4.3.2. Sources fainter than this limit do not have reliable photo- $z$  estimates and are not included in the galaxy catalog. Figure 4.2 shows the magnitude distributions of the remaining sources.

### Host Galaxy Photometric Redshifts

Host galaxy photometric redshift estimation is performed independently for the deep and shallow SN fields, consisting of two and eight fields, respectively, as described in Section 4.3.2. For each galaxy in each field, we have a set of  $griz$  photometric flux measurements and their corresponding uncertainties. Using this data, we train a *Self-Organizing Map* (SOM) to characterize and discretize the photometric space of host galaxies, using the SOM algorithm described in the Appendix of Sánchez et al. (2020). This SOM algorithm uses unsupervised learning to project the 4-dimensional photometric data ( $griz$ ) onto a lower-dimensional grid, in our case a 2-dimensional grid, while attempting to preserve the topology of the 4-dimensional space. This means that similar objects in the 4-D space will be grouped together in the SOM, enabling a visual understanding of features.

The particular SOM algorithm used in this work differs from the SOM algorithm used in previous DES analyses (such as Myles et al., 2021; Giannini et al., 2022) in order to improve the classification of galaxies with low- and modest-S/N photometry, which is relevant given the faint nature of many SN host galaxies. First, we alter the distance metric used by the SOM algorithm to incorporate flux uncertainties. Next, we include flux information, not just colors, and we do not impose periodic boundary conditions on the map. For the application in this work, we build a SOM of size  $22 \times 22$ , with a total of 484 cells. These alterations are described in detail in Sánchez et al. (2020).

After the SOM is constructed, we use the subset of SN host galaxies with spectroscopic redshifts to populate the SOM and compute the redshift distribution of each SOM cell. The spectroscopic subset for deep SN fields has a total of 45,937 galaxies, while the one for shallow SN fields has a total of 78,887 galaxies. Once we populate the SOMs with redshift information, we assign to each galaxy the redshift distribution of the cell it is assigned to. Even if these spectroscopic subsets provide a good coverage of the corresponding photometric spaces, some SOM cells do not contain redshift information and therefore we do not estimate redshifts for galaxies in them. This is the case for 3.9% of galaxies in the deep SN fields, and 6.7% of galaxies in the shallow SN fields.

To validate this procedure, we split the spectroscopic samples into separate training and validation samples, with a random 90% of galaxies going into training and the remaining 10% into validation. Next, we compare the estimated and spectroscopic redshifts for galaxies in the validation sample to assess the quality of the reconstruction. For this purpose, and to enable comparisons with previous DES estimates, we use photo- $z$  metrics from Sánchez et al. (2014). We construct the  $\Delta z \equiv z_{phot} - z_{spec}$  distribution, and we compute two different metrics:

1. We estimate the photo- $z$  precision by calculating the 68-percentile width  $\sigma_{68}$  of the  $\Delta z$  distribution around its median value. This estimator,  $\sigma_{68}$ , measures the width of the core of the  $\Delta z$  distribution. In particular, it is defined as half of the width of the distribution, measured with respect to the median, where 68% of the data are enclosed.
2. We estimate the fraction of photo- $z$  outliers by calculating the fraction of objects with  $3\sigma$  de-

viations in  $\Delta z$ ,  $\text{out}_{3\sigma} \equiv |\Delta z| > 3\sigma_z$ , where  $\sigma_z$  is the standard deviation of the  $\Delta z$  distribution.

For the photo- $z$  estimation procedure described above, we find  $\sigma_{68} = 0.124$  and  $\text{out}_{3\sigma} = 0.017$  for the deep SN fields, and  $\sigma_{68} = 0.124$  and  $\text{out}_{3\sigma} = 0.015$  for the shallow SN fields. For the wide-field DES survey, the photo- $z$  requirements set prior to the start of the survey specified  $\sigma_{68} < 0.12$  and  $\text{out}_{3\sigma} < 0.015$  for 90% of the sample of galaxies. The values we find are slightly above these requirements, but it is important to point out that galaxy samples from the SN fields reach significantly fainter magnitudes than wide-field DES galaxies, and hence it is more difficult to satisfy the wide-field requirements. However, the SOM model is constructed such that it is primarily sensitive to color, and the color-redshift relation should be agnostic to galaxy brightness. In addition, the numbers we find are similar to those reported by several photo- $z$  codes in Sánchez et al. (2014), demonstrating the comparable performance of our method when applied to fainter galaxies.

### Profile Fitting

Both the measured profile, which was used to calculate DLR values and described in Section 4.2.1, and the *intrinsic* galaxy light profile are used in this work.

The intrinsic light profile is used to determine the location of each simulated SN within its assigned host galaxy (see Section 4.4.1). To calculate the intrinsic light profile, each galaxy in the catalog is fit with a Sérsic profile (Sérsic, 1963) that describes the variation of galaxy intensity  $I$  with radius  $R$ :

$$I(R) = I_e \exp\left\{-b_n \left[\left(\frac{R}{R_e}\right)^{1/n} - 1\right]\right\} \quad (4.3)$$

$I_e$  is the galaxy intensity at the half-light radius  $R_e$ ,  $n$  is the Sérsic index describing the cuspieness of the profile, and  $b_n$  is a known function of  $n$ . The fitting was performed by *sExtractor*, which fits for  $R_e$  as well as additional parameters *theta* and *aspect*, which describe the angle relative to the positive RA axis and the ellipticity of the galaxy, respectively. These additional parameters enable us to model each galaxy as an ellipse and determine its semimajor and semiminor axes, which we denote  $a, b$ . These quantities are calculated with  $R_e = \sqrt{ab}$ ,  $\text{aspect} = \frac{a}{b}$ . The fitted Sérsic half-light radii were scaled by a factor of 0.8 to obtain better data-simulation agreement (see Section 4.5.2

Table 4.1: Cuts applied to the host galaxy library and resulting galaxy counts.

Cut Requirement	Galaxies Remaining
Full catalog	8,401,139
Removed duplicate galaxies	7,860,305
Has photo- $z$ or spec- $z$	5,118,585
Has CIGALE galaxy parameter fit	5,108,812
$5 < \log(M_*/M_\odot) < 14$	4,938,372
Has reasonable Sérsic fit	4,221,001
<b>Final</b>	<b>4,221,001</b>

for details on the data-simulation matching procedure and Section 4.7.3 for comparisons with and without this scaling factor). This is notably the same scaling factor found to best match the DES3YR data when comparing distributions of host galaxy surface brightness at the SN position (see Figure 6 of Abbott et al., 2019a).

### Catalog Cuts and Parameter Fitting

Several selection criteria are applied to select `sExtractor` sources that balance the trade-off between preserving realistic catalog depth/density, and maintaining the quality of the galaxy photometry. The list of cuts as well as the number of galaxies remaining after each is shown in Table 4.1.

First, duplicate observations of galaxies are removed, prioritizing deep field observations when possible. The duplication is due to the slight overlap of certain DES SN fields, causing galaxies in the overlapping regions to appear in multiple coadded images. Next, galaxies without a spectroscopic redshift determination or photometric redshift estimate are removed, because simulated SNe cannot be associated with such galaxies. As stated in Section 4.3.2, galaxies fainter than  $i = 25.5$  mag do not have reliable photometric redshift estimates and are removed. In addition to the  $i = 25.5$  mag cut, 3.9% of galaxies in the deep SN fields and 6.7% of galaxies in the shallow SN fields were not successfully assigned a redshift estimate by the SOM and are removed as well.

Certain galaxy properties are known to be correlated with SN Ia rate (S06; Mannucci et al., 2005; Graur et al., 2017; Wiseman et al., 2021), and we use these known correlations to assign suitable host galaxies in the simulation. We estimate the total stellar mass ( $M_*$ ) and the star formation rate (SFR) for galaxies in our catalog using CIGALE (Boquien et al., 2019). CIGALE uses grid search



Table 4.2: Summary of host galaxy matching for the DES Y5 sample.

	Number of SNe	Percent of Total
Total sample size	2,186	100%
Has $\geq 1$ host match	2,047	94%
Has $\geq 2$ host matches	126	6%

to find the best-fit (lowest- $\chi^2$ ) combination of user-specified model parameters given galaxy photometry and redshift estimates. For the galaxy parameter fits, we assume a delayed star formation history, where SFR is defined by

$$\text{SFR}(t) \propto \frac{t}{\tau^2} \exp(-t/\tau), \quad 0 \leq t \leq t_0 \quad (4.4)$$

with  $t_0$  the age of the onset of star formation and  $\tau$  the time at which the SFR peaks. The bc03 (Bruzual and Charlot, 2003) library of single stellar populations with a Salpeter initial mass function is used to compute the intrinsic stellar spectrum. Attenuation from dust and other sources is parameterized by the Calzetti et al. (2000) starburst attenuation curve extended with the Leitherer et al. (2002) curve. Nebular emission is modeled by templates from Inoue (2011). We remove a small subset of galaxies with poorly constrained CIGALE parameter fits by restricting our library to galaxies with  $5 < \log(M_*/M_\odot) < 14$ .

We found by manual inspection that in some cases, such as very diffuse galaxies with low Sérsic index, the Sérsic profile fit fails catastrophically and produces greatly exaggerated estimates of  $R_e$ . This will result in SNe placed very far from the galaxy center in simulations, potentially creating a clear mismatch with SN-galaxy separations measured from the DES data. To remove galaxies with these pathological fits, we calculate ellipse areas from `sExtractor` parameters ( $A_{\text{sExtractor}} = A\_IMAGE * B\_IMAGE$ ) as well as from Sérsic ellipse parameters ( $A_{\text{Sérsic}} = ab$ ). We select galaxies with a “reasonable” Sérsic fit, which we define to be  $\frac{A_{\text{sExtractor}}}{A_{\text{Sérsic}}} \geq 0.25$ .

### 4.3.3. DES Data Host Matching

Host galaxy matching for the DES Y5 sample is performed using the DLR method with the host galaxy catalog described in Section 4.3.2.  $d_{\text{DLR}}$  values are computed for all galaxies in the catalog

within 15" of the SN position. Galaxies with  $d_{\text{DLR}} > 4$  are discarded, following the SDSS convention (Sako et al., 2018a), and those with lowest and second lowest  $d_{\text{DLR}}$  values are identified as the most likely and next most likely host match (HOSTGAL1 and HOSTGAL2). If fewer than two galaxies have  $d_{\text{DLR}} \leq 4$ , those SNe are considered to be missing a host match or (if one galaxy has  $d_{\text{DLR}} \leq 4$ ) missing a second host match. Summary statistics for the DES data with host matches is shown in Table 4.2.

Ideally, matching should be done with the full catalog, including galaxies without a known redshift. This would allow for us to remove SNe hosted by galaxies without known redshifts, rather than match them incorrectly to a galaxy with known redshift. However, we find that  $\sim 98\%$  of DES SNe have the same host match when matched with the full catalog, and those that do not mostly become "hostless" when the cuts are employed. Thus, we conclude that matching with the cut catalog is a valid method, as these SNe are ineligible for the analysis regardless of the cuts.

#### 4.4. Simulations and event selection

##### 4.4.1. Simulations

All simulations for this work are produced with the SuperNova ANALYSIS (SNANA) software (Kessler et al., 2009c). The SNANA simulation starts with a SN spectral template and generates survey-specific photometry under realistic observing conditions by utilizing a cadence library containing zero points, sky noise, and PSF information for each telescope pointing on each observing night.

We note that overlaying simulated SNe on actual galaxy images is the ideal method of performing a host matching analysis; however, it would be very computationally expensive to run the volume of simulations needed to develop and constrain the host mismatch systematic. For improved computational efficiency, we use the catalog-level simulation from SNANA.

#### **SN Models**

SN Ia simulations for this work are created using the SALT2 model (Guy et al., 2007) with training parameters determined from the Joint Lightcurve Analysis (JLA, Betoule et al., 2014). The SALT2

model defines several restframe parameters for SN lightcurves: the time of SN peak brightness  $t_0$ , a stretch-like parameter  $x_1$ , a color parameter  $c$  and the lightcurve normalization parameter  $x_0$ . Nuisance parameters  $\alpha, \beta$  are determined according to Scolnic and Kessler (2016), while the color ( $c$ ) and stretch ( $x_1$ ) populations follow Popovic et al. (2021). The SNe Ia are simulated with a redshift-dependent volumetric rate, using measured rates from Dilday et al. (2010) and Perrett et al. (2012) and recomputed by Frohmaier et al. (2018). To model empirically measured Hubble scatter after the SN Ia standardization procedure, we use the spectral-variation intrinsic scatter model in Kessler et al. (2013b) that is based on the model uncertainties determined in Guy et al. (2010c). The simulations include two separate populations: the DES-like photometric sample and a spectroscopically confirmed low- $z$  anchor. For simplicity, the low- $z$  anchor is an ad-hoc DES simulation applied to  $0 < z < 0.1$  with an inflated rate to match the true number of low- $z$  events in the DES-SN5YR sample.

Two types of core-collapse SNe as well as two types of peculiar SNe Ia are simulated alongside the SNe Ia to evaluate the effects of host galaxy mismatch on redshift-dependent photometric classification: SNIIdc, SNIbc, SNIax, and SNIa-91bg. These simulations use the SED templates introduced in Vincenzi et al. (2019) with luminosity functions and rates following Vincenzi et al. (2021). We use relative rates as measured by Shivvers et al. (2017) anchored by an overall rate following the cosmic star formation history presented in Madau and Dickinson (2014) normalized by the local SN rate from Frohmaier et al. (2021).

All simulations are generated assuming a flat  $\Lambda$ CDM cosmology with  $H_0 = 70 \text{ km s}^{-1} \text{ Mpc}^{-1}$  and  $\Omega_M = 0.311$ .

### Host Association and Matching

To associate a simulated SN with a host galaxy, the simulation first generates properties for each SN, including color, stretch, redshift, and sky location (RA, DEC). Subsequently, all galaxies whose redshifts match the true SN redshift within a small tolerance ( $dz_{\text{tol}} = \max|z_{\text{SN}} - z_{\text{GAL}}| = 0.002 + 0.04z$ ) are selected. The *assigned* host galaxy is chosen from this subset using the host mass-dependent weighting shown in Wiseman et al. (2021). The simulated host association and matching use the

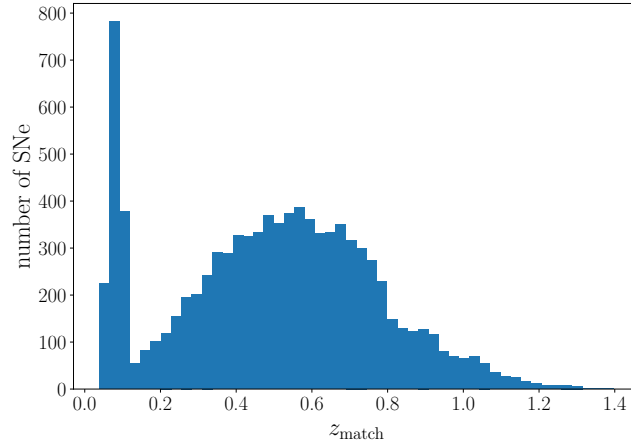


Figure 4.3: Redshift distribution of matched host galaxies in one realization of the SNIa-only simulations. Since we find the mismatch rate resulting from the DLR method to be quite low (see Table 4.3), the true redshift distribution is not visibly different and was not included in this plot.

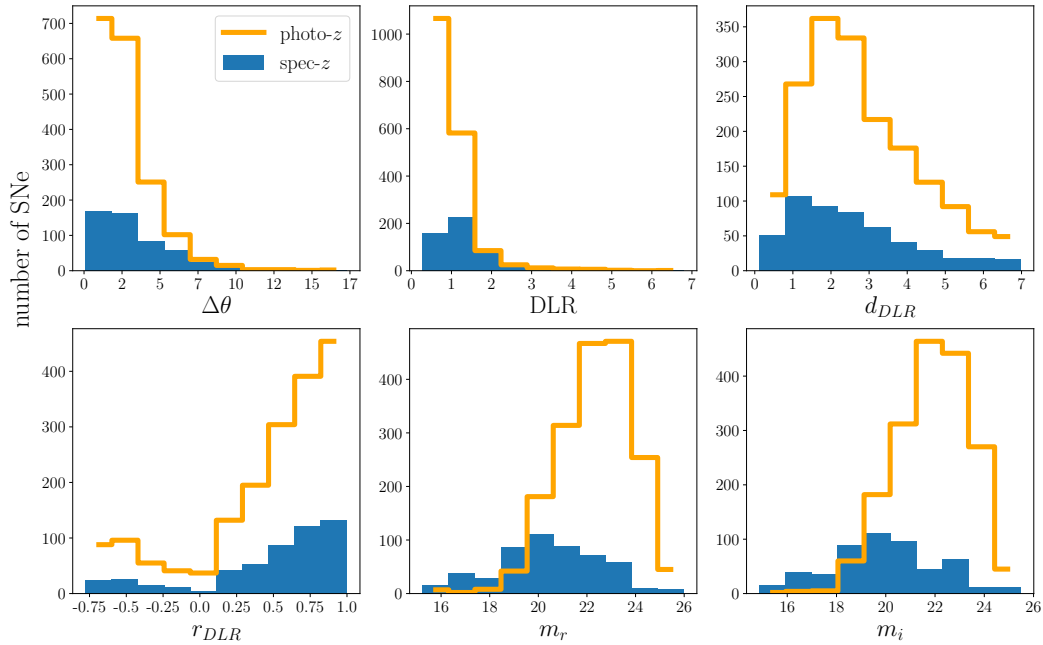


Figure 4.4: Parameter distributions of matched host galaxies in one realization of the SNIa-only simulations split into two populations: galaxies with spectroscopic redshifts and those with photometric redshift estimates only. Details and definitions of these parameters can be found in Section 4.5.2. Since we find the mismatch rate resulting from the DLR method to be quite low (see Table 4.3), the true distributions are not visibly different and were not included in this plot.

same deep coadded DES galaxy catalog used for the data analysis.

Note that the process of assigning a host for a simulated SN does not take into account the locations of the host or the SN, only the redshifts of the SN and galaxy as well as the galaxy stellar mass. The host and its neighboring galaxies are moved near the SN such that it satisfies the simulated SN-host separation as well as models host confusion in the analysis. This strategy is efficient for modeling SN-host correlation and incorrect host matches, but it does not model large scale structure.

The SN-host separation is determined by placing the SN at a radial distance  $R$  from the center of the assigned host galaxy according to the probability distribution  $p(R) \sim I(R)$ , where  $I(R)$  is the galaxy intensity at radius  $R$  described by the galaxy's fitted Sérsic profile (see Equation 4.3). This approach follows past work using SNANA such as Abbott et al. (2019a).

To replicate the host matching procedure used for real data, we apply host galaxy matching with the DLR method to the simulated SNe. The simulation computes  $d_{\text{DLR}}$  values for up to 10 galaxies within a 10" radius of the assigned host and saves the galaxies with the lowest and second lowest  $d_{\text{DLR}}$  values as the most and next most likely host match (HOSTGAL1 and HOSTGAL2), as long as  $d_{\text{DLR}} \leq 4$ . The redshift distribution of the matched host galaxies for one realization of a SNIa-only simulation is shown in Figure 4.3 and relevant population parameter distributions (e.g.  $d_{\text{DLR}}$ ) are shown for host galaxies with spectroscopic and photometric redshifts in Figure 4.4. The host matching procedure is run for the full set of simulations, including the low- $z$  population, though low- $z$  mismatches are rare.

#### 4.4.2. Event Selection

##### **Lightcurve Fitting**

All DES-SN observed and simulated SN lightcurves are fit with the same SALT2 model with JLA parameters that was used to simulate the SNe Ia. The fit is performed with a  $\chi^2$ -minimization program included in SNANA and determines several parameters under the assumption that the event is a SN Ia: the time of SN peak brightness  $t_0$ , a stretch-like parameter  $x_1$ , a color parameter  $c$  and the lightcurve normalization parameter  $x_0$ , as well as their uncertainties and covariances (i.e.,

Table 4.3: Summary of the mismatch rate averaged over 25 realizations after each selection cut on the SNIa+CC simulated dataset, split by Ia vs. non-Ia SNe. The non-Ia SNe include SNIax, SNIa-91bg, SNIIf, and SNIbc. All results using SNe Ia only are using the SN Ia subset of this dataset.

Cut	SN Ia			non-Ia SNe		
	Mismatches	Total	Mismatch Rate	Mismatches	Total	Mismatch Rate
No cuts	233	9,356	2.5%	151	5,957	2.5%
$ x_1  < 3,  c  < 0.3$	95	5,562	1.7%	22	800	2.8%
$\sigma_{x_1} < 1$	83	4,886	1.7%	15	545	2.8%
$\sigma_{t_0} < 2$	83	4,870	1.7%	15	543	2.8%

$\sigma_{t_0}$ , etc.). These parameters are used to calculate the distance modulus  $\mu$ , allowing the SNe to be placed on the Hubble diagram.

We apply selection cuts on these fitted parameters and select SN lightcurves well described by the SALT2 model. Specifically, we restrict our sample to SNe satisfying the following criteria:

- $|x_1| < 3$ ,
- $|c| < 0.3$ ,
- $\sigma_{x_1} < 1$ , and
- $\sigma_{t_0} < 2$  days.

A summary of these cuts on our simulations can be found in Table 4.3. The right panel of Figure 4.5 shows the effect of these cuts on the redshift error distribution between the matched and true hosts. These data show that the cuts not only reduce the average mismatch rate over 25 realizations from 2.5% to 1.7%, but also significantly reduce the spread in redshift error. Quantitatively, the cuts reduced the middle 90% of the  $z_{\text{match}} - z_{\text{true}}$  distribution for mismatched pairs from 1.1 (left panel of Figure 4.5) to 0.6 after cuts (right panel).

### Photometric Classification

In the absence of SN spectra, we rely on photometric classifiers to remove non-Ia contaminants from the cosmological sample. We choose two recent neural-network-based classifiers with high

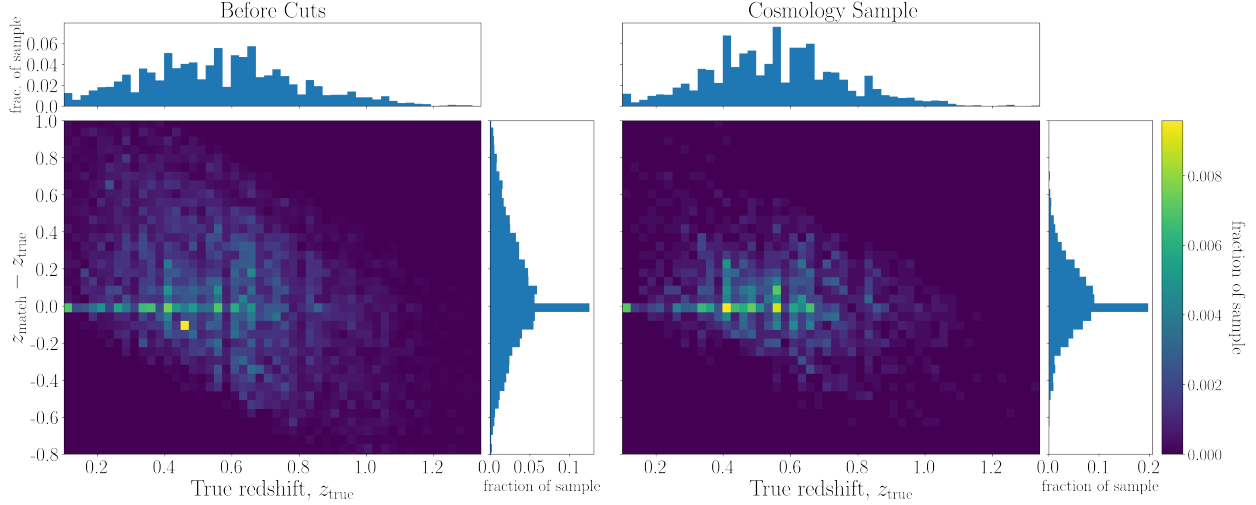


Figure 4.5: Redshift differences ( $\Delta z \equiv z_{\text{match}} - z_{\text{true}}$ ) for simulated SNe Ia with mismatched hosts. (left)  $\Delta z$  as a function of  $z_{\text{true}}$  for the full simulated sample prior to applying any selection cuts. (right)  $\Delta z$  as a function of  $z_{\text{true}}$  after all selection cuts (described in Section 4.4.2) and removal of SNe without a valid bias correction (described in Section 4.6.2). Our selection process not only reduces the mismatch rate (see Table 4.3) but also removes SNe with extremely biased redshift estimates from mismatched hosts, reducing the spread in  $\Delta z$ . Quantitatively, the spread in  $z_{\text{match}} - z_{\text{true}}$  characterized by the middle 90% of the distribution is reduced from 1.1 before cuts to 0.6 after cuts.

demonstrated accuracies for this work: SuperNNova (SNN, Möller and de Boissière, 2020b) and SCONE (Qu et al., 2021). High quality SN redshifts have been shown to improve SNN accuracy classifying SN Ia vs. non-Ia, so we test SNN in both redshift-dependent and redshift-independent configurations to evaluate the impact of misidentified redshifts. SNN models were trained in both the redshift-independent and dependent configurations following Vincenzi et al. (2022). SCONE is redshift-independent and performs classification based on SN lightcurves alone, so these results should not be affected by host misidentification. Each classifier outputs  $P_{\text{Ia}}$  values, the predicted probability of each SN to be a type Ia. The SNIa-only simulations are not run through photometric classification; all objects are simply labeled as SNe Ia.

## 4.5. Comparing Data with Simulations

### 4.5.1. Host Matching Rates and Hostless SNe

First, we compare the fraction of simulated and observed DES SNe that pass our selection cuts with one or more matched hosts. Since we have reliable SN Ia photometric classifiers, we compare

simulated true SNe Ia with DES SNe Ia as predicted by SCONE (Qu et al., 2021). Since most of the redshifts for the DES SNe come from host galaxies, we chose to use SCONE for this comparison as it does not require redshift information.

After applying the cuts specified in Table 4.3 to both data and simulations, the DLR algorithm is able to find at least one host galaxy match in 98.3% of SNe in our SN Ia-only simulations compared to 98.2% of SCONE-classified SNe Ia in the DES data. The remaining  $\sim 2\%$  of SNe in our data and simulations is the rate of “hostless” SNe. SNe can appear hostless because their host galaxies are too faint to be detected and our imposed  $d_{\text{DLR}} \leq 4$  cut on potential host matches avoids matching to unrealistically faraway galaxies.

SNe in galaxy-dense regions have multiple potential host matches with  $d_{\text{DLR}} \leq 4$ . We find that  $(9.35 \pm 0.09)\%$  of simulated SN Ia have more than one host match, compared to  $(8.71 \pm 1.06)\%$  of SCONE-classified DES SNe Ia. The agreement in the fraction of hostless and multiple-host events provides confidence in our simulated data sample.

#### 4.5.2. Comparing Parameter Distributions

To further verify that the host mismatch rate estimates and resulting cosmological biases derived from our simulations are representative of the DES sample, we compare simulations and data over five relevant parameter distributions: SN-galaxy separation ( $\Delta\theta$ ), DLR,  $d_{\text{DLR}}$ ,  $r$ -band host galaxy magnitude ( $m_{r,\text{gal}}$ ), and the HOSTGAL1 to HOSTGAL2  $d_{\text{DLR}}$  ratio ( $r_{\text{DLR}}$ ), following Popovic et al. (2020). A comparison of these distributions for the DES-SNY5YR sample (shown in points) and the simulations (shown in filled/unfilled bars) used for this analysis is shown in Figure 4.6.

The top row of Figure 4.6 shows the parameter distributions of data and simulations for SNe with a single host galaxy match (i.e. only one galaxy with  $d_{\text{DLR}} \leq 4$ ). The second row shows the same parameter distributions for SNe with at least two host galaxy matches, where green shows distributions for the closest host galaxy match (smallest  $d_{\text{DLR}}$  value, labeled HOSTGAL1) and orange denotes the second closest host galaxy match (labeled HOSTGAL2).

The angular separation between the center of the galaxy and the SN position,  $\Delta\theta$ , is shown in pan-



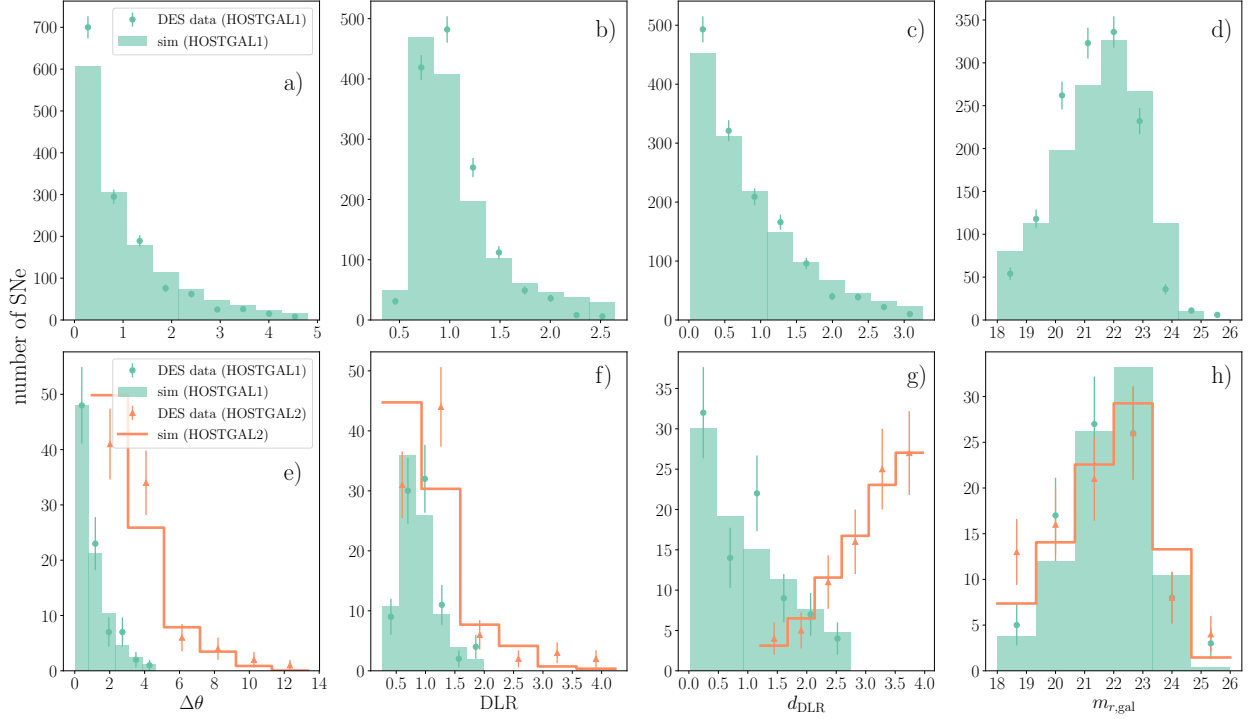


Figure 4.6: Histograms comparing our simulated SNe Ia against DES Y5 photometrically confirmed SNe Ia for angular SN-galaxy separation ( $\Delta\theta$ , arcsec), directional light radius (DLR), the DLR-normalized SN-galaxy separation ( $d_{\text{DLR}} = \frac{\Delta\theta}{\text{DLR}}$ ), and  $r$ -band host galaxy magnitude ( $m_{r,\text{gal}}$ ) (see Section 4.5 for explanations of each). For ease of comparison, the simulation histograms are normalized to match the integral of the data histogram and the  $x$  axis limits of each histogram are determined by the middle 90% of the data distribution to remove outliers. In both rows, points with error bars represent parameter distributions measured from the DES data and filled or unfilled histograms represent the analogous quantities for simulations. (top row) Histograms of parameter values for closest host galaxy match (HOSTGAL1) for SNe with only one host galaxy match. (bottom row) Histograms of parameter values for closest (HOSTGAL1) and second closest (HOSTGAL2) host galaxy match for SNe with 2 or more host galaxy matches.

els a) and e) of Figure 4.6. Good agreement in the data vs. simulation  $\Delta\theta$  distribution validates that (1) the algorithm used by the simulation to place SNe within their host galaxies is representative of real observations, and (2) the Sérsic ellipse parameters  $a, b$  used to place SNe within their host galaxies are well estimated. Note that, as described in Section 4.3.2, the fitted Sérsic parameters were scaled by a factor of 0.8. The distributions from data and simulations match very well overall, but the simulations slightly underestimate HOSTGAL1 matches at the very low end of the  $\Delta\theta$  distribution.

DLR, shown in panels b) and f), corresponds to the size of the matched host and is measured as in Section 4.2.1. Agreement in this parameter verifies that matched hosts are similar in size between data and simulations. The data and simulations agree well for both HOSTGAL1 and HOSTGAL2.

The distribution of  $d_{\text{DLR}}$  values is shown in panels c) and g).  $d_{\text{DLR}}$  agreement is an important quantity, since it is used to determine which galaxies are host matches, and shows that simulated SNe are placed at reasonable distances from the host center. These distributions largely show the same trend as the  $\Delta\theta$  distributions, where the HOSTGAL2 distributions match very well but the HOSTGAL1 distributions from simulations appear to be skewed slightly higher than those of the DES data.

$m_{r,\text{gal}}$ , the host galaxy  $r$ -band magnitude, is shown in panels d) and h). Agreement in this parameter is an additional validation of similarity in the overall populations of host galaxies between data and simulations. The slight discrepancy between these distributions can likely be attributed to the fact that the spectroscopic efficiency is defined using MAG\_AUTO, but we applied the efficiency to MAG\_MODEL magnitudes, which tend to be slightly fainter.

Finally, we define

$$r_{\text{DLR}} = \frac{d_{\text{DLR,HOSTGAL1}}}{d_{\text{DLR,HOSTGAL2}}}. \quad (4.5)$$

Figure 4.7 shows the distributions of this parameter for DES data and our simulations. Since the definition requires  $d_{\text{DLR,HOSTGAL2}}$ , only SNe with at least 2 host galaxy matches are included. Consistency in  $r_{\text{DLR}}$  and the HOSTGAL2 distributions indicate that the galaxy catalog is sufficiently dense, since the spacing between galaxies will affect the HOSTGAL2 parameter distributions much more

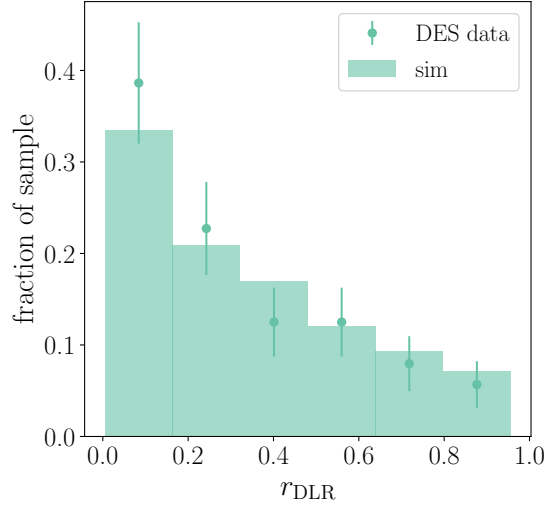


Figure 4.7: Distributions of the ratio  $r_{\text{DLR}} = \frac{d_{\text{DLR,HOSTGAL1}}}{d_{\text{DLR,HOSTGAL2}}}$  for DES Y5 photometrically confirmed SNe Ia and our simulated SNe Ia.

than HOSTGAL1.

## 4.6. Cosmological Parameter Estimation

### 4.6.1. Cosmology Analysis Overview

The cosmology analysis pipeline is orchestrated end-to-end by the Pippin framework (Hinton and Brout, 2020), beginning with simulations or data as input and concluding with cosmological parameter estimates. After SNe are simulated, the resulting lightcurves are fit with an empirical model that outputs characteristics for each SN, such as color and stretch (see Section 4.4.2). SNe that are fit successfully are then assigned a SN Ia probability by a photometric classifier (see Section 4.4.2) and bias corrections on distance moduli are computed for each SN based on its fitted parameters as well as SN Ia probability. Finally, the bias corrected distance moduli are used to determine constraints on cosmological parameters.

### 4.6.2. Bias Corrections

Biases due to core collapse contamination and survey selection are modeled and corrected for with the BEAMS with Bias Corrections framework (BBC, Kessler and Scolnic, 2017), an extension of BEAMS (Kunz et al., 2007), which allows photometrically classified SNe Ia to be used for cosmol-

ogy. The primary output of the BBC framework applied on a SN sample is a redshift-binned Hubble diagram corrected for biases from selection effects and non-SNIa contamination.

First, systematic biases due to selection effects are modeled by a large simulation of SNe Ia ( $\sim 800,000$  SNe Ia). We found empirically that our current framework for modeling and correcting for biases, typically used for e.g. the Malmquist bias, is not suited for including wrong hosts in our bias correction simulations. Thus, our bias correction simulation includes only assigned hosts for our primary results. In Section 4.7.3, we explore incorporating host matching (and thus mismatched hosts) into the bias correction simulations.

Using this large SN sample, distance moduli are calculated using the Tripp formula (Tripp, 1998),

$$\mu_{\text{obs}} = m_B + \alpha x_1 - \beta c + M_B + \Delta\mu_{\text{bias}} \quad (4.6)$$

for each SN.  $m_B = -2.5\log_{10}(x_0)$  and  $M_B$  is the absolute magnitude of a SN Ia with  $x_1 = c = 0$  and  $\alpha, \beta$  are nuisance parameters determined according to Scolnic and Kessler (2016). Biases from a reference cosmology,  $\Delta\mu_{\text{bias}}$ , are calculated in a 3-dimensional grid of  $\{z, x_1, c\}$  bins using the method described above. We use this grid of estimated biases to correct all of our distance moduli prior to cosmology fitting. A small percentage of SNe with parameter values that do not fit into the grid are discarded. Finally, the BEAMS method is used to estimate binned distance moduli from the bias-corrected distance moduli from the previous step in the presence of core-collapse contamination. This is done by minimizing the BEAMS likelihood, which models the SNe Ia population and a population of contaminants separately. These terms are weighted by  $P_{\text{Ia}}$ , the probability of each SN to be a type Ia as output by a photometric classifier. We omit the mass step correction in Equation 4.6; details on the mass step and the impact of host mismatches can be found in Section 4.7.1.

#### 4.6.3. Cosmological Parameters

We fit for  $w$  and  $\Omega_m$  using `wfit`, a fast cosmology grid-search program in SNANA, assuming a diagonal covariance matrix  $C_{\text{stat}}$  and an approximate CMB prior computed with the  $R$ -shift parameter

(see e.g. Equation 69 in Komatsu et al. (2009)) from the same cosmological parameters used to generate the SNe Ia. The  $R$  uncertainty is  $\sigma_R = 0.006$ , tuned to have the same constraining power as Planck Collaboration et al. (2020). As we are only interested in the impact of host mismatches on cosmology, the approximation of a diagonal covariance matrix is sufficient for our purposes. `wfit` calculates the  $\chi^2$  of the SN likelihood to compute our final cosmological fit,

$$\chi^2 = \Delta\mu_{\text{model}}^T \cdot \mathcal{C}_{\text{stat}}^{-1} \cdot \Delta\mu_{\text{model}} \quad (4.7)$$

where

$$\Delta\mu_{\text{model}} = \mu - \mu_{\text{model}}(\Omega_m, w). \quad (4.8)$$

#### 4.7. Results and Discussion

We use the cosmological parameter estimation framework described in Section 4.6 to evaluate the effects of host galaxy mismatch on the resulting best fit cosmology. We focus primarily on shifts in the best fit value for  $w$ , the dark energy equation of state parameter. We quantify this shift by creating two sets of identical simulations that differ only in whether or not the DLR method is run to determine the matched hosts using the procedure described in Section 4.4.1. We define  $S_{\text{match}}$  as simulations with matched hosts and  $S_{\text{truehost}}$  as simulations with perfect host matching. In  $S_{\text{truehost}}$ , we do not calculate matched hosts using the DLR method; we instead force a match to the true hosts assigned by the simulation. This ensures that there will be no mismatches and serves as a baseline for comparison.

We define the  $w$  shift as the difference between the inferred  $w$  values from  $S_{\text{match}}$  ( $w_{\text{match}}$ ) and  $S_{\text{truehost}}$  ( $w_{\text{truehost}}$ ). We average over 25 realizations with the same simulation parameters. Explicitly, we define the  $w$  shift as

$$\Delta w = \langle w_{\text{match}} - w_{\text{truehost}} \rangle_{(25 \text{ realizations})} \quad (4.9)$$

where  $\langle \rangle$  denotes the inverse-variance weighted average. We calculate the associated uncertainty

on  $\Delta w$  as follows:

$$\sigma_{\Delta w} = \sqrt{\frac{\sum_i (w_{\text{match},i} - w_{\text{truehost},i})^2}{25}}. \quad (4.10)$$

#### 4.7.1. Cosmological Biases with SNe Ia Only

For simulations with SNe Ia only, we find  $\Delta w = 0.0013 \pm 0.0026$ . **In the flat  $w_0 w_a$  CDM model, we find biases of  $\Delta w_0 = 0.037 \pm 0.041$ ,  $\Delta w_a = -0.22 \pm 0.25$ . Biases in both cosmological models are consistent with zero.** In Figure 4.8, we show the biases on the binned Hubble diagram comparing distance moduli  $\mu$  from simulations with DLR matched hosts ( $\mu_{\text{match}}$ ) and true hosts ( $\mu_{\text{truehost}}$ ). We define

$$\Delta\mu = \mu_{\text{match}} - \mu_{\text{truehost}}. \quad (4.11)$$

We see that the bias is consistent with 0 until  $z \sim 1$ , where the sample becomes very sparse (see Figure 4.3 for the redshift distribution of the sample).

Figure 4.9 shows the Hubble diagram and Hubble residuals for a single realization of simulations with mismatches. In this particular realization, 79 SNe were matched to the wrong host out of 5,811 total simulated SNe, which translates to a 1.4% mismatch rate. The mismatched SNe, shown in red circles, show similar Hubble residuals compared to the correctly matched SNe, which is consistent with the small recovered bias on  $w$ . The observed similarity in Hubble residuals is likely due to the fact that catastrophic outliers in redshift are removed by the selection criteria described in Table 4.3 and shown in Figure 4.5.

The binned Hubble residuals for all 25 simulations with mismatch are shown in Figure 4.10. This plot shows  $\Delta\mu = \mu_{\text{match}} - \mu_{\text{model}}$ , as opposed to Figure 4.8, which shows  $\mu_{\text{match}} - \mu_{\text{truehost}}$ . This allows us to compare residuals from the subpopulations of SNe with wrong and correct host match with respect to a fiducial cosmology. Aggregated over all 25 simulations, the bias from SNe with the wrong host match (shown in orange) is clearly distinct from the nearly unbiased subset of SNe with the correct host match (teal). Although wrong hosts clearly lead to biases on the Hubble diagram, SNe with the wrong host match make up  $< 2\%$  of the sample, resulting in the small  $\Delta w$  value we observe.

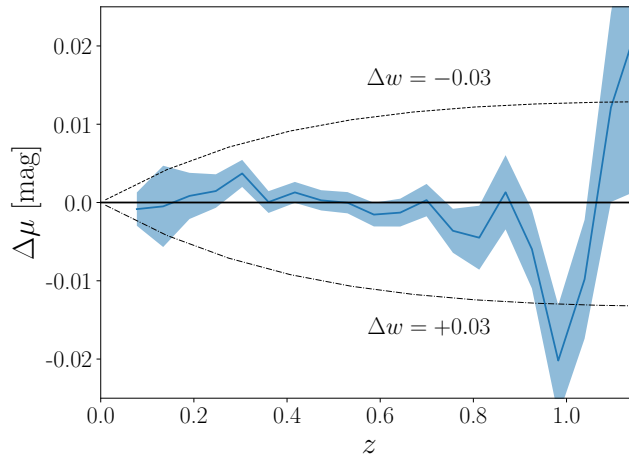


Figure 4.8: Biases in binned Hubble residuals for the SN Ia-only sample between samples with and without mismatched host galaxies,  $\Delta\mu = \mu_{\text{match}} - \mu_{\text{truehost}}$ , as a function of redshift. Uncertainties are shown as the shaded region and calculated from the binned standard deviations of  $\mu_{\text{match}}$  and  $\mu_{\text{truehost}}$ . Lines showing  $\Delta w = \pm 0.03$  are also plotted for reference.

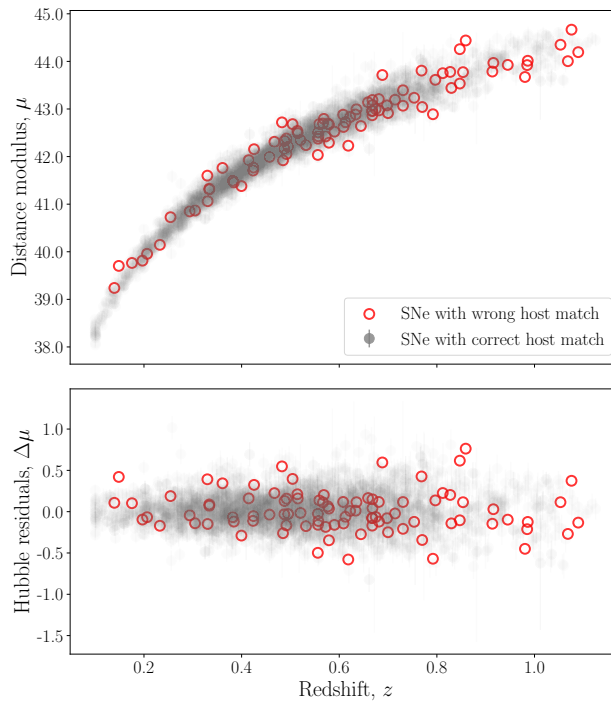


Figure 4.9: Hubble diagram for a single realization of our SNIa-only simulation with matched hosts. This realization has 79 SNe matched to an incorrect host out of 5,811 total SNe, a 1.4% mismatch rate. The low- $z$  sample is omitted from this plot, since it is not part of the main DES sample.

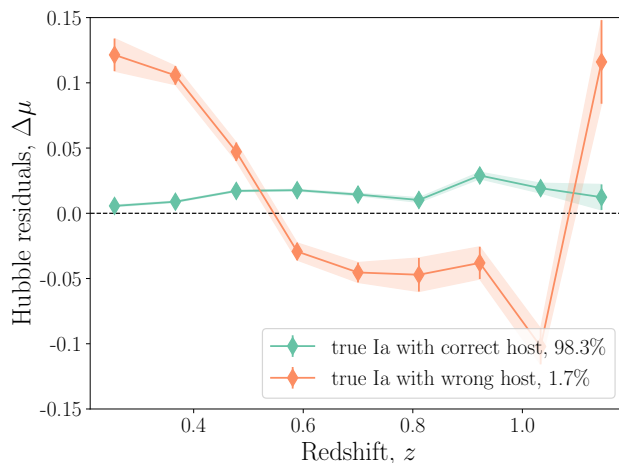


Figure 4.10: Binned Hubble residuals ( $\mu_{\text{match}} - \mu_{\text{model}}$ ) for all 25 realizations of our SNIa-only simulation with mismatch. The percentages in the legend show the fraction of the sample represented by each population in the plot.

Classifier	SNe	$\Delta w$	Ia vs. non-Ia Classification Accuracy		
			with host mismatch	no host mismatch	change
Perfect	Ia only	$0.0013 \pm 0.0026$	100%	100%	0%
Perfect	Ia+CC	$0.0011 \pm 0.0027$	100%	100%	0%
SNN <sub>+Z</sub>	Ia+CC	$0.0032 \pm 0.0040$	97.94%	98.06%	-0.1%
SNN <sub>NoZ</sub>	Ia+CC	$0.0009 \pm 0.0028$	97.05%	97.05%	0%
SCONE	Ia+CC	$0.0016 \pm 0.0032$	96.13%	96.13%	0%

Table 4.4:  $\Delta w$  and classification accuracies for each classifier. Accuracy change is only expected for the SNN<sub>+Z</sub> classifier, as it is the only classifier tested that requires redshift information. Accuracy change is defined as Accuracy (with mismatch) – Accuracy (no mismatch).



## Host Mismatch and the Mass Step

The ‘mass step’ is the observed correlation between SNe Ia intrinsic luminosity and host galaxy stellar mass,  $M_*$ . Specifically, SNe Ia in more massive galaxies are more luminous after lightcurve corrections than their counterparts occurring in galaxies with lower stellar mass, with the average corrected luminosity distribution following a two-part step function with a break at  $\log(M_*/M_\odot) \sim 10$  (Kelly et al., 2010; Sullivan et al., 2011; Betoule et al., 2014; Smith et al., 2020b; Kelsey et al., 2021, 2023). Though the underlying astrophysical cause is unknown, recent cosmological analyses have incorporated a correction in which SN luminosities in hosts with  $\log(M_*/M_\odot) \geq 10$  and those in hosts with  $\log(M_*/M_\odot) < 10$  are fit for separately. When this two-part fit is employed, incorrect host matches will produce additional bias through incorrect host mass estimates, leading to different best fit values for SN luminosities. We observe that 34.3% of our simulated SNe Ia with the wrong host match “switch sides”, i.e. the correct host is on one side of the mass step but the matched host is on the other. Given that the rate of mismatches averaged over 50 realizations is 1.7% after selection cuts for our Ia-only sample, the overall fraction of SNe Ia that switch sides of the mass step is  $\sim 0.6\%$ . We assume that such a small percentage of the sample switching sides makes little impact and we do not pursue this aspect of the analysis further.

### 4.7.2. Cosmological Biases with Photometric Classification

Some photometric classifiers, such as SuperNNova (SNN), rely on SN redshift information to improve classification accuracy. To evaluate the impact of incorrect redshifts from host galaxy mismatches on the predictions from photometric classifiers, we jointly simulate SNe Ia, two types of peculiar SNe Ia, and two types of core collapse SNe: SNII, SNIbc, SNIax, and SNIa-91bg. Details on these simulations can be found in Section 4.4.1 and Table 4.3.

We tested 4 different photometric classifiers on our SNIa+CC simulations: the baseline perfect classification, SNN with redshift information ( $\text{SNN}_{+Z}$ ), SNN without redshift information ( $\text{SNN}_{NoZ}$ ), and SCONE. SNN is typically used with SN redshift information and has been shown to produce highly accurate Ia vs. non-Ia classification results in this paradigm, so testing both redshift-dependent and redshift-independent configurations will show which effect is more detrimental

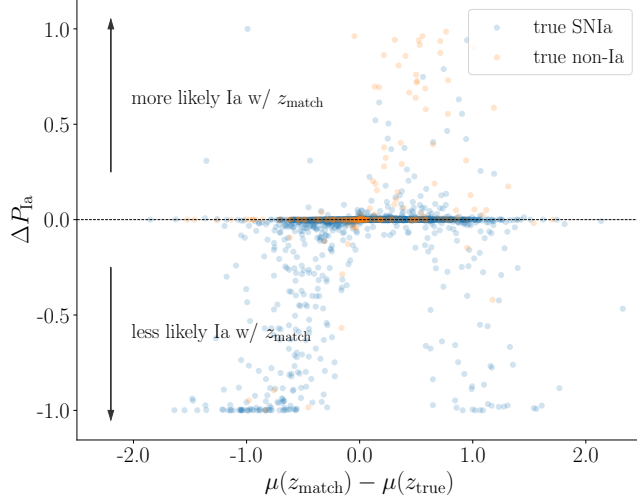


Figure 4.11: Visualization of the impact of incorrect redshifts on  $\text{SNN}_{+Z}$  predictions.  $\Delta P_{\text{Ia}} = P_{\text{Ia,wronghost}} - P_{\text{Ia,correcthost}}$  is the difference between  $P_{\text{Ia}}$  values output by the  $\text{SNN}_{+Z}$  classifier given the wrong host redshift ( $P_{\text{Ia,wronghost}}$ ) and the correct host redshift ( $P_{\text{Ia,correcthost}}$ ) for SNe with mismatched hosts.  $\Delta P_{\text{Ia}}$  values are plotted against the difference between the distance modulus  $\mu$  calculated at the wrong ( $\mu(z_{\text{match}})$ ) and correct host redshifts ( $\mu(z_{\text{true}})$ ). As  $\mu(z_{\text{match}}) - \mu(z_{\text{true}})$  deviate from 0, we would expect larger deviations in  $P_{\text{Ia}}$  values, i.e.  $|\Delta P_{\text{Ia}}| > 0$ . Non-Ia SNe (orange points) more likely to be misclassified as Ia with the wrong redshift will appear in the upper half of the plot ( $\Delta P_{\text{Ia}} > 0$ ), whereas SNe Ia (blue points) more likely to be misclassified as non-Ia with the wrong redshift will appear in the lower half. 7% of mismatched SNe are incorrectly classified as a result of wrong host redshifts, leading to an overall 0.1% reduction in classification accuracy compared to a simulation with correct host redshifts.

to performance: incorrect redshift information or lack of redshift information altogether. SCONE uses SN lightcurves alone without the need for redshift information, so its predictions are not affected by host matching. For this analysis, we choose to define an SN Ia classification as  $P_{\text{Ia}} \geq 0.5$ .

Following the same approach as the Ia-only analysis,  $w$  shifts were calculated for each photometric classifier by comparing two sets of identical simulations with and without mismatches. The results are shown in Table 4.4.

$\text{SNN}_{+Z}$  is the only classifier that should be impacted by host galaxy mismatches, and this relationship is observed in the larger  $\Delta w$  value and lower classification accuracy for simulations with mismatched host galaxies. Figure 4.11 shows the difference between predicted SN Ia probability output by the  $\text{SNN}_{+Z}$  classifier given the wrong host redshift ( $P_{\text{Ia,wronghost}}$ ) as opposed to the

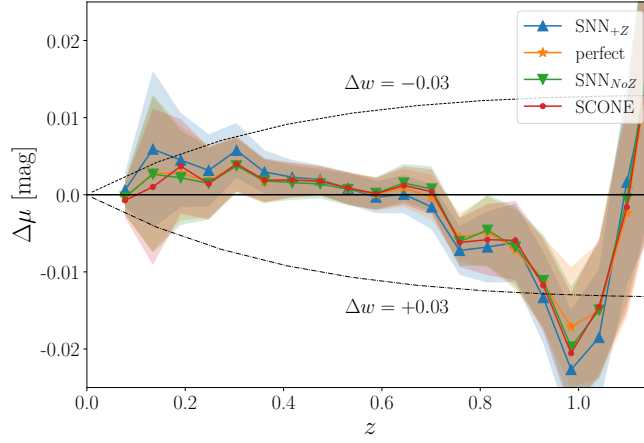


Figure 4.12: Biases in binned Hubble residuals for all 4 photometric classifiers between samples with and without host galaxy mismatch. Uncertainties are shown as the shaded region and calculated from the binned standard deviations of  $\mu_{\text{match}}$  and  $\mu_{\text{truehost}}$ . Lines showing  $\Delta w = \pm 0.03$  are also plotted for reference.

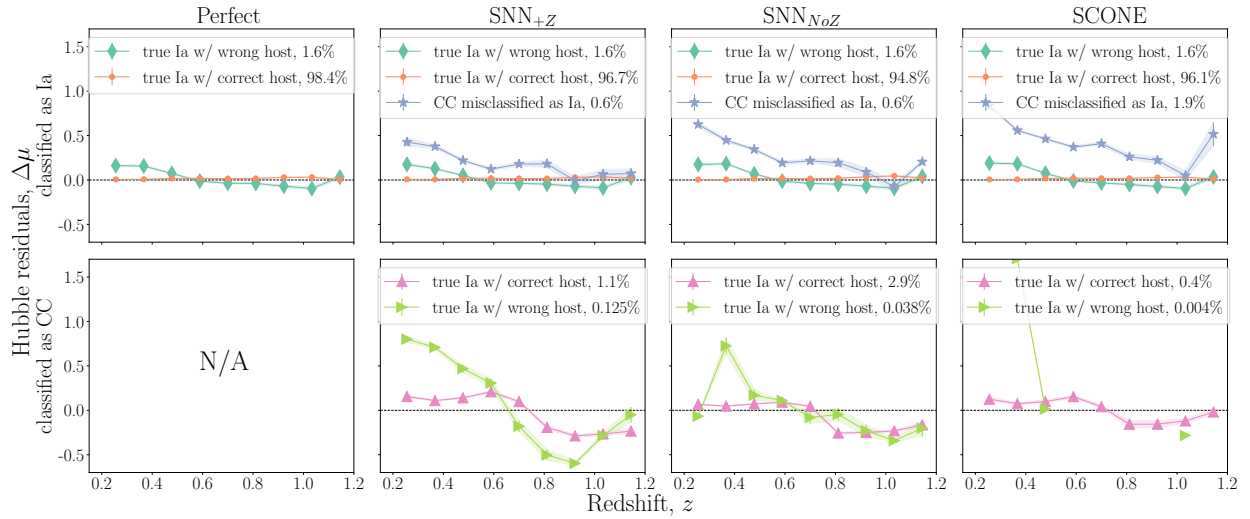


Figure 4.13: Binned Hubble residuals,  $\Delta\mu = \mu_{\text{match}} - \mu_{\text{model}}$ , for the 4 photometric classifiers for our SNIa+CC simulation with mismatch. (top) SN populations classified as SNe Ia by each photometric classifier, including true SNe Ia with mismatched hosts as well as core collapse contamination. (bottom) SN populations classified as CC SNe, including SNe with mismatched hosts.

correct host redshift ( $P_{\text{Ia,correcthost}}$ ). Wrong redshifts indeed cause SNN to produce incorrect predictions for both Ia and non-Ia SNe, leading to the observed drop in accuracy with wrong redshifts. SCONE and  $\text{SNN}_{NoZ}$  are oblivious to any host matching changes and produce the same predictions for both sets of simulations, as expected.

Figure 4.12 shows the biases on the binned Hubble diagram for each of the photometric classifiers with  $\Delta\mu$  defined as in Equation 4.11. Overall, the classifiers perform quite similarly and exhibit very small differences in  $\Delta\mu$  over the full redshift range. As expected from the small  $\Delta w$  values, the  $\Delta\mu$  curves for the Ia+CC simulations exhibit a slight redshift-dependent bias, though still mostly consistent with 0 up to high redshifts. Further validating the observed  $\Delta w$  values for each classifier, we see that the two classifiers with most similar  $w$  shifts, the perfect classifier (shown in orange) and  $\text{SNN}_{NoZ}$  (green), have the most similar  $\Delta\mu$  values.  $\text{SNN}_{+Z}$  (shown in blue), which has the largest  $w$  shift, also consistently appears furthest from  $\Delta\mu = 0$  across all redshift bins.

The binned Hubble residuals of SNe Ia in the Ia+CC simulations as predicted by the 4 photometric classifiers are shown in Figure 4.13. This plot shows  $\Delta\mu = \mu_{\text{match}} - \mu_{\text{model}}$ , as opposed to Figure 4.12, which shows  $\mu_{\text{match}} - \mu_{\text{truehost}}$ . This allows us to compare residuals from the subpopulations of SNe with wrong and correct host match with respect to a fiducial cosmology. The biases on Hubble residuals from SNe Ia with wrong hosts (shown in teal diamonds on the top row) appear similar between the four classifiers, reflecting the small recovered  $\Delta w$  values shown in Table 4.4. We also observe that the bias from wrong hosts is much more pronounced in SNe Ia misclassified as CC (shown in green triangles on the bottom row), particularly in the  $\text{SNN}_{+Z}$  panel, indicating that  $\text{SNN}_{+Z}$  was able to identify severe redshift outliers and rejected them from the SN Ia sample.

### 4.7.3. Robustness of Cosmological Biases

#### Impact of CMB Prior

The  $w - \Omega_m$  contour estimated from measurements of the CMB exhibits a nearly orthogonal direction of degeneracy to the SN-only contour for a flat  $w$ CDM model, providing strong constraints and drastically reducing the impact of systematics that act along the SN degeneracy direction. All

Parameter	with CMB prior	no CMB prior
$\Delta w$	$0.0013 \pm 0.0026$	$-0.062 \pm 0.072$
$\Delta\Omega_m$	$0.0014 \pm 0.0017$	$0.028 \pm 0.029$

Table 4.5:  $\Delta w$  and  $\Delta\Omega_m$  values for the Ia-only SN population with and without a CMB prior. The values in the  $\Delta w$  with CMB prior cell are reproduced from Table 4.4.

$\Delta w$  values reported in Sections 4.7.1 and 4.7.2 were calculated with a CMB prior. In this section, we evaluate the impact of the CMB prior on cosmological biases.

The cosmological biases on both  $w$  and  $\Omega_m$  with and without the CMB prior are shown in Table 4.5 for the SNIa-only sample. The associated cosmological contours are shown in Figure 4.14. Both  $\Delta w$  and  $\Delta\Omega_m$  are significantly inflated without the CMB prior, though still within their uncertainties (right column). The larger shift in  $w$  and  $\Omega_m$  are visible when comparing the contours in Figure 4.14. The contours computed with a CMB prior (top panel) are very nearly identical, whereas with a flat  $\Omega_m$  prior, the contour with matched hosts is visibly shifted from the true hosts contour. However, these results are still consistent with 0 for the analysis we performed for the DES data, but should be studied further in future surveys.

### Bias Correction Simulations with Mismatch

In the earlier sections, distance moduli from both  $S_{\text{match}}$  and  $S_{\text{truehost}}$  are bias corrected using a large simulation of SNe Ia generated with the same parameters as  $S_{\text{truehost}}$ , i.e. each SN is matched to its true host. We define this set of perfectly matched bias correction simulations as  $B_{\text{truehost}}$ . An alternative bias correction strategy is to “correct like with like”, i.e. generating two separate bias correction simulations, one identical to  $S_{\text{match}}$  as well as the existing one identical to  $S_{\text{truehost}}$ . We define this new set of DLR-matched bias correction simulations as  $B_{\text{match}}$ .  $B_{\text{match}}$  models the biases arising from mismatched hosts in the bias correction simulations in order to correct for these biases in the simulated data. The reference  $w$  value,  $w_{\text{truehost}}$  is still computed from  $S_{\text{truehost}}$  corrected with the baseline bias correction simulations with correct hosts only ( $B_{\text{truehost}}$ ). In this scheme, we define  $w(S, B)$  as the best-fit  $w$  value computed from simulations  $S$  corrected with bias correction

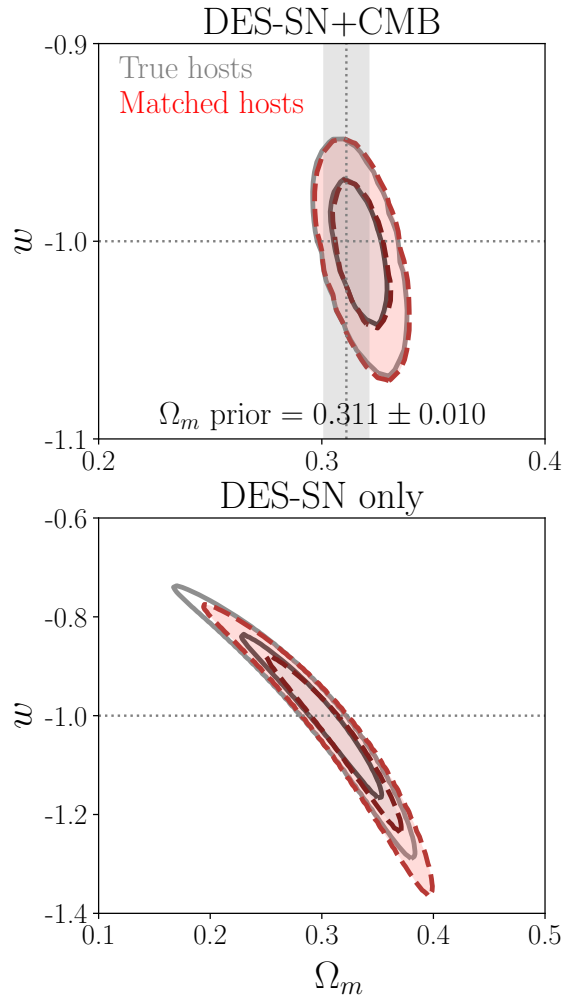


Figure 4.14: Cosmological contours computed with one realization of simulated DES Y5 SNe Ia with (red) and without host galaxy mismatch (gray). (top) SN+CMB contours, in which an approximate CMB prior  $\Omega_m = 0.311 \pm 0.010$  prior is applied (see Section 4.6.3 for details). This results in good agreement between the two contours. (bottom) SN-only contours showing a substantial shift in best fit  $w, \Omega_m$  between the two contours.

Table 4.6:  $\Delta w$  values for the Ia-only and Ia+CC simulated SN populations with an alternative bias correction scheme ("bcor+mismatch") that includes mismatched hosts in the bias correction simulations. The values in the  $\Delta w$ , baseline column are reproduced from Table 4.4.

Classifier	SNe	$\Delta w$ , baseline	$\Delta w$ , bcor+mismatch
Perfect	Ia only	$0.0013 \pm 0.0026$	$-0.0094 \pm 0.0099$
Perfect	Ia+CC	$0.0011 \pm 0.0027$	$-0.0110 \pm 0.0120$
SNN <sub>+Z</sub>	Ia+CC	$0.0032 \pm 0.0040$	$-0.0081 \pm 0.0086$
SNN <sub>NoZ</sub>	Ia+CC	$0.0009 \pm 0.0028$	$-0.0100 \pm 0.0012$
SCONE	Ia+CC	$0.0016 \pm 0.0032$	$-0.0099 \pm 0.0100$

simulations  $B$ . The resulting  $\Delta w$  equation then becomes

$$\Delta w, \text{ bcor} + \text{ mismatch} = \langle w(S_{\text{match}}, B_{\text{match}}) - w(S_{\text{truehost}}, B_{\text{truehost}}) \rangle_{(25 \text{ realizations})}. \quad (4.12)$$

The  $\Delta w$  values following this approach are shown in Table 4.6. While the  $\Delta w$  values using this bias correction scheme are still consistent with zero, the uncertainties are larger than those using bias correction simulations with perfect host matching; this may arise from comparing  $w$  values corrected with two statistically independent sets of bias correction simulations, i.e.  $S_{\text{match}}$  is corrected with  $B_{\text{match}}$ , whereas  $S_{\text{truehost}}$  is corrected with  $B_{\text{truehost}}$ . Further investigation of the interplay of bias correction simulations with different sources of bias, including incorrect redshifts from host mismatch, will be addressed in a future work.

### Results from Varying Sérsic Scale

We vary the scaling of the fitted Sérsic  $a$  and  $b$  parameters, which describe each galaxy's semi-major and semi-minor axes, respectively. Simulated SNe are placed according to the intrinsic light profile described by these parameters. The scaled parameters  $a'$  and  $b'$  are calculated as  $a' = ka, b' = kb$ , where  $k$  is the scaling parameter we vary. We tested  $k \in [0.5, 1.2]$  with an interval of 0.1 and evaluated  $\chi^2$  values on the histograms in Figure 4.6 to find the best match between data and simulations. We found that  $k = 0.8$  minimized the  $\chi^2$  and was thus chosen for the main analysis, as described in Section 4.3.2. We note that our conclusion runs contrary to that of Li et al. (2016), which found

Table 4.7:  $\Delta w$  values for the Ia-only and Ia+CC simulated SN populations with and without Sérsic scaling ( $k = 0.8$  and  $k = 1$ ). The primary results presented in this work (Sections 4.7.1 and 4.7.2) use simulations scaled with  $k = 0.8$ . The  $\text{SNN}_{+Z}$  results with  $k = 1$  have an inflated  $\Delta w$  as well as  $\sigma_{\Delta w}$  due to a realization with poor  $\chi^2$  fit from `wfit`.

Classifier	SNe	$\Delta w(k = 0.8)$	$\Delta w(k = 1)$
Perfect	Ia only	$0.0013 \pm 0.0026$	$0.0030 \pm 0.0042$
Perfect	Ia+CC	$0.0011 \pm 0.0027$	$0.0016 \pm 0.0026$
$\text{SNN}_{+Z}$	Ia+CC	$0.0032 \pm 0.0040$	$0.0120 \pm 0.0640$
$\text{SNN}_{NoZ}$	Ia+CC	$0.0009 \pm 0.0028$	$0.0021 \pm 0.0031$
SCONE	Ia+CC	$0.0016 \pm 0.0032$	$0.0025 \pm 0.0034$

that the Sérsic effective radius,  $R_e = \sqrt{ab}$ , is underestimated for stacked galaxy images rather than overestimated, as we discovered.

We performed cosmological parameter estimation using simulations with and without Sérsic scaling ( $k = 0.8$  and  $k = 1$ ) and found a modest benefit of using the  $k = 0.8$  scaling for redshift-independent photometric classifiers as well as perfectly classified SNe Ia, but a noticeable improvement for SNe classified using the redshift-dependent classifier,  $\text{SNN}_{+Z}$ . This seems to indicate that the Sérsic scaling improves the host matching efficiency significantly, since  $\text{SNN}_{+Z}$  is most affected by incorrect redshifts. This is notably the same scaling factor found to best match the DES3YR data when comparing distributions of host galaxy surface brightness at the SN position (see Figure 6 of Abbott et al., 2019a). The recovered biases on  $w$  from mismatched hosts ( $\Delta w$ ) with and without Sérsic scaling for all simulations and classifiers are shown in Table 4.7.

### Host Confusion Parameter

Equation 3 in Gupta et al. (2016) defines a quantity characterizing the likelihood of a wrong match: the host confusion parameter, or  $HC$ . This parameter is a function of the  $d_{\text{DLR}}$  values of each galaxy in the search radius around a SN, and aims to distinguish situations with a clear correct host from those without. In this analysis, we attempt to remove wrong hosts by cutting out SNe with high host confusion ( $HC \geq -2.5$ ). The distribution of  $HC$  values for wrong and correct hosts in our simulations is shown in Figure 4.15. The  $-2.5$  threshold was chosen by visual inspection of this distribution. The  $HC$  distributions for both populations look quite similar, but 72% of SNe with



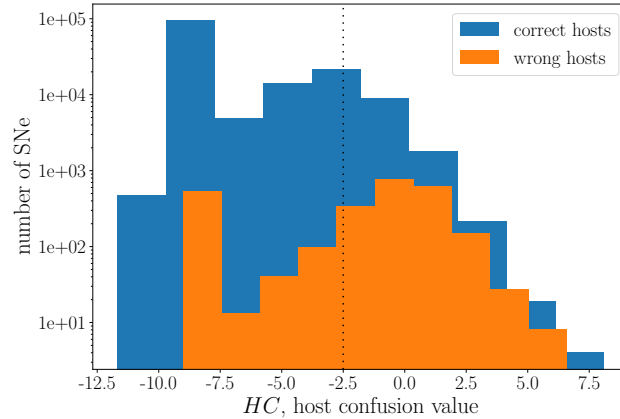


Figure 4.15: Distributions of  $HC$  values for SNe with wrong and correct host matches. The dotted line is drawn at our chosen threshold of  $HC = -2.5$ .

an incorrect host match are removed by the  $HC \geq -2.5$  cut, while 12% of SNe with correct host matches are removed.

We performed a full cosmology analysis with perfectly classified Ia-only simulations and find  $\Delta w = -0.0043 \pm 0.0047$  by comparing Ia populations with and without wrong hosts, both subject to the  $HC < -2.5$  selection requirement. In this cosmology analysis, we use bias correction simulations with host matching (i.e.  $B_{\text{match}}$  from Section 4.7.3) and select only the subset of the bias correction simulations with the same  $HC < -2.5$  requirement for consistency. Both simulations (with perfectly matched hosts and with wrong hosts) are bias corrected with  $B_{\text{match}}$  in order to apply the  $HC$  selection requirement globally, but it may not be suitable to correct simulations without wrong hosts in this way. The magnitude of this  $\Delta w$  value is larger than that of the baseline (i.e. no  $HC$  selection requirement), likely due to our inclusion of wrong hosts in the bias correction simulations, but is still consistent with zero.

## 4.8. Conclusions

Matching SNe to their host galaxies is a non-trivial problem when using 2-dimensional images of 3-dimensional space. Accurate host galaxy matches are important for cosmology because host galaxies are used to measure the vast majority of SN redshifts. Identifying incorrect host galaxies

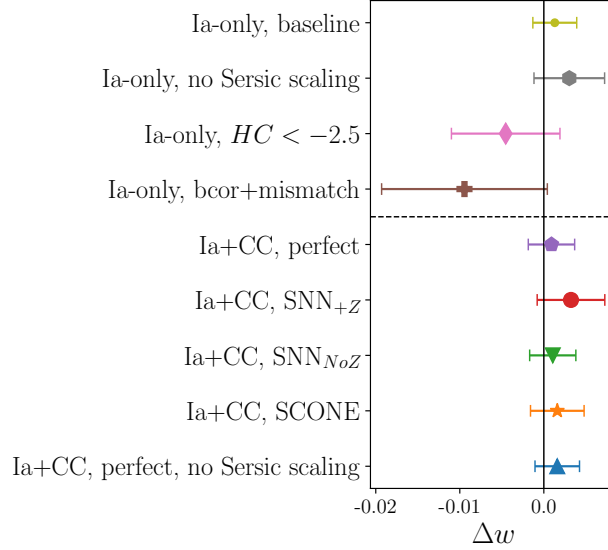


Figure 4.16:  $\Delta w$  values from all tested variants of simulated DES SNe with CMB prior. Note that the total uncertainty on  $w$  from the DES3YR analysis (Abbott et al., 2019b),  $\delta w = 0.059$ , is much larger than the bounds of this plot. Details about each variant can be found in Section 4.7.

alters the shape of the Hubble diagram and can impact the resulting fitted cosmological parameters.

In this work, we investigated the impact of mismatched host galaxies for the DES Y5 SN cosmology analysis. To this end, we created a galaxy catalog from DES deep field images that was sufficiently deep and dense, and calculated photometric redshifts, galaxy parameters, as well as Sérsic parameter fits for these 4 million galaxies. Simulations using this galaxy catalog were verified to be sufficiently similar to the DES Y5 photometric SN Ia sample using distributions such as Figure 4.6. This simulation enabled us to predict the prevalence of mismatched host galaxies in DES data and, in turn, characterize the effect of host mismatches on cosmological parameter estimates.

Host matching was performed using the directional light radius (DLR) method, a technique that identifies the host galaxy by minimizing SN-galaxy distance normalized by galaxy radius. This analysis aims to characterize the systematic error due to host misidentification by the DLR method for the DES Y5 cosmology analysis.

The main findings of this work are summarized in Figure 4.16, which shows the observed shifts in

the dark energy equation of state parameter  $w$  as a result of host galaxy mismatches with different approaches to the analysis. We defined  $\Delta w$  by producing two identical sets of simulations: one with perfect host matching and one with host matches from the DLR method. We also probed the interplay between host galaxy mismatches and photometric classification, as classifiers such as SuperNNova use SN redshift estimates for more accurate SN type predictions. Finally, we explored the impact of variations to our analysis, such as the choice of  $\Omega_m$  prior, bias correction simulations, Sérsic scaling factor, and additional selection cuts to remove incorrect host matches.

We found that the baseline  $w$  shift with perfectly classified type Ia SNe is  $\Delta w = 0.0013 \pm 0.0026$ , and changes in certain properties can increase this to  $|\Delta w| \sim 0.004$ . We also find that the choice of photometric classifier makes an impact on the  $w$  shift: classifiers requiring redshift estimates for prediction tend to misclassify SNe with the wrong redshift, leading to a larger  $w$ -bias. When the CMB prior is replaced with a flat  $\Omega_m$  prior, the  $\Delta w$  value changes to  $-0.062 \pm 0.072$ . Though the  $\Delta w$  uncertainty is larger with the flat  $\Omega_m$  prior, the shift is still consistent with 0 given the associated inflation in uncertainty.

In conclusion, we find that our current estimate on the systematic error associated with host galaxy mismatch is substantially smaller than the statistical error for DES Y5, but as future surveys continue to discover more SNe Ia, we encourage continued study and improvement of the accuracy of host galaxy matching and prevalence of catastrophic errors in redshift.

## Acknowledgements

H.Q., J.L., and M.S. were supported by DOE grant DE-FOA-0002424 and NSF grant AST-2108094. L.G. acknowledges financial support from the Spanish Ministerio de Ciencia e Innovación (MCIN), the Agencia Estatal de Investigación (AEI) 10.13039/501100011033, and the European Social Fund (ESF) "Investing in your future" under the 2019 Ramón y Cajal program RYC2019-027683-I and the PID2020-115253GA-I00 HOSTFLOWS project, from Centro Superior de Investigaciones Científicas (CSIC) under the PIE project 20215AT016, and the program Unidad de Excelencia María de Maeztu CEX2020-001058-M. PW acknowledges support from the Science and Technology Facilities Council (STFC) grant ST/R000506/1. L.K. thanks the UKRI Future Leaders Fellowship for support through

the grant MR/T01881X/1.

This work was completed in part with resources provided by the University of Chicago's Research Computing Center, as well as resources of the National Energy Research Scientific Computing Center (NERSC), a DOE Office of Science User Facility supported by the Office of Science of the U.S. Department of Energy under Contract No. DE-AC02-05CH11231.

Funding for the DES Projects has been provided by the U.S. Department of Energy, the U.S. National Science Foundation, the Ministry of Science and Education of Spain, the Science and Technology Facilities Council of the United Kingdom, the Higher Education Funding Council for England, the National Center for Supercomputing Applications at the University of Illinois at Urbana-Champaign, the Kavli Institute of Cosmological Physics at the University of Chicago, the Center for Cosmology and Astro-Particle Physics at the Ohio State University, the Mitchell Institute for Fundamental Physics and Astronomy at Texas A&M University, Financiadora de Estudos e Projetos, Fundação Carlos Chagas Filho de Amparo à Pesquisa do Estado do Rio de Janeiro, Conselho Nacional de Desenvolvimento Científico e Tecnológico and the Ministério da Ciência, Tecnologia e Inovação, the Deutsche Forschungsgemeinschaft and the Collaborating Institutions in the Dark Energy Survey.

The Collaborating Institutions are Argonne National Laboratory, the University of California at Santa Cruz, the University of Cambridge, Centro de Investigaciones Energéticas, Medioambientales y Tecnológicas-Madrid, the University of Chicago, University College London, the DES-Brazil Consortium, the University of Edinburgh, the Eidgenössische Technische Hochschule (ETH) Zürich, Fermi National Accelerator Laboratory, the University of Illinois at Urbana-Champaign, the Institut de Ciències de l'Espai (IEEC/CSIC), the Institut de Física d'Altes Energies, Lawrence Berkeley National Laboratory, the Ludwig-Maximilians Universität München and the associated Excellence Cluster Universe, the University of Michigan, NSF's NOIRLab, the University of Nottingham, The Ohio State University, the University of Pennsylvania, the University of Portsmouth, SLAC National Accelerator Laboratory, Stanford University, the University of Sussex, Texas A&M University, and the OzDES Membership Consortium.

Based in part on observations at Cerro Tololo Inter-American Observatory at NSF's NOIRLab (NOIRLab Prop. ID 2012B-0001; PI: J. Frieman), which is managed by the Association of Universities for Research in Astronomy (AURA) under a cooperative agreement with the National Science Foundation.

The DES data management system is supported by the National Science Foundation under Grant Numbers AST-1138766 and AST-1536171. The DES participants from Spanish institutions are partially supported by MICINN under grants ESP2017-89838, PGC2018-094773, PGC2018-102021, SEV-2016-0588, SEV-2016-0597, and MDM-2015-0509, some of which include ERDF funds from the European Union. IFAE is partially funded by the CERCA program of the Generalitat de Catalunya. Research leading to these results has received funding from the European Research Council under the European Union's Seventh Framework Program (FP7/2007-2013) including ERC grant agreements 240672, 291329, and 306478. We acknowledge support from the Brazilian Instituto Nacional de Ciência e Tecnologia (INCT) do e-Universo (CNPq grant 465376/2014-2).

This manuscript has been authored by Fermi Research Alliance, LLC under Contract No. DE-AC02-07CH11359 with the U.S. Department of Energy, Office of Science, Office of High Energy Physics.

## CHAPTER 5

# Photo- $z$ SNthesis: Converting Type Ia Supernova Lightcurves to Redshift Estimates via Deep Learning

### Abstract

Upcoming photometric surveys will discover tens of thousands of Type Ia supernovae (SNe Ia), vastly outpacing the capacity of our spectroscopic resources. In order to maximize the science return of these observations in the absence of spectroscopic information, we must accurately extract key parameters, such as SN redshifts, with photometric information alone. We present Photo- $z$ SNthesis, a convolutional neural network-based method for predicting full redshift probability distributions from multi-band supernova lightcurves, tested on both simulated Sloan Digital Sky Survey (SDSS) and Vera C. Rubin Legacy Survey of Space and Time (LSST) data as well as observed SDSS SNe. We show major improvements over predictions from existing methods on both simulations and real observations as well as minimal redshift-dependent bias, which is a challenge due to selection effects, e.g. Malmquist bias. Specifically, we show a  $61\times$  improvement in prediction bias  $\langle\Delta z\rangle$  on PLAsTiCC simulations and  $5\times$  improvement on real SDSS data compared to results from a widely used photometric redshift estimator, LCFIT+Z. The PDFs produced by this method are well-constrained and will maximize the cosmological constraining power of photometric SNe Ia samples.

### 5.1. Introduction

The study of Type Ia supernovae (SNe Ia) has proven to be a crucial tool in modern cosmology, providing insight into the expansion rate of the universe and the properties of dark energy (Riess, 1998; Perlmutter et al., 1999). Measuring the cosmological redshift of each SN, a proxy quantity for recession velocity, is essential for accurate estimation of the distance-redshift relation and resulting cosmological analyses. However, traditional methods of measuring redshifts are time-consuming and resource-intensive, primarily relying on spectroscopic observations of the SNe themselves or their host galaxies. Using host galaxy redshifts can also lead to cosmological biases if the host is

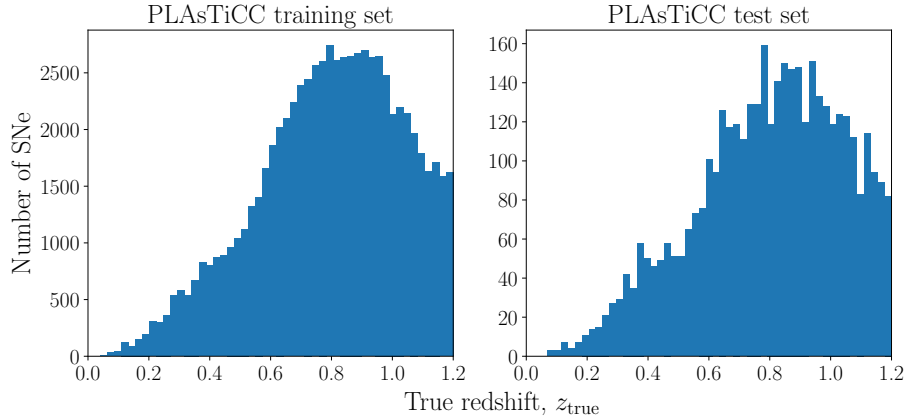


Figure 5.1: True redshift distribution of the 73,620 simulated SNe Ia in the LSST (PLAsTiCC) training dataset (left) and 4,057 simulated SNe Ia in the test dataset (right).

incorrectly identified (Qu et al., in prep).

Most SNe Ia cosmological analyses so far have relied on SN spectra for SN type confirmation as well as redshift information, but only with samples of up to  $\sim 1,500$  SNe (e.g. Abbott et al., 2019c; Brout et al., 2022). Spectroscopic follow-up of all SNe Ia candidates or their host galaxies will become infeasible with future sky surveys such as the Legacy Survey of Space and Time at the Vera C. Rubin Observatory (LSST), which will discover tens of thousands of SNe Ia over the course of their observational lifetimes (LSST Science Collaboration et al., 2009b). Recent improvements in photometric SN classification (e.g. Möller and de Boissière, 2020b; Qu et al., 2021) have drastically reduced the likelihood of non-Ia contamination in photometric SNe Ia samples and enabled cosmological analyses with photometrically classified samples (Vincenzi et al., 2023). However, spectroscopic redshifts were still available for the host galaxies of these photometrically confirmed SNe Ia and were used as the SN redshifts. SN redshift estimates independent of host galaxy redshift can also serve as an independent cross-check for host galaxy association, ensuring accurate studies of host galaxy correlations and corrections for the mass step (e.g. Rigault et al., 2020). Accurate photometric redshift estimates for SNe that are independent of host galaxy spectroscopic redshifts are thus the final building block required to enable SN Ia cosmology for the LSST era.

Cosmological inference frameworks that account for the inflated uncertainties from photometric

redshifts are currently being developed. Mitra et al. (2022); Dai et al. (2018) show promising results with simulated LSST samples and SN photometric redshifts fitted using host galaxy redshift priors. In particular, Dai et al. (2018) recovers a fitted  $\Omega_m$  value consistent with the input cosmology when using SN photo- $z$ s fitted with a host galaxy photo- $z$  prior. Mitra et al. (2022) shows a 2% effect on fitted cosmological parameters of an assumed systematic uncertainty due to the use of SN photo- $z$ s of 0.01. Using observed data from the Dark Energy Survey, Chen et al. (2022) performed a cosmological analysis using a subset of  $\sim 100$  SNe Ia hosted by galaxies in the redMaGiC catalog, which have both photometric and spectroscopic redshifts. The difference in best-fit cosmological parameters between using spectroscopic and photometric redshifts was found to be minimal,  $\Delta w \sim 0.005$ . redMaGiC galaxies were chosen for this analysis due to their particularly well-constrained photometric redshift estimates, which is not representative of the full population of SN host galaxies. However, even with a sound cosmological inference framework, galaxy photometric redshifts are often inaccurate or plagued with large uncertainties, and requiring host galaxy information to produce SN photometric redshift estimates may introduce additional biases.

These issues with traditional redshift determination along with the development of a cosmological framework for photometric redshifts has led to a growing interest in alternative techniques for predicting redshifts for Type Ia supernovae. In this work, we introduce a novel machine learning algorithm to predict full redshift probability distributions for Type Ia supernovae based solely on lightcurve data. Our estimator harnesses the constraining power on redshift of the SN lightcurves and can additionally provide an independent cross-check on host galaxy matches, minimizing mismatch rates. We present a detailed analysis of our model, including its accuracy and limitations, and discuss the potential implications of our findings for future cosmological studies.

### 5.1.1. Photo- $z$ Estimation

Most of the existing literature on photometric redshift estimation is on galaxy photo- $z$ s. These approaches generally use either (1) a training set of galaxy photometric observables, such as colors and magnitudes, to determine a mapping to spectroscopic redshifts (e.g. Brunner et al., 1997); or (2) template fitting, in which observed properties are compared with redshifted template spec-



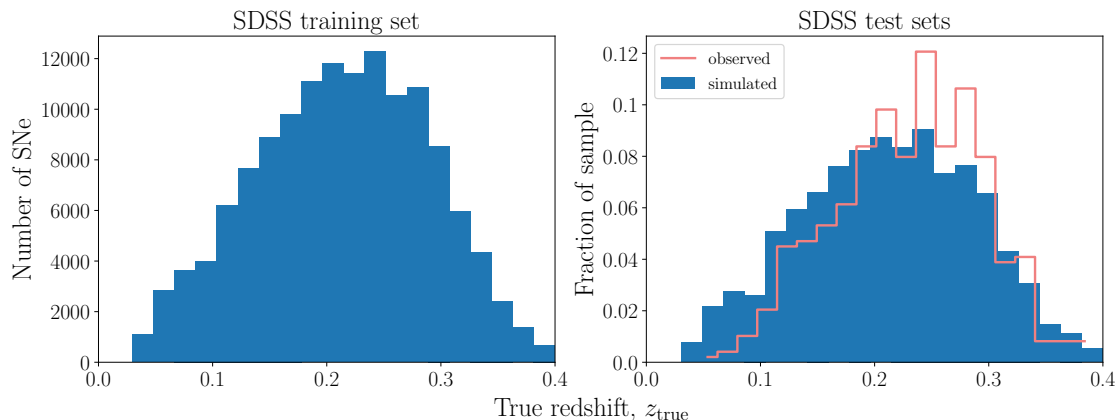


Figure 5.2: True redshift distribution of the 135,521 simulated SNe Ia in the SDSS training dataset (left) and the 5,274 simulated SNe Ia and 489 observed photometrically confirmed SNe Ia in the SDSS test sets (right).

tra to determine the best fit redshift value (e.g., Benitez, 2000). There have also been successful machine learning-based galaxy photo- $z$  models developed, e.g. D’Isanto, A. and Polsterer, K. L. (2018); Pasquet et al. (2018) using convolutional neural networks on galaxy images, and Buchs et al. (2019) using a self-organizing map to relate color-magnitude space and redshifts.

Photometric redshift estimation for SNe uses many of the same techniques. Kim and Miquel (2007) used the SALT2 lightcurve model (Guy et al., 2007) to determine photometric redshifts and distances as well as uncertainties using the Fisher information matrix. Palanque-Delabrouille et al. (2010) and Kessler et al. (2010a, LCFIT+Z) extended the SALT2 lightcurve fit to include redshift as a fitted parameter, and incorporating the host galaxy redshift as a prior. These approaches find the best fit redshift by comparing photometric observables to those expected from the SALT2 model via  $\chi^2$  minimization. An analytic approach was presented in Wang et al. (2015) which assumed a functional form for the redshifts as a function of multi-band photometric fluxes and fit for free parameters using a training set of SNe Ia with spectroscopic redshifts. de Oliveira et al. (2022) applied machine learning techniques to this problem, performing regression using features obtained from principal component analysis. However, many of these results suffer from redshift-dependent bias, in which photo- $z$ s for high-redshift SNe are systematically underestimated (see e.g. Figure 6 of Kessler et al. (2010a), Figure 7 of de Oliveira et al. (2022)). Most of these stud-

ies also estimate a redshift value and uncertainty rather than the full probability density function (PDF).

### 5.1.2. Overview

In this work we present Photo- $z$ SNthesis, a convolutional neural network model that uses multi-band photometry to predict a full redshift PDF. Our approach uses the raw photometric data and does not require any manual feature engineering to determine the most predictive features. We evaluated Photo- $z$ SNthesis using LSST and SDSS simulated SNe Ia as well as the SDSS photometric SN Ia sample, and show that our redshift predictions have low scatter and suffer from minimal redshift-dependent bias on all tested SN samples. Our results are a promising step towards precision photometric SN Ia cosmology.

We introduce the simulated and observed data samples used for evaluation in §2, as well as the preprocessing step used to transform multi-band lightcurves into convolutional neural network inputs. In §3, we describe the model architecture and training strategy. We present results, comparisons with LCFIT+Z, and further experiments in §4, and conclude in §5.

## 5.2. Data

### 5.2.1. Data Sources

We present results on simulated SNe Ia from two surveys: LSST (Ivezić et al., 2019b) and the SDSS-II SN survey (Frieman et al., 2008). We also demonstrate that our model generalizes well to an observed photometric SN Ia dataset by showing photo- $z$  predictions on SDSS SNe classified as type Ia by SuperNNova (Möller and de Boissière, 2020b). We use the SuperNova ANALYSIS software (SNANA, Kessler et al., 2009c) to produce all simulated SN lightcurves used in this work.

#### **Simulated LSST SNe Ia (PLAsTiCC)**

LSST is a ground-based dark energy survey program that will discover millions of SNe over the 10 year survey duration. The 8.4m Simonyi Survey optical telescope at the Rubin Observatory uses a state-of-the-art 3200 megapixel camera with a 9.6 deg<sup>2</sup> field of view that will provide deeper and wider views of the universe with unprecedented quality. LSST will observe nearly half the night

sky each week to a depth of 24<sup>th</sup> magnitude in *ugrizY* photometric bands spanning wavelengths from ultraviolet to near-infrared.

We simulate LSST-like observations of SNe Ia in *ugrizY* photometric bands following the model, rates, and LSST observing conditions developed for the PLAsTiCC dataset (The PLAsTiCC team et al., 2018b; Kessler et al., 2019a) for  $0.05 < z < 1.2$ . We use the SALT2 lightcurve model (Guy et al., 2007) with training parameters derived from the Joint Lightcurve Analysis (Betoule et al., 2014) extended into the ultraviolet and near-infrared by Hounsell et al. (2018) following the procedure described in Pierel et al. (2018d). While PLAsTiCC included two LSST observing strategies, the Deep Drilling Fields (DDF) as well as the Wide-Fast-Deep (WFD), we simulate only the DDF subsample. We coadd all observations within the same night, following PLAsTiCC, resulting in observations that are  $\sim 2.5\times$  more frequent and  $\sim 1.5$  mag deeper than the WFD sample. Though we focused on the DDF sample for this work, evaluating the performance of Photo-*z*SNthesis on WFD simulations is an important direction for future studies.

As PLAsTiCC is the name of the dataset we emulated while LSST is the survey we simulate, we will use both interchangeably to denote "simulated LSST SN lightcurves following the PLAsTiCC dataset".

### **Simulated SDSS SNe Ia**

The SDSS-II Supernova Survey identified and measured light curves for intermediate-redshift ( $0.05 < z < 0.4$ ) SNe Ia using repeated five-band (*ugriz*) imaging of Stripe 82, a stripe  $2.5^\circ$  wide centered on the celestial equator in the Southern Galactic Cap. The primary instrument for this survey is the SDSS CCD camera mounted on a dedicated 2.5m telescope at Apache Point Observatory, New Mexico. Over the three observing seasons between 2005 and 2007, SDSS discovered 10,258 transient and variable objects, with 536 spectroscopically confirmed SNe Ia and an additional 907 photometrically classified SNe Ia candidates (Sako et al., 2018b). Frieman et al. (2008) provides an in-depth review of the SDSS-II SN survey.

We simulate SDSS SNe Ia in *ugriz* photometric bands using the SALT3 model described by Kenworthy et al.

(2021) due to its improved wavelength range coverage in the near infrared, allowing  $z$  band observations to be simulated for SNe at low redshifts. We additionally extend this model to 500Å to simulate  $u$  band observations at high redshifts. We use simulated observing conditions from Kessler et al. (2013c) and host galaxy spectroscopic detection efficiency from Kessler et al. (2009c). We simulate a *photometric* SDSS SNe Ia dataset using the host spectroscopic detection efficiency rather than a SN spectroscopic detection efficiency to demonstrate the performance of Photo- $z$ SNthesis on the practical use case of a photometric sample.

### Observed SDSS SNe Ia

In addition to simulated SNe, we test Photo- $z$ SNthesis on SDSS lightcurves from Sako et al. (2018b) classified by SuperNNova (Möller and de Boissière, 2020b) as likely SNe Ia, defined as SNe with SNIa probability  $P_{\text{Ia}} \geq 0.5$ . "True" redshifts  $z_{\text{true}}$  for the sample are from spectra of the SNe themselves or their host galaxies. Details on the training data and training procedure for the SuperNNova model used here can be found in Popovic et al., in prep. 489 lightcurves remain after the selection cuts described in Sections 5.2.1 and 5.2.2. The number of SDSS lightcurves remaining after each set of cuts is shown in Table 5.1.

### Lightcurve Selection

We apply basic selection cuts to the simulated LSST sample. We require

- at least 5 observations of each SN
- signal-to-noise ratio (SNR)  $> 3$  for at least one observation each in 2 of the *griz* filters

We apply selection cuts, following Popovic et al. (2020), to both the simulated and observed SDSS data to remove poor quality lightcurves. We define a rest-frame age,  $T_{\text{rest}} = (t - t_{\text{peak}})/(1 + z)$ , where  $t$  is the observation date,  $t_{\text{peak}}$  is the estimated epoch of SN peak brightness from SNANA, and  $z$  is the redshift of the event. We require

- $0 < T_{\text{rest}} < 10$
- SNR  $> 5$  for at least one observation each in 2 of the *griz* filters

Cut	Number of SNe
Full sample	10,258
Lightcurve selection (§5.2.1)	2,044
Likely SNe Ia ( $P_{\text{Ia}} \geq 0.5$ )	1,037
SALT fit cuts (§5.2.2)	555
Successful LCFIT+Z fit	489

Table 5.1: Number of SDSS lightcurves remaining after each selection cut. We evaluate Photo- $z$ SNthesis on the remaining 489 SNe.

We additionally require SNe in the SDSS data to have a spectroscopic redshift from either the SN spectrum or the SN host galaxy.

### 5.2.2. Data Preprocessing

All SNe in all datasets are fit with a  $\chi^2$ -minimization program included in SNANA to determine several restframe parameters under the assumption that the event is a SN Ia: the time of SN peak brightness  $t_{\text{peak}}$ , a stretch-like parameter  $x_1$ , a color parameter  $c$ , and the lightcurve normalization parameter  $x_0$ , as well as their uncertainties and covariances (i.e.,  $\sigma_{x_1}$ , etc.). These parameters are used to calculate the distance modulus  $\mu$ , allowing the SNe to be placed on the Hubble diagram. SDSS datasets are fit with the SALT3 model while the LSST dataset is fit with the same extended SALT2 model used for the simulations.

We additionally select only SNe in our datasets that are well-described by the SALT model. These criteria were chosen following those used in past cosmology analyses, e.g. Betoule et al. (2014):

- $|c| < 0.3$
- $|x_1| < 3$
- $\sigma_{x_1} \leq 1$
- $\sigma_{t_{\text{peak}}} \leq 2$

Finally, we choose SNe within the redshift range  $0.01 \leq z \leq 0.4$  for SDSS and  $0.01 \leq z \leq 1.2$  for LSST that have a successful LCFIT+Z (Kessler et al., 2010a) fit, in order to draw direct compar-

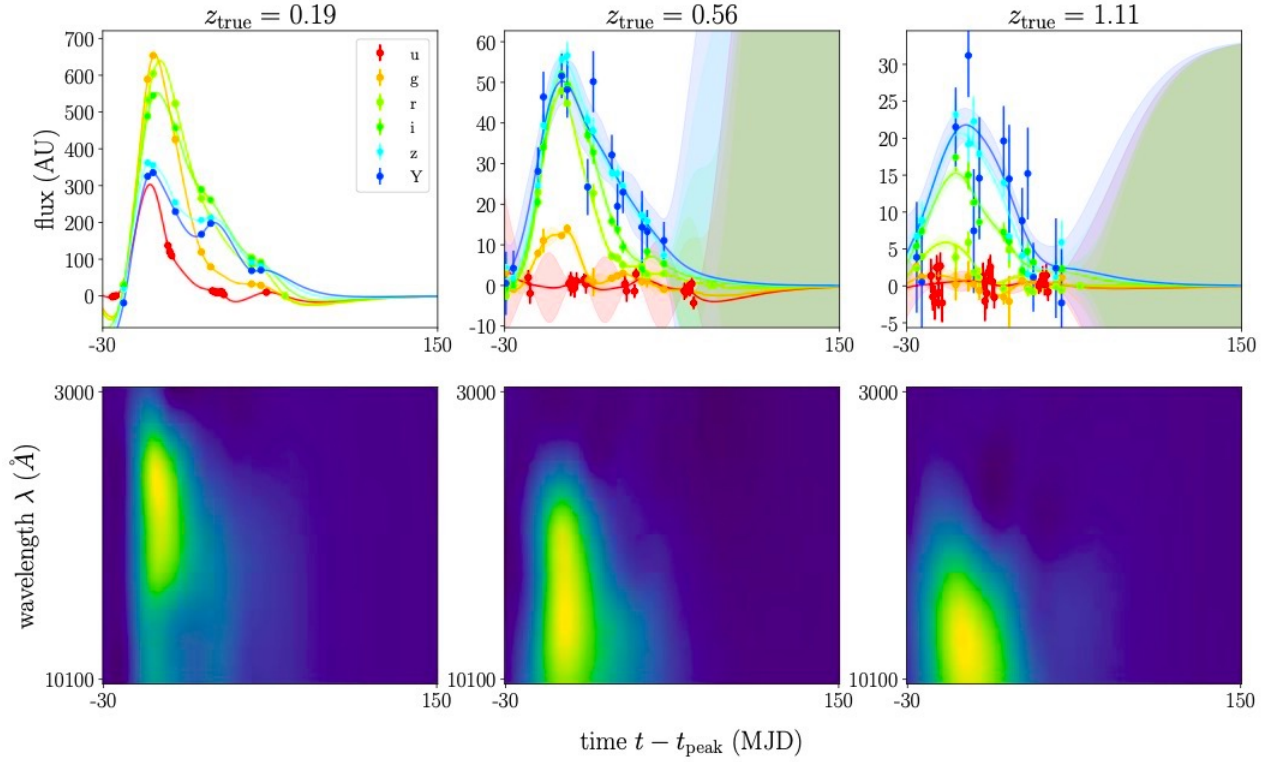


Figure 5.3: Examples of a low (left), medium (middle), and high (right) redshift simulated PLAS-TiCC SN. **(top panel)** The multi-band lightcurves are shown in colored points, with Gaussian process predictions and uncertainties for this lightcurve shown in colored lines and shaded regions, respectively. **(bottom panel)** The flux matrix created from the lightcurve in the top panel (see §5.2.2 for details). Large flux values are colored in yellow while lower flux values are in dark blue. The physical effects of redshifting, including longer wavelengths and longer transient durations, are observed in the flux matrices in the downward (towards higher wavelengths) shift of the yellow high flux region and the increased width of the yellow region with increasing redshift.

isons between the performance of Photo- $z$ SNthesis and LCFIT+Z. A more detailed description of LCFIT+Z can be found in §5.4.1.

146,069 simulated SDSS SNe Ia and 81,734 simulated LSST SNe Ia remain after all cuts, as well as 489 observed SDSS SNe photometrically classified as SNe Ia. The number of observed SDSS lightcurves remaining after each cut is described in Table 5.1. The redshift distributions of the PLAsTiCC training and test datasets after selection cuts are shown in Figure 5.1, while the redshift distributions of the SDSS simulated and observed datasets are shown in Figure 5.2. We note that, while most machine learning classifiers perform better when trained on a dataset with balanced classes (i.e. flat redshift distribution), we found that this was not the case for Photo- $z$ SNthesis. While our simulations are able to generate any artificial redshift distribution, an unphysical one such as a flat distribution could lead to strange artifacts in the dataset, confusing the classifier.

### Lightcurve Preprocessing

To preprocess each lightcurve, we first take observations within the range  $t_{\text{peak}} - 30 \leq t \leq t_{\text{peak}} + 150$ , where  $t_{\text{peak}}$  is the epoch of SN peak brightness estimated by SNANA. This is to ensure the lightcurves contain just the SN and no extraneous information.

We use 2-dimensional Gaussian process (GP) regression to model each SN lightcurve in time ( $t$ ) and wavelength ( $\lambda$ ) space, then use the predictions of the fitted GP on a fixed  $(\lambda, t)$  grid as the input to our neural network model. Modelling lightcurves of astronomical transients using 2D Gaussian processes was originally introduced in Boone (2019a); and Qu et al. (2021, Q21) used the GP models to create “images” from lightcurve data, which is the technique used for this work. Following Q21, we use the Matérn kernel ( $\nu = 3/2$ ) with a fixed  $6000\text{\AA}$  length scale in wavelength space and fit for the time length scale as well as the amplitude using maximum likelihood estimation. This GP model is fit separately to each lightcurve and used to produce a smooth 2D representation of the lightcurve by predicting flux values at each point in a  $(\lambda, t)$  grid. We choose 32 equally spaced points in the range  $3,000\text{\AA} \leq \lambda \leq 10,100\text{\AA}$  ( $\delta\lambda = 221.875\text{\AA}$ ) and 180 points in the range  $t_{\text{peak}} - 30 \leq t \leq t_{\text{peak}} + 150$  ( $\delta t = 1$  day). This produces a  $32 \times 180$  matrix of predicted flux values. We also produce a matrix of prediction uncertainties at each  $\lambda_i, t_j$  of equal size.

We stack the flux and uncertainty matrices depthwise to produce a  $32 \times 180 \times 2$  tensor and divide elementwise by the maximum flux value to constrain all entries to  $[0,1]$ .

We show low, medium, and high redshift examples of PLAsTiCC lightcurves, the fitted GP models and their uncertainties, and the resulting flux matrices in Figure 5.3. Redshifting increases the wavelength of light, which we see in the figure as the yellow (high flux) region moving down (toward  $\lambda = 10, 100\text{\AA}$ ) with increasing redshift. We also expect to observe a longer duration for higher redshift transients, which is evident in the increase in width of the yellow region. This data format is particularly well suited to the redshift prediction task, as we are able to visibly see expected physical results of redshifting in the flux matrices.

### Redshift Preprocessing

The redshift range for each survey is discretized into  $n_z$  discrete and non-overlapping bins ( $0.01 \leq z \leq 0.4, n_z = 50$  for SDSS and  $0.01 \leq z \leq 1.2, n_z = 150$  for LSST). We chose these  $n_z$  values to preserve the approximate width of each redshift bin across surveys ( $\delta z \sim 0.0078$ ). The bin corresponding to the true redshift of each SN is one-hot encoded and passed into the model as the training label.

### 5.3. Model

Photo- $z$ SNthesis is a convolutional neural network model (e.g. LeCun et al., 1989a; Zeiler and Fergus, 2014; Simonyan and Zisserman, 2014a; Krizhevsky et al., 2017) that takes in GP-interpolated lightcurves as well as the GP prediction uncertainties, prepared as described in §5.2.2, and predicts a probability distribution over fine-grained redshift bins. This approach allows us to produce a discretized full PDF over redshift space for each individual SN without any assumptions on the underlying distribution, and has been used in a variety of contexts including image generation (van den Oord et al., 2016) and prediction of precipitation probabilities (Sønderby et al., 2020). Treating this as a categorical classification problem using the cross-entropy loss function has also been shown to accurately approximate Bayesian posterior probabilities (Richard and Lippmann, 1991).



### 5.3.1. Convolutional Neural Networks

The convolutional neural network (CNN) is a class of artificial neural network with properties particularly suited to object and image recognition. It requires fewer trainable parameters than the standard feedforward network due to the convolution operation, learning a single weight matrix for small neighborhoods of the input image. This property is not only parameter-efficient but also imparts CNNs with translation-equivariance, i.e. the same feature shifted by  $n$  pixels will produce the same response shifted by  $n$  pixels. These convolutional layers are paired with pooling layers, which downsample the input to allow for the next set of convolutional layers to learn hierarchically more complex features. CNNs are prized in the machine learning community for being simple yet performant on image recognition benchmark datasets such as ImageNet (Russakovsky et al., 2015).

### 5.3.2. Residual Learning

We implement residual learning (He et al., 2016a) due to its state-of-the-art performance on the ImageNet benchmark at the time of publication as well as its widespread adoption over vanilla CNNs. Residual learning was presented as a solution to the degradation problem in CNNs, in which performance degraded past a certain threshold of network depth. Since the additional layers could simply act as identity mappings and not affect the network performance, He et al. (2016a) decreased the difficulty by not only feeding inputs sequentially through a series of layers, but also adding the inputs back in to the outputs of those layers. This allows the layers to learn the zero mapping rather than the identity mapping. Since these layers are tasked with learning the *residual* with respect to the input, this is known as *residual learning* and the stack of layers is known as a *residual block*. The residual connections in the Photo- $z$ SNthesis architecture are shown as lines curving around each residual block in Figure 5.4.

### 5.3.3. Architecture

Our model (Figure 5.4) takes as input a  $32 \times 180 \times 2$  tensor containing the GP-interpolated lightcurve data on a  $32 \times 180$  grid of wavelength and time values, and the GP uncertainties at each of those points. Table 5.2 shows input and output dimensions of example layers in the model architecture. We also provide the model with the one-hot encoded vector specifying the correct redshift bin as

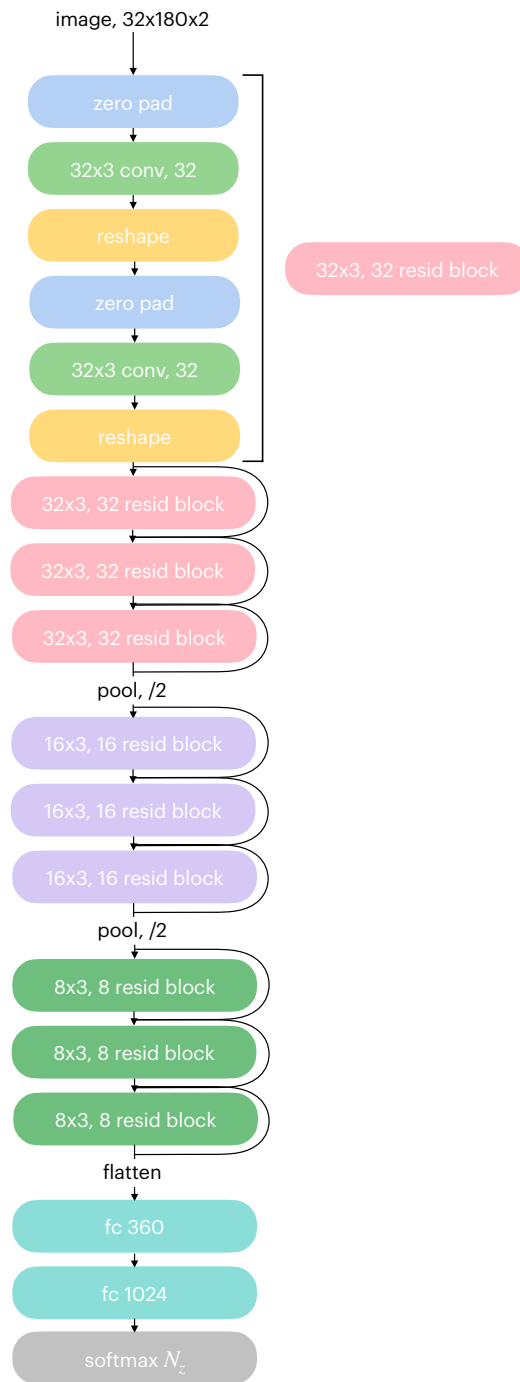


Figure 5.4: The model architecture developed for this work, described in the text in §5.3.3. A layer shown in the figure as “ $h \times d$  conv,  $n_{\text{filters}}$ ” is a 2D convolutional layer with a kernel size of  $h \times d$  and  $n_{\text{filters}}$  filters. Similarly, “ $h \times d, n_{\text{filters}}$  resid block” defines a residual block containing two  $h \times d$  conv,  $n_f$  convolutional layers. “fc  $n_{\text{nodes}}$ ” denotes a fully connected layer with  $n_{\text{nodes}}$  nodes. The pooling layers apply max pooling, downsampling both the height and width by 2. The output softmax layer has  $N_z$  nodes,  $N_z = 50$  for SDSS and  $N_z = 150$  for LSST.

Layer	Input Shape	Output Shape
Zero Padding	$32 \times 180 \times 2$	$32 \times 182 \times 2$
$32 \times 3$ Convolutional	$32 \times 182 \times 2$	$180 \times 32 \times 1$
Reshape	$180 \times 32 \times 1$	$32 \times 180 \times 1$
Max Pooling	$32 \times 180 \times 1$	$16 \times 90 \times 1$

Table 5.2: Description of example layers in the model architecture.

the training label.

The input is zero-padded on both sides to  $32 \times 182 \times 2$  to ensure that feature maps output by the convolutional layers retain the original shape, then passed through a convolutional layer with 32 filters and kernel size  $32 \times 3$ . Since the convolutional kernel determines the receptive field of each unit in the layer, we choose a convolutional kernel that spans the wavelength space to allow each unit to learn from all wavelengths simultaneously while preserving the linearity of time. The output of this convolutional layer is  $1 \times 180 \times 32$ , which we then reshape back to  $32 \times 180 \times 1$ . This first feature map is now passed through a series of residual blocks.

Each residual block contains two convolutional blocks, each consisting of a ReLU nonlinearity, batch normalization, and the zero-padding, convolutional layer, and reshaping layer identical to the ones described above. The input to each residual block is then added to the output as described in §5.3.2. After each series of three residual blocks, the output is passed through a  $2 \times 2$  max-pooling layer, downsampling the height and width of the output by a factor of 2.

Finally, the output is flattened and passed through a fully connected layer with 1,024 hidden nodes, which connects to the final softmax layer. The nodes in this layer correspond to redshift bins, thus it has 50 nodes for processing SDSS data and 150 for LSST data. The array of output probabilities is interpreted as the probability density over redshifts for our input SN.

#### 5.3.4. Calibration

We also performed temperature scaling (Guo et al., 2017) to ensure that the probabilities output by Photo- $z$ SNthesis are properly calibrated. In this process, we learn a single “temperature” parameter used to scale the output probabilities.

Before scaling, the output probabilities  $\mathbf{p}_i$  for input SN  $i$  are derived from the softmax function

$$\mathbf{p}_i^{(k)} = \sigma_{\text{SM}}(\mathbf{q}_i)^{(k)} = \frac{\exp(\mathbf{q}_i^{(k)})}{\sum_{j=1}^K \exp(\mathbf{q}_i^{(j)})} \quad (5.1)$$

where  $\mathbf{q}_i$  is the vector of network logits corresponding to SN  $i$ , i.e. the output of the final hidden layer of the network. The temperature parameter  $T$  is learned by minimizing the cross-entropy loss between the one-hot encoded labels and the scaled probabilities,  $\mathbf{p}'_i$ ,

$$\mathbf{p}'_i = \sigma_{\text{SM}}(\mathbf{q}_i/T) \quad (5.2)$$

Reliability diagrams (DeGroot and Fienberg, 1983; Niculescu-Mizil and Caruana, 2005) and the expected calibration error statistic (ECE, Naeini et al., 2015) are common evaluation methods for calibration. Reliability diagrams show the prediction accuracy as a function of *confidence*, which is defined as the probability associated with the predicted class:  $\max(\mathbf{p}_i)$ . A reliability diagram for a perfectly calibrated classifier will show the identity function, and any deviation from a perfect diagonal is a sign of miscalibration. The reliability diagram before and after temperature scaling for the PLAsTiCC model is shown in Figure 5.5. The scaled probabilities are much closer to the diagonal, representing a significant improvement in calibration.

ECE is a weighted average of the difference between the accuracy and the confidence in bins of confidence values. ECE is more precisely defined as

$$\text{ECE} = \sum_{m=1}^M \frac{|B_m|}{N} |\text{acc}(B_m) - \text{conf}(B_m)| \quad (5.3)$$

where  $B_m$  is the  $m^{\text{th}}$  confidence bin and  $N$  is the total number of samples in the dataset. Prior to temperature scaling, the ECE for the PLAsTiCC model probabilities was 0.24, which improved to 0.08 after scaling.

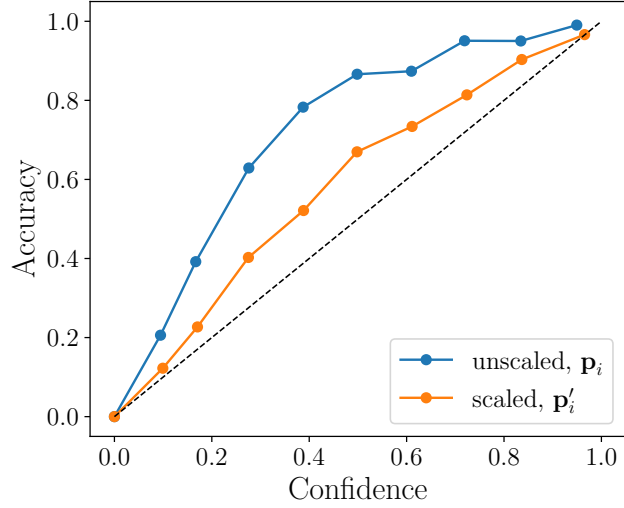


Figure 5.5: Reliability diagram showing PLAsTiCC model calibration before and after temperature scaling.

### 5.3.5. Implementation Details

We split both the SDSS and LSST datasets into 90% training, 5% validation, and 5% test datasets and trained both models with batch sizes of 2048 for 750 epochs. We minimize the cross-entropy loss function with the Adam optimizer (Kingma and Ba, 2014) with an initial learning rate of  $1e-3$  that is halved after 25 epochs of no improvement in the validation loss. The total number of trainable parameters in the SDSS model is 451,654 and 554,154 for the LSST model due to the difference in number of redshift bins and resulting difference in output layer size. To prevent overfitting, we use a weight decay of  $1e-3$  as well as dropout layers (Hinton et al., 2012). Calibration was performed with the validation set of both datasets and with an initialization of  $T = 1$ . We minimize a cross-entropy loss function using Adam and find  $T_{\text{SDSS}} = 0.82$  and  $T_{\text{LSST}} = 0.64$ .

## 5.4. Results and Discussion

Examples of lightcurves and their corresponding predicted redshift PDFs are shown in Figure 5.6. We chose spectroscopically confirmed SDSS SNe Ia lightcurves, and selected a high accuracy ( $\Delta z < 0.005$ ,  $\Delta z \equiv \frac{z_{\text{pred}} - z_{\text{true}}}{1 + z_{\text{true}}}$ ), medium accuracy ( $0.01 \leq \Delta z \leq 0.05$ ), and an outlier ( $\Delta z > 0.05$ ) example.

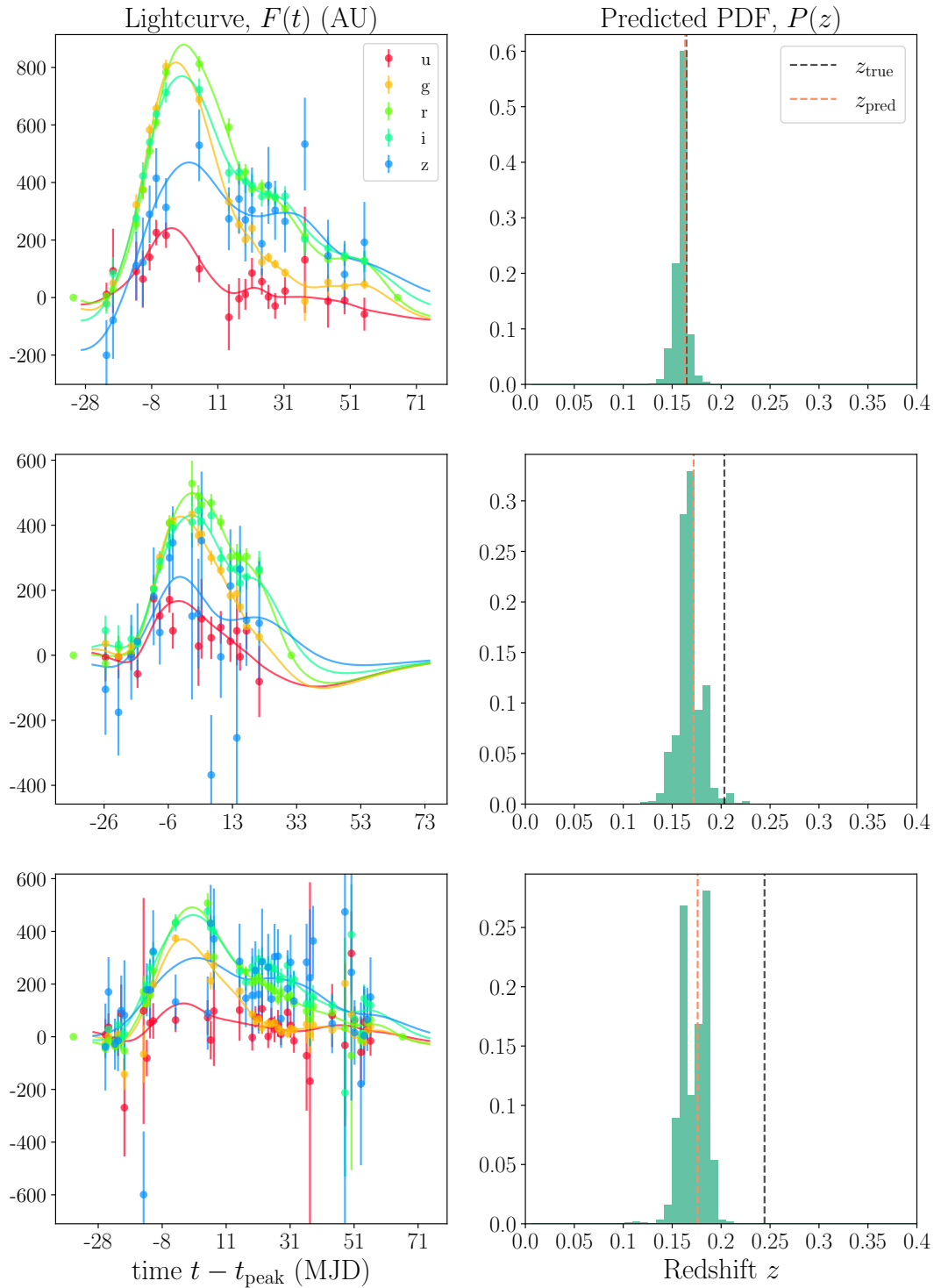


Figure 5.6: Examples of a high accuracy ( $\Delta z < 0.005$ , top), medium accuracy ( $0.01 \leq \Delta z \leq 0.05$ , middle), and outlier ( $\Delta z > 0.05$ , bottom) lightcurve and Gaussian process fit from the SDSS spectroscopic sample and their predicted PDFs. The true (spectroscopic) redshift is shown in the black dotted line, while the predicted redshift (mean(PDF)) is shown in orange. The medium and poor accuracy lightcurves have larger errors and scatter than the high accuracy lightcurve, and the low accuracy lightcurve appears to have much fewer points.

### 5.4.1. Evaluation Metrics and Basis for Comparison

#### Point Estimates and Metrics

Although full photometric redshift PDFs are preferred for further statistical analyses (i.e. cosmological analyses), point estimates can also be computed from each PDF. We require these point estimates to evaluate our model performance against the true redshift values. We compare two possible methods to condense a PDF into a point estimate:

$$\text{mean}(\text{PDF}) = \frac{1}{2} \sum_i p(Z_i) \frac{[Z_i]^2 - [Z_i]}{[Z_i] - [Z_i]} \quad (5.4)$$

where  $Z$  represents the vector of redshift bins,  $[Z_i]$  the right edge of bin  $i$ ,  $[Z_i]$  the left edge of bin  $i$ , and  $p(Z_i)$  the output probability assigned by the model to bin  $i$ ; and

$$\text{max}(\text{PDF}) = \tilde{Z}_{\text{argmax}_i(p(Z_i))} \quad (5.5)$$

where  $\tilde{Z}$  represents the array of midpoints of the redshift bins  $Z$ . Taking the weighted mean is a common summary statistic for PDFs, while taking the bin with maximum probability as the predicted output is typical for classification tasks. As shown in Tables 5.3 and 5.4 and Figures 5.7 and 5.9, the two methods give similar results with  $\text{mean}(\text{PDF})$  performing slightly better on the real SDSS dataset, and thus we use the mean point estimate for Figures 5.8, 5.10, 5.11, 5.12, and 5.13.

We compute the following metrics for both of our point estimates, following e.g. Pasquet et al. (2018):

- the residuals  $\Delta z \equiv \frac{z_{\text{pred}} - z_{\text{true}}}{1 + z_{\text{true}}}$ ,
- the bias  $\langle \Delta z \rangle$ ,
- the mean absolute deviation  $\sigma_{\text{MAD}} = 1.4826 \times \text{median}(|\Delta z - \text{median}(\Delta z)|)$ ,
- the fraction of outliers  $\eta$  with  $|\Delta z| > 0.05$ .

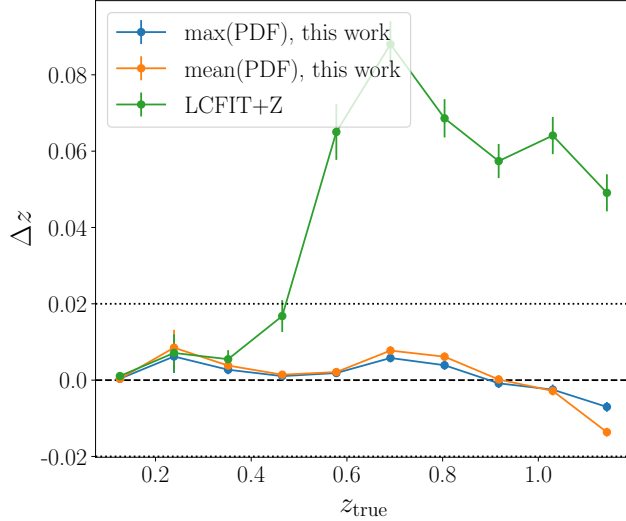


Figure 5.7: Mean binned residuals  $\Delta z$  as a function of true redshift  $z_{\text{true}}$  for the PLAsTiCC simulated SNe Ia test set. Predictions from our model have much lower biases as well as scatter compared to predictions from LCFIT+Z. The max(PDF) and mean(PDF) point estimates for our model also agree quite well, resulting in similar  $\Delta z$  values. Dotted lines are plotted at  $\Delta z = \pm 0.02$  for reference.

We evaluate Photo- $z$ SNthesis using these metrics on the PLAsTiCC dataset as well as the simulated and observed SDSS datasets, and show the results in Tables 5.3 and 5.4.

### Comparison with LCFIT+Z

LCFIT+Z (Kessler et al., 2010a) is an extension of the lightcurve fitting code described in §5.2.1 that treats redshift as an additional free parameter. It determines the best fit lightcurve parameters by minimizing  $\chi^2$  values of the observed and model fluxes, which are computed as a function of the free parameters (4 lightcurve parameters  $t_{\text{peak}}$ , stretch  $x_1$ , color  $c$ , flux normalization  $x_0$ ; and redshift  $z_{\text{phot}}$ ). LCFIT+Z is actively used for recent and ongoing experiments performing full cosmological analyses with photometric redshifts (e.g. Dai et al., 2018; Mitra et al., 2022). LCFIT+Z produces point estimates with uncertainties as opposed to a full PDF, so we perform comparisons using our point estimates.

We compare our results with LCFIT+Z as opposed to other SN photometric redshift estimators (e.g., Wang et al., 2015; de Oliveira et al., 2022) due to its demonstrated performance, widespread use, and integration into SNANA. We run LCFIT+Z on the same datasets used to evaluate our



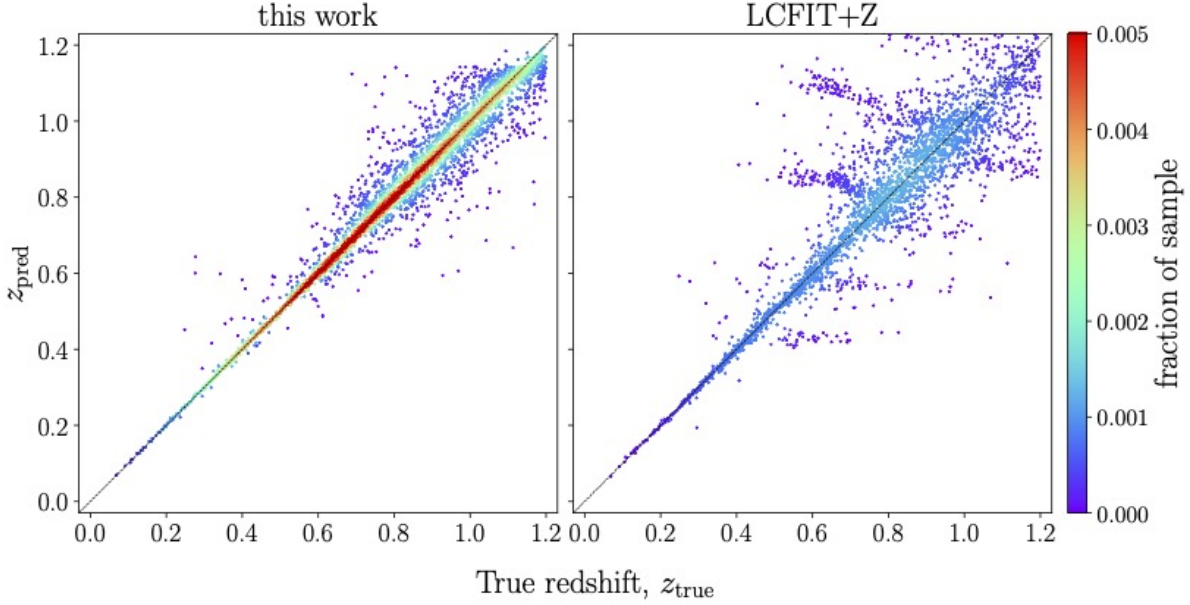


Figure 5.8: Predicted vs. true redshifts for the PLAsTiCC simulated SNe Ia sample colored by the fraction of each sample represented by each point. **(left)** Predictions from Photo- $z$ SNthesis described in this work, **(right)** predictions from LCFIT+Z.

model, enabling a direct comparison. Note that most documented uses of LCFIT+Z place a prior on the redshift fit using the redshift of the SN host galaxy, resulting in much more constrained fits. However, since (1) host spectroscopic redshifts are unavailable in future survey environments, and (2) to draw direct comparisons with Photo- $z$ SNthesis, which does not require any host galaxy information, we omit the host galaxy redshift prior when running LCFIT+Z. In order to compare how these methods perform using all available information in the photometric survey era, we test Photo- $z$ SNthesis and LCFIT+Z with host galaxy *photometric* redshift priors in Section 5.4.4.

#### 5.4.2. LSST (PLAsTiCC) Results

We evaluate our model and our baseline for comparison, LCFIT+Z, on a test set of 4,057 simulated PLAsTiCC-like lightcurves with true redshift distribution shown in the right panel of Figure 5.1. The values of the evaluation metrics for results from this work as well as LCFIT+Z are shown in Table 5.3. The two methods for obtaining point estimates from Photo- $z$ SNthesis PDFs, mean and max, give similar results, though the mean point estimates have a degraded  $\sigma_{\text{MAD}}$  value compared to the max point estimates but a smaller outlier rate. However, the differences between mean and

Metric	this work		LCFIT+Z
	mean	max	
bias $\langle \Delta z \rangle$	0.00095	<b>0.00075</b>	0.058
$\sigma_{\text{MAD}}$	0.0081	<b>0.0025</b>	0.0450
outlier rate $\eta$	<b>3.87%</b>	4.24%	32.3%

Table 5.3: Evaluation metrics computed for the PLAsTiCC test dataset for both the mean(PDF) and max(PDF) point estimates for our model as well as LCFIT+Z. The best result for each metric is shown in bold.

max point estimates are orders of magnitude smaller than the improvement we see relative to LCFIT+Z. The mean gives a  $\sim 3.2\times$  larger result than max on  $\sigma_{\text{MAD}}$ , compared with a  $\sim 180\times$  larger result from LCFIT+Z.

We show the mean binned residuals,  $\Delta z$ , as a function of true redshift for our model and LCFIT+Z in Figure 5.7. We see that while the residuals of our model and LCFIT+Z match quite well up to  $z_{\text{true}} \sim 0.4$ , LCFIT+Z has a tendency to dramatically overestimate at higher redshifts. We also see that the spread within each residual bin in LCFIT+Z results is much larger, as shown in the size of the error bars on each point. In contrast, our model shows a relatively flat  $\Delta z$  over the full redshift range with minimal redshift-dependent bias, which has not been achieved by other SN photometric redshift estimators.

Figure 5.8 more clearly shows the spread of predicted redshifts, where  $z_{\text{pred}}$  is calculated as the mean(PDF) for our model. The predictions produced by our model (left panel) lie much closer to the  $z_{\text{pred}} = z_{\text{true}}$  line with approximately equal amounts of scatter on either side, reinforcing the minimal redshift-dependent bias shown in Figure 5.7. The dark red area along the  $z_{\text{pred}} = z_{\text{true}}$  line also indicates that most of the sample is localized there. The LCFIT+Z results (right panel) have much larger spread and little localization, as evidenced by the lack of red in the plot.

#### 5.4.3. SDSS Results

We evaluate our model and LCFIT+Z on a test set of 5,274 simulated SDSS lightcurves and 489 real observed SDSS lightcurves with true redshift distributions shown in the right panel of Figure 5.2.

Table 5.4 shows the evaluation metrics calculated with the mean and max point estimates on the

Metric	SDSS simulated			SDSS real		
	this work (mean)	this work (max)	LCFIT+Z	this work (mean)	this work (max)	LCFIT+Z
bias $\langle \Delta z \rangle$	<b>7.8e-5</b>	0.00073	0.023	<b>0.0050</b>	0.0052	0.023
$\sigma_{\text{MAD}}$	0.011	<b>0.010</b>	0.028	<b>0.018</b>	0.020	0.041
outlier rate $\eta$	<b>0.85%</b>	1.16%	19.9%	<b>5.14%</b>	5.78%	26.1%

Table 5.4: Evaluation metrics computed for the SDSS simulated and real test datasets for both the mean(PDF) and max(PDF) point estimates for our model as well as LCFIT+Z. The best result for each metric and dataset is shown in bold.

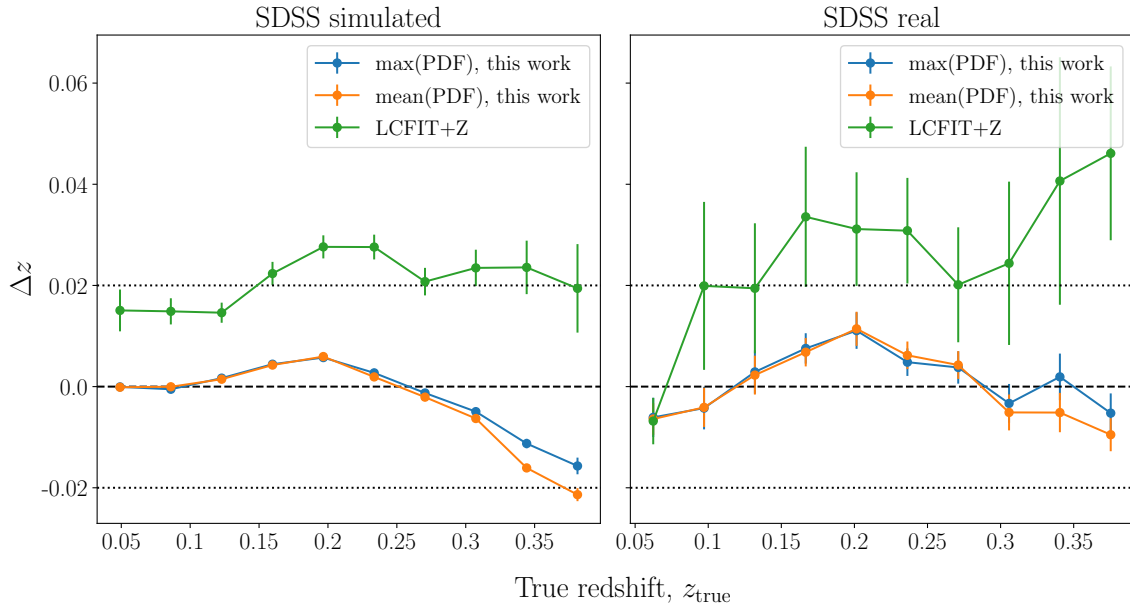


Figure 5.9: Mean binned residuals  $\Delta z$  as a function of true redshift  $z_{\text{true}}$  for the SDSS simulated and real SNe Ia samples. Predictions from this work have much lower biases as well as scatter compared to predictions from LCFIT+Z. We also show that two common methods of condensing redshift PDFs into point estimates, max(PDF) and mean(PDF), resulting in similar errors for our model. Dotted lines are plotted at  $\Delta z = \pm 0.02$  for reference.

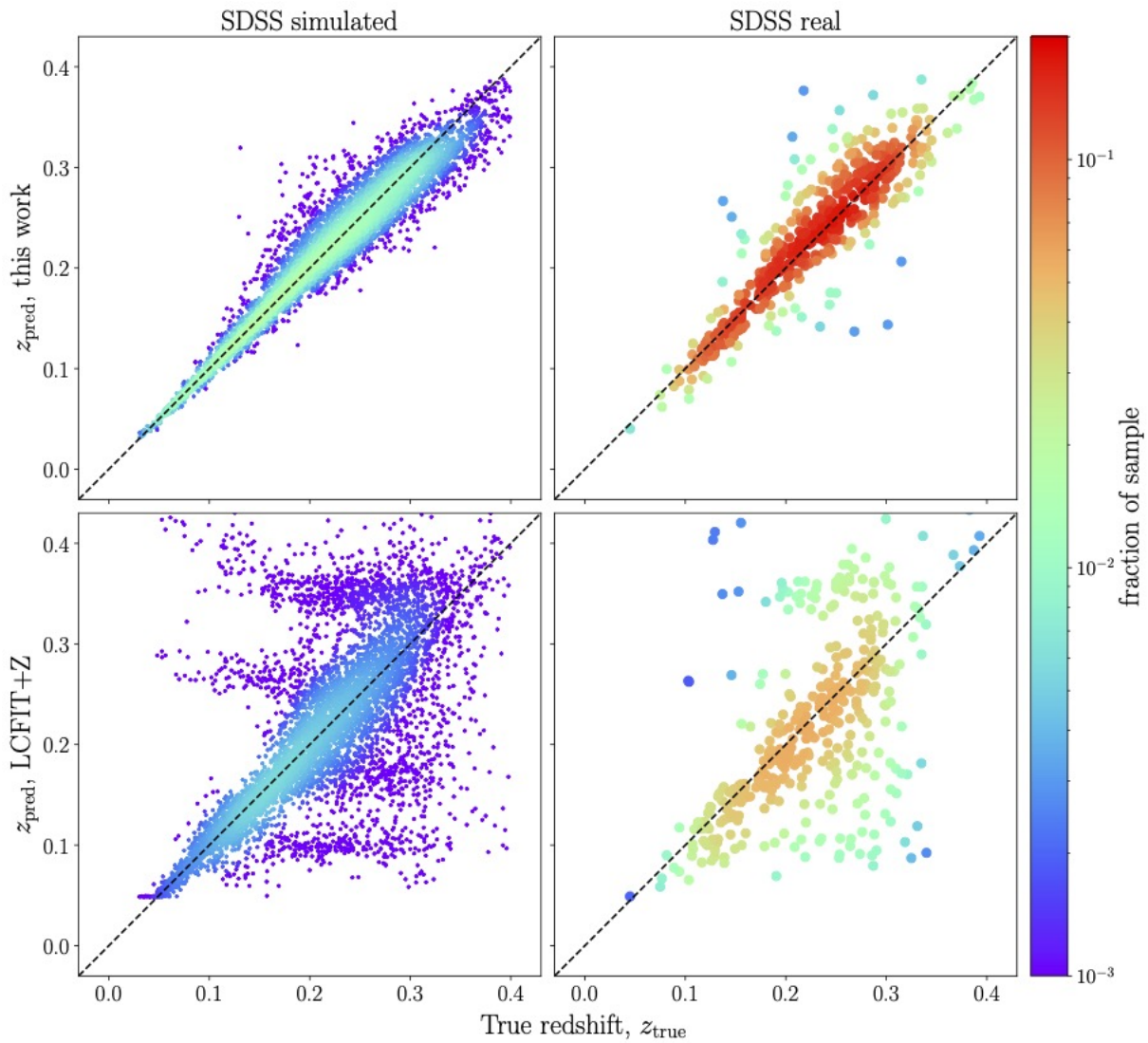


Figure 5.10: Predicted vs. true redshifts for the SDSS simulated and real SNe Ia samples colored by the fraction of each sample represented by each point. (**Top row**) Predictions from Photo- $z$ SNthesis described in this work, (**bottom row**) predictions from LCFIT+Z.

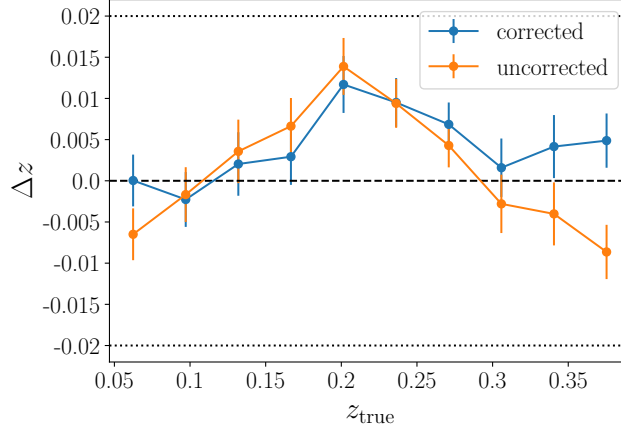


Figure 5.11: Predicted redshift error,  $\Delta z$ , as a function of true redshift,  $z_{\text{true}}$ , for the SDSS real SNe Ia sample with and without bias correction computed from the simulated results. The point estimates used in this figure are computed using the mean(PDF) method. Dotted lines are plotted at  $\Delta z = \pm 0.02$  for reference.

simulated and observed SDSS datasets, as well as the LCFIT+Z point estimates. With the SDSS datasets, the similarity between the mean and max point estimates is more pronounced. We also note that though our model’s performance degrades slightly between the simulated test set and the observed test set, all metrics still strongly favor our model as the better performer compared to LCFIT+Z. However, the  $\sigma_{\text{MAD}}$  values differ less between our model and LCFIT+Z compared to the PLAsTiCC test dataset, only offering a  $2\times$  improvement as opposed to a  $55 - 180\times$  improvement for the PLAsTiCC test dataset. This could be due to the narrower redshift range of SDSS, as the LCFIT+Z performance on the PLAsTiCC dataset degrades significantly after  $z_{\text{true}} \sim 0.4$ .

The mean binned residuals for our model and LCFIT+Z evaluated on the simulated and real SDSS datasets are shown in Figure 5.9. The residuals from both models are much more constrained for SDSS than PLAsTiCC, as expected from the less significant differences in evaluation metrics. LCFIT+Z still exhibits larger mean  $\Delta z$  values for both the simulated and real datasets as well as a larger spread in each bin. Both models generalize relatively well from simulations to real data, with our mean residuals staying within  $|\Delta z| < 0.02$  and LCFIT within  $|\Delta z| < 0.05$ ; however, an overall increase in  $|\Delta z|$  values is noticeable between simulated and real data.

We show the comparison between predicted and true redshifts in Figure 5.10 for the same datasets

used in Figure 5.9. Our model (top row) clearly produces more constrained predictions, as they lie much closer to the  $z_{\text{true}} = z_{\text{pred}}$  line with a high density of points (shown in red) along the line. In contrast with the PLAsTiCC results, in which LCFIT+Z performed relatively well at lower redshifts, the performance over the full SDSS redshift range is poor.

### Bias Correction

Simulations not only allow deep learning methods such as Photo- $z$ SNthesis to train on large datasets that would be infeasible with real data alone, but also give valuable estimates of the biases produced from those models that can be used to correct the results on real data. Here, we test this bias correction method on the results of Photo- $z$ SNthesis on the SDSS simulated and real data. We compute the average  $\Delta z$  values for the simulated SDSS sample in 10 bins of  $z_{\text{true}}$  values and bin the real SDSS sample in the same way. We then subtract the simulated  $\Delta z$  value associated with the bin of each real  $z_{\text{pred}}$  estimate to produce the corrected curve in Figure 5.11. Specifically, the corrected value of the  $i^{\text{th}}$  SN in the real SDSS dataset belonging to bin  $m$  is computed as

$$z_{\text{corrected},i} = z_i - \langle \Delta z_{\text{sim},m} \rangle \quad (5.6)$$

where  $z_{\text{corrected},i}$  is the corrected prediction,  $z_i$  is the uncorrected prediction, and  $\langle \Delta z_{\text{sim},m} \rangle$  is the average  $\Delta z$  from the simulated SNe in bin  $m$ . The corrected  $\Delta z$  values are computed as defined in §5.4.1,

$$\Delta z_{\text{corrected}} = \frac{z_{\text{corrected}} - z_{\text{true}}}{1 + z_{\text{true}}} \quad (5.7)$$

The corrected curve exhibits smaller biases than the uncorrected curve, showing that this bias correction method is valid in cases where the simulation is sufficiently representative of the real data.

#### 5.4.4. Further Experiments

##### Using Photo- $z$ SNthesis photo- $z$ s for Cosmology

Though producing a full cosmological analysis using photo- $z$ s predicted by Photo- $z$ SNthesis is outside the scope of this work, we provide some intuition for the quality of our estimates in the

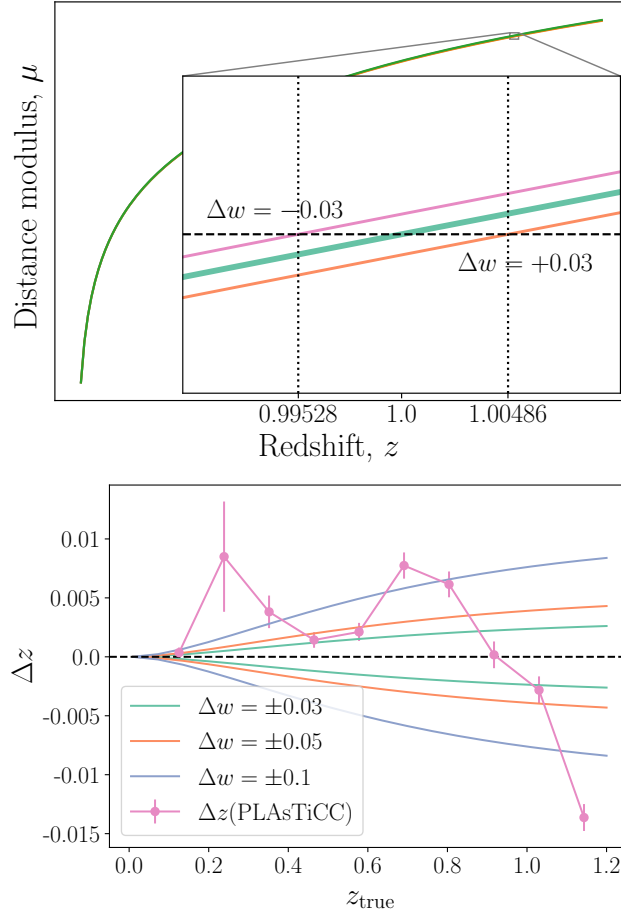


Figure 5.12: An illustration of our estimated cosmological biases arising from photo- $z$  errors. **(top)** A Hubble diagram zoomed in to the neighborhood of  $z_{\text{model}} = 1$  showing a fiducial cosmology (green:  $w = -1, \Omega_m = 0.3$ ) and two biased cosmologies (pink:  $\Delta w = -0.03$ , orange:  $\Delta w = +0.03$ ). The dashed black line shows the distance modulus value at  $z_{\text{model}} = 1$  for the fiducial cosmology,  $\mu_{\text{model}}(z_{\text{model}} = 1)$ . The two dotted lines show the redshifts that correspond to the value of  $\mu_{\text{model}}(z_{\text{model}} = 1)$  for the two biased cosmologies, i.e.  $\mu_{\text{model}}(z_{\text{model}} = 1) = \mu_{\Delta w = -0.03}(z = 0.99528) = \mu_{\Delta w = +0.03}(z = 1.00486)$ . The values of these redshifts are labeled on the redshift axis. We approximate the redshift error required to create a bias of, e.g.  $\Delta w = +0.03$ , as the difference between the biased and fiducial redshift values,  $dz_{\text{bias}} = 1 - 1.00486 = -0.00486$ . **(bottom)**  $\Delta z = dz/(1+z)$  values for various choices of  $\Delta w$ , compared to the mean binned residuals  $\Delta z$  produced by the mean point estimates of Photo- $z$ SNthesis PDFs (pink, reproduced from Figure 5.7).

context of cosmology. The redshift error  $dz_{\text{bias}}$  that results in a  $w$  bias of  $\Delta w$  at a particular redshift,  $z_{\text{model}}$ , can be approximated by the redshift difference

$$dz_{\text{bias}} = z_{\text{model}} - z_{\Delta w} \quad (5.8)$$

where  $z_{\Delta w}$  is the redshift associated with the distance modulus  $\mu_{\text{model}}(z_{\text{model}})$  for the biased cosmology, i.e.

$$\mu_{\text{model}}(z_{\text{model}}) = \mu_{\Delta w}(z_{\Delta w}) \quad (5.9)$$

where  $\mu_{\text{model}}, \mu_{\Delta w}$  are the distance moduli associated with the model and biased cosmologies, respectively.

A concrete example of this is illustrated in the top panel of Figure 5.12, which shows a zoomed-in portion of the Hubble diagram in the neighborhood of our chosen  $z_{\text{model}} = 1$  for our fiducial cosmology ( $w = -1, \Omega_m = 0.3$ ) as well as examples of biases on  $w$  ( $\Delta w \pm 0.03$ ) plotted on either side. Our choice of  $z_{\text{model}} = 1$  is motivated by the importance of high redshift SNe on the constraining power on  $w$ , so we compare with our PLAsTiCC results. We choose to focus on the  $\Delta w = +0.03$  cosmology as our redshifts are slightly underestimated at  $z = 1$ . In this example,  $z_{\Delta w=+0.03} = 1.00486$  at  $z_{\text{model}} = 1$  is shown as the dotted vertical line on the right. We approximate  $dz_{\text{bias}}$  for  $\Delta w = +0.03$  at  $z_{\text{model}} = 1$  to be

$$dz_{\text{bias}} = z_{\text{model}} - z_{\Delta w=+0.03} = 1 - 1.00486 = -0.00486 \quad (5.10)$$

This corresponds to half the distance between the dotted vertical lines in the figure. The mean redshift error for our results on the PLAsTiCC dataset at  $z_{\text{true}} = 1$  are

$$\Delta z = \frac{z_{\text{pred}} - z_{\text{true}}}{1 + z_{\text{true}}} = -0.002 \quad (5.11)$$

translating to an expected redshift difference of

$$z_{\text{pred}} - z_{\text{true}} = (1 + z_{\text{true}}) \cdot -0.002 = -0.004 \quad (5.12)$$



This is below the expected  $dz_{\text{bias}}$  associated with a  $w$  shift of  $\Delta w = +0.03$ .

The bottom panel of Figure 5.12 shows  $\Delta z$  values for different choices of cosmological biases (here we choose to vary  $w$ ) across the full LSST redshift range, along with the  $\Delta z$  values produced by Photo- $z$ SNthesis on the PLAsTiCC dataset. Note that the  $y$  axis of this plot is  $\Delta z = dz/(1+z)$ , i.e.  $dz_{\text{bias}}$  normalized by  $(1+z_{\text{model}})$ , for ease of comparison with Photo- $z$ SNthesis mean residual  $\Delta z$  values. This comparison over all redshifts shows that Photo- $z$ SNthesis redshifts lack the precision to constrain cosmology to  $\Delta w = \pm 0.03$ , since the pink line representing Photo- $z$ SNthesis redshift errors mostly does not lie in the area within the  $\Delta w = \pm 0.03$  teal lines. However, this high-level analysis is an overestimate of the expected impact on cosmology, and a thorough cosmological analysis with Photo- $z$ SNthesis photo- $z$ 's will be the subject of a future work.

### Comparison with LCFIT+Z with Host Galaxy Redshift Prior

In §5.4.2 and §5.4.3, we showed results for Photo- $z$ SNthesis and LCFIT+Z with no host galaxy information included. Photo- $z$ SNthesis was formulated not to require a host redshift prior in order to prevent biases due to incorrect host redshifts. However, in a context in which host mismatches are rare and host redshifts are reliable, we want to use all available information to produce the most constrained SN photo- $z$  estimates.

We test both Photo- $z$ SNthesis and LCFIT+Z with a prior on  $z_{\text{pred}}$ , the predicted redshift, given by the host galaxy photometric redshift estimate. We choose to use photometric redshifts as opposed to spectroscopic to more closely emulate a future scenario in which most host galaxies will not have spectroscopic information available.

We model this prior,  $P(Z_{\text{host}})$ , as a Gaussian centered on the photo- $z$  of the host galaxy,  $z_{\text{host}}$ , and use the estimated uncertainty,  $\sigma_{z_{\text{host}}}$ , as the standard deviation:

$$Z_{\text{host}} \sim \mathcal{N}(z_{\text{host}}, \sigma_{z_{\text{host}}}) \quad (5.13)$$

We treat Photo- $z$ SNthesis PDFs,  $P(Z_{\text{Photo-}z\text{SN}})$ , as Bayesian posteriors and apply the host prior us-

Metric	this work		LCFIT+Z	
	no prior	with prior	no prior	with prior
bias $\langle \Delta z \rangle$	<b>0.0050</b>	0.0061	0.027	0.021
$\sigma_{\text{MAD}}$	0.018	<b>0.017</b>	0.057	0.025
outlier rate $\eta$	5.14%	<b>4.93%</b>	26.1%	17.6%

Table 5.5: Evaluation metrics computed for the SDSS observed photometric SNe Ia sample both with and without a host galaxy photo- $z$  prior. The best results for each metric and dataset are shown in bold.

ing Bayes' theorem:

$$\begin{aligned}
 P(Z_{\text{pred}}) &= \frac{P(Z_{\text{Photo-}z\text{SN}}|Z_{\text{host}})P(Z_{\text{host}})}{P(Z_{\text{Photo-}z\text{SN}})} \\
 &= \frac{P(Z_{\text{Photo-}z\text{SN}})P(Z_{\text{host}})}{\sum_i P(Z_{\text{Photo-}z\text{SN},i})P(Z_{\text{host},i})}
 \end{aligned} \tag{5.14}$$

simplified by the fact that  $P(Z_{\text{host}})$  and  $P(Z_{\text{Photo-}z\text{SN}})$  are statistically independent.

LCFIT+Z uses a Markov chain Monte Carlo (MCMC) process to sample from the posterior distribution over a 5-dimensional parameter space: 4 SALT fit parameters color  $c$ , stretch-luminosity parameter  $x_1$ , time of peak brightness  $t_0$ , flux normalization parameter  $x_0$ ; and redshift  $z_{\text{phot}}$ . The host prior constrains the search space, resulting in a higher likelihood of convergence to a global minimum.

In Figure 5.13, we show  $\Delta z$  values for the SDSS photometric SNe Ia dataset for Photo- $z$ SNthesis and LCFIT+Z with and without a host photo- $z$  prior. The  $\Delta z$  results with no host prior are identical to those in the right panel of Figure 5.9. The host prior noticeably improves LCFIT+Z results on  $z_{\text{true}} < 0.2$  and  $z_{\text{true}} > 0.3$ , as well as the scatter across the full redshift range, shown in the smaller error bars. The Photo- $z$ SNthesis results with and without host prior are very similar, however, as the host prior is often less constraining than the Photo- $z$ SNthesis PDFs themselves. We show the bias,  $\sigma_{\text{MAD}}$ , and outlier rate for both models with and without the host prior in Table 5.5. These results show that Photo- $z$ SNthesis outperforms LCFIT+Z even in the presence of a host galaxy redshift prior.

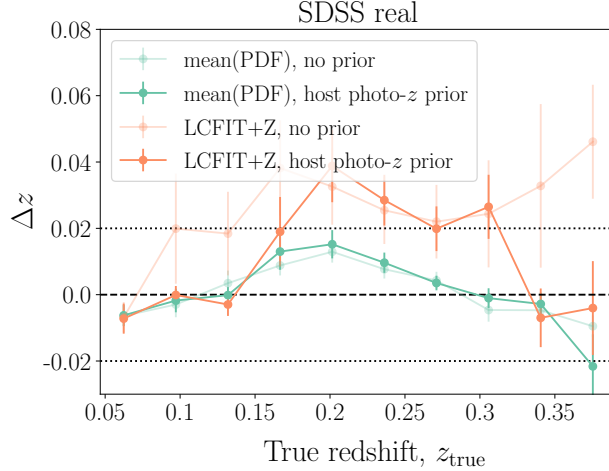


Figure 5.13: Mean binned residuals,  $\Delta z \equiv \frac{z_{\text{pred}} - z_{\text{true}}}{1 + z_{\text{true}}}$ , as a function of true redshift,  $z_{\text{true}}$ , for the SDSS observed photometric SNe Ia sample. Errors from both Photo- $z$ SNthesis and LCFIT+Z are shown with (darker) and without (lighter) a prior on  $z_{\text{pred}}$  from the host galaxy photometric redshift. The lighter (no prior) curves are identical to those in Figure 5.9, with the max(PDF) curves omitted for clarity.

## 5.5. Conclusions

In this work we presented Photo- $z$ SNthesis, a convolutional neural network model that predicts full redshift PDFs from multi-band photometric SNe Ia lightcurves. We evaluated its performance on simulated SDSS and LSST lightcurves, as well as a photometrically confirmed SDSS SN Ia sample. We compared our results against LCFIT+Z, the most frequently used photometric redshift estimation method for SNe, and showed superior performance across all evaluation metrics. Our model also exhibits minimal redshift-dependent bias, which has plagued redshift estimators in the past, and generalizes well between simulated and observed data.

Though Photo- $z$ SNthesis does not require host galaxy information to produce accurate SN photo- $z$  estimates, host galaxy redshifts can be incorporated as a prior to further improve our predictions. We tested Photo- $z$ SNthesis and LCFIT+Z with a host galaxy photometric redshift prior to demonstrate the performance of these models in the LSST era when host galaxy spectroscopic redshifts will not be widely available. We show that while the host galaxy prior improves LCFIT+Z estimates, Photo- $z$ SNthesis still produces more accurate photo- $z$  point estimates as well as constrained

PDFs.

We envision Photo- $z$ SNthesis to be useful for many tasks in supernova science, including precise volumetric rate calculations, discovery of incorrect host galaxy matches via redshift discrepancies, and photometric SN Ia cosmology. We briefly explored the cosmological constraints that can be expected from Photo- $z$ SNthesis photo- $z$ s and concluded that the bias on  $w$  may be on the order of  $\Delta w \sim 0.1$ .

In future work, we intend to develop a framework for incorporating redshift PDFs and their associated uncertainties into the Hubble diagram and produce more accurately modeled cosmological constraints from Photo- $z$ SNthesis redshift PDFs. We also plan to explore the use of Photo- $z$ SNthesis redshift predictions as a method of identifying host confusion and potential mismatches for LSST. Though Photo- $z$ SNthesis was developed for SNe Ia with cosmological applications in mind, the data processing and model architecture can be generalized for use with any astronomical time-domain events.

Accurate photometric redshift estimation for SNe Ia will become vital in the imminent era of photometric SN Ia cosmology. We believe that the approach and model presented here will allow us to maximize the constraining power of these new datasets.

## Acknowledgments

H.Q. and M.S. were supported by DOE grant DE-FOA-0002424 and NSF grant AST-2108094. The authors would like to thank Sang Michael Xie for insightful discussions on the network architecture and training process, Brodie Popovic for providing SDSS simulations, Rebecca Chen for helpful discussions and LCFIT+Z setup, Rick Kessler for assisting with LCFIT+Z, SNANA, and LSST simulations, and Carles Sánchez and Jaemyoung Lee for helpful discussions.

This research used resources of the National Energy Research Scientific Computing Center (NERSC), a U.S. Department of Energy Office of Science User Facility located at Lawrence Berkeley National Laboratory, operated under Contract No. DE-AC02-05CH11231. This work was completed in part with resources provided by the University of Chicago’s Research Computing Center.

## Appendix A: Survey-Agnostic Model Performance

Due to the 2D Gaussian process regression in both wavelength and time dimensions that is performed in order to create the input images (details in §5.2.2), data from different surveys with different photometric bands can be processed into the same image format. This creates the potential for a survey-agnostic model that can be trained on data from a single survey and applied to data from others. To test this hypothesis, we evaluated our model trained on PLAsTiCC data, described in §5.4.2, on 248 spectroscopically confirmed SNe Ia from the first 3 years of the Dark Energy Survey supernova program (DES3YR, Brout et al., 2019). We show these results in Figure 5.14.

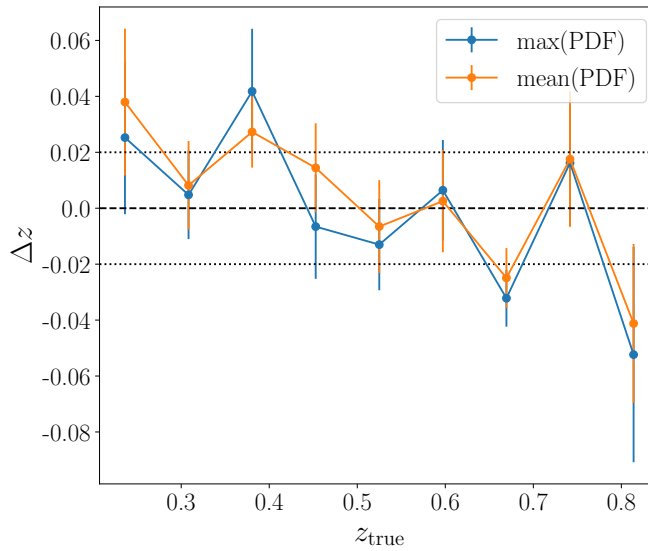


Figure 5.14: Mean binned residuals,  $\Delta z \equiv \frac{z_{\text{pred}} - z_{\text{true}}}{1 + z_{\text{true}}}$ , as a function of true redshift,  $z_{\text{true}}$ , for the DES3YR SNe Ia sample produced by a model trained on the PLAsTiCC dataset. The max(PDF) and mean(PDF) methods of obtaining point estimates from Photo- $z$ SNthesis PDFs are described in §5.4.1.

The scatter and redshift-dependent bias are certainly more prominent in this result than the others presented in this work (Figures 5.7 and 5.9), but is nevertheless an impressive result considering that this 2D Gaussian process regression method uniquely makes cross-survey results possible. We also highlight that these observed SNe Ia cover a much larger redshift range than the SDSS observed sample, demonstrating the applicability of Photo- $z$ SNthesis on high-redshift, deep sky surveys such as LSST. While training a fresh model with a full suite of Dark Energy Survey SNe

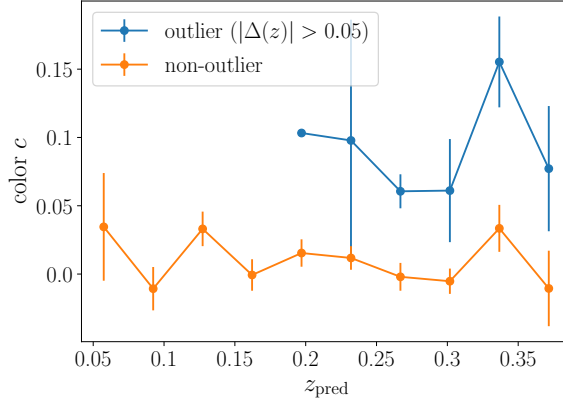


Figure 5.15: Mean binned SALT2 color,  $c$ , as a function of predicted redshift,  $z_{\text{pred}}$ , for the Photo- $z$ SNthesis prediction outliers and non-outliers in the SDSS observed photometric SN Ia sample.

Ia simulations would certainly produce improved results, we posit that improvements could be attained relatively inexpensively by "fine-tuning" an existing trained model using a small volume of SNe Ia simulated in the target survey. We leave these interesting extensions to future work.

### 5.6. Redshift Prediction Outliers of the Real SDSS Dataset

We investigate the 29 Photo- $z$ SNthesis prediction outliers, defined as objects with  $\Delta z > 0.05$ , in the observed SDSS dataset. We find that the population of outliers is noticeably redder than their non-outlier counterparts at the same predicted redshift (Figure 5.15), which could explain the prediction failure.

We also attempted to use the predicted PDF shapes to remove outliers, assuming that poor predictions may be correlated with wider PDFs, representing the model's lack of confidence in less accurate predictions. Although we found a slight correlation, it is not strong enough for this metric to be useful: 48% of outliers have "wide" PDFs (defined as  $\sigma > 0.025$  empirically) as well as 18% of non-outliers.

## CHAPTER 6

### Connect Later: Improving Fine-tuning for Robustness with Targeted Augmentations

#### Abstract

Models trained on a labeled source domain (e.g., labeled images from wildlife camera traps) often generalize poorly when deployed on an out-of-distribution (OOD) target domain (e.g., images from new camera trap locations). In the domain adaptation setting where unlabeled target data is available, self-supervised pretraining (e.g., masked autoencoding or contrastive learning) is a promising method to mitigate this performance drop. Pretraining improves OOD error when the generic data augmentations used (e.g., masking or cropping) connect the source and target domains, which may be far apart in the input space. In this paper, we show on real-world tasks that standard fine-tuning after pretraining does not consistently improve OOD error over simply training from scratch on labeled source data. To better leverage pretraining for distribution shifts, we propose Connect Later: after pretraining with generic augmentations, fine-tune with *targeted augmentations* designed with knowledge of the distribution shift. Pretraining learns good representations within the source and target domains, while targeted augmentations connect the domains better during fine-tuning. Connect Later improves average OOD error over standard fine-tuning and supervised learning with targeted augmentations on 4 real-world datasets: Connect Later achieves the state-of-the-art on astronomical time-series classification (ASTROCLASSIFICATION) by 2.5%, wildlife species identification (IWILDCAM-WILDS) with ResNet-50 by 0.9%, and tumor identification (CAMELYON17-WILDS) with DenseNet121 by 1.1%; as well as best performance on a new dataset for astronomical time-series redshift prediction (REDSHIFTS) by 0.03 RMSE (11% relative).<sup>2</sup>

#### 6.1. Introduction

In many real-world scenarios, machine learning models are deployed on data that differ significantly from the training data (Quiñonero-Candela et al., 2009; Koh et al., 2021). We focus on unsupervised domain adaptation (Shimodaira, 2000; Blitzer et al., 2006; Sugiyama et al., 2007), where

---

<sup>2</sup>Code and datasets are available at <https://github.com/helenqu/connect-later>.

we have labeled data from a source domain and unlabeled data from a target domain. We aim to learn a model that generalizes well to these out-of-distribution (OOD) target domain inputs. A real-world example is wildlife identification, where the task is to identify animal species from static camera trap images. However, human labels are only available for images from a small subset of these cameras. Images from labeled cameras may not be representative of the habitats and characteristics of unlabeled camera images.

Pretraining on broad unlabeled data has shown promising results on improving OOD error in real-world problems (Caron et al., 2020; Shen et al., 2022; Radford et al., 2021; Sagawa et al., 2022). In particular, contrastive pretraining has been shown to learn representations that transfer well across domains (Shen et al., 2022; HaoChen et al., 2022). In contrast to conventional domain adaptation methods that focus on learning domain-invariant features (Ganin et al., 2016; Kang et al., 2019; Tzeng et al., 2017; Saenko et al., 2010; Sun et al., 2016; Hoffman et al., 2018), contrastive pretraining learns representations that are not domain-invariant, but instead decompose the class and domain information, facilitating transfer across domains (Shen et al., 2022). A favorable decomposition depends on the generic data augmentations used during contrastive pretraining to connect the source and target domains in a structured way. Intuitively, augmented (e.g. masked or cropped) source and target inputs are more likely to look similar if they are from the same class (e.g., cropping out the face of a lion in different habitats) than from different classes (e.g., no body parts of elephants and lions are alike). However, these generic augmentations must connect the domains without knowledge of the distribution shift.

In this paper, we find on real-world benchmarks that standard fine-tuning after contrastive pretraining is not always effective for improving OOD error over purely supervised learning from scratch with labeled source data (Section 6.3). On the other hand, supervised learning with *targeted augmentations* (Gao et al., 2023) designed for the distribution shift improves OOD error over the supervised learning baseline on all datasets without access to any target unlabeled data. Thus, pretraining does not always learn representations that transfer across domains with standard fine-tuning.



To better leverage pretraining for domain adaptation, we propose the Connect Later framework (Figure 6.1): after pretraining with generic augmentations, fine-tune with targeted augmentations (Section 6.4). Intuitively, pretraining learns good representations within each domain, while targeted augmentations better connect the domains. On a simple theoretical example where contrastive pretraining fails, Connect Later generalizes well to the target domain. We provide a general methodology for constructing these targeted augmentations, where the augmented inputs match the target distribution on a feature space where the domains differ.

We evaluate our framework on 4 real-world datasets: wildlife identification (iWILDCAM-WILDS, Beery et al., 2020; Sagawa et al., 2022), tumor detection (CAMELYON17-WILDS, Bandi et al., 2018; Sagawa et al., 2022) and 2 astronomical time series tasks, ASTROCLASSIFICATION and REDSHIFTS, which we curate from team et al. (2018). In Section 6.5, we show that Connect Later improves ID and OOD performance over standard fine-tuning or supervised learning with targeted augmentations across all datasets. Although our understanding stems from contrastive learning, we empirically apply Connect Later to better leverage pretrained representations from both masked autoencoding and contrastive learning. Connect Later achieves the state-of-the-art on three benchmarks, improving OOD accuracy on ASTROCLASSIFICATION by 3% (Boone, 2019a), iWILDCAM-WILDS with ResNet-50 by 0.9%, and CAMELYON17-WILDS with DenseNet121 by 1.1%. We also contribute the REDSHIFTS dataset, on which Connect Later produces 11% and 14% relative improvement over standard fine-tuning and supervised learning with targeted augmentations, respectively.

## 6.2. Setup

We consider a prediction problem from an input space  $\mathcal{X}$  to a label space  $\mathcal{Y}$ , where  $\mathcal{Y} = \{1, \dots, k\}$  for classification and  $\mathcal{Y} \in \mathbb{R}$  for regression.

**Domain adaptation.** Let  $P_S$  and  $P_T$  be the source and target input distributions over  $\mathcal{X}$ , respectively. We consider unsupervised domain adaptation, where we have access to source inputs  $x \sim P_S$ , with corresponding labels  $y \in \mathcal{Y}$  sampled from the label distribution  $p^*(\cdot | x)$ , along with unlabeled target inputs sampled from the target distribution  $P_T$ . Let the unlabeled distribution  $P_U = \beta P_S + (1 - \beta) P_T$  be a mixture of the source and target, where  $\beta \in [0, 1]$ . In practice,  $P_U$

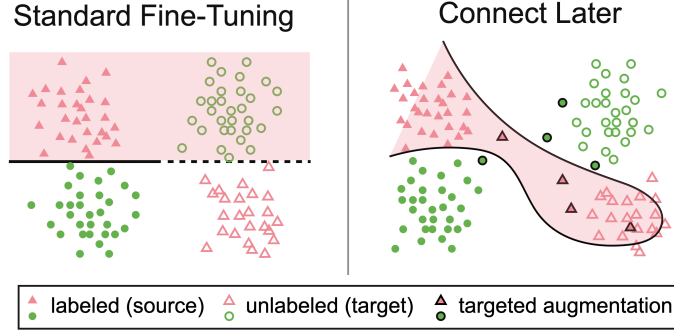


Figure 6.1: Overview of the Connect Later framework for domain adaptation applied to a toy binary classification problem with two domains (filled and unfilled points), showing the representations from contrastive pretraining in  $\mathbb{R}^2$ . **(Left)** After contrastive pretraining with generic augmentations, the classes within each domain are linearly separable in representation space. Since the domains are far apart in input space, generic augmentations may not connect the domains, resulting in misalignment in the pretrained representations. In this case, a classifier (with a linearly extrapolating decision boundary, dashed and solid line) learned on labeled source data will misclassify the target data. **(Right)** Connect Later employs targeted augmentations (filled points with black border), which are designed with knowledge of the distribution shift, to connect the domains better, resulting in a classifier that generalizes well to the target domain.

may also be a broader unlabeled distribution. The goal is to learn a model  $f : \mathcal{X} \rightarrow \mathcal{Y}$  that minimizes error on the target domain  $L_T(f) = \mathbb{E}_{x \sim P_T, y \sim p^*(\cdot|x)}[\ell(f(x), y)]$ . For example,  $\ell : \mathcal{Y} \times \mathcal{Y} \rightarrow \mathbb{R}$  is the 0-1 loss in classification and squared loss in regression.

**Augmentations.** Augmented inputs  $x' \in \mathcal{X}$  are drawn from an augmentation distribution  $\mathcal{A}(\cdot|x)$ , given an input  $x \in \mathcal{X}$ . Training with augmented inputs is often used to improve robustness (Hendrycks et al., 2019, 2020) and is a crucial part of the objective in contrastive pretraining (Caron et al., 2020; Shen et al., 2022; Devlin et al., 2019). In this work, we define two distinct augmentation distributions,  $\mathcal{A}_{\text{pre}}$  and  $\mathcal{A}_{\text{ft}}$ , for the pretraining and fine-tuning steps, respectively. Typically, the pretraining augmentations  $\mathcal{A}_{\text{pre}}$  are generic transformations, such as random cropping in vision or masking in NLP (Caron et al., 2020; Chen et al., 2020; He et al., 2020; Radford et al., 2021; Shen et al., 2022; He et al., 2022; Devlin et al., 2019). Fine-tuning augmentations  $\mathcal{A}_{\text{ft}}$  have not been studied extensively and are typically also generic or simply the identity transformation (Sagawa et al., 2022; Devlin et al., 2019).

**Contrastive pretraining for domain adaptation.** Contrastive pretraining for domain adaptation consists of two steps: self-supervised pretraining on unlabeled data, then supervised fine-tuning on labeled source data (Shen et al., 2022). For simplicity below, we consider the population objectives. Contrastive learning aims to learn an encoder which maps augmented views of the same input to similar features (“positive pairs”) and views of different inputs to dissimilar features (“negative pairs”), according to some distance metric. Formally, let  $S_+(x, x^+) = \mathbb{E}_{\bar{x} \sim P_U} [\mathcal{A}_{\text{pre}}(x | \bar{x}) \mathcal{A}_{\text{pre}}(x^+ | \bar{x})]$  be the distribution over positive pairs, which are augmentations of a single input  $\bar{x}$ . We pretrain an encoder  $\phi : \mathcal{X} \rightarrow \mathbb{R}^k$  to minimize the distance  $d_+$  between positive pair embeddings and maximize the distance  $d_-$  between negative pair embeddings:

$$\mathcal{L}_{\text{pretrain}}(\phi) = \mathbb{E}_{(x, x^+) \sim S_+} [d_+(\phi(x), \phi(x^+))] - \mathbb{E}_{x, x' \sim P_U} [d_-(\phi(x), \phi(x')))]. \quad (6.1)$$

The output of the pretraining step is a pretrained encoder  $\hat{\phi} = \arg \min_{\phi} \mathcal{L}_{\text{pretrain}}(\phi)$ .

Fine-tuning then learns a prediction head  $h : \mathbb{R}^k \rightarrow \mathbb{R}^n$  (for regression, we let  $n = 1$ ) on top of the pretrained encoder using labeled source data with the objective

$$\mathcal{L}_{\text{ft}}(h) = \mathbb{E}_{x \sim P_S, y \sim p^*(\cdot | x), x' \sim \mathcal{A}_{\text{ft}}(\cdot | x)} [\text{loss}_{\text{ft}}(h(\hat{\phi}(x')), y; \theta)] \quad (6.2)$$

where  $\text{loss}_{\text{ft}} : \mathbb{R}^n \times \mathcal{Y} \rightarrow \mathbb{R}$  is a fine-tuning objective such as softmax cross entropy loss for classification or squared error for regression. The learned head is  $\hat{h} = \arg \min_h \mathcal{L}_{\text{ft}}(h)$ . In practice, we jointly fine-tune the head  $h$  and the encoder  $\hat{\phi}$ .

**Standard fine-tuning.** We refer to **standard fine-tuning** as the pretraining+fine-tuning procedure where  $\mathcal{A}_{\text{ft}}(x' | x) = 1$  if  $x' = x$  (no fine-tuning augmentations). In our experiments, the standard fine-tuning procedure is linear probing then fine-tuning (LP-FT) (Kumar et al., 2022), which has been shown to improve ID and OOD performance over vanilla fine-tuning. In LP-FT, we first learn a linear predictor on top of frozen pretrained features before fine-tuning all the parameters jointly.

Table 6.1: Contrastive pretraining with standard fine-tuning substantially improves OOD performance for CAMELYON17-WILDS but is not as effective for iWILDCAM-WILDS. Results are averaged over 15 trials for iWILDCAM-WILDS and 20 trials for CAMELYON17-WILDS, and we report the 95% confidence intervals on each mean estimate.

	iWildCam (Macro F1, $\uparrow$ )		Camelyon17 (Avg Acc, $\uparrow$ )	
	ID Test	OOD Test	ID Val	OOD Test
ERM	$46.4 \pm 0.5$	$30.4 \pm 0.6$	$89.3 \pm 0.9$	$65.2 \pm 1.1$
Standard fine-tuning	$46.4 \pm 0.8$	$31.2 \pm 0.6$	$92.3 \pm 0.2$	$91.4 \pm 0.9$

**ERM with augmentations.** As a baseline, we consider empirical risk minimization (ERM) with data augmentation, which optimizes the fine-tuning objective (Equation 6.2) on labeled source data with randomly initialized parameters. In this paper, we refer to **ERM** as the instantiation where  $\mathcal{A}_{\text{ft}}(x' | x) = 1$  if  $x' = x$  (no augmentations) and **ERM + targeted augmentations** as the instantiation with  $\mathcal{A}_{\text{ft}}$  that is designed with knowledge of the distribution shift.

### 6.3. Pretraining may not improve OOD performance

We compare ERM and standard fine-tuning on two benchmark datasets, iWILDCAM-WILDS (wildlife species identification) and CAMELYON17-WILDS (tumor detection). In Table 6.1, we show that standard fine-tuning on a model pretrained using SwAV contrastive learning (Caron et al., 2020) makes minimal gains over ERM on iWILDCAM-WILDS ( $46.4 \rightarrow 46.4$  ID,  $30.4 \rightarrow 31.2$  OOD) compared to CAMELYON17-WILDS ( $89.3 \rightarrow 92.3$  ID,  $65.2 \rightarrow 91.4$  OOD). This result runs contrary to empirical results demonstrating that contrastive pretraining is an effective domain adaptation method (Caron et al., 2020; Shen et al., 2022; Radford et al., 2021; Sagawa et al., 2022). We hypothesize that the generic pretraining augmentations connect the domains better for some tasks and distribution shifts than others.

**Simple example with misaligned connectivity structure.** To understand this phenomenon, we provide a simple binary classification example of when contrastive pretraining fails for domain adaptation, following a similar augmentation graph construction to Shen et al. (2022), in Appendix 6.7. When the connectivity structure misaligns the source and target domains, such that examples from the same class are less “connected” than examples from different classes across the domains, a linear classifier trained on these pretrained representations will not transfer from source to target.

Table 6.2: Empirically estimated connectivity measures for iWILDCAM-WILDS and CAMELYON17-WILDS. From Shen et al. (2022), contrastive pretraining theoretically learns transferable representations for UDA when both across-domain ( $\alpha$ ) and across-class ( $\beta$ ) connectivity is greater than across-both ( $\gamma$ ), using notation from (Shen et al., 2022). In iWILDCAM-WILDS, across-both connectivity  $>$  across-class, which violates the condition, while CAMELYON17-WILDS satisfies the condition.

	across-domain ( $\alpha$ )	across-class ( $\beta$ )	across-both ( $\gamma$ )
iWILDCAM-WILDS	0.116	0.071	0.076
CAMELYON17-WILDS	0.16	0.198	0.152

This could happen, for example, when the source and target are far apart in input space and connectivity is low between examples from the same class across different domains.

### 6.3.1. Robustness gains from pretraining depend on dataset connectivity

To test this hypothesis, we empirically measure connectivity as defined in Shen et al. (2022). We follow (Shen et al., 2022) and work in the augmentation graph setting, where nodes are inputs and edge weights are the positive-pair probabilities given by  $S_+$ . We define connectivity between a class-domain pair  $((y_1, d_1), (y_2, d_2))$  under four scenarios:

$$\left\{ \begin{array}{l} \rho \quad y_1 = y_2, d_1 = d_2 \quad (\text{same class, same domain}) \\ \alpha \quad y_1 = y_2, d_1 \neq d_2 \quad (\text{same class, different domain}) \\ \beta \quad y_1 \neq y_2, d_1 = d_2 \quad (\text{different class, same domain}) \\ \gamma \quad y_1 \neq y_2, d_1 \neq d_2 \quad (\text{different class and domain}) \end{array} \right., \quad (6.3)$$

where each value is an average edge weight over the edges that satisfy each case. Shen et al. (2022) show in simple augmentation graphs that contrastive pretraining theoretically learns transferable representations when  $\alpha > \gamma$  and  $\beta > \gamma$ , and that the ratios  $\frac{\alpha}{\gamma}$  and  $\frac{\beta}{\gamma}$  empirically correlate well with OOD accuracy. Intuitively, the pretraining augmentations are less likely to change both the domain and class of an input than changing just domain or just class.

**Empirical evaluations of connectivity.** To better understand why contrastive pretraining performs differently on iWILDCAM-WILDS and CAMELYON17-WILDS, we empirically evaluate the con-

nectivity measures for `iWILDCAM-WILDS` and `CAMELYON17-WILDS`, following Shen et al. (2022). Using augmented inputs from 2 class-domain pairs, we train a binary classifier to predict the class-domain pair of each input, and interpret the test error of the classifier as an estimate for connectivity. We average each connectivity value over 15 class-domain pairs (see Appendix 6.7 for details). Our results, summarized in Table 6.2, show that `iWILDCAM-WILDS` connectivity measures violate the condition for contrastive pretraining in the UDA setting, since across-both connectivity  $>$  across-class ( $\gamma > \beta$ ). This finding is consistent with our observation that contrastive pretraining fails for `iWILDCAM-WILDS` while producing gains for `CAMELYON17-WILDS`, and further underscores the need for domain adaptation methods that correct the misaligned connectivity structure.

#### 6.4. Connect Later: Pretrain First, Targeted Augmentations Later

Even when generic augmentations applied during pretraining misalign the connectivity structure, the pretrained representations are still useful since the classes are linearly separable *within* each domain. How do we leverage these pretrained representations when they may not transfer well across domains? In this work, we propose the Connect Later framework (Figure 6.1):

1. Pretrain on unlabeled data with generic augmentations as in Equation 6.1, producing a pretrained encoder  $\hat{\phi}$ .
2. Design a targeted augmentation  $\mathcal{A}_{\text{ft}}$  (discussed below) and use augmented source data to fine-tune the pretrained encoder  $\hat{\phi}$  jointly with a prediction head  $h$  as in Equation 6.2.

Intuitively, pretraining learns good representations of the source and target domains and allows us to reuse the pretrained model for multiple downstream tasks, while targeted augmentations better connect the domains for the particular task.

**Simple example where Connect Later achieves 0 OOD error.** In our simple binary classification example in Appendix 6.7, we show that when the connectivity structure is misaligned, both standard fine-tuning with contrastive pretraining and ERM + targeted augmentations have high OOD error, while Connect Later achieves 0 OOD error. In this setting, ERM with targeted augmentations is unable to achieve 0 OOD error since some target inputs are “unreachable” via targeted augmen-

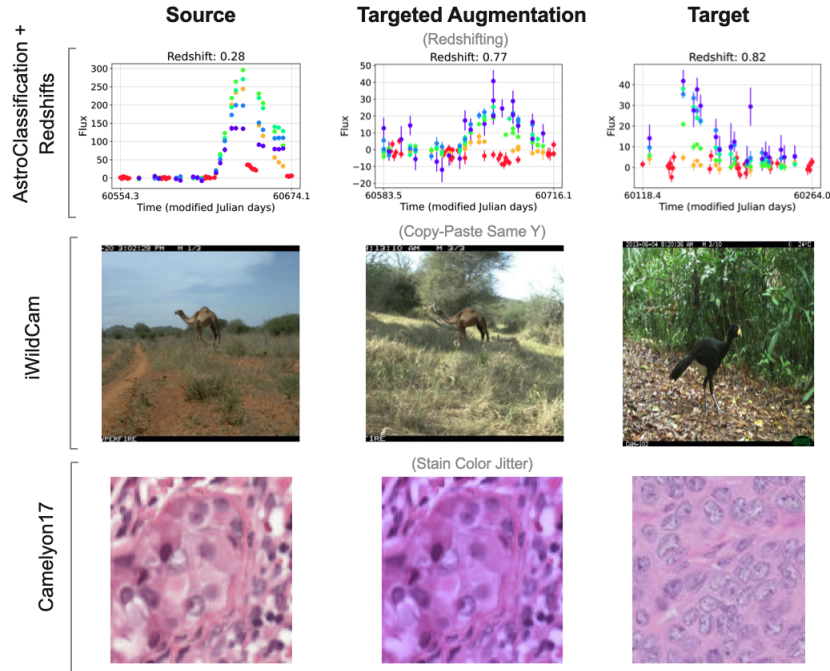


Figure 6.2: An example from the source dataset (left), an augmented version of the source example (middle), and an example from the target dataset (right) for our 3 tasks. (**Top row**) The target dataset in `ASTROCLASSIFICATION` and `REDSHIFTS` is much higher redshift than the source dataset. We apply the redshifting augmentation to simulate placing source objects at a higher redshift to better match the target dataset. The flux errors and flux values of the augmented example (middle) show much better resemblance of the target example. (**Bottom row**) The `iWILDCAM-WILDS` target dataset is composed of images from cameras unseen during fine-tuning, which are in potentially new habitats, so we randomize the habitat background by applying the Copy-Paste Same Y augmentation. This algorithm places source dataset animals into empty backgrounds from other cameras that have observed the same species. `iWILDCAM-WILDS` image examples shown here are from Gao et al. (2023).

tations of source inputs. The pretraining step in Connect Later uses unlabeled target data to learn representations where label information from source data can propagate to all target inputs.

#### 6.4.1. Real-world examples of targeted augmentations

We design targeted augmentations for 4 real-world tasks: species identification from wildlife camera trap images, tumor detection, and astronomical time-series classification and redshift prediction. We show examples from the source, augmented, and target datasets for these tasks in Figure 6.2.

**Wildlife species classification (iWILDCAM-WILDS).** For iWILDCAM-WILDS (Beery et al., 2020; Sagawa et al., 2022), the task is to identify the wildlife species from static camera trap images. These cameras are placed in a wide variety of environments, which all have unique habitat conditions (e.g., African savannah vs. tropical rainforest) and camera characteristics (e.g., angles, resolutions). In this dataset, we use labeled data from 243 camera traps to learn a model that can generalize to data from 48 unseen camera traps.

- **Source:** 243 camera traps
- **Target:** 48 unseen camera traps
- **Targeted Augmentation:** We augment the labeled dataset with the Copy-Paste Same Y algorithm, which uses image segmentation to copy-paste the animal onto different background images from cameras that have observed the same species (Gao et al., 2023).
- **Task:** 182-class wildlife species classification

**Tumor detection (CAMELYON17-WILDS).** The task in CAMELYON17-WILDS (Bandi et al., 2018) is to classify whether a patch of a histopathology slide contains a tumor. These slides are contributed from multiple hospitals, which use different stain colors and also vary in distributions of patient cancer stage.

- **Source:** Hospitals 1-3.
- **Target:** Hospitals 4 and 5.
- **Targeted Augmentation:** We augment the labeled dataset with the Stain Color Jitter algorithm, which jitters the color of the slide image in the hematoxylin and eosin staining color space (Tellez et al., 2018).
- **Task:** Binary classification of whether a slide contains a tumor.

**Astronomical object classification (ASTROCLASSIFICATION).** Astronomical object classification (Boone, 2019a; Allam Jr. and McEwen, 2022) involves predicting the object type (e.g., type II su-



pernova) from a time series of an object’s brightness at multiple wavelengths (*light curves*). We curate this dataset from the Photometric LSST Astronomical Time Series Classification Challenge (PLAsTiCC, team et al., 2018) (details in Appendix 6.7).

- **Source:** Time-series of bright, nearby objects with expert labels
- **Target:** Time-series of all observed objects from the telescope, often faint and distant (higher redshift). Follow-up observation, which is required for expert labeling, is too expensive for these objects.
- **Targeted Augmentation:** We augment the labeled dataset by redshifting each object, i.e., simulating its observed properties as if it were further away (details in Appendix 6.7).
- **Task:** 14-class astronomical object classification

**Redshift regression (REDSHIFTS).** Similar to object type, redshift information is also available only for bright, nearby objects. We predict the scalar redshift value of each object and minimize mean squared error. This task has been studied for individual object types, such as quasars (Nakoneczny et al., 2021) and type Ia supernovae (Qu and Sako, 2023), but we consider a more realistic set of multiple object types. The labeled and unlabeled data are derived from the PLAsTiCC dataset. REDSHIFTS is a new dataset that we contribute as part of this work.

- **Source:** Time-series of bright, nearby labeled objects.
- **Target:** Time-series of all observed objects from the telescope, often faint and distant (higher redshift).
- **Targeted Augmentation:** Redshifting (same as ASTROCLASSIFICATION, Appendix 6.7).
- **Task:** Redshift regression

#### 6.4.2. Designing targeted augmentations

How do we design these targeted augmentations? We provide a general methodology based on matching the target distribution on a feature space:

1. Identify a feature space  $\mathcal{Z}$ . We assume that we can label  $z \in \mathcal{Z}$  for each input and that the source and target domains largely differ on this feature space. One such example is the space of spurious, domain-dependent features (e.g., camera angle or resolution for iWILDCAM-WILDS), which is the approach followed by Gao et al. (2023).
2. Fit a transformed feature distribution  $\hat{p}_T(z'|z)$  to the target feature distribution.
3. Create a transformation distribution  $T(x'|x, z')$  where  $x'$  is the augmented version of  $x$  with  $z = z'$ . In this paper, we define  $T$  with domain knowledge.
4. Given an input  $x$ , generate augmentations by sampling a new feature  $z'$  from  $\hat{p}_T(z' | z)$ , then sampling an augmentation from  $T(x'|x, z')$ . The resulting targeted augmentation probabilities are  $\mathcal{A}_{\text{fit}}(x' | x) = \sum_{z'} T(x' | x, z') \hat{p}_T(z' | z)$ .

**Targeted augmentation example.** We follow the procedure outlined above to design a targeted augmentation for ASTROCLASSIFICATION and REDSHIFTS, two astronomical time-series datasets (see Appendix 6.7 for details). In these datasets, expert labels are only available for time-series of bright, nearby astronomical objects, while the unlabeled dataset contains mostly faint, distant objects. We describe distances in terms of *cosmological redshift*: nearby objects have lower redshift values than distant objects, causing the source and target redshift distributions to be mismatched (Appendix Figure 6.4).

1. The source and target domains primarily differ on their redshift distributions, so we identify this scalar feature as  $z$ .
2. We roughly fit the target redshift distribution while constraining the transformed redshift value to not be too far from the original redshift  $z$ , such that  $\hat{p}_T(z' | z)$  is distributed as  $\text{loguniform}(0.95z, \min(1.5(1 + z) - 1, 5z))$ , following Boone (2019a).
3. We define a transformation distribution  $T(x'|x, z')$ , where  $x$  is a time-series of flux values at multiple wavelengths and  $z'$  is a new redshift value to transform to. We first fit a Gaussian process that models  $x$  as a function of time and wavelength. Given  $z'$ , we rescale the

timestamps and wavelengths of the original input to account for the physical effects of the new redshift value. Then, we sample  $\tilde{x}'$  from the Gaussian process at these new timestamps and wavelengths. Finally, we produce the transformed input  $x'$  by scaling the flux values to account for  $z'$ .

4. We sample  $z'$  from  $\hat{p}_T(z' | z)$  and then sample augmentations  $x'$  from  $T(x'|x, z')$ .

## 6.5. Experiments

We empirically test Connect Later with contrastive pretraining (iWILDCAM-WILDS, CAMELYON17-WILDS) as well as pretraining with masked autoencoding (ASTROCLASSIFICATION, REDSHIFTS) to demonstrate Connect Later as a general fine-tuning method.

**Training procedure.** For iWILDCAM-WILDS, we use a ResNet-50 model pretrained on unlabeled ImageNet data with SwAV contrastive learning (Caron et al., 2020). We use a DenseNet121 pretrained on the unlabeled data provided in Sagawa et al. (2022) with SwAV for CAMELYON17-WILDS. To test Connect Later with other pretraining strategies, we use the masked autoencoding objective for ASTROCLASSIFICATION and REDSHIFTS by masking 60% of observations from each light curve (Appendix 6.7). The same pretrained model is used for both tasks to demonstrate the reusability of pretrained features. We note that masked autoencoding has been linked to contrastive learning (Zhang et al., 2022). In particular, Zhang et al. (2022) show that the masked autoencoding objective upper bounds the contrastive loss between positive pairs — thus, masked autoencoding implicitly aligns the positive pairs induced by the masking augmentations.

We fine-tune the pretrained models with linear probing then fine-tuning (LP-FT) (Kumar et al., 2022), which has been shown to improve OOD performance.

**Baselines.** We evaluate our framework against three baselines: ERM, ERM+targeted augs, and standard fine-tuning. We include Avocado (Boone, 2019a), the previous state-of-the-art model for ASTROCLASSIFICATION. We also include a self-training baseline for ASTROCLASSIFICATION and REDSHIFTS, which has been shown to perform well on some real-world datasets (Sagawa et al., 2022). For the self-training baseline, we pseudo-label the target dataset with a trained ERM+targeted

Table 6.3: ID and OOD accuracy (%) for ASTROCLASSIFICATION and RMSE for REDSHIFTS of each method. Results are averaged over 5 trials and rows with means within 1 STD of the best mean are bolded.

	AstroClassification		Redshift	
	ID Test Acc ( $\uparrow$ )	OOD Acc ( $\uparrow$ )	ID Test RMSE ( $\downarrow$ )	OOD RMSE ( $\downarrow$ )
ERM	71.59 $\pm$ 1.10	61.26 $\pm$ 1.10	0.274 $\pm$ 0.016	0.320 $\pm$ 0.009
Standard fine-tuning	78.84 $\pm$ 0.97	67.84 $\pm$ 0.70	<b>0.246 <math>\pm</math> 0.015</b>	0.277 $\pm$ 0.004
ERM + targeted augs	68.75 $\pm$ 0.95	67.54 $\pm$ 0.32	0.310 $\pm$ 0.006	0.286 $\pm$ 0.007
Self-Training	77.72 $\pm$ 0.59	65.15 $\pm$ 0.67	0.304 $\pm$ 0.010	0.289 $\pm$ 0.003
Avocado (Boone, 2019a)	-	77.40	-	-
Connect Later	<b>80.54 <math>\pm</math> 1.20</b>	<b>79.90 <math>\pm</math> 0.60</b>	<b>0.256 <math>\pm</math> 0.005</b>	<b>0.247 <math>\pm</math> 0.005</b>

Table 6.4: ID and OOD performance for each method on iWILDCAM-WILDS and CAMELYON17-WILDS. Results are averaged over 15 trials for iWILDCAM-WILDS and 20 trials for CAMELYON17-WILDS, and we report 95% confidence intervals on each mean estimate. Rows with means within 1 interval of the best mean are bolded.

	iWildCam (Macro F1, $\uparrow$ )		Camelyon17 (Avg Acc, $\uparrow$ )	
	ID Test	OOD Test	ID Val	OOD Test
ERM	46.4 $\pm$ 0.5	30.4 $\pm$ 0.6	89.3 $\pm$ 0.9	65.2 $\pm$ 1.1
Standard fine-tuning	46.4 $\pm$ 0.8	31.2 $\pm$ 0.6	92.3 $\pm$ 0.2	91.4 $\pm$ 0.9
ERM + targeted augs	<b>51.4 <math>\pm</math> 0.6</b>	36.1 $\pm$ 0.7	96.7 $\pm$ 0.0	90.5 $\pm$ 0.4
DANN (Sagawa et al., 2022)	48.5 $\pm$ 3.2	31.9 $\pm$ 1.6	86.1 $\pm$ 1.3	64.5 $\pm$ 1.2
CORAL (Sagawa et al., 2022)	40.5 $\pm$ 1.6	27.9 $\pm$ 0.5	92.3 $\pm$ 0.7	62.3 $\pm$ 1.9
Noisy Student (Sagawa et al., 2022)	47.5 $\pm$ 1.0	32.1 $\pm$ 0.8	-	-
ICON	50.6 $\pm$ 1.3	34.5 $\pm$ 1.4	90.1 $\pm$ 0.4	93.8 $\pm$ 0.3
Connect Later	<b>51.7 <math>\pm</math> 0.8</b>	<b>36.9 <math>\pm</math> 0.7</b>	<b>98.5 <math>\pm</math> 0.0</b>	<b>94.9 <math>\pm</math> 0.4</b>

augs model, then perform the same targeted augmentation on the pseudo-labeled target dataset. We then train a model with the pseudo-labeled and augmented target dataset combined with the labeled source dataset. We include additional domain adaptation baselines for iWILDCAM-WILDS and CAMELYON17-WILDS: domain-adversarial neural networks (DANN) (Ganin et al., 2016), correlation alignment (CORAL) (Sun et al., 2016), Noisy Student (Xie et al., 2020b), and ICON<sup>3</sup>.

### 6.5.1. Main results

Tables 6.3 and 6.4 compare the results of Connect Later with baseline methods. On iWILDCAM-WILDS, Connect Later produces improvements in both ID and OOD performance despite the fail-

<sup>3</sup><https://github.com/a-tea-guy/ICON>

ure of standard fine-tuning. Connect Later substantially outperforms all other variants on the OOD metric, including state-of-the-art performances on ASTROCLASSIFICATION by 3% OOD, iWILDCAM-WILDS by 0.8% OOD for ResNet-50, and CAMELYON17-WILDS by 1.1% OOD for DenseNet121.

**iWildCam.** On iWILDCAM-WILDS, standard fine-tuning does not improve over ERM in ID performance and minimally improves over ERM in OOD performance, while ERM+targeted augmentations improves by 6% ID and OOD over both ERM and standard fine-tuning. While 3 of the domain adaptation baselines made ID and OOD improvements over standard fine-tuning (DANN: 46.4%  $\rightarrow$  48.5% ID, 31.2%  $\rightarrow$  31.9% OOD; Noisy Student: 46.4%  $\rightarrow$  47.5% ID, 30.4%  $\rightarrow$  32.1% OOD; ICON: 46.4%  $\rightarrow$  50.6% ID, 30.4%  $\rightarrow$  34.5%), all fall short of ERM+targeted augs. Connect Later improves over both standard fine-tuning (30.4%  $\rightarrow$  37.2%) and ERM+targeted augs (36.3%  $\rightarrow$  37.2%) in OOD performance, achieving a new state-of-the-art performance for ResNet-50 on the iWILDCAM-WILDS benchmark.

**Camelyon17.** On CAMELYON17-WILDS, standard fine-tuning produces significant gains over ERM in both ID (89.3%  $\rightarrow$  92.3%) and OOD (65.2%  $\rightarrow$  91.4%) average accuracy. ERM+targeted augmentations outperforms standard fine-tuning in ID accuracy (92.3%  $\rightarrow$  96.7%), but does not improve OOD. DANN underperforms ERM in both ID and OOD accuracy, while CORAL produces similar ID accuracy as standard fine-tuning but poor OOD performance. Connect Later sets a new state-of-the-art on CAMELYON17-WILDS with DenseNet121, improving on the best ID performance by 1.8% (ERM+targeted augs, 96.7%  $\rightarrow$  98.5%) and OOD performance by 1.1% (ICON, 93.8%  $\rightarrow$  94.9%).

**AstroClassification.** For ASTROCLASSIFICATION, standard fine-tuning provides a significant performance boost over ERM: 71.6%  $\rightarrow$  78.9% ID, 61.3%  $\rightarrow$  67.8% OOD. ERM+targeted augs underperforms in ID accuracy compared to ERM alone (71.6%  $\rightarrow$  68.8%) and standard fine-tuning (78.9%  $\rightarrow$  68.8%), likely due to relatively strong targeted augmentations toward the redshift distribution of distant, faint objects present in the target distribution. However, OOD accuracy of ERM+targeted augs is competitive with standard fine-tuning, outperforming ERM. Self-training improves both ID and OOD performance compared to ERM but underperforms standard fine-tuning in both domains. Connect Later outperforms the best baseline, standard fine-tuning, by

12% OOD and 2% ID. The ID accuracy improves over standard fine-tuning despite the drop in ID accuracy from adding targeted augmentations to ERM, showing a complementary benefit between pretraining and targeted augmentations. Connect Later sets a new state-of-the-art OOD performance on ASTROCLASSIFICATION by 3% over Avocado, a heavily tuned random forest model with expert-designed features (Boone, 2019a).

**Redshifts.** Similarly to ASTROCLASSIFICATION, standard fine-tuning significantly improves over ERM in both ID ( $0.27 \rightarrow 0.25$ , 7% relative) and OOD ( $0.32 \rightarrow 0.28$ , 13% relative) RMSE. Self-training performs similarly to ERM+targeted augs, while Connect Later outperforms the best baseline variant, standard fine-tuning, by 0.03 RMSE (11% relative) with comparable ID error. We use the same pretrained model for both ASTROCLASSIFICATION and REDSHIFTS for standard fine-tuning and Connect Later, demonstrating the reusability of pretrained representations.

### 6.5.2. Ablations

We performed ablations on the model size, strength of pretraining augmentations (masking percentage for masked autoencoding), and LP-FT on ASTROCLASSIFICATION. We find that downstream performance is quite robust to masking percentage, while scaling up model size and LP-FT improve performance for pretrained models.

**Model scale.** We tested Connect Later with a larger model ( $\sim 3\times$  the parameters of our model, 21M  $\rightarrow$  69M), and find that scaling up model size improves both ID and OOD accuracy (Table 6.5). This suggests that scaling up the model is a promising way to further improve performance with Connect Later.

**Strength of pretraining augmentations (masking percentage).** We vary the strength of pretraining augmentations, which changes the connectivity between domains. This is most straightforward

Table 6.5: Scaling up model size of Connect Later produces improvements in both ID and OOD performance on the ASTROCLASSIFICATION task.

Number of Parameters	ID Accuracy ( $\uparrow$ )	OOD Accuracy ( $\uparrow$ )
21M (default)	78.47	79.49
69M	80.38	80.55

Table 6.6: Linear probing (LP) in addition to fine-tuning (FT) hurts performance for the ERM+targeted augs model but improves performance for Connect Later (tested on the ASTROCLASSIFICATION task).

	Connect Later		ERM+targeted augs	
	ID Accuracy ( $\uparrow$ )	OOD Accuracy ( $\uparrow$ )	ID Accuracy ( $\uparrow$ )	OOD Accuracy ( $\uparrow$ )
FT only	78.07	78.6	77.88	68.43
LP-FT	78.47	79.49	65.68	67.07

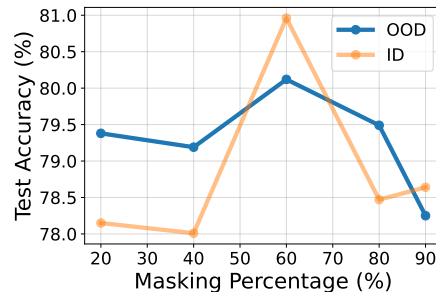


Figure 6.3: On the ASTROCLASSIFICATION task, Connect Later is relatively robust to pretraining masking percentage both ID and OOD, but 60% masking performs best out of the percentages we tested.

with the MAE objective, as augmentation strength is parameterized solely by masking percentage. We tested pretraining masking percentages  $\{20, 40, 60, 80, 90\}$ % while keeping the masking strategy unchanged (replace 10% of masked indices with random values from the lightcurve, another 10% are kept unchanged, and 80% are replaced with the mask token, which we choose to be 0). We show the ID and OOD test accuracy of each variant in Figure 6.3. Both ID and OOD performance peak at 60% masking, although we find that the performance of Connect Later is quite robust to the masking percentage, particularly for OOD performance. All of the masking percentages we tried improve on OOD performance over standard fine-tuning or ERM with targeted augmentations. Particularly, even with the strongest pretraining augmentations (90% masking), which should connect the domains more, the OOD performance did not improve over weaker augmentations. We hypothesize that increasing the strength of generic augmentations may indiscriminately increase the connectivity between all source and target examples, including examples from different classes that should not be strongly connected.

**Linear probing then fine-tuning.** Kumar et al. (2022) showed that linear probing (with fixed neural embeddings) and then fine-tuning (LP-FT) the entire model improves both ID and OOD performance. Intuitively, full fine-tuning with a randomly initialized linear probe can destroy the pretrained features, and training the linear probe first mitigates this. We test LP-FT against FT only (all model weights are fine-tuned) with the Connect Later model and the ERM+targeted augs baseline. We find that LP-FT improves OOD accuracy by 0.9% over FT only when applied to Connect Later on ASTROCLASSIFICATION (Table 6.6). On the other hand, LP-FT decreased OOD accuracy by 1.4% when applied to ERM+targeted augs, which uses random initialization (no pretraining). As a result, we use LP-FT on pretrained models but not on ERM or ERM+targeted augs.

## 6.6. Discussion and Related Work

**Augmentations for pretraining.** Data augmentations such as cropping or masking have been vital to semi- and self-supervised learning objectives. Masking or noising the data and training a model to reconstruct the original inputs have been shown to produce useful pretrained representations across multiple modalities (Devlin et al., 2019; Lewis et al., 2020; He et al., 2022; Raffel et al., 2019; Chen et al., 2020; He et al., 2020; Caron et al., 2020). In contrastive learning, models are trained to distinguish augmented “views” of the same input from views of a different input (Chen et al., 2020; Caron et al., 2020; He et al., 2020). Our results demonstrating inconsistent OOD performance across datasets brings up the important future question of how to choose the best pretraining augmentation and algorithm for learning transferable representations.

**Augmentations for robustness.** Data augmentation has been used to improve model robustness and avoid catastrophic failures due to spurious, label-independent changes (e.g. translation or rotation in vision) (Hendrycks et al., 2019; Rebuffi et al., 2021; Ng et al., 2020). The augmentation strategies used in prior work are generic perturbations that aim to increase the diversity of inputs (e.g., Simard et al., 2003; Krizhevsky et al., 2012b; Cubuk et al., 2019, 2020; DeVries and Taylor, 2017; Zhang et al., 2017), though a number of studies have shown that the type of data augmentations matters for performance (Chen et al., 2020; Xie et al., 2020a). Augmentations have also been leveraged in the self-training paradigm, which improves generalization to unseen data by training on the pseudo-labeled full dataset (Xie et al., 2020b; Sohn et al., 2020; Yang et al., 2021). We show



that a self-training baseline with pseudo-labels from an ERM+targeted augs model does not outperform Connect Later, indicating that pretraining is an important component of the framework. Connect Later exposes targeted augmentations as a design interface for improving robustness with knowledge of the distribution shift, while still leveraging pretrained representations.

**Targeted augmentations.** In problems with domain shift, Gao et al. (2023) show that targeted augmentations outperform generic augmentations on unseen data. They identify spurious domain-dependent, label-independent features in the source dataset and construct targeted augmentations by randomizing these features. Gao et al. (2023) consider the domain generalization setting, in which no data from the target dataset is available. We consider targeted augmentations in the domain adaptation setting, in which we can model the target distribution of these spurious features with the unlabeled target data. In general, designing targeted augmentations specific to each distribution shift may be difficult and require expert guidance. As part of the Connect Later framework, we provide a general methodology for the design of such augmentations. Certain aspects, such as the selection of feature space  $z$  and transformation distribution  $T$  could be learned from the unlabeled data itself, which we leave for future work. We show that targeted augmentations better leverage pretrained representations for complementary gains in OOD performance.

## 6.7. Conclusion

We show that pretraining with generic augmentations is not a panacea for all distribution shifts and tasks, and sometimes does not outperform supervised learning on labeled source data. Pure supervised learning, however, does not use the unlabeled data or produce reusable representations. The Connect Later framework allows for better leverage of pretrained representations for OOD performance by applying targeted augmentations at fine-tuning time. Future work could focus on learning targeted augmentations from the source and target data distributions as well as further understanding of how the choice of pretraining augmentations affects downstream ID/OOD performance.

## Appendix A. Additional Dataset Details

### A.1. AstroClassification, Redshifts Datasets

The `ASTROCLASSIFICATION` and `REDSHIFTS` datasets were adapted from the 2019 Photometric LSST Astronomical Time-Series Classification Challenge (team et al., 2018)<sup>4</sup>. This diverse dataset contains 14 types of astronomical time-varying objects, simulated using the expected instrument characteristics and survey strategy of the upcoming Legacy Survey of Space and Time (LSST Ivezić et al., 2019c) conducted at the Vera C. Rubin Observatory. It includes two overall categories of time-series objects: *transients*, short-lived events such as supernovae, and *variable* sources, those with fluctuating brightness such as pulsating stars. Specifically, the dataset includes the following transients: type Ia supernovae (SNIa), SNIax, SNIa-91bg, SNIbc, SNII, superluminous supernovae (SLSN), tidal disruption events (TDE), and single lens microlensing events ( $\mu$ Lens-Single); and the following variable objects: active galactic nuclei (AGN), Mira variables, eclipsing binary systems (EB), and RR Lyrae (RRL).

Millions of potential new objects are discovered per observing night, and important metadata such as object type, redshift, or other physical parameters, require astronomers to take time-intensive *spectra* of each object. Spectra are a granular brightness vs. wavelength measurement at a single point in time, and are typically only taken for bright, nearby objects which require less exposure time than faint, faraway objects. The vast majority of discovered objects, however, will not have spectra but instead a time series of imaging data taken in 6 broad wavelength ranges, or *photometric bands*. The time-varying behavior of these objects in these coarse wavelength bands does offer important clues about these physical parameters, but expert interpretation of spectra are traditionally required for confident labeling. Thus, our labeled training data for both `ASTROCLASSIFICATION` and `REDSHIFTS` come from the unrepresentative subset of objects with spectra.

In these tasks, we are specifically interested in predicting the object type (e.g. type II supernova) and the cosmological redshift of objects in the unlabeled dataset. *Cosmological redshift* is a proxy for distance in the universe, and an important piece of metadata for understanding an object’s physical

---

<sup>4</sup><https://zenodo.org/record/2539456>

processes as well as other applications, such as estimating the expansion rate of the universe with type Ia supernovae.

**Problem Setting.** The task is to predict object type for `ASTROCLASSIFICATION` (redshift for `REDSHIFTS`) from time-series of object brightness. The input  $x$  consists of flux measurements and associated uncertainties at times  $t$  and photometric band that each measurement was taken in  $b$ :  $\{F(t_i, b_j)\}_{i=1, j=1}^{T, W}, \{F_{\text{err}}(t_i, b_j)\}_{i=1, j=1}^{T, W}$ . For this work, we map each  $b \in \mathbf{b}$  to the central wavelength of the  $b$  band, which we denote  $w$ . The domain  $d$  is binary, corresponding to whether the object has a spectrum (and thus a label). The labels  $y$  are available only for objects with spectra, and are one of 14 types of astronomical time-varying objects for `ASTROCLASSIFICATION` (redshift of the object for `REDSHIFTS`). We seek to optimize performance on the unlabeled data, which are generally fainter and further away than the labeled subset. We evaluate on these examples as well as held-out examples from the labeled subset.

**Data.** The training set of 7,846 objects is designed to emulate a sample of objects with spectra and thus biased toward brighter, more nearby objects compared to the test set of 3,492,888 objects. A random subset of 10,000 test set objects was selected for evaluation.

1. **Source:** 6,274 objects
2. **ID Test:** 782 objects
3. **OOD Test:** 10,000 objects

All data were simulated with the SuperNova ANALysis (SNANA, Kessler et al., 2009b) software library. Further details about the astrophysical models and LSST instrument characteristics used in the simulation can be found in Kessler et al. (2019).

## Appendix B. Data Augmentations

### B.1. Generic Augmentations for Pretraining

**AstroClassification and Redshifts.** For the `ASTROCLASSIFICATION` and `REDSHIFTS` datasets, we randomly mask a subset of the input sequence using the masked language modeling paradigm in-

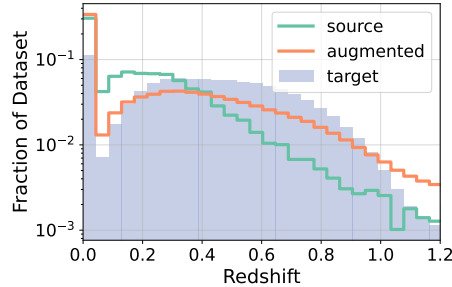


Figure 6.4: Redshift distributions of source, augmented, and target datasets for the ASTROCLASSIFICATION and REDSHIFTS tasks.

troduced by Devlin et al. (2019). Given an unlabeled input sequence  $x$ , a training input  $x'$  can be generated by randomly masking elements of  $x$  while the associated label  $y$  consists of the original, unmasked values. The model is trained to use contextual information (unmasked elements) to successfully reconstruct most of the sequence. From our ablation experiments, we find that a masking percentage of 60% produces the best downstream results. We follow an existing implementation for astronomical time-series (Donoso-Oliva et al., 2023) and set 80% of the masked elements to 0, replace 10% with a random element from the sequence, and keep the remaining 10% unchanged.

**iWildCam and Camelyon17.** For iWILDCAM-WILDS, we use a ResNet-50 model pretrained on ImageNet with SwAV, a contrastive learning algorithm Caron et al. (2020). For CAMELYON17-WILDS, we use a DenseNet121 pretrained with SwAV on the unlabeled CAMELYON17-WILDS dataset from Sagawa et al. (2022). SwAV uses random cropping augmentations of different resolutions.

## B.2. Targeted Augmentations for Fine-Tuning

**Redshifting for AstroClassification and Redshifts.** The OOD test set of the ASTROCLASSIFICATION and REDSHIFTS datasets have many more high redshift objects than the source dataset, leading us to adopt an augmentation scheme to alleviate this shift. Figure 6.4 shows the redshift distributions of the source, augmented, and target datasets. Redshifting places each object at a new redshift and recomputes its light curve sampling, fluxes, and flux uncertainties accordingly. This augmentation algorithm was adapted from Boone (2019a).

An input  $\mathbf{X} \in \mathbb{R}^{T \times W}$  is a multivariate time series of flux values at specified times and observed

wavelengths,  $\{F(t_i, w_j)\}_{i=1, j=1}^{T, W}$ . We also have  $\mathbf{X}_{\text{err}} \in \mathbb{R}^{T \times W}$ , representing the flux errors corresponding to each element of  $\mathbf{X}$ . We denote the elements of  $\mathbf{X}'_{\text{err}}$  by  $\{F'_{\text{err}}(t_i, w_j)\}_{i=1, j=1}^{T, W}$ . Our goal is to model  $F, F_{\text{err}} : \mathbb{R} \times \mathbb{R} \rightarrow \mathbb{R}$  at a new chosen redshift,  $z'$ , to produce augmented inputs  $\mathbf{X}', \mathbf{X}'_{\text{err}}$ .

- We first construct a distribution from which to sample the new redshift, taking into account the current redshift of the object  $z_{\text{orig}}$  as well as the target redshift distribution. We then sample a new redshift,  $z' \sim \text{loguniform}(0.95z_{\text{orig}}, \min(1.5(1 + z_{\text{orig}}) - 1, 5z_{\text{orig}}))$ .
- We fit a Gaussian process (GP) model for  $F$  with training observations  $\mathbf{X}$  queried at the training input values  $(\mathbf{t}, \mathbf{w})$ , and denote the predictive mean and variance of the GP as  $F', F'_{\text{err}}$ .
- Given the new redshift value  $z'$ , we rescale the timestamps and wavelengths of the original observations to account for the physical effects of the new redshift value:  $\mathbf{t}_{\text{new}} = \frac{1+z'}{1+z_{\text{orig}}}\mathbf{t}$ ,  $\mathbf{w}_{\text{new}} = \frac{1+z'}{1+z_{\text{orig}}}\mathbf{w}$ . We also randomly drop out 10% as well as a large swath of  $(\mathbf{t}_{\text{new}}, \mathbf{w}_{\text{new}})$  to simulate distinct observing seasons (telescope observing only occurs in the winter).
- We obtain GP predictions at test inputs  $\{F'(t_{\text{new}, i}, w_{\text{new}, j})\}_{i=1, j=1}^{T, W}$ ,  $\{F'_{\text{err}}(t_{\text{new}, i}, w_{\text{new}, i})\}_{i=1, j=1}^{T, W}$  and scale them by the log ratio of the new and original distances:

$$\tilde{\mathbf{X}}' = 10^{0.4(d(z') - d(z_{\text{orig}}))} \{F'(t_{\text{new}, i}, w_{\text{new}, j})\}_{i=1, j=1}^{T, W},$$

$$\tilde{\mathbf{X}}'_{\text{err}} = 10^{0.4(d(z') - d(z_{\text{orig}}))} \{F'_{\text{err}}(t_{\text{new}, i}, w_{\text{new}, j})\}_{i=1, j=1}^{T, W},$$

where  $d(z)$  is the distance corresponding to redshift  $z$ .

- We roughly model the observational noise of the telescope from the target data as a function of wavelength and sample  $\epsilon \in \mathbb{R}^W$  from it. We define

$$\mathbf{X}' = \{\tilde{\mathbf{X}}'_{:,j} + \epsilon_j\}_{j=1}^W, \mathbf{X}'_{\text{err}} = \left\{ \sqrt{\tilde{\mathbf{X}}'^2_{\text{err},:,j} + \epsilon_j^2} \right\}_{j=1}^W.$$

- We model the observational capabilities of the telescope to ensure that our augmented in-

put  $\mathbf{X}'$ ,  $\mathbf{X}'_{\text{err}}$  does not fall below the threshold of detection. We “accept” an augmented input  $\mathbf{X}'$ ,  $\mathbf{X}'_{\text{err}}$  if the signal-to-noise ratio (SNR) of at least two observations is over 5, i.e.  $\text{SNR}(\mathbf{X}'_{i,j}, \mathbf{X}'_{\text{err},i,j}) \geq 5$  for at least 2 of  $i \in \{1, \dots, T\}, j \in \{1, \dots, W\}$ . We define  $\text{SNR}(x, x_{\text{err}}) = \frac{|x|}{x_{\text{err}}}$ .

**Copy-Paste (Same Y) for iWildCam.** This augmentation strategy randomizes the backgrounds of wildlife images to reduce the model’s dependence on these spurious features for species classification. Specifically, a segmentation mask is applied to each image to separate the animal from the background, and the animal is “copy-pasted” into a new background from a camera that has observed that animal species. This was the best performing augmentation strategy from Gao et al. (2023).

**Stain Color Jitter for Camelyon17.** This augmentation, originally from Tellez et al. (2018), alters the pixel values of the slide images to emulate different staining procedures used by different hospitals. The augmentation uses a pre-specified Optical Density (OD) matrix to project images from RGB space to a three-channel hematoxylin, eosin, and DAB space before applying a random linear combination. This was the best performing augmentation strategy from Gao et al. (2023).

## Appendix C. Experimental Details

**AstroClassification and Redshifts.** For ASTROCLASSIFICATION and REDSHIFTS, we pretrain with a masked autoencoding objective:

$$\mathcal{L}_{\text{MAE}}(\phi) = \mathbb{E}_{x \sim P_U, x' \sim \mathcal{A}_{\text{pre}}(\cdot|x)}[(\phi(x') - x)^2] \quad (6.4)$$

We use an encoder-only Informer model (Zhou et al., 2021) with 8 encoder layers of 12 attention heads each. The model hidden dimension was chosen to be 768 and the layer MLPs have hidden dimension 256. Due to the 2-dimensional position data (each element of the time-series has an associated time and photometric band/wavelength) and irregular sampling of our dataset, we train a positional encoding based on learnable Fourier features following Li et al. (2021). We also select

a random window of length 300 from each example (and zero-pad examples with fewer than 300 observations) to produce inputs of uniform shape. We perform pretraining with a batch size of 256 and learning rate  $1e-4$  (selected from  $1e-3 \sim 1e-6$ ) for 75,000 steps. We finetune the pretrained model with linear probing for 20,000 steps (for pretrained models only) and learning rate  $1e-4$ , then fine-tuning for 10,000 steps at learning rate of  $4e-5$ . We increase the learning rate for models without pretraining to  $1e-4$  for FT. The REDSHIFTS task uses LP learning rate of  $5e-4$  and FT learning rate of  $1e-4$ . We decrease the learning rate per step with a linear scheduler.

**iWildCam.** For pretraining, we use ResNet-50 pretrained on ImageNet with SwAV (Caron et al., 2020). During fine-tuning, we train all models for 15 epochs with early stopping on OOD validation performance, following Gao et al. (2023). For pretrained models, we also do 10 epochs of linear probing before fine-tuning (LP-FT, Kumar et al., 2022) for 15 epochs, where the linear probe is trained with Adam and the linear probe weights used to initialize the fine-tuning stage is chosen with OOD validation performance. To reduce the noise in OOD results, for all methods we select the epoch in the last 5 epochs with the best OOD validation performance and report OOD test results with that version of the model. Following Gao et al. (2023), we allow for 10 hyperparameter tuning runs, where we sample the following hyperparameters independently from the following distributions: the linear probe learning rate ( $10^{\text{Uniform}[-3,-2]}$ ), fine-tuning learning rate ( $10^{\text{Uniform}[-5,-2]}$ ), and probability of applying the augmentation ( $\text{Uniform}[0.5, 0.9]$ ) and pick the hyperparameter configuration with the best OOD validation performance. For ERM and ERM+targeted augmentations, we use the tuned hyperparameters from Gao et al. (2023). To decrease the confidence interval due to an outlier seed, the reported performance of Connect Later is averaged over 15 seeds. All other results are averaged over 5 seeds.

**Camelyon17.** For pretraining, we use DenseNet121 pretrained on the unlabeled CAMELYON17-WILDS dataset presented in Sagawa et al. (2022) with SwAV (Caron et al., 2020). During fine-tuning, we train all models for 15 epochs with early stopping on OOD validation performance, following Gao et al. (2023). For pretrained models, we also do 10 epochs of linear probing before fine-tuning (LP-FT, Kumar et al., 2022) for 15 epochs, where the linear probe is trained with Adam and the linear probe weights used to initialize the fine-tuning stage is chosen with OOD validation

Table 6.7: Empirically estimated connectivity measures for `iWILDCAM-WILDS`, `ASTROCLASSIFICATION`, and `CAMELYON17-WILDS`. `iWILDCAM-WILDS` and `ASTROCLASSIFICATION` results are averaged over 15 randomly selected class-domain pairs, while `CAMELYON17-WILDS` results are averaged over all possible class-domain pairs.

	across-domain	across-class	across-both
<code>iWILDCAM-WILDS</code>	0.116	0.071	0.076
<code>ASTROCLASSIFICATION</code>	0.287	0.159	0.097
<code>CAMELYON17-WILDS</code>	0.16	0.198	0.152

performance. To reduce the noise in OOD results, for all methods we select the epoch with the best OOD validation performance and report OOD test results with that version of the model. Following Gao et al. (2023), we allow for 10 hyperparameter tuning runs, where we sample the following hyperparameters independently from the following distributions: the linear probe learning rate ( $10^{\text{Uniform}[-3, -2]}$ ), fine-tuning learning rate ( $10^{\text{Uniform}[-5, -2]}$ ), probability of applying the augmentation ( $\text{Uniform}[0.5, 0.9]$ ), and augmentation strength ( $\text{Uniform}[0.05, 0.1]$ ), and pick the hyperparameter configuration with the best OOD validation performance. All results are averaged over 20 seeds.

#### Appendix D. Empirical Estimates of Connectivity

We empirically estimate connectivity measures for all of the datasets we tested on following the procedure outlined in Appendix D of Shen et al. (2022). Specifically, we train binary classifiers from scratch to predict the class-domain pair of a given input example. We randomly select 15 class-domain pairs for `iWILDCAM-WILDS` and `ASTROCLASSIFICATION`, while for `CAMELYON17-WILDS` we use all class-domain pairs since `CAMELYON17-WILDS` is a binary classification task. We label these class-domain examples following Appendix D of Shen et al. (2022) and create a dataset with 80/10/10 train/validation/test split. We train using the same hyperparameters described in Appendix 6.7 for 3,000 steps with early stopping on the validation accuracy. Our results are presented in Table 6.7.



## Appendix E. Simple construction where Connect Later improves over pretraining or targeted augmentations alone

We give a simple construction for contrastive pretraining based on the construction in Proposition 3 (Appendix A.2) of Shen et al. (2022), where Connect Later improves over pretraining (standard fine-tuning) or targeted augmentations alone.

**Data distribution.** We consider binary classification with 2 domains. Let  $\mathcal{S} = \{x \in \mathcal{X} : d_x = 1\}$  and  $\mathcal{T} = \{x \in \mathcal{T} : d_x = 2\}$ , and assume that  $P_S$  and  $P_T$  are uniform over  $\mathcal{S}$  and  $\mathcal{T}$ . The unlabeled distribution for pretraining is the uniform distribution over  $\mathcal{X}$ . The source domain  $\mathcal{S} = \{1, 2\}$  contains 2 points and the target domain  $\mathcal{T} = \{3, 4, 5, 6, 7, 8\}$  contains 6 points. For simplicity, we let the labels  $y_x$  be a deterministic function of the input  $x$ . The label space is  $\mathcal{Y} = \{-1, 1\}$ . The label for  $x \in \{1, 3, 5, 7\}$  is  $y_x = 1$  and the label for  $x \in \{2, 4, 6, 8\}$  is  $y_x = -1$ . Only the source data is labeled.

**ERM with targeted augmentations.** ERM with targeted augmentations learns a model on source labeled data. To specialize to this section, the ERM objective is

$$\mathcal{L}_{\text{ERM}}(f) = \mathbb{E}_{x \sim P_S, x' \sim \mathcal{A}_{\text{ft}}(\cdot|x)}[\ell(f(x'), y_x)]. \quad (6.5)$$

ERM returns a classifier  $\hat{f}_{\text{erm}} \in \arg \min_f \mathcal{L}_{\text{ERM}}(f)$ .

**Spectral contrastive learning.** Following HaoChen et al. (2021) and Shen et al. (2022), we analyze contrastive learning from an augmentation graph perspective, where inputs  $x$  are connected via augmentations with edge weights  $S_+(x, x')$ , which represent the probability of  $x, x'$  being a positive pair (augmentations of the same input  $x$ ). For theoretical analysis, we analyze the spectral contrastive learning objective:

$$\mathcal{L}_{\text{pretrain}}(\phi) = -2 \cdot \mathbb{E}_{(x, x^+) \sim S_+} [\phi(x)^\top \phi(x^+)] + \mathbb{E}_{x, x' \sim P_U} \left[ \left( \phi(x)^\top \phi(x') \right)^2 \right]. \quad (6.6)$$

The result of pretraining to optimize the above objective is an encoder  $\hat{\phi} : \mathcal{X} \rightarrow \mathbb{R}^k$ .

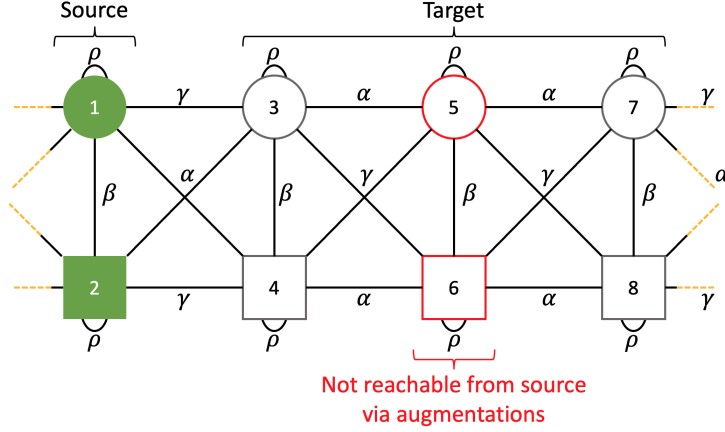


Figure 6.5: Example distribution of data and augmentations for contrastive learning where Connect Later improves OOD performance over contrastive pretraining+standard fine-tuning and ERM+targeted augmentations. The augmentation graph is similar to Shen et al. (2022) except the edge weights connecting 1,2 and 3,4 are swapped. The shapes represent classes, while the labeled data is shaded in green. The generic augmentation probabilities are marked as edge weights, where we assume that  $\alpha > \gamma + \beta$ . Here, targeted augmentations which first swap inputs 1 and 2 before applying a generic augmentation help to align the source and target. However, some target inputs are not reachable via augmentations from source inputs. Standard fine-tuning can generalize throughout the target domain, but only in conjunction with targeted augmentations that align the source and target. The orange dotted lines on the far ends connect to each other (the graph wraps around).

**Linear probing (fine-tuning step).** Instead of analyzing fine-tuning, we follow Shen et al. (2022) and analyze linear probing on top of the pretrained representations from the encoder. We train a linear model with parameters  $B \in \mathbb{R}^{r \times k}$ , where  $r$  is the number of classes. We minimize the objective:

$$\mathcal{L}(B) = \mathbb{E}_{x \sim P_S} \left[ \ell(B\hat{\phi}(x), y_x) \right] + \eta \|B\|_F^2, \quad (6.7)$$

where  $\ell$  is the squared loss and we take  $y_x \in \mathbb{R}^k$  to be a one-hot encoding of the class label. The resulting classifier is  $\hat{f}(x) = \arg \max_{i \in [r]} (\hat{B}\hat{\phi}(x))_i$ .

**Pretraining augmentations (Figure 6.5)** We define the pretraining augmentation distribution  $\mathcal{A}_{\text{pre}}(\cdot | x)$  to be

$$\mathcal{A}_{\text{pre}}(x' | x) = \begin{cases} \rho' & x = x' \\ \alpha' & \{x', x\} \in \{\{1, 4\}, \{3, 5\}, \{5, 7\}, \{2, 5\}, \{4, 6\}, \{6, 8\}, \{1, 8\}, \{2, 7\}\} \\ \beta' & \{x', x\} \in \{\{1, 2\}, \{3, 4\}, \{5, 6\}, \{7, 8\}\} \\ \gamma' & \{x', x\} \in \{\{1, 3\}, \{2, 4\}, \{3, 6\}, \{4, 5\}, \{5, 8\}, \{6, 7\}, \{1, 7\}, \{2, 8\}\} \end{cases} . \quad (6.8)$$

Notice that the weight between 1,3 is  $\gamma'$  and the weight between 1,4 is  $\alpha'$ , and the weights are similarly swapped for 2,4, and 2,5. We assume that  $\rho', \alpha', \beta'$ , and  $\gamma'$  are in  $(0, 1)$  and are distinct. We also assume that the augmentation probabilities satisfy  $\rho' > \max\{\alpha', \beta'\}$  and  $\min\{\alpha', \beta'\} > \gamma'$ . Following Shen et al. (2022), we can convert these to positive pair probabilities  $\rho, \alpha, \beta, \gamma$  with similar properties by renormalizing.

Given the above setting, the following is a simplified form of Proposition 3 from Shen et al. (2022), if we instead use the following augmentation distribution, which swaps the edge weight magnitudes that involve nodes 1 and 2:

$$\mathcal{A}_{\text{prop}}(x' | x) = \begin{cases} \rho' & x = x' \\ \alpha' & \{x', x\} \in \{\{1, 3\}, \{3, 5\}, \{5, 7\}, \{2, 4\}, \{4, 6\}, \{6, 8\}, \{1, 7\}, \{2, 8\}\} \\ \beta' & \{x', x\} \in \{\{1, 2\}, \{3, 4\}, \{5, 6\}, \{7, 8\}\} \\ \gamma' & \{x', x\} \in \{\{1, 4\}, \{2, 3\}, \{3, 6\}, \{4, 5\}, \{5, 8\}, \{6, 7\}, \{1, 8\}, \{2, 7\}\} \end{cases} . \quad (6.9)$$

**Proposition 1** (Shen et al. (2022)). *With the above construction for the input space  $\mathcal{X}$ , unlabeled distribution  $P_U$ , and data augmentation  $\mathcal{A}_{\text{prop}}$ , for some feature dimension  $k \in \mathbb{Z}^+$  a linear probe trained on contrastive pre-trained features achieves 0 target error:  $\mathcal{L}_{0-1}(\hat{f}) = 0$ . However, for all  $k \in \mathbb{Z}^+$ , there exists a minimizer  $\hat{f}_{\text{erm}}$  of the ERM objective (with data augmentations according to  $\mathcal{A}_{\text{prop}}$ ) that has non-zero error:  $\mathcal{L}_{0-1}(\hat{f}_{\text{erm}}) = 1/3$ .*

**ERM with targeted augmentations can get high OOD error.** In general, we proceed by defining the following targeted augmentation, which allows us to reduce to the setting of Proposition 1:

$$\mathcal{A}_{\text{ft}}(x' | x) = \begin{cases} 1 & \{x', x\} \in \{1, 4\}, \{2, 3\} \\ 1 & x = x' \text{ and } x \notin \{1, 2\} \\ 0 & \text{otherwise} \end{cases} \quad (6.10)$$

which transforms input 1 to 4 and the input 2 to 3, while keeping all other inputs the same. Since the ERM with augmentations objective will not contain a term involving inputs 5,6,7, or 8 and thus the prediction on these inputs do not affect the objective, there exists a minimizer of the ERM objective (Equation 6.5) that predicts the wrong label for inputs 5,6,7,8 and has target error  $2/3$ . This is because these nodes are unreachable via augmentations of the source inputs, and thus the ERM objective can be minimized with any arbitrary prediction on these inputs.

**Standard fine-tuning has high OOD error.** By Proposition 1, standard fine-tuning after contrastive pretraining has zero target (OOD) error when the pretraining augmentations do not have swapped edges. By symmetry, standard fine-tuning (contrastive pretraining + linear probing) on our augmentation graph with pretraining augmentations  $\mathcal{A}_{\text{pre}}$  outputs the opposite label for all target inputs, resulting in an OOD error of 1. This is because the source and target domains are misaligned in our augmentation graph.

**Connect Later achieves zero OOD error.** Connect Later applies targeted augmentations  $\mathcal{A}_{\text{ft}}$  during the linear probing step (on top of contrastive pretrained representations). This choice of targeted augmentations reduces to the setting of Proposition 1 where the labeled source domain consists of the inputs 3,4 instead. By the symmetry of the graph and applying Proposition 1, Connect Later achieves 0 OOD error.

## CHAPTER 7

### Conclusions and Future Directions

Time domain astronomy and SN Ia cosmology are entering a new era of big data, with next-generation surveys on the horizon that will discover more time domain objects and SNe Ia than ever before. This unprecedented data volume will allow us to perform SN Ia cosmological analyses with remarkable precision, discover new and rare types of time domain objects, and deepen our understanding of the progenitor population and physical processes underlying these objects. However, it also presents immediate challenges to our traditional analysis framework, such as our heavy reliance on spectroscopic follow-up observation to determine SN properties. This thesis investigates and proposes solutions to these issues to ensure optimal science returns for these datasets.

We study photometric supernova classification, which is an important step towards reducing our reliance on spectroscopy for SN Ia cosmology. We present SCONE, a convolutional neural network model capable of finding type Ia with  $> 99\%$  accuracy and classifying 6 SN types with  $> 95\%$  accuracy. SCONE is currently an integral part of DES, LSST, and Roman analysis pipelines. We also demonstrate that SCONE can classify 6 SN types with up to 75% accuracy on the night of trigger, which will be essential for optimal allocation of spectroscopic resources. We then turn our attention to measuring redshift for SNe Ia, typically a spectroscopic redshift measurement of the host galaxy. We investigate the directional light radius host galaxy matching technique for DES-like simulations and quantify the cosmological biases associated with incorrect host matches. We also present an alternative method for redshift estimation, Photo-zSNthesis, which predicts a redshift PDF from photometric SNe Ia data. Finally, we propose a new method for improving the robustness of machine learning algorithms trained on an unrepresentative training set, Connect Later, and demonstrate significant improvements on the Photometric LSST Astronomical Classification Challenge dataset as well as tumor detection and wildlife identification benchmark datasets.

The future is an exciting new frontier for time domain astrophysics and SN Ia cosmology. Large real-time data streams from surveys like LSST will necessitate the development of automated

photometric anomaly detection methods in addition to models that classify into known types. Anomaly detection methods will be able to surface new and rare time domain events that we could observe for the first time thanks to the power of the Vera C. Rubin Observatory and Roman Space Telescope. In addition to photometric time-series data, we often have other modes of data available for a particular time domain object (e.g., spectra, images, auxiliary information about the host galaxy environment). A powerful perspective on multi-modal data is as a natural data augmentation, which disentangles spurious features (e.g., wavelength or type of observation) from intrinsic physical properties (e.g., type of object). In astronomy, multi-modal models can combine different “views” of the same object to construct a more complete understanding of the object’s physical processes. Finally, the increasing reliance on machine learning models (e.g., for photometric classification or simulation-based inference) necessitates greater awareness of the robustness of these models and the dangers of unrepresentative training samples.

Looking forward for SN Ia cosmology, additional statistical infrastructure may allow us to maximize the constraining power of upcoming datasets. A statistical framework for incorporating uncertainties from photometric redshift estimates is needed for the LSST SN cosmology analysis, which will be the first to incorporate photometric SN Ia redshifts. In addition, current analysis pipelines implicitly assume a Gaussian likelihood for computing posteriors over cosmological parameters, while studies suggest that a more principled likelihood estimation can improve constraining power. Modern statistical techniques, such as simulation-based inference, is able to model arbitrary likelihood functions at a fraction of the computational cost of traditional methods and may offer a way forward.

This is an important moment in SN Ia and time domain science, as we are the ones catalyzing a multifaceted transition: from manual to automated, from spectroscopy- to photometry-oriented, from individual events to populations. The terabytes of data collected by LSST and the Roman Space Telescope will contain the answers to many pressing questions in cosmology and astrophysics, but we will need to build the tools to find them.

## BIBLIOGRAPHY

- T. M. C. Abbott, A. Alarcon, S. Allam, P. Andersen, F. Andrade-Oliveira, J. Annis, J. Asorey, S. Avila, D. Bacon, N. Banik, B. A. Bassett, E. Baxter, K. Bechtol, M. R. Becker, G. M. Bernstein, E. Bertin, J. Blazek, S. L. Bridle, D. Brooks, D. Brout, D. L. Burke, J. Calcino, H. Camacho, A. Campos, A. Carnero Rosell, D. Carollo, M. Carrasco Kind, J. Carretero, F. J. Castander, R. Cawthon, P. Challis, K. C. Chan, C. Chang, M. Childress, M. Crocce, C. E. Cunha, C. B. D'Andrea, L. N. da Costa, C. Davis, T. M. Davis, J. De Vicente, D. L. DePoy, J. DeRose, S. Desai, H. T. Diehl, J. P. Dietrich, S. Dodelson, P. Doel, A. Drlica-Wagner, T. F. Eifler, J. Elvin-Poole, J. Estrada, A. E. Evrard, E. Fernandez, B. Flaugher, R. J. Foley, P. Fosalba, J. Frieman, L. Galbany, J. García-Bellido, M. Gatti, E. Gaztanaga, D. W. Gerdes, T. Giannantonio, K. Glazebrook, D. A. Goldstein, D. Gruen, R. A. Gruendl, J. Gschwend, G. Gutierrez, W. G. Hartley, S. R. Hinton, D. L. Hollowood, K. Honscheid, J. K. Hoormann, B. Hoyle, D. Huterer, B. Jain, D. J. James, M. Jarvis, T. Jeltema, E. Kasai, S. Kent, R. Kessler, A. G. Kim, N. Kokron, E. Krause, R. Kron, K. Kuehn, N. Kuropatkin, O. Lahav, J. Lasker, P. Lemos, G. F. Lewis, T. S. Li, C. Lidman, M. Lima, H. Lin, E. Macaulay, N. MacCrann, M. A. G. Maia, M. March, J. Marriner, J. L. Marshall, P. Martini, R. G. McMahon, P. Melchior, F. Menanteau, R. Miquel, J. J. Mohr, E. Morganson, J. Muir, A. Möller, E. Neilsen, R. C. Nichol, B. Nord, R. L. C. Ogando, A. Palmese, Y. C. Pan, H. V. Peiris, W. J. Percival, A. A. Plazas, A. Porredon, J. Prat, A. K. Romer, A. Roodman, R. Rosenfeld, A. J. Ross, E. S. Rykoff, S. Samuroff, C. Sánchez, E. Sanchez, V. Scarpine, R. Schindler, M. Schubnell, D. Scolnic, L. F. Secco, S. Serrano, I. Sevilla-Noarbe, R. Sharp, E. Sheldon, M. Smith, M. Soares-Santos, F. Sobreira, N. E. Sommer, E. Swann, M. E. C. Swanson, G. Tarle, D. Thomas, R. C. Thomas, M. A. Troxel, B. E. Tucker, S. A. Uddin, P. Vielzeuf, A. R. Walker, M. Wang, N. Weaverdyck, R. H. Wechsler, J. Weller, B. Yanny, B. Zhang, Y. Zhang, J. Zuntz, and DES Collaboration. Cosmological Constraints from Multiple Probes in the Dark Energy Survey. *PRL*, 122(17):171301, May 2019. doi: 10.1103/PhysRevLett.122.171301.
- T. M. C. Abbott, S. Allam, P. Andersen, C. Angus, J. Asorey, A. Avelino, S. Avila, B. A. Bassett, K. Bechtol, G. M. Bernstein, E. Bertin, D. Brooks, D. Brout, P. Brown, D. L. Burke, J. Calcino, A. Carnero Rosell, D. Carollo, M. Carrasco Kind, J. Carretero, R. Casas, F. J. Castander, R. Cawthon, P. Challis, M. Childress, A. Clocchiatti, C. E. Cunha, C. B. D'Andrea, L. N. da Costa, C. Davis, T. M. Davis, J. De Vicente, D. L. DePoy, S. Desai, H. T. Diehl, P. Doel, A. Drlica-Wagner, T. F. Eifler, A. E. Evrard, E. Fernandez, A. V. Filippenko, D. A. Finley, B. Flaugher, R. J. Foley, P. Fosalba, J. Frieman, L. Galbany, J. García-Bellido, E. Gaztanaga, T. Giannantonio, K. Glazebrook, D. A. Goldstein, S. González-Gaitán, D. Gruen, R. A. Gruendl, J. Gschwend, R. R. Gupta, G. Gutierrez, W. G. Hartley, S. R. Hinton, D. L. Hollowood, K. Honscheid, J. K. Hoormann, B. Hoyle, D. J. James, T. Jeltema, M. W. G. Johnson, M. D. Johnson, E. Kasai, S. Kent, R. Kessler, A. G. Kim, R. P. Kirshner, E. Kovacs, E. Krause, R. Kron, K. Kuehn, S. Kuhlmann, N. Kuropatkin, O. Lahav, J. Lasker, G. F. Lewis, T. S. Li, C. Lidman, M. Lima, H. Lin, E. Macaulay, M. A. G. Maia, K. S. Mandel, M. March, J. Marriner, J. L. Marshall, P. Martini, F. Menanteau, C. J. Miller, R. Miquel, V. Miranda, J. J. Mohr, E. Morganson, D. Muthukrishna, A. Möller, E. Neilsen, R. C. Nichol, B. Nord, P. Nugent, R. L. C. Ogando, A. Palmese, Y.-C. Pan, A. A. Plazas, M. Pursiainen, A. K. Romer, A. Roodman, E. Roza, E. S. Rykoff, M. Sako, E. Sanchez, V. Scarpine, R. Schindler, M. Schubnell, D. Scolnic, S. Serrano, I. Sevilla-Noarbe, R. Sharp, M. Smith, M. Soares-Santos,

- F. Sobreira, N. E. Sommer, H. Spinka, E. Suchyta, M. Sullivan, E. Swann, G. Tarle, D. Thomas, R. C. Thomas, M. A. Troxel, B. E. Tucker, S. A. Uddin, A. R. Walker, W. Wester, P. Wiseman, R. C. Wolf, B. Yanny, B. Zhang, and Y. Zhang. First cosmology results using type ia supernovae from the dark energy survey: Constraints on cosmological parameters. *The Astrophysical Journal Letters*, 872(2):L30, February 2019a. ISSN 2041-8213. doi: 10.3847/2041-8213/ab04fa. URL <http://dx.doi.org/10.3847/2041-8213/ab04fa>.
- T. M. C. Abbott, S. Allam, P. Andersen, C. Angus, J. Asorey, A. Avelino, S. Avila, B. A. Bassett, K. Bechtol, G. M. Bernstein, E. Bertin, D. Brooks, D. Brout, P. Brown, D. L. Burke, J. Calcinò, A. Carnero Rosell, D. Carollo, M. Carrasco Kind, J. Carretero, R. Casas, F. J. Castander, R. Cawthon, P. Challis, M. Childress, A. Clocchiatti, C. E. Cunha, C. B. D'Andrea, L. N. da Costa, C. Davis, T. M. Davis, J. De Vicente, D. L. DePoy, S. Desai, H. T. Diehl, P. Doel, A. Drlica-Wagner, T. F. Eifler, A. E. Evrard, E. Fernandez, A. V. Filippenko, D. A. Finley, B. Flaugher, R. J. Foley, P. Fosalba, J. Frieman, L. Galbany, J. Garcí a-Bellido, E. Gaztanaga, T. Giannantonio, K. Glazebrook, D. A. Goldstein, S. González-Gaitán, D. Gruen, R. A. Gruendl, J. Gschwend, R. R. Gupta, G. Gutierrez, W. G. Hartley, S. R. Hinton, D. L. Hollowood, K. Honscheid, J. K. Hoormann, B. Hoyle, D. J. James, T. Jeltema, M. W. G. Johnson, M. D. Johnson, E. Kasai, S. Kent, R. Kessler, A. G. Kim, R. P. Kirshner, E. Kovacs, E. Krause, R. Kron, K. Kuehn, S. Kuhlmann, N. Kuropatkin, O. Lahav, J. Lasker, G. F. Lewis, T. S. Li, C. Lidman, M. Lima, H. Lin, E. Macaulay, M. A. G. Maia, K. S. Mandel, M. March, J. Marriner, J. L. Marshall, P. Martini, F. Menanteau, C. J. Miller, R. Miquel, V. Miranda, J. J. Mohr, E. Morganson, D. Muthukrishna, A. Möller, E. Neilsen, R. C. Nichol, B. Nord, P. Nugent, R. L. C. Ogando, A. Palmese, Y.-C. Pan, A. A. Plazas, M. Pursiainen, A. K. Romer, A. Roodman, E. Roza, E. S. Rykoff, M. Sako, E. Sanchez, V. Scarpine, R. Schindler, M. Schubnell, D. Scolnic, S. Serrano, I. Sevilla-Noarbe, R. Sharp, M. Smith, M. Soares-Santos, F. Sobreira, N. E. Sommer, H. Spinka, E. Suchyta, M. Sullivan, E. Swann, G. Tarle, D. Thomas, R. C. Thomas, M. A. Troxel, B. E. Tucker, S. A. Uddin, A. R. Walker, W. Wester, P. Wiseman, R. C. Wolf, B. Yanny, B. Zhang, and Y. Zhang and. First cosmology results using type ia supernovae from the dark energy survey: Constraints on cosmological parameters. *The Astrophysical Journal*, 872(2):L30, feb 2019b. doi: 10.3847/2041-8213/ab04fa.
- T. M. C. Abbott, S. Allam, P. Andersen, C. Angus, J. Asorey, A. Avelino, S. Avila, B. A. Bassett, K. Bechtol, G. M. Bernstein, E. Bertin, D. Brooks, D. Brout, P. Brown, D. L. Burke, J. Calcinò, A. Carnero Rosell, D. Carollo, M. Carrasco Kind, J. Carretero, R. Casas, F. J. Castander, R. Cawthon, P. Challis, M. Childress, A. Clocchiatti, C. E. Cunha, C. B. D'Andrea, L. N. da Costa, C. Davis, T. M. Davis, J. De Vicente, D. L. DePoy, S. Desai, H. T. Diehl, P. Doel, A. Drlica-Wagner, T. F. Eifler, A. E. Evrard, E. Fernandez, A. V. Filippenko, D. A. Finley, B. Flaugher, R. J. Foley, P. Fosalba, J. Frieman, L. Galbany, J. Garcí a-Bellido, E. Gaztanaga, T. Giannantonio, K. Glazebrook, D. A. Goldstein, S. González-Gaitán, D. Gruen, R. A. Gruendl, J. Gschwend, R. R. Gupta, G. Gutierrez, W. G. Hartley, S. R. Hinton, D. L. Hollowood, K. Honscheid, J. K. Hoormann, B. Hoyle, D. J. James, T. Jeltema, M. W. G. Johnson, M. D. Johnson, E. Kasai, S. Kent, R. Kessler, A. G. Kim, R. P. Kirshner, E. Kovacs, E. Krause, R. Kron, K. Kuehn, S. Kuhlmann, N. Kuropatkin, O. Lahav, J. Lasker, G. F. Lewis, T. S. Li, C. Lidman, M. Lima, H. Lin, E. Macaulay, M. A. G. Maia, K. S. Mandel, M. March, J. Marriner, J. L. Marshall, P. Martini, F. Menanteau, C. J. Miller, R. Miquel, V. Miranda, J. J. Mohr, E. Morganson, D. Muthukrishna, A. Möller, E. Neilsen, R. C. Nichol, B. Nord, P. Nugent, R. L. C. Ogando, A. Palmese, Y.-C. Pan, A. A.



- Plazas, M. Pursiainen, A. K. Romer, A. Roodman, E. Roza, E. S. Rykoff, M. Sako, E. Sanchez, V. Scarpine, R. Schindler, M. Schubnell, D. Scolnic, S. Serrano, I. Sevilla-Noarbe, R. Sharp, M. Smith, M. Soares-Santos, F. Sobreira, N. E. Sommer, H. Spinka, E. Suchyta, M. Sullivan, E. Swann, G. Tarle, D. Thomas, R. C. Thomas, M. A. Troxel, B. E. Tucker, S. A. Uddin, A. R. Walker, W. Wester, P. Wiseman, R. C. Wolf, B. Yanny, B. Zhang, and Y. Zhang and. First cosmology results using type ia supernovae from the dark energy survey: Constraints on cosmological parameters. *The Astrophysical Journal*, 872(2):L30, feb 2019c. doi: 10.3847/2041-8213/ab04fa. URL <https://doi.org/10.3847/2041-8213/ab04fa>.
- Tatiana Acero-Cuellar, Federica Bianco, Gregory Dobler, Masao Sako, and Helen Qu. What's the difference? the potential for convolutional neural networks for transient detection without template subtraction. *The Astronomical Journal*, 166(3):115, August 2023. ISSN 1538-3881. doi: 10.3847/1538-3881/ace9d8. URL <http://dx.doi.org/10.3847/1538-3881/ace9d8>.
- C. Aguirre, K. Pichara, and I. Becker. Deep multi-survey classification of variable stars. *MNRAS*, 482(4):5078–5092, February 2019. doi: 10.1093/mnras/sty2836.
- Jr. Allam, Tarek and Jason D. McEwen. Paying Attention to Astronomical Transients: Photometric Classification with the Time-Series Transformer. *arXiv e-prints*, art. arXiv:2105.06178, May 2021.
- Tarek Allam Jr. and Jason D. McEwen. Paying attention to astronomical transients: Introducing the time-series transformer for photometric classification, 2022.
- P. Armstrong, B. E. Tucker, A. Rest, R. Ridden-Harper, Y. Zenati, A. L. Piro, S. Hinton, C. Lidman, S. Margheim, G. Narayan, E. Shaya, P. Garnavich, D. Kasen, V. Villar, A. Zenteno, I. Arcavi, M. Drout, R. J. Foley, J. Wheeler, J. Anais, A. Campillay, D. Coulter, G. Dimitriadis, D. Jones, C. D. Kilpatrick, N. Muñoz-Elgueta, C. Rojas-Bravo, J. Vargas-González, J. Bulger, K. Chambers, M. Huber, T. Lowe, E. Magnier, B. J. Shappee, S. Smartt, K. W. Smith, T. Barclay, G. Barentsen, J. Dotson, M. Gully-Santiago, C. Hedges, S. Howell, A. Cody, K. Auchetl, A. Bódi, Zs Bognár, J. Brimacombe, P. Brown, B. Cseh, L. Galbany, D. Hiramatsu, T. W. S. Holoien, D. A. Howell, S. W. Jha, R. Könyves-Tóth, L. Kriskovics, C. McCully, P. Milne, J. Muñoz, Y. Pan, A. Pál, H. Sai, K. Sárneczky, N. Smith, Á. Sódor, R. Szabó, R. Szakáts, S. Valenti, J. Vinkó, X. Wang, K. Zhang, and G. Zsidi. SN2017jgh: a high-cadence complete shock cooling light curve of a SN IIb with the Kepler telescope. *MNRAS*, 507(3):3125–3138, November 2021. doi: 10.1093/mnras/stab2138.
- Peter Bandi, Oscar Geessink, Quirine Manson, Marcory Van Dijk, Maschenka Balkenhol, Meyke Hermsen, Babak Ehteshami Bejnordi, Byungjae Lee, Kyunghyun Paeng, Aoxiao Zhong, et al. From detection of individual metastases to classification of lymph node status at the patient level: the camelyon17 challenge. *IEEE transactions on medical imaging*, 38(2):550–560, 2018.
- Julian E Bautista, Romain Paviot, Mariana Vargas Magaña, Sylvain de la Torre, Sebastien Fromenteau, Hector Gil-Marín, Ashley J Ross, Etienne Burtin, Kyle S Dawson, Jiamin Hou, Jean-Paul Kneib, Arnaud de Mattia, Will J Percival, Graziano Rossi, Rita Tojeiro, Cheng Zhao, Gong-Bo Zhao, Shadab Alam, Joel Brownstein, Michael J Chapman, Peter D Choi, Chia-Hsun Chuang, Stéphanie Escoffier, Axel de la Macorra, Hélión du Mas des Bourboux, Faizan G Mo-

- hammad, Jeongin Moon, Eva-Maria Müller, Seshadri Nadathur, Jeffrey A Newman, Donald Schneider, Hee-Jong Seo, and Yuting Wang. The completed SDSS-IV extended Baryon Oscillation Spectroscopic Survey: measurement of the BAO and growth rate of structure of the luminous red galaxy sample from the anisotropic correlation function between redshifts 0.6 and 1. *Monthly Notices of the Royal Astronomical Society*, 500(1):736–762, 09 2020. ISSN 0035-8711. doi: 10.1093/mnras/staa2800. URL <https://doi.org/10.1093/mnras/staa2800>.
- G. Bazin, V. Ruhlmann-Kleider, N. Palanque-Delabrouille, J. Rich, E. Aubourg, P. Astier, C. Balland, S. Basa, R. G. Carlberg, A. Conley, D. Fouchez, J. Guy, D. Hardin, I. M. Hook, D. A. Howell, R. Pain, K. Perrett, C. J. Pritchett, N. Regnault, M. Sullivan, N. Fourmanoit, S. González-Gaitán, C. Lidman, S. Perlmutter, P. Ripoche, and E. S. Walker. Photometric selection of Type Ia supernovae in the Supernova Legacy Survey. *A&A*, 534:A43, October 2011. doi: 10.1051/0004-6361/201116898.
- Sara Beery, Elijah Cole, and Arvi Gjoka. The iwildcam 2020 competition dataset. *arXiv preprint arXiv:2004.10340*, 2020.
- Narciso Benitez. Bayesian photometric redshift estimation. *The Astrophysical Journal*, 536(2):571–583, jun 2000. doi: 10.1086/308947. URL <https://doi.org/10.1086%2F308947>.
- E. Bertin. Automated Morphometry with SExtractor and PSFEx. In I. N. Evans, A. Accomazzi, D. J. Mink, and A. H. Rots, editors, *Astronomical Data Analysis Software and Systems XX*, volume 442 of *Astronomical Society of the Pacific Conference Series*, page 435, July 2011.
- M. Betoule, R. Kessler, J. Guy, J. Mosher, D. Hardin, R. Biswas, P. Astier, P. El-Hage, M. König, S. Kuhlmann, J. Marriner, R. Pain, N. Regnault, C. Balland, B. A. Bassett, P. J. Brown, H. Campbell, R. G. Carlberg, F. Cellier-Holzem, D. Cinabro, A. Conley, C. B. D’Andrea, D. L. DePoy, M. Doi, R. S. Ellis, S. Fabbro, A. V. Filippenko, R. J. Foley, J. A. Frieman, D. Fouchez, L. Galbany, A. Goobar, R. R. Gupta, G. J. Hill, R. Hlozek, C. J. Hogan, I. M. Hook, D. A. Howell, S. W. Jha, L. Le Guillou, G. Leloudas, C. Lidman, J. L. Marshall, A. Möller, A. M. Mourão, J. Neveu, R. Nichol, M. D. Olmstead, N. Palanque-Delabrouille, S. Perlmutter, J. L. Prieto, C. J. Pritchett, M. Richmond, A. G. Riess, V. Ruhlmann-Kleider, M. Sako, K. Schahmaneche, D. P. Schneider, M. Smith, J. Sollerman, M. Sullivan, N. A. Walton, and C. J. Wheeler. Improved cosmological constraints from a joint analysis of the SDSS-II and SNLS supernova samples. *A&A*, 568:A22, August 2014. doi: 10.1051/0004-6361/201423413.
- John Blitzer, Ryan McDonald, and Fernando Pereira. Domain adaptation with structural correspondence learning. In *Empirical Methods in Natural Language Processing (EMNLP)*, 2006.
- Kyle Boone. Avocado: Photometric classification of astronomical transients with gaussian process augmentation. *The Astronomical Journal*, 158(6):257, Dec 2019a. ISSN 1538-3881. doi: 10.3847/1538-3881/ab5182. URL <http://dx.doi.org/10.3847/1538-3881/ab5182>.
- Kyle Boone. Avocado: Photometric classification of astronomical transients with gaussian process augmentation. *The Astronomical Journal*, 158(6):257, December 2019b. ISSN 1538-3881. doi:

10.3847/1538-3881/ab5182. URL <http://dx.doi.org/10.3847/1538-3881/ab5182>.

Kyle Boone. Parsnip: Generative models of transient light curves with physics-enabled deep learning. *The Astronomical Journal*, 162(6):275, December 2021. ISSN 1538-3881. doi: 10.3847/1538-3881/ac2a2d. URL <http://dx.doi.org/10.3847/1538-3881/ac2a2d>.

M. Boquien, D. Burgarella, Y. Roehlly, V. Buat, L. Ciesla, D. Corre, A. K. Inoue, and H. Salas. CIGALE: a python Code Investigating GALaxy Emission. *A&A*, 622:A103, February 2019. doi: 10.1051/0004-6361/201834156.

D. Brout, M. Sako, D. Scolnic, R. Kessler, C. B. D'Andrea, T. M. Davis, S. R. Hinton, A. G. Kim, J. Lasker, E. Macaulay, A. Möller, R. C. Nichol, M. Smith, M. Sullivan, R. C. Wolf, S. Allam, B. A. Bassett, P. Brown, F. J. Castander, M. Childress, R. J. Foley, L. Galbany, K. Herner, E. Kasai, M. March, E. Morganson, P. Nugent, Y.-C. Pan, R. C. Thomas, B. E. Tucker, W. Wester, T. M. C. Abbott, J. Annis, S. Avila, E. Bertin, D. Brooks, D. L. Burke, A. Carnero Rosell, M. Carrasco Kind, J. Carretero, M. Crocce, C. E. Cunha, L. N. da Costa, C. Davis, J. De Vicente, S. Desai, H. T. Diehl, P. Doel, T. F. Eifler, B. Flaugher, P. Fosalba, J. Frieman, J. Garcí a-Bellido, E. Gaztanaga, D. W. Gerdes, D. A. Goldstein, D. Gruen, R. A. Gruendl, J. Gschwend, G. Gutierrez, W. G. Hartley, D. L. Hollowood, K. Honscheid, D. J. James, K. Kuehn, N. Kuropatkin, O. Lahav, T. S. Li, M. Lima, J. L. Marshall, P. Martini, R. Miquel, B. Nord, A. A. Plazas, A. Roodman, E. S. Rykoff, E. Sanchez, V. Scarpine, R. Schindler, M. Schubnell, S. Serrano, I. Sevilla-Noarbe, M. Soares-Santos, F. Sobreira, E. Suchyta, M. E. C. Swanson, G. Tarle, D. Thomas, D. L. Tucker, A. R. Walker, B. Yanny, and Y. Zhang and. First cosmology results using type ia supernovae from the dark energy survey: Photometric pipeline and light-curve data release. *The Astrophysical Journal*, 874(1):106, mar 2019. doi: 10.3847/1538-4357/ab06c1. URL <https://doi.org/10.3847%2F1538-4357%2Fab06c1>.

Dillon Brout, Dan Scolnic, Brodie Popovic, Adam G. Riess, Anthony Carr, Joe Zuntz, Rick Kessler, Tamara M. Davis, Samuel Hinton, David Jones, W. D'Arcy Kenworthy, Erik R. Peterson, Khaled Said, Georgie Taylor, Noor Ali, Patrick Armstrong, Pranav Charvu, Arianna Dwomoh, Cole Meldorf, Antonella Palmese, Helen Qu, Benjamin M. Rose, Bruno Sanchez, Christopher W. Stubbs, Maria Vincenzi, Charlotte M. Wood, Peter J. Brown, Rebecca Chen, Ken Chambers, David A. Coulter, Mi Dai, Georgios Dimitriadis, Alexei V. Filippenko, Ryan J. Foley, Saurabh W. Jha, Lisa Kelsey, Robert P. Kirshner, Anais Möller, Jessie Muir, Seshadri Nadathur, Yen-Chen Pan, Armin Rest, Cesar Rojas-Bravo, Masao Sako, Matthew R. Siebert, Mat Smith, Benjamin E. Stahl, and Phil Wiseman. The Pantheon+ Analysis: Cosmological Constraints. *ApJ*, 938(2):110, October 2022. doi: 10.3847/1538-4357/ac8e04.

Robert J. Brunner, Andrew J. Connolly, Alexander S. Szalay, and Matthew A. Bershad. Toward more precise photometric redshifts: Calibration via CCD photometry. *The Astrophysical Journal*, 482(1):L21–L24, jun 1997. doi: 10.1086/310674. URL <https://doi.org/10.1086%2F310674>.

G. Bruzual and S. Charlot. Stellar population synthesis at the resolution of 2003. *MNRAS*, 344(4): 1000–1028, October 2003. doi: 10.1046/j.1365-8711.2003.06897.x.

R Buchs, C Davis, D Gruen, J DeRose, A Alarcon, G M Bernstein, C Sánchez, J Myles, A Roodman,

- S Allen, A Amon, A Choi, D C Masters, R Miquel, M A Troxel, R H Wechsler, T M C Abbott, J Annis, S Avila, K Bechtol, S L Bridle, D Brooks, E Buckley-Geer, D L Burke, A Carnero Rosell, M Carrasco Kind, J Carretero, F J Castander, R Cawthon, C B D'Andrea, L N da Costa, J De Vicente, S Desai, H T Diehl, P Doel, A Drlica-Wagner, T F Eifler, A E Evrard, B Flaugher, P Fosalba, J Frieman, J García-Bellido, E Gaztanaga, R A Gruendl, J Gschwend, G Gutierrez, W G Hartley, D L Hollowood, K Honscheid, D J James, K Kuehn, N Kuropatkin, M Lima, H Lin, M A G Maia, M March, J L Marshall, P Melchior, F Menanteau, R L C Ogando, A A Plazas, E S Rykoff, E Sanchez, V Scarpine, S Serrano, I Sevilla-Noarbe, M Smith, M Soares-Santos, F Sobreira, E Suchyta, M E C Swanson, G Tarle, D Thomas, V Vikram, and (DES Collaboration). Phenotypic redshifts with self-organizing maps: A novel method to characterize redshift distributions of source galaxies for weak lensing. *Monthly Notices of the Royal Astronomical Society*, 489(1):820–841, 08 2019. ISSN 0035-8711. doi: 10.1093/mnras/stz2162. URL <https://doi.org/10.1093/mnras/stz2162>.
- Daniela Calzetti, Lee Armus, Ralph C. Bohlin, Anne L. Kinney, Jan Koornneef, and Thaisa Storchi-Bergmann. The Dust Content and Opacity of Actively Star-forming Galaxies. *ApJ*, 533(2):682–695, April 2000. doi: 10.1086/308692.
- Heather Campbell, Chris B. D'Andrea, Robert C. Nichol, Masao Sako, Mathew Smith, Hubert Lampeitl, Matthew D. Olmstead, Bruce Bassett, Rahul Biswas, Peter Brown, David Cinabro, Kyle S. Dawson, Ben Dilday, Ryan J. Foley, Joshua A. Frieman, Peter Garnavich, Renee Hlozek, Saurabh W. Jha, Steve Kuhlmann, Martin Kunz, John Marriner, Ramon Miquel, Michael Richmond, Adam Riess, Donald P. Schneider, Jesper Sollerman, Matt Taylor, and Gong-Bo Zhao. Cosmology with Photometrically Classified Type Ia Supernovae from the SDSS-II Supernova Survey. *ApJ*, 763(2):88, February 2013. doi: 10.1088/0004-637X/763/2/88.
- Heather Campbell, Chris B D'Andrea, Robert C. Nichol, Masao Sako, Mathew Smith, Hubert Lampeitl, Matthew D. Olmstead, Bruce Bassett, Rahul Biswas, Peter Brown, David Cinabro, Kyle S. Dawson, Ben Dilday, Ryan J. Foley, Joshua A. Frieman, Peter Garnavich, Renee Hlozek, Saurabh W. Jha, Steve Kuhlmann, Martin Kunz, John Marriner, Ramon Miquel, Michael Richmond, Adam Riess, Donald P. Schneider, Jesper Sollerman, Matt Taylor, and Gong-Bo Zhao. Cosmology with photometrically classified type ia supernovae from the sdss-ii supernova survey. *The Astrophysical Journal*, 763(2):88, January 2013. ISSN 1538-4357. doi: 10.1088/0004-637x/763/2/88. URL <http://dx.doi.org/10.1088/0004-637X/763/2/88>.
- Michele Cappellari, Eric Emsellem, Davor Krajnović, Richard M. McDermid, Nicholas Scott, G. A. Verdoes Kleijn, Lisa M. Young, Katherine Alatalo, R. Bacon, Leo Blitz, Maxime Bois, Frédéric Bournaud, M. Bureau, Roger L. Davies, Timothy A. Davis, P. T. de Zeeuw, Pierre-Alain Duc, Sadegh Khochfar, Harald Kuntschner, Pierre-Yves Lablanche, Raffaella Morganti, Thorsten Naab, Tom Oosterloo, Marc Sarzi, Paolo Serra, and Anne-Marie Weijmans. The ATLAS<sup>3D</sup> project - I. A volume-limited sample of 260 nearby early-type galaxies: science goals and selection criteria. *MNRAS*, 413(2):813–836, May 2011. doi: 10.1111/j.1365-2966.2010.18174.x.
- Mathilde Caron, Ishan Misra, Julien Mairal, Priya Goyal, Piotr Bojanowski, and Armand Joulin. Unsupervised learning of visual features by contrasting cluster assignments. In *Advances in Neu-*

- R. Carrasco-Davis, E. Reyes, C. Valenzuela, F. Förster, P. A. Estévez, G. Pignata, F. E. Bauer, I. Reyes, P. Sánchez-Sáez, G. Cabrera-Vives, S. Eyheramendy, M. Catelan, J. Arredondo, E. Castillo-Navarrete, D. Rodríguez-Mancini, D. Ruz-Mieres, A. Moya, L. Sabatini-Gacitúa, C. Sepúlveda-Cobo, A. A. Mahabal, J. Silva-Farfán, E. Camacho-Iñiguez, and L. Galbany. Alert classification for the ALerCE broker system: The real-time stamp classifier. 162(6):231, nov 2021. doi: 10.3847/1538-3881/ac0ef1. URL <https://doi.org/10.3847/1538-3881/ac0ef1>.
- K. C. Chambers, E. A. Magnier, N. Metcalfe, H. A. Flewelling, M. E. Huber, C. Z. Waters, L. Denneau, P. W. Draper, D. Farrow, D. P. Finkbeiner, C. Holmberg, J. Koppenhoefer, P. A. Price, A. Rest, R. P. Saglia, E. F. Schlafly, S. J. Smartt, W. Sweeney, R. J. Wainscoat, W. S. Burgett, S. Chastel, T. Grav, J. N. Heasley, K. W. Hodapp, R. Jedicke, N. Kaiser, R. P. Kudritzki, G. A. Luppino, R. H. Lupton, D. G. Monet, J. S. Morgan, P. M. Onaka, B. Shiao, C. W. Stubbs, J. L. Tonry, R. White, E. Bañados, E. F. Bell, R. Bender, E. J. Bernard, M. Boegner, F. Boffi, M. T. Botticella, A. Calamida, S. Casertano, W. P. Chen, X. Chen, S. Cole, N. Deacon, C. Frenk, A. Fitzsimmons, S. Gezari, V. Gibbs, C. Goessl, T. Goggia, R. Gourgue, B. Goldman, P. Grant, E. K. Grebel, N. C. Hambly, G. Hasinger, A. F. Heavens, T. M. Heckman, R. Henderson, T. Henning, M. Holman, U. Hopp, W. H. Ip, S. Isani, M. Jackson, C. D. Keyes, A. M. Koekemoer, R. Kotak, D. Le, D. Liska, K. S. Long, J. R. Lucey, M. Liu, N. F. Martin, G. Masci, B. McLean, E. Mindel, P. Misra, E. Morganson, D. N. A. Murphy, A. Obaika, G. Narayan, M. A. Nieto-Santisteban, P. Norberg, J. A. Peacock, E. A. Pier, M. Postman, N. Primak, C. Rae, A. Rai, A. Riess, A. Riffeser, H. W. Rix, S. Röser, R. Russel, L. Rutz, E. Schilbach, A. S. B. Schultz, D. Scolnic, L. Strolger, A. Szalay, S. Seitz, E. Small, K. W. Smith, D. R. Soderblom, P. Taylor, R. Thomson, A. N. Taylor, A. R. Thakar, J. Thiel, D. Thilker, D. Unger, Y. Urata, J. Valenti, J. Wagner, T. Walder, F. Walter, S. P. Watters, S. Werner, W. M. Wood-Vasey, and R. Wyse. The Pan-STARRS1 Surveys. *arXiv e-prints*, art. arXiv:1612.05560, December 2016.
- Tom Charnock and Adam Moss. Deep recurrent neural networks for supernovae classification. *The Astrophysical Journal*, 837(2):L28, Mar 2017. ISSN 2041-8213. doi: 10.3847/2041-8213/aa603d. URL <http://dx.doi.org/10.3847/2041-8213/aa603d>.
- Tom Charnock and Adam Moss. Deep Recurrent Neural Networks for Supernovae Classification. *ApJ*, 837(2):L28, March 2017. doi: 10.3847/2041-8213/aa603d.
- R. Chen, D. Scolnic, E. Rozo, E. S. Rykoff, B. Popovic, R. Kessler, M. Vincenzi, T. M. Davis, P. Armstrong, D. Brout, L. Galbany, L. Kelsey, C. Lidman, A. Möller, B. Rose, M. Sako, M. Sullivan, G. Taylor, P. Wiseman, J. Asorey, A. Carr, C. Conselice, K. Kuehn, G. F. Lewis, E. Macaulay, M. Rodriguez-Monroy, B. E. Tucker, T. M. C. Abbott, M. Agüena, S. Allam, F. Andrade-Oliveira, J. Annis, D. Bacon, E. Bertin, S. Bocquet, D. Brooks, D. L. Burke, A. Carnero Rosell, M. Carrasco Kind, J. Carretero, R. Cawthon, M. Costanzi, L. N. da Costa, M. E. S. Pereira, S. Desai, H. T. Diehl, P. Doel, S. Everett, I. Ferrero, B. Flaugher, D. Friedel, J. Frieman, J. García-Bellido, M. Gatti, E. Gaztanaga, D. Gruen, S. R. Hinton, D. L. Hollowood, K. Honscheid, D. J. James, O. Lahav, M. Lima, M. March, F. Menanteau, R. Miquel, R. Morgan, A. Palmese, F. Paz-Chinchón, A. Pieres, A. A. Plazas Malagón, J. Prat, A. K. Romer, A. Roodman, E. Sanchez, M. Schubnell,

- S. Serrano, I. Sevilla-Noarbe, M. Smith, M. Soares-Santos, E. Suchyta, G. Tarle, D. Thomas, C. To, D. L. Tucker, and T. N. Varga. Measuring Cosmological Parameters with Type Ia Supernovae in redMaGiC Galaxies. *ApJ*, 938(1):62, October 2022. doi: 10.3847/1538-4357/ac8b82.
- Ting Chen, Simon Kornblith, Mohammad Norouzi, and Geoffrey Hinton. A simple framework for contrastive learning of visual representations. In *International Conference on Machine Learning (ICML)*, pages 1597–1607, 2020.
- Alison L. Coil, Michael R. Blanton, Scott M. Burles, Richard J. Cool, Daniel J. Eisenstein, John Moustakas, Kenneth C. Wong, Guangtun Zhu, James Aird, Rebecca A. Bernstein, Adam S. Bolton, and David W. Hogg. The PRISM MUlti-object Survey (PRIMUS). I. Survey Overview and Characteristics. *ApJ*, 741(1):8, November 2011. doi: 10.1088/0004-637X/741/1/8.
- Matthew Colless, Gavin Dalton, Steve Maddox, Will Sutherland, Peder Norberg, Shaun Cole, Joss Bland-Hawthorn, Terry Bridges, Russell Cannon, Chris Collins, Warrick Couch, Nicholas Cross, Kathryn Deeley, Roberto De Propriis, Simon P. Driver, George Efstathiou, Richard S. Ellis, Carlos S. Frenk, Karl Glazebrook, Carole Jackson, Ofer Lahav, Ian Lewis, Stuart Lumsden, Darren Madgwick, John A. Peacock, Bruce A. Peterson, Ian Price, Mark Seaborne, and Keith Taylor. The 2dF Galaxy Redshift Survey: spectra and redshifts. *MNRAS*, 328(4):1039–1063, December 2001. doi: 10.1046/j.1365-8711.2001.04902.x.
- A. Conley, J. Guy, M. Sullivan, N. Regnault, P. Astier, C. Balland, S. Basa, R. G. Carlberg, D. Fouchez, D. Hardin, I. M. Hook, D. A. Howell, R. Pain, N. Palanque-Delabrouille, K. M. Perrett, C. J. Pritchett, J. Rich, V. Ruhlmann-Kleider, D. Balam, S. Baumont, R. S. Ellis, S. Fabbro, H. K. Fakhouri, N. Fourmanoit, S. González-Gaitán, M. L. Graham, M. J. Hudson, E. Hsiao, T. Kronborg, C. Lidman, A. M. Mourao, J. D. Neill, S. Perlmutter, P. Ripoche, N. Suzuki, and E. S. Walker. Supernova constraints and systematic uncertainties from the first three years of the supernova legacy survey\*. *The Astrophysical Journal Supplement Series*, 192(1):1, dec 2010. doi: 10.1088/0067-0049/192/1/1. URL <https://dx.doi.org/10.1088/0067-0049/192/1/1>.
- Michael C. Cooper et al. The Arizona CDFS Environment Survey (ACES): A Magellan/IMACS Spectroscopic Survey of the Chandra Deep Field South. *Mon. Not. Roy. Astron. Soc.*, 425:2116, 2012. doi: 10.1111/j.1365-2966.2012.21524.x.
- Kyle Cranmer, Johann Brehmer, and Gilles Louppe. The frontier of simulation-based inference. *Proceedings of the National Academy of Sciences*, 117(48):30055–30062, May 2020. ISSN 1091-6490. doi: 10.1073/pnas.1912789117. URL <http://dx.doi.org/10.1073/pnas.1912789117>.
- Ekin D Cubuk, Barret Zoph, Dandelion Mane, Vijay Vasudevan, and Quoc V Le. Autoaugment: Learning augmentation policies from data. In *Computer Vision and Pattern Recognition (CVPR)*, 2019.
- Ekin D Cubuk, Barret Zoph, Jonathon Shlens, and Quoc V Le. Randaugment: Practical automated data augmentation with a reduced search space. In *Computer Vision and Pattern Recognition (CVPR)*, pages 702–703, 2020.

- Mi Dai, Steve Kuhlmann, Yun Wang, and Eve Kovacs. Photometric classification and redshift estimation of lsst supernovae. *Monthly Notices of the Royal Astronomical Society*, 477(3):4142–4151, Apr 2018. ISSN 1365-2966. doi: 10.1093/mnras/sty965. URL <http://dx.doi.org/10.1093/mnras/sty965>.
- Felipe M. F. de Oliveira, Marcelo Vargas dos Santos, and Ribamar R. R. Reis. Data-driven photometric redshift estimation from type Ia supernovae light curves. *Mon. Not. Roy. Astron. Soc.*, 518(2):2385–2397, 2022. doi: 10.1093/mnras/stac3202.
- Morris H. DeGroot and Stephen E. Fienberg. The comparison and evaluation of forecasters. *Journal of the Royal Statistical Society. Series D (The Statistician)*, 32(1/2):12–22, 1983. ISSN 00390526, 14679884. URL <http://www.jstor.org/stable/2987588>.
- F. Delgado and G. Schumacher. The LSST OCS scheduler design. In *Society of Photo-Optical Instrumentation Engineers (SPIE) Conference Series*, volume 9149 of *Society of Photo-Optical Instrumentation Engineers (SPIE) Conference Series*, page 91490G, August 2014. doi: 10.1117/12.2056871.
- DES Collaboration, T. M. C. Abbott, M. Acevedo, M. Agüena, A. Alarcon, S. Allam, O. Alves, A. Amon, F. Andrade-Oliveira, J. Annis, P. Armstrong, J. Asorey, S. Avila, D. Bacon, B. A. Bassett, K. Bechtol, P. H. Bernardinelli, G. M. Bernstein, E. Bertin, J. Blazek, S. Bocquet, D. Brooks, D. Brout, E. Buckley-Geer, D. L. Burke, H. Camacho, R. Camilleri, A. Campos, A. Carnero Rosell, D. Carollo, A. Carr, J. Carretero, F. J. Castander, R. Cawthon, C. Chang, R. Chen, A. Choi, C. Conselice, M. Costanzi, L. N. da Costa, M. Crocce, T. M. Davis, D. L. DePoy, S. Desai, H. T. Diehl, M. Dixon, S. Dodelson, P. Doel, C. Doux, A. Drlica-Wagner, J. Elvin-Poole, S. Everett, I. Ferrero, A. Ferté, B. Flaugher, R. J. Foley, P. Fosalba, D. Friedel, J. Frieman, C. Frohmaier, L. Galbany, J. García-Bellido, M. Gatti, E. Gaztanaga, G. Giannini, K. Glazebrook, O. Graur, D. Gruen, R. A. Gruendl, G. Gutierrez, W. G. Hartley, K. Herner, S. R. Hinton, D. L. Hollowood, K. Honscheid, D. Huterer, B. Jain, D. J. James, N. Jeffrey, L. Kelsey, S. Kent, R. Kessler, A. G. Kim, R. P. Kirshner, E. Kovacs, K. Kuehn, O. Lahav, J. Lee, S. Lee, G. F. Lewis, T. S. Li, C. Lidman, H. Lin, J. L. Marshall, P. Martini, J. Mena-Fernández, F. Menanteau, R. Miquel, J. J. Mohr, J. Mould, J. Muir, A. Möller, E. Neilsen, R. C. Nichol, P. Nugent, R. L. C. Ogando, A. Palmese, Y. C. Pan, M. Paterno, W. J. Percival, M. E. S. Pereira, A. Pieres, A. A. Plazas Malagón, B. Popovic, A. Porredon, J. Prat, H. Qu, M. Raveri, M. Rodríguez-Monroy, A. K. Romer, A. Roodman, B. Rose, M. Sako, E. Sanchez, D. Sanchez Cid, M. Schubnell, D. Scolnic, I. Sevilla-Noarbe, P. Shah, J. Allyn. Smith, M. Smith, M. Soares-Santos, E. Suchyta, M. Sullivan, N. Suntzeff, M. E. C. Swanson, B. O. Sánchez, G. Tarle, G. Taylor, D. Thomas, C. To, M. Toy, M. A. Troxel, B. E. Tucker, D. L. Tucker, S. A. Uddin, M. Vincenzi, A. R. Walker, N. Weaverdyck, R. H. Wechsler, J. Weller, W. Wester, P. Wiseman, M. Yamamoto, F. Yuan, B. Zhang, and Y. Zhang. The dark energy survey: Cosmology results with 1500 new high-redshift type Ia supernovae using the full 5-year dataset, 2024.
- Jacob Devlin, Ming-Wei Chang, Kenton Lee, and Kristina Toutanova. BERT: Pre-training of deep bidirectional transformers for language understanding. In *Association for Computational Linguistics (ACL)*, pages 4171–4186, 2019.
- Terrance DeVries and Graham W Taylor. Improved regularization of convolutional neural networks

with cutout. *arXiv preprint arXiv:1708.04552*, 2017.

Felipe M F de Oliveira, Marcelo Vargas dos Santos, and Ribamar R R Reis. Data-driven photometric redshift estimation from type Ia supernovae light curves. *Monthly Notices of the Royal Astronomical Society*, 518(2):2385–2397, 11 2022. ISSN 0035-8711. doi: 10.1093/mnras/stac3202. URL <https://doi.org/10.1093/mnras/stac3202>.

Benjamin Dilday, Bruce Bassett, Andrew Becker, Ralf Bender, Francisco Castander, David Cinabro, Joshua A. Frieman, Lluís Galbany, Peter Garnavich, Ariel Goobar, Ulrich Hopp, Yutaka Ihara, Saurabh W. Jha, Richard Kessler, Hubert Lampeitl, John Marriner, Ramon Miquel, Mercedes Mollá, Robert C. Nichol, Jakob Nordin, Adam G. Riess, Masao Sako, Donald P. Schneider, Mathew Smith, Jesper Sollerman, J. Craig Wheeler, Linda Östman, Dmitry Bizyaev, Howard Brewington, Elena Malanushenko, Viktor Malanushenko, Dan Oravetz, Kaike Pan, Audrey Simmons, and Stephanie Snedden. A Measurement of the Rate of Type Ia Supernovae in Galaxy Clusters from the SDSS-II Supernova Survey. *ApJ*, 715(2):1021–1035, June 2010. doi: 10.1088/0004-637X/715/2/1021.

D’Isanto, A. and Polsterer, K. L. Photometric redshift estimation via deep learning - generalized and pre-classification-less, image based, fully probabilistic redshifts. *A&A*, 609:A111, 2018. doi: 10.1051/0004-6361/201731326. URL <https://doi.org/10.1051/0004-6361/201731326>.

C. Donoso-Oliva, I. Becker, P. Protopapas, G. Cabrera-Vives, M. Vishnu, and H. Vardhan. AS-TROMER. *Astronomy & Astrophysics*, 670:A54, feb 2023. doi: 10.1051/0004-6361/202243928. URL <https://doi.org/10.1051/0004-6361/202243928>.

Simon P. Driver, Peder Norberg, Ivan K. Baldry, Steven P. Bamford, Andrew M. Hopkins, Jochen Liske, Jon Loveday, John A. Peacock, D. T. Hill, L. S. Kelvin, A. S. G. Robotham, N. J. G. Cross, H. R. Parkinson, M. Prescott, C. J. Conselice, L. Dunne, S. Brough, H. Jones, R. G. Sharp, E. van Kampen, S. Oliver, I. G. Roseboom, J. Bland-Hawthorn, S. M. Croom, S. Ellis, E. Cameron, S. Cole, C. S. Frenk, W. J. Couch, A. W. Graham, R. Proctor, R. De Propris, I. F. Doyle, E. M. Edmondson, R. C. Nichol, D. Thomas, S. A. Eales, M. J. Jarvis, K. Kuijken, O. Lahav, B. F. Madore, M. Seibert, M. J. Meyer, L. Staveley-Smith, S. Phillipps, C. C. Popescu, A. E. Sansom, W. J. Sutherland, R. J. Tuffs, and S. J. Warren. GAMA: towards a physical understanding of galaxy formation. *Astronomy and Geophysics*, 50(5):5.12–5.19, October 2009. doi: 10.1111/j.1468-4004.2009.50512.x.

A. V. Filippenko. Supernovae and Their Massive Star Progenitors. In R. Humphreys and K. Stanek, editors, *The Fate of the Most Massive Stars*, volume 332 of *Astronomical Society of the Pacific Conference Series*, page 34, September 2005.

B. Flaugher, H. T. Diehl, K. Honscheid, T. M. C. Abbott, O. Alvarez, R. Angstadt, J. T. Annis, M. Antonik, O. Ballester, L. Beaufore, G. M. Bernstein, R. A. Bernstein, B. Bigelow, M. Bonati, D. Boprie, D. Brooks, E. J. Buckley-Geer, J. Campa, L. Cardiel-Sas, F. J. Castander, J. Castilla, H. Cease, J. M. Cela-Ruiz, S. Chappa, E. Chi, C. Cooper, L. N. da Costa, E. Dede, G. Derylo, D. L. DePoy, J. de Vicente, P. Doel, A. Drlica-Wagner, J. Eiting, A. E. Elliott, J. Emes, J. Estrada, A. Fausti Neto, D. A. Finley, R. Flores, J. Frieman, D. Gerdes, M. D. Gladders, B. Gregory, G. R. Gutierrez, J. Hao,



- S. E. Holland, S. Holm, D. Huffman, C. Jackson, D. J. James, M. Jonas, A. Karcher, I. Karliner, S. Kent, R. Kessler, M. Kozlovsky, R. G. Kron, D. Kubik, K. Kuehn, S. Kuhlmann, K. Kuk, O. Lahav, A. Lathrop, J. Lee, M. E. Levi, P. Lewis, T. S. Li, I. Mandrichenko, J. L. Marshall, G. Martinez, K. W. Merritt, R. Miquel, F. Muñoz, E. H. Neilsen, R. C. Nichol, B. Nord, R. Ogando, J. Olsen, N. Palaio, K. Patton, J. Peoples, A. A. Plazas, J. Rauch, K. Reil, J. P. Rheault, N. A. Roe, H. Rogers, A. Roodman, E. Sanchez, V. Scarpine, R. H. Schindler, R. Schmidt, R. Schmitt, M. Schubnell, K. Schultz, P. Schurter, L. Scott, S. Serrano, T. M. Shaw, R. C. Smith, M. Soares-Santos, A. Stefanik, W. Stuermer, E. Suchyta, A. Sypniewski, G. Tarle, J. Thaler, R. Tighe, C. Tran, D. Tucker, A. R. Walker, G. Wang, M. Watson, C. Weaverdyck, W. Wester, R. Woods, B. Yanny, and DES Collaboration. The Dark Energy Camera. *AJ*, 150(5):150, November 2015. doi: 10.1088/0004-6256/150/5/150.
- Ryan J. Foley and Kaisey Mandel. Classifying Supernovae Using Only Galaxy Data. *ApJ*, 778(2): 167, December 2013. doi: 10.1088/0004-637X/778/2/167.
- Francisco Förster, Alejandra M. Muñoz Arancibia, Ignacio Reyes-Jainaga, Alexander Gagliano, Dylan Britt, Sara Cuellar-Carrillo, Felipe Figueroa-Tapia, Ava Polzin, Yara Yousef, Javier Arredondo, Diego Rodríguez-Mancini, Javier Correa-Orellana, Amelia Bayo, Franz E. Bauer, Márcio Catelan, Guillermo Cabrera-Vives, Raya Dastidar, Pablo A. Estévez, Giuliano Pignata, Lorena Hernández-García, Pablo Huijse, Esteban Reyes, Paula Sánchez-Sáez, Mauricio Ramírez, Daniela Grandón, Jonathan Pineda-García, Francisca Chabour-Barra, and Javier Silva-Farfán. DELIGHT: Deep Learning Identification of Galaxy Hosts of Transients using Multiresolution Images. *AJ*, 164(5):195, November 2022. doi: 10.3847/1538-3881/ac912a.
- Wendy L. Freedman, Barry F. Madore, Dylan Hatt, Taylor J. Hoyt, In Sung Jang, Rachael L. Beaton, Christopher R. Burns, Myung Gyoon Lee, Andrew J. Monson, Jillian R. Neeley, M. M. Phillips, Jeffrey A. Rich, and Mark Seibert. The Carnegie-Chicago Hubble Program. VIII. An Independent Determination of the Hubble Constant Based on the Tip of the Red Giant Branch. *ApJ*, 882(1): 34, September 2019. doi: 10.3847/1538-4357/ab2f73.
- Joshua A. Frieman, Bruce Bassett, Andrew Becker, Changsu Choi, David Cinabro, Fritz DeJongh, Darren L. Depoy, Ben Dilday, Mamoru Doi, Peter M. Garnavich, Craig J. Hogan, Jon Holtzman, Myungshin Im, Saurabh Jha, Richard Kessler, Kohki Konishi, Hubert Lampeitl, John Marinier, Jennifer L. Marshall, David McGinnis, Gajus Miknaitis, Robert C. Nichol, Jose Luis Prieto, Adam G. Riess, Michael W. Richmond, Roger Romani, Masao Sako, Donald P. Schneider, Mathew Smith, Naohiro Takanashi, Kouichi Tokita, Kurt van der Heyden, Naoki Yasuda, Chen Zheng, Jennifer Adelman-McCarthy, James Annis, Roberto J. Assef, John Barentine, Ralf Bender, Roger D. Blandford, William N. Boroski, Malcolm Bremer, Howard Brewington, Chris A. Collins, Arlin Crotts, Jack Dembicky, Jason Eastman, Alastair Edge, Edmond Edmondson, Edward Elson, Michael E. Eyler, Alexei V. Filippenko, Ryan J. Foley, Stephan Frank, Ariel Goobar, Tina Gueth, James E. Gunn, Michael Harvanek, Ulrich Hopp, Yutaka Ihara, Želko Ivezić, Steven Kahn, Jared Kaplan, Stephen Kent, William Ketzeback, Scott J. Kleinman, Wolfram Kollatschny, Richard G. Kron, Jurek Krzesiński, Dennis Lamenti, Giorgos Leloudas, Huan Lin, Daniel C. Long, John Lucey, Robert H. Lupton, Elena Malanushenko, Viktor Malanushenko, Russet J. McMillan, Javier Mendez, Christopher W. Morgan, Tomoki Morokuma, Atsuko Nitta, Linda Ostman, Kaike Pan, Constance M. Rockosi, A. Kathy Romer, Pilar Ruiz-Lapuente, Gabrelle Saurage, Katie

- Schlesinger, Stephanie A. Snedden, Jesper Sollerman, Chris Stoughton, Maximilian Stritzinger, Mark Subba Rao, Douglas Tucker, Petri Vaisanen, Linda C. Watson, Shannon Watters, J. Craig Wheeler, Brian Yanny, and Donald York. The Sloan Digital Sky Survey-II Supernova Survey: Technical Summary. *AJ*, 135(1):338–347, January 2008. doi: 10.1088/0004-6256/135/1/338.
- C. Frohmaier, C. R. Angus, M. Vincenzi, M. Sullivan, M. Smith, P. E. Nugent, S. B. Cenko, A. Gal-Yam, S. R. Kulkarni, N. M. Law, and R. M. Quimby. From core collapse to superluminous: the rates of massive stellar explosions from the Palomar Transient Factory. *MNRAS*, 500(4):5142–5158, January 2021. doi: 10.1093/mnras/staa3607.
- Chris Frohmaier, Mark Sullivan, Kate Maguire, and Peter Nugent. The Volumetric Rate of Calcium-rich Transients in the Local Universe. *ApJ*, 858(1):50, May 2018. doi: 10.3847/1538-4357/aabc0b.
- Alex Gagliano, Gautham Narayan, Andrew Engel, Matias Carrasco Kind, and LSST Dark Energy Science Collaboration. GHOST: Using Only Host Galaxy Information to Accurately Associate and Distinguish Supernovae. *ApJ*, 908(2):170, February 2021. doi: 10.3847/1538-4357/abd02b.
- Yaroslav Ganin, Evgeniya Ustinova, Hana Ajakan, Pascal Germain, Hugo Larochelle, Francois Laviolette, Mario March, and Victor Lempitsky. Domain-adversarial training of neural networks. *Journal of Machine Learning Research (JMLR)*, 17, 2016.
- Irena Gao, Shiori Sagawa, Pang Wei Koh, Tatsunori Hashimoto, and Percy Liang. Out-of-domain robustness via targeted augmentations. In *International Conference on Machine Learning (ICML)*, 2023.
- G. Giannini, A. Alarcon, M. Gatti, A. Porredon, M. Croce, G. M. Bernstein, R. Cawthon, C. Sánchez, C. Doux, J. Elvin-Poole, M. Raveri, J. Myles, A. Amon, S. Allam, O. Alves, F. Andrade-Oliveira, E. Baxter, K. Bechtol, M. R. Becker, J. Blazek, H. Camacho, A. Campos, A. Carnero Rosell, M. Carrasco Kind, A. Choi, J. Cordero, J. De Vicente, J. DeRose, H. T. Diehl, S. Dodelson, A. Drlica-Wagner, K. Eckert, S. Everett, X. Fang, A. Farahi, P. Fosalba, O. Friedrich, D. Gruen, R. A. Gruendl, J. Gschwend, I. Harrison, W. G. Hartley, E. M. Huff, M. Jarvis, E. Krause, N. Kuropatkin, P. Lemos, N. MacCrann, J. McCullough, J. Muir, S. Pandey, J. Prat, M. Rodriguez-Monroy, A. J. Ross, E. S. Rykoff, S. Samuroff, L. F. Secco, I. Sevilla-Noarbe, E. Sheldon, M. A. Troxel, D. L. Tucker, N. Weaverdyck, B. Yanny, B. Yin, Y. Zhang, T. M. C. Abbott, M. Aguena, D. Bacon, E. Bertin, S. Bocquet, D. Brooks, D. L. Burke, J. Carretero, F. J. Castander, M. Costanzi, L. N. da Costa, M. E. S. Pereira, S. Desai, P. Doel, I. Ferrero, B. Flaugher, D. Friedel, J. Frieman, J. García-Bellido, D. W. Gerdes, G. Gutierrez, S. R. Hinton, D. L. Hollowood, K. Honscheid, D. J. James, S. Kent, K. Kuehn, O. Lahav, C. Lidman, M. Lima, P. Melchior, J. Mena-Fernández, F. Menanteau, R. Miquel, R. L. C. Ogando, M. Paterno, F. Paz-Chinchón, A. Pieres, A. A. Plazas Malagón, A. Roodman, E. Sanchez, V. Scarpine, M. Smith, E. Suchyta, M. E. C. Swanson, G. Tarle, D. Thomas, C. To, and M. Vincenzi. Dark Energy Survey Year 3 Results: Redshift Calibration of the MagLim Lens Sample from the combination of SOMPZ and clustering and its impact on Cosmology. *arXiv e-prints*, art. arXiv:2209.05853, September 2022.
- D. A. Goldstein, C. B. D’Andrea, J. A. Fischer, R. J. Foley, R. R. Gupta, R. Kessler, A. G. Kim, R. C.

- Nichol, P. E. Nugent, A. Papadopoulos, M. Sako, M. Smith, M. Sullivan, R. C. Thomas, W. Wester, R. C. Wolf, F. B. Abdalla, M. Banerji, A. Benoit-Lévy, E. Bertin, D. Brooks, A. Carnero Rosell, F. J. Castander, L. N. da Costa, R. Covarrubias, D. L. DePoy, S. Desai, H. T. Diehl, P. Doel, T. F. Eifler, A. Fausti Neto, D. A. Finley, B. Flaugher, P. Fosalba, J. Frieman, D. Gerdes, D. Gruen, R. A. Gruendl, D. James, K. Kuehn, N. Kuropatkin, O. Lahav, T. S. Li, M. A. G. Maia, M. Makler, M. March, J. L. Marshall, P. Martini, K. W. Merritt, R. Miquel, B. Nord, R. Ogando, A. A. Plazas, A. K. Romer, A. Roodman, E. Sanchez, V. Scarpine, M. Schubnell, I. Sevilla-Noarbe, R. C. Smith, M. Soares-Santos, F. Sobreira, E. Suchyta, M. E. C. Swanson, G. Tarle, J. Thaler, and A. R. Walker. Automated Transient Identification in the Dark Energy Survey. *AJ*, 150(3):82, September 2015. doi: 10.1088/0004-6256/150/3/82.
- Or Graur, Federica B. Bianco, Shan Huang, Maryam Modjaz, Isaac Shivvers, Alexei V. Filippenko, Weidong Li, and J. J. Eldridge. LOSS Revisited. I. Unraveling Correlations Between Supernova Rates and Galaxy Properties, as Measured in a Reanalysis of the Lick Observatory Supernova Search. *ApJ*, 837(2):120, March 2017. doi: 10.3847/1538-4357/aa5eb8.
- J. Guillochon, M. Nicholl, V. A. Villar, B. Mockler, G. Narayan, K. S. Mandel, E. Berger, and P. K. G. Williams. MOSFiT: Modular Open Source Fitter for Transients. *apjs*, 236:6, May 2018a. doi: 10.3847/1538-4365/aab761.
- J. Guillochon, M. Nicholl, V. A. Villar, B. Mockler, G. Narayan, K. S. Mandel, E. Berger, and P. K. G. Williams. MOSFiT: Modular Open Source Fitter for Transients. *apjs*, 236:6, May 2018b. doi: 10.3847/1538-4365/aab761.
- J. Guillochon, M. Nicholl, V. A. Villar, B. Mockler, G. Narayan, K. S. Mandel, E. Berger, and P. K. G. Williams. MOSFiT: Modular Open Source Fitter for Transients. *apjs*, 236:6, May 2018c. doi: 10.3847/1538-4365/aab761.
- Chuan Guo, Geoff Pleiss, Yu Sun, and Kilian Q. Weinberger. On calibration of modern neural networks, 2017.
- Ravi R. Gupta, Steve Kuhlmann, Eve Kovacs, Harold Spinka, Richard Kessler, Daniel A. Goldstein, Camille Liotine, Katarzyna Pomian, Chris B. D'Andrea, Mark Sullivan, Jorge Carretero, Francisco J. Castander, Robert C. Nichol, David A. Finley, John A. Fischer, Ryan J. Foley, Alex G. Kim, Andreas Papadopoulos, Masao Sako, Daniel M. Scolnic, Mathew Smith, Brad E. Tucker, Syed Uddin, Rachel C. Wolf, Fang Yuan, Tim M. C. Abbott, Filipe B. Abdalla, Aurélien Benoit-Lévy, Emmanuel Bertin, David Brooks, Aurelio Carnero Rosell, Matias Carrasco Kind, Carlos E. Cunha, Luiz N. da Costa, Shantanu Desai, Peter Doel, Tim F. Eifler, August E. Evrard, Brenna Flaugher, Pablo Fosalba, Enrique Gaztañaga, Daniel Gruen, Robert Gruendl, David J. James, Kyler Kuehn, Nikolay Kuropatkin, Marcio A. G. Maia, Jennifer L. Marshall, Ramon Miquel, Andrés A. Plazas, A. Kathy Romer, Eusebio Sánchez, Michael Schubnell, Ignacio Sevilla-Noarbe, Flávia Sobreira, Eric Suchyta, Molly E. C. Swanson, Gregory Tarle, Alistair R. Walker, and William Wester. Host Galaxy Identification for Supernova Surveys. *AJ*, 152(6):154, December 2016. doi: 10.3847/0004-6256/152/6/154.

- Ravi R. Gupta, Steve Kuhlmann, Eve Kovacs, Harold Spinka, Richard Kessler, Daniel A. Goldstein, Camille Liotine, Katarzyna Pomian, Chris B. D'Andrea, Mark Sullivan, Jorge Carretero, Francisco J. Castander, Robert C. Nichol, David A. Finley, John A. Fischer, Ryan J. Foley, Alex G. Kim, Andreas Papadopoulos, Masao Sako, Daniel M. Scolnic, Mathew Smith, Brad E. Tucker, Syed Uddin, Rachel C. Wolf, Fang Yuan, Tim M. C. Abbott, Filipe B. Abdalla, Aurélien Benoit-Lévy, Emmanuel Bertin, David Brooks, Aurelio Carnero Rosell, Matias Carrasco Kind, Carlos E. Cunha, Luiz N. da Costa, Shantanu Desai, Peter Doel, Tim F. Eifler, August E. Evrard, Brenna Flaugher, Pablo Fosalba, Enrique Gaztañaga, Daniel Gruen, Robert Gruendl, David J. James, Kyler Kuehn, Nikolay Kuropatkin, Marcio A. G. Maia, Jennifer L. Marshall, Ramon Miquel, Andrés A. Plazas, A. Kathy Romer, Eusebio Sánchez, Michael Schubnell, Ignacio Sevilla-Noarbe, Flávia Sobreira, Eric Suchyta, Molly E. C. Swanson, Gregory Tarle, Alistair R. Walker, and William Wester. Host galaxy identification for supernova surveys. *The Astronomical Journal*, 152(6):154, November 2016. ISSN 1538-3881. doi: 10.3847/0004-6256/152/6/154. URL <http://dx.doi.org/10.3847/0004-6256/152/6/154>.
- J. Guy, P. Astier, S. Baumont, D. Hardin, R. Pain, N. Regnault, S. Basa, R. G. Carlberg, A. Conley, S. Fabbro, D. Fouchez, I. M. Hook, D. A. Howell, K. Perrett, C. J. Pritchett, J. Rich, M. Sullivan, P. Antilogus, E. Aubourg, G. Bazin, J. Bronder, M. Filiol, N. Palanque-Delabrouille, P. Ripoche, and V. Ruhlmann-Kleider. Salt2: using distant supernovae to improve the use of type Ia supernovae as distance indicators. *Astronomy & Astrophysics*, 466(1):11–21, February 2007. ISSN 1432-0746. doi: 10.1051/0004-6361:20066930. URL <http://dx.doi.org/10.1051/0004-6361:20066930>.
- J. Guy, M. Sullivan, A. Conley, N. Regnault, P. Astier, C. Balland, S. Basa, R. G. Carlberg, D. Fouchez, D. Hardin, I. M. Hook, D. A. Howell, R. Pain, N. Palanque-Delabrouille, K. M. Perrett, C. J. Pritchett, J. Rich, V. Ruhlmann-Kleider, D. Balam, S. Baumont, R. S. Ellis, S. Fabbro, H. K. Fakhouri, N. Fourmanoit, S. González-Gaitán, M. L. Graham, E. Hsiao, T. Kronborg, C. Lidman, A. M. Mourao, S. Perlmutter, P. Ripoche, N. Suzuki, and E. S. Walker. The Supernova Legacy Survey 3-year sample: Type Ia supernovae photometric distances and cosmological constraints. *A&A*, 523:A7, November 2010b. doi: 10.1051/0004-6361/201014468.
- J. Guy, M. Sullivan, A. Conley, N. Regnault, P. Astier, C. Balland, S. Basa, R. G. Carlberg, D. Fouchez, D. Hardin, I. M. Hook, D. A. Howell, R. Pain, N. Palanque-Delabrouille, K. M. Perrett, C. J. Pritchett, J. Rich, V. Ruhlmann-Kleider, D. Balam, S. Baumont, R. S. Ellis, S. Fabbro, H. K. Fakhouri, N. Fourmanoit, S. González-Gaitán, M. L. Graham, E. Hsiao, T. Kronborg, C. Lidman, A. M. Mourao, S. Perlmutter, P. Ripoche, N. Suzuki, and E. S. Walker. The Supernova Legacy Survey 3-year sample: Type Ia supernovae photometric distances and cosmological constraints. *A&A*, 523:A7, November 2010c. doi: 10.1051/0004-6361/201014468.
- J. Guy, M. Sullivan, A. Conley, N. Regnault, P. Astier, C. Balland, S. Basa, R. G. Carlberg, D. Fouchez, D. Hardin, I. M. Hook, D. A. Howell, R. Pain, N. Palanque-Delabrouille, K. M. Perrett, C. J. Pritchett, J. Rich, V. Ruhlmann-Kleider, D. Balam, S. Baumont, R. S. Ellis, S. Fabbro, H. K. Fakhouri, N. Fourmanoit, S. González-Gaitán, M. L. Graham, E. Hsiao, T. Kronborg, C. Lidman, A. M. Mourao, S. Perlmutter, P. Ripoche, N. Suzuki, and E. S. Walker. The Supernova Legacy

- Survey 3-year sample: Type Ia supernovae photometric distances and cosmological constraints. *A&A*, 523:A7, November 2010a. doi: 10.1051/0004-6361/201014468.
- L. Guzzo, M. Scodreggio, B. Garilli, B. R. Granett, A. Fritz, U. Abbas, C. Adami, S. Arnouts, J. Bel, M. Bolzonella, D. Bottini, E. Branchini, A. Cappi, J. Coupon, O. Cucciati, I. Davidzon, G. De Lucia, S. de la Torre, P. Franzetti, M. Fumana, P. Hudelot, O. Ilbert, A. Iovino, J. Krywult, V. Le Brun, O. Le Fèvre, D. Maccagni, K. Małek, F. Marulli, H. J. McCracken, L. Paioro, J. A. Peacock, M. Polletta, A. Pollo, H. Schlegelhauser, L. A. M. Tasca, R. Tojeiro, D. Vergani, G. Zamorani, A. Zanichelli, A. Burden, C. Di Porto, A. Marchetti, C. Marinoni, Y. Mellier, L. Moscardini, R. C. Nichol, W. J. Percival, S. Phleps, and M. Wolk. The VIMOS Public Extragalactic Redshift Survey (VIPERS). An unprecedented view of galaxies and large-scale structure at  $0.5 < z < 1.2$ . *A&A*, 566:A108, June 2014. doi: 10.1051/0004-6361/201321489.
- Jeff Z. HaoChen, Colin Wei, Adrien Gaidon, and Tengyu Ma. Provable guarantees for self-supervised deep learning with spectral contrastive loss. *arXiv preprint arXiv:2106.04156*, 2021.
- Jeff Z. HaoChen, Colin Wei, Ananya Kumar, and Tengyu Ma. Beyond separability: Analyzing the linear transferability of contrastive representations to related subpopulations. *arXiv*, 2022.
- Kaiming He, Xiangyu Zhang, Shaoqing Ren, and Jian Sun. Deep residual learning for image recognition. In *Proceedings of the IEEE conference on computer vision and pattern recognition*, pages 770–778, 2016a.
- Kaiming He, Xiangyu Zhang, Shaoqing Ren, and Jian Sun. Deep residual learning for image recognition. In *Proceedings of the IEEE conference on computer vision and pattern recognition*, pages 770–778, 2016b.
- Kaiming He, Haoqi Fan, Yuxin Wu, Saining Xie, and Ross Girshick. Momentum contrast for unsupervised visual representation learning. In *Computer Vision and Pattern Recognition (CVPR)*, 2020.
- Kaiming He, Xinlei Chen, Saining Xie, Yanghao Li, Piotr Dollár, and Ross B. Girshick. Masked autoencoders are scalable vision learners. In *Computer Vision and Pattern Recognition (CVPR)*, 2022.
- Dan Hendrycks, Norman Mu, Ekin D Cubuk, Barret Zoph, Justin Gilmer, and Balaji Lakshminarayanan. Augmix: A simple data processing method to improve robustness and uncertainty. In *International Conference on Learning Representations (ICLR)*, 2019.
- Dan Hendrycks, Steven Basart, Norman Mu, Saurav Kadavath, Frank Wang, Evan Dorundo, Rahul Desai, Tyler Zhu, Samyak Parajuli, Mike Guo, Dawn Song, Jacob Steinhardt, and Justin Gilmer. The many faces of robustness: A critical analysis of out-of-distribution generalization. *arXiv preprint arXiv:2006.16241*, 2020.
- Geoffrey E. Hinton, Nitish Srivastava, Alex Krizhevsky, Ilya Sutskever, and Ruslan R. Salakhutdinov.

- nov. Improving neural networks by preventing co-adaptation of feature detectors. *arXiv e-prints*, art. arXiv:1207.0580, July 2012.
- Samuel Hinton and Dillon Brout. Pippin: A pipeline for supernova cosmology. *The Journal of Open Source Software*, 5(47):2122, March 2020. doi: 10.21105/joss.02122.
- R. Hložek, K. A. Ponder, A. I. Malz, M. Dai, G. Narayan, E. E. O. Ishida, Jr Allam, T., A. Bahmanyar, R. Biswas, L. Galbany, S. W. Jha, D. O. Jones, R. Kessler, M. Lochner, A. A. Mahabal, K. S. Mandel, J. R. Martínez-Galarza, J. D. McEwen, D. Muthukrishna, H. V. Peiris, C. M. Peters, and C. N. Setzer. Results of the Photometric LSST Astronomical Time-series Classification Challenge (PLAsTiCC). *arXiv e-prints*, art. arXiv:2012.12392, December 2020.
- S. Hochreiter and J. Schmidhuber. Long short-term memory. *Neural Computation*, 9:1735–1780, 1997.
- Judy Hoffman, Eric Tzeng, Taesung Park, Jun-Yan Zhu, Phillip Isola, Kate Saenko, Alexei A. Efros, and Trevor Darrell. Cycada: Cycle consistent adversarial domain adaptation. In *International Conference on Machine Learning (ICML)*, 2018.
- Kurt Hornik, Maxwell Stinchcombe, and Halbert White. Multilayer feedforward networks are universal approximators. *Neural Networks*, 2(5):359–366, 1989. ISSN 0893-6080. doi: [https://doi.org/10.1016/0893-6080\(89\)90020-8](https://doi.org/10.1016/0893-6080(89)90020-8). URL <https://www.sciencedirect.com/science/article/pii/0893608089900208>.
- R. Hounsell, D. Scolnic, R. J. Foley, R. Kessler, V. Miranda, A. Avelino, R. C. Bohlin, A. V. Filippenko, J. Frieman, S. W. Jha, P. L. Kelly, R. P. Kirshner, K. Mandel, A. Rest, A. G. Riess, S. A. Rodney, and L. Strolger. Simulations of the WFIRST Supernova Survey and Forecasts of Cosmological Constraints. *ApJ*, 867(1):23, November 2018. doi: 10.3847/1538-4357/aac08b.
- E. P. Hubble. Extragalactic nebulae. *ApJ*, 64:321–369, December 1926. doi: 10.1086/143018.
- Edwin Hubble. A Relation between Distance and Radial Velocity among Extra-Galactic Nebulae. *Proceedings of the National Academy of Science*, 15(3):168–173, March 1929. doi: 10.1073/pnas.15.3.168.
- Akio K. Inoue. Rest-frame ultraviolet-to-optical spectral characteristics of extremely metal-poor and metal-free galaxies. *MNRAS*, 415(3):2920–2931, August 2011. doi: 10.1111/j.1365-2966.2011.18906.x.
- Željko Ivezić, Steven M. Kahn, J. Anthony Tyson, Bob Abel, Emily Acosta, Robyn Allsman, David Alonso, Yusra AlSayyad, Scott F. Anderson, John Andrew, James Roger P. Angel, George Z. Angeli, Reza Ansari, Pierre Antilogus, Constanza Araujo, Robert Armstrong, Kirk T. Arndt, Pierre Astier, Éric Aubourg, Nicole Auza, Tim S. Axelrod, Deborah J. Bard, Jeff D. Barr, Aurelian Barrau, James G. Bartlett, Amanda E. Bauer, Brian J. Bauman, Sylvain Baumont, Ellen Bechtol, Keith Bechtol, Andrew C. Becker, Jacek Becla, Cristina Beldica, Steve Bellavia, Federica B. Bianco,

Rahul Biswas, Guillaume Blanc, Jonathan Blazek, Roger D. Blandford, Josh S. Bloom, Joanne Bogart, Tim W. Bond, Michael T. Booth, Anders W. Borgland, Kirk Borne, James F. Bosch, Dominique Boutigny, Craig A. Brackett, Andrew Bradshaw, William Nielsen Brandt, Michael E. Brown, James S. Bullock, Patricia Burchat, David L. Burke, Gianpietro Cagnoli, Daniel Calabrese, Shawn Callahan, Alice L. Callen, Jeffrey L. Carlin, Erin L. Carlson, Srinivasan Chandrasekharan, Glenaver Charles-Emerson, Steve Chesley, Elliott C. Cheu, Hsin-Fang Chiang, James Chiang, Carol Chirino, Derek Chow, David R. Ciardi, Charles F. Claver, Johann Cohen-Tanugi, Joseph J. Cockrum, Rebecca Coles, Andrew J. Connolly, Kem H. Cook, Asantha Cooray, Kevin R. Covey, Chris Cribbs, Wei Cui, Roc Cutri, Philip N. Daly, Scott F. Daniel, Felipe Daruich, Guillaume Daubard, Greg Daues, William Dawson, Francisco Delgado, Alfred Dellapenna, Robert de Peyster, Miguel de Val-Borro, Seth W. Digel, Peter Doherty, Richard Dubois, Gregory P. Dubois-Felsmann, Josef Durech, Frossie Economou, Tim Eifler, Michael Eracleous, Benjamin L. Emmons, Angelo Fausti Neto, Henry Ferguson, Enrique Figueroa, Merlin Fisher-Levine, Warren Focke, Michael D. Foss, James Frank, Michael D. Freemon, Emmanuel Gangler, Eric Gawiser, John C. Geary, Perry Gee, Marla Geha, Charles J. B. Gessner, Robert R. Gibson, D. Kirk Gilmore, Thomas Glanzman, William Glick, Tatiana Goldina, Daniel A. Goldstein, Iain Goodenow, Melissa L. Graham, William J. Gressler, Philippe Gris, Leanne P. Guy, Augustin Guyonnet, Gunther Haller, Ron Harris, Patrick A. Hascall, Justine Haupt, Fabio Hernandez, Sven Herrmann, Edward Hileman, Joshua Hoblitt, John A. Hodgson, Craig Hogan, James D. Howard, Dajun Huang, Michael E. Huffer, Patrick Ingraham, Walter R. Innes, Suzanne H. Jacoby, Bhuvnesh Jain, Fabrice Jammes, M. James Jee, Tim Jenness, Garrett Jernigan, Darko Jevremović, Kenneth Johns, Anthony S. Johnson, Margaret W. G. Johnson, R. Lynne Jones, Claire Juramy-Gilles, Mario Jurić, Jason S. Kalirai, Nitya J. Kallivayalil, Bryce Kalmbach, Jeffrey P. Kantor, Pierre Karst, Mansi M. Kasliwal, Heather Kelly, Richard Kessler, Veronica Kinnison, David Kirkby, Lloyd Knox, Ivan V. Kotov, Victor L. Krabbendam, K. Simon Krughoff, Petr Kubánek, John Kuczewski, Shri Kulkarni, John Ku, Nadine R. Kurita, Craig S. Lage, Ron Lambert, Travis Lange, J. Brian Langton, Laurent Le Guillou, Deborah Levine, Ming Liang, Kian-Tat Lim, Chris J. Lintott, Kevin E. Long, Margaux Lopez, Paul J. Lotz, Robert H. Lupton, Nate B. Lust, Lauren A. MacArthur, Ashish Mahabal, Rachel Mandelbaum, Thomas W. Markiewicz, Darren S. Marsh, Philip J. Marshall, Stuart Marshall, Morgan May, Robert McKercher, Michelle McQueen, Joshua Meyers, Myriam Migliore, Michelle Miller, David J. Mills, Connor Miraval, Joachim Moeyens, Fred E. Moolekamp, David G. Monet, Marc Moniez, Serge Monkewitz, Christopher Montgomery, Christopher B. Morrison, Fritz Mueller, Gary P. Muller, Freddy Muñoz Arancibia, Douglas R. Neill, Scott P. Newbry, Jean-Yves Nief, Andrei Nomerotski, Martin Nordby, Paul O'Connor, John Oliver, Scot S. Olivier, Knut Olsen, William O'Mullane, Sandra Ortiz, Shawn Osier, Russell E. Owen, Reynald Pain, Paul E. Palecek, John K. Parejko, James B. Parsons, Nathan M. Pease, J. Matt Peterson, John R. Peterson, Donald L. Petravick, M. E. Libby Petrick, Cathy E. Petry, Francesco Pierfederici, Stephen Pietrowicz, Rob Pike, Philip A. Pinto, Raymond Plante, Stephen Plate, Joel P. Plutchak, Paul A. Price, Michael Prouza, Veljko Radeka, Jayadev Rajagopal, Andrew P. Rasmussen, Nicolas Regnault, Kevin A. Reil, David J. Reiss, Michael A. Reuter, Stephen T. Ridgway, Vincent J. Riot, Steve Ritz, Sean Robinson, William Roby, Aaron Roodman, Wayne Rosing, Cecille Roucelle, Matthew R. Rumore, Stefano Russo, Abhijit Saha, Benoit Sassolas, Terry L. Schalk, Pim Schellart, Rafe H. Schindler, Samuel Schmidt, Donald P. Schneider, Michael D. Schneider, William Schoening, German Schumacher, Megan E. Schwamb, Jacques Sebag, Brian Selvy, Glenn H. Sembroski, Lynn G. Seppala, Andrew Serio, Eduardo Serrano, Richard A. Shaw, Ian Shipsey, Jonathan Sick, Nicole Silvestri,

Colin T. Slater, J. Allyn Smith, R. Chris Smith, Shahram Sobhani, Christine Soldahl, Lisa Storrie-Lombardi, Edward Stover, Michael A. Strauss, Rachel A. Street, Christopher W. Stubbs, Ian S. Sullivan, Donald Sweeney, John D. Swinbank, Alexander Szalay, Peter Takacs, Stephen A. Tether, Jon J. Thaler, John Gregg Thayer, Sandrine Thomas, Adam J. Thornton, Vaikunth Thukral, Jeffrey Tice, David E. Trilling, Max Turri, Richard Van Berg, Daniel Vanden Berk, Kurt Vetter, Francoise Virieux, Tomislav Vucina, William Wahl, Lucianne Walkowicz, Brian Walsh, Christopher W. Walter, Daniel L. Wang, Shin-Yawn Wang, Michael Warner, Oliver Wiecha, Beth Willman, Scott E. Winters, David Wittman, Sidney C. Wolff, W. Michael Wood-Vasey, Xiuqin Wu, Bo Xin, Peter Yoachim, and Hu Zhan. *LSST: From Science Drivers to Reference Design and Anticipated Data Products*. *ApJ*, 873(2):111, March 2019a. doi: 10.3847/1538-4357/ab042c.

Željko Ivezić, Steven M. Kahn, J. Anthony Tyson, Bob Abel, Emily Acosta, Robyn Allsman, David Alonso, Yusra AlSayyad, Scott F. Anderson, John Andrew, James Roger P. Angel, George Z. Angeli, Reza Ansari, Pierre Antilogus, Constanza Araujo, Robert Armstrong, Kirk T. Arndt, Pierre Astier, Éric Aubourg, Nicole Auza, Tim S. Axelrod, Deborah J. Bard, Jeff D. Barr, Aurelian Barrau, James G. Bartlett, Amanda E. Bauer, Brian J. Bauman, Sylvain Baumont, Ellen Bechtol, Keith Bechtol, Andrew C. Becker, Jacek Becla, Cristina Beldica, Steve Bellavia, Federica B. Bianco, Rahul Biswas, Guillaume Blanc, Jonathan Blazek, Roger D. Blandford, Josh S. Bloom, Joanne Bogart, Tim W. Bond, Michael T. Booth, Anders W. Borgland, Kirk Borne, James F. Bosch, Dominique Boutigny, Craig A. Brackett, Andrew Bradshaw, William Nielsen Brandt, Michael E. Brown, James S. Bullock, Patricia Burchat, David L. Burke, Gianpietro Cagnoli, Daniel Calabrese, Shawn Callahan, Alice L. Callen, Jeffrey L. Carlin, Erin L. Carlson, Srinivasan Chandrasekharan, Glenaver Charles-Emerson, Steve Chesley, Elliott C. Cheu, Hsin-Fang Chiang, James Chiang, Carol Chirino, Derek Chow, David R. Ciardi, Charles F. Claver, Johann Cohen-Tanugi, Joseph J. Cockrum, Rebecca Coles, Andrew J. Connolly, Kem H. Cook, Asantha Cooray, Kevin R. Covey, Chris Cribbs, Wei Cui, Roc Cutri, Philip N. Daly, Scott F. Daniel, Felipe Daruich, Guillaume Daubard, Greg Daues, William Dawson, Francisco Delgado, Alfred Dellapenna, Robert de Peyster, Miguel de Val-Borro, Seth W. Digel, Peter Doherty, Richard Dubois, Gregory P. Dubois-Felsmann, Josef Durech, Frossie Economou, Tim Eifler, Michael Eracleous, Benjamin L. Emmons, Angelo Fausti Neto, Henry Ferguson, Enrique Figueroa, Merlin Fisher-Levine, Warren Focke, Michael D. Foss, James Frank, Michael D. Freemon, Emmanuel Gangler, Eric Gawiser, John C. Geary, Perry Gee, Marla Geha, Charles J. B. Gessner, Robert R. Gibson, D. Kirk Gilmore, Thomas Glanzman, William Glick, Tatiana Goldina, Daniel A. Goldstein, Iain Goodenow, Melissa L. Graham, William J. Gressler, Philippe Gris, Leanne P. Guy, Augustin Guyonnet, Gunther Haller, Ron Harris, Patrick A. Hascall, Justine Haupt, Fabio Hernandez, Sven Herrmann, Edward Hileman, Joshua Hoblitt, John A. Hodgson, Craig Hogan, James D. Howard, Dajun Huang, Michael E. Huffer, Patrick Ingraham, Walter R. Innes, Suzanne H. Jacoby, Bhuvnesh Jain, Fabrice Jammes, M. James Jee, Tim Jenness, Garrett Jernigan, Darko Jevremović, Kenneth Johns, Anthony S. Johnson, Margaret W. G. Johnson, R. Lynne Jones, Claire Juramy-Gilles, Mario Jurić, Jason S. Kalirai, Nitya J. Kallivayalil, Bryce Kalmbach, Jeffrey P. Kantor, Pierre Karst, Mansi M. Kasliwal, Heather Kelly, Richard Kessler, Veronica Kinnison, David Kirkby, Lloyd Knox, Ivan V. Kotov, Victor L. Krabbendam, K. Simon Krughoff, Petr Kubánek, John Kuczewski, Shri Kulkarni, John Ku, Nadine R. Kurita, Craig S. Lage, Ron Lambert, Travis Lange, J. Brian Langton, Laurent Le Guillou, Deborah Levine, Ming Liang, Kian-Tat Lim, Chris J. Lintott, Kevin E. Long, Margaux Lopez, Paul J. Lotz, Robert H. Lupton, Nate B. Lust, Lauren A. MacArthur, Ashish Mahabal, Rachel Man-



delbaum, Thomas W. Markiewicz, Darren S. Marsh, Philip J. Marshall, Stuart Marshall, Morgan May, Robert McKercher, Michelle McQueen, Joshua Meyers, Myriam Migliore, Michelle Miller, David J. Mills, Connor Miraval, Joachim Moeyens, Fred E. Moolekamp, David G. Monet, Marc Moniez, Serge Monkewitz, Christopher Montgomery, Christopher B. Morrison, Fritz Mueller, Gary P. Muller, Freddy Muñoz Arancibia, Douglas R. Neill, Scott P. Newbry, Jean-Yves Nief, Andrei Nomerotski, Martin Nordby, Paul O'Connor, John Oliver, Scot S. Olivier, Knut Olsen, William O'Mullane, Sandra Ortiz, Shawn Osier, Russell E. Owen, Reynald Pain, Paul E. Palecek, John K. Parejko, James B. Parsons, Nathan M. Pease, J. Matt Peterson, John R. Peterson, Donald L. Petravick, M. E. Libby Petrick, Cathy E. Petry, Francesco Pierfederici, Stephen Pietrowicz, Rob Pike, Philip A. Pinto, Raymond Plante, Stephen Plate, Joel P. Plutchak, Paul A. Price, Michael Prouza, Veljko Radeka, Jayadev Rajagopal, Andrew P. Rasmussen, Nicolas Regnault, Kevin A. Reil, David J. Reiss, Michael A. Reuter, Stephen T. Ridgway, Vincent J. Riot, Steve Ritz, Sean Robinson, William Roby, Aaron Roodman, Wayne Rosing, Cecille Roucelle, Matthew R. Rumore, Stefano Russo, Abhijit Saha, Benoit Sassolas, Terry L. Schalk, Pim Schellart, Rafe H. Schindler, Samuel Schmidt, Donald P. Schneider, Michael D. Schneider, William Schoening, German Schumacher, Megan E. Schwamb, Jacques Sebag, Brian Selvy, Glenn H. Sembroski, Lynn G. Seppala, Andrew Serio, Eduardo Serrano, Richard A. Shaw, Ian Shipsey, Jonathan Sick, Nicole Silvestri, Colin T. Slater, J. Allyn Smith, R. Chris Smith, Shahram Sobhani, Christine Soldahl, Lisa Storrie-Lombardi, Edward Stover, Michael A. Strauss, Rachel A. Street, Christopher W. Stubbs, Ian S. Sullivan, Donald Sweeney, John D. Swinbank, Alexander Szalay, Peter Takacs, Stephen A. Tether, Jon J. Thaler, John Gregg Thayer, Sandrine Thomas, Adam J. Thornton, Vaikunth Thukral, Jeffrey Tice, David E. Trilling, Max Turri, Richard Van Berg, Daniel Vanden Berk, Kurt Vetter, Francoise Virieux, Tomislav Vucina, William Wahl, Lucianne Walkowicz, Brian Walsh, Christopher W. Walter, Daniel L. Wang, Shin-Yawn Wang, Michael Warner, Oliver Wiecha, Beth Willman, Scott E. Winters, David Wittman, Sidney C. Wolff, W. Michael Wood-Vasey, Xiuqin Wu, Bo Xin, Peter Yoachim, and Hu Zhan. *LSST: From Science Drivers to Reference Design and Anticipated Data Products*. *ApJ*, 873(2):111, March 2019b. doi: 10.3847/1538-4357/ab042c.

Željko Ivezić, Steven M. Kahn, J. Anthony Tyson, Bob Abel, Emily Acosta, Robyn Allsman, David Alonso, Yusra AlSayyad, Scott F. Anderson, John Andrew, James Roger P. Angel, George Z. Angeli, Reza Ansari, Pierre Antilogus, Constanza Araujo, Robert Armstrong, Kirk T. Arndt, Pierre Astier, Éric Aubourg, Nicole Auza, Tim S. Axelrod, Deborah J. Bard, Jeff D. Barr, Aurelian Barrau, James G. Bartlett, Amanda E. Bauer, Brian J. Bauman, Sylvain Baumont, Ellen Bechtol, Keith Bechtol, Andrew C. Becker, Jacek Becla, Cristina Beldica, Steve Bellavia, Federica B. Bianco, Rahul Biswas, Guillaume Blanc, Jonathan Blazek, Roger D. Blandford, Josh S. Bloom, Joanne Bogart, Tim W. Bond, Michael T. Booth, Anders W. Borgland, Kirk Borne, James F. Bosch, Dominique Boutigny, Craig A. Brackett, Andrew Bradshaw, William Nielsen Brandt, Michael E. Brown, James S. Bullock, Patricia Burchat, David L. Burke, Gianpietro Cagnoli, Daniel Calabrese, Shawn Callahan, Alice L. Callen, Jeffrey L. Carlin, Erin L. Carlson, Srinivasan Chandrasekharan, Glenaver Charles-Emerson, Steve Chesley, Elliott C. Cheu, Hsin-Fang Chiang, James Chiang, Carol Chirino, Derek Chow, David R. Ciardi, Charles F. Claver, Johann Cohen-Tanugi, Joseph J. Cockrum, Rebecca Coles, Andrew J. Connolly, Kem H. Cook, Asantha Cooray, Kevin R. Covey, Chris Cribbs, Wei Cui, Roc Cutri, Philip N. Daly, Scott F. Daniel, Felipe Daruich, Guillaume Daubard, Greg Daues, William Dawson, Francisco Delgado, Alfred Dellapenna, Robert de Peyster, Miguel de Val-Borro, Seth W. Digel, Peter Doherty, Richard Dubois, Gregory P. Dubois-

Felsmann, Josef Durech, Frossie Economou, Tim Eifler, Michael Eracleous, Benjamin L. Emmons, Angelo Fausti Neto, Henry Ferguson, Enrique Figueroa, Merlin Fisher-Levine, Warren Focke, Michael D. Foss, James Frank, Michael D. Freeman, Emmanuel Gangler, Eric Gawiser, John C. Geary, Perry Gee, Marla Geha, Charles J. B. Gessner, Robert R. Gibson, D. Kirk Gilmore, Thomas Glanzman, William Glick, Tatiana Goldina, Daniel A. Goldstein, Iain Goodenow, Melissa L. Graham, William J. Gressler, Philippe Gris, Leanne P. Guy, Augustin Guyonnet, Gunther Haller, Ron Harris, Patrick A. Hascall, Justine Haupt, Fabio Hernandez, Sven Herrmann, Edward Hileman, Joshua Hoblitt, John A. Hodgson, Craig Hogan, James D. Howard, Dajun Huang, Michael E. Huffer, Patrick Ingraham, Walter R. Innes, Suzanne H. Jacoby, Bhuvnesh Jain, Fabrice Jammes, M. James Jee, Tim Jenness, Garrett Jernigan, Darko Jevremović, Kenneth Johns, Anthony S. Johnson, Margaret W. G. Johnson, R. Lynne Jones, Claire Juramy-Gilles, Mario Jurić, Jason S. Kalirai, Nitya J. Kallivayalil, Bryce Kalmbach, Jeffrey P. Kantor, Pierre Karst, Mansi M. Kasliwal, Heather Kelly, Richard Kessler, Veronica Kinnison, David Kirkby, Lloyd Knox, Ivan V. Kotov, Victor L. Krabbendam, K. Simon Krughoff, Petr Kubánek, John Kuczewski, Shri Kulkarni, John Ku, Nadine R. Kurita, Craig S. Lage, Ron Lambert, Travis Lange, J. Brian Langton, Laurent Le Guillou, Deborah Levine, Ming Liang, Kian-Tat Lim, Chris J. Lintott, Kevin E. Long, Margaux Lopez, Paul J. Lotz, Robert H. Lupton, Nate B. Lust, Lauren A. MacArthur, Ashish Mahabal, Rachel Mandelbaum, Thomas W. Markiewicz, Darren S. Marsh, Philip J. Marshall, Stuart Marshall, Morgan May, Robert McKercher, Michelle McQueen, Joshua Meyers, Myriam Migliore, Michelle Miller, David J. Mills, Connor Miraval, Joachim Moeyens, Fred E. Moolekamp, David G. Monet, Marc Moniez, Serge Monkewitz, Christopher Montgomery, Christopher B. Morrison, Fritz Mueller, Gary P. Muller, Freddy Muñoz Arancibia, Douglas R. Neill, Scott P. Newbry, Jean-Yves Nief, Andrei Nomerotski, Martin Nordby, Paul O'Connor, John Oliver, Scot S. Olivier, Knut Olsen, William O'Mullane, Sandra Ortiz, Shawn Osier, Russell E. Owen, Reynald Pain, Paul E. Palecek, John K. Parejko, James B. Parsons, Nathan M. Pease, J. Matt Peterson, John R. Peterson, Donald L. Petravick, M. E. Libby Petrick, Cathy E. Petry, Francesco Pierfederici, Stephen Pietrowicz, Rob Pike, Philip A. Pinto, Raymond Plante, Stephen Plate, Joel P. Plutchak, Paul A. Price, Michael Prouza, Veljko Radeka, Jayadev Rajagopal, Andrew P. Rasmussen, Nicolas Regnault, Kevin A. Reil, David J. Reiss, Michael A. Reuter, Stephen T. Ridgway, Vincent J. Riot, Steve Ritz, Sean Robinson, William Roby, Aaron Roodman, Wayne Rosing, Cecille Roucelle, Matthew R. Rumore, Stefano Russo, Abhijit Saha, Benoit Sassolas, Terry L. Schalk, Pim Schellart, Rafe H. Schindler, Samuel Schmidt, Donald P. Schneider, Michael D. Schneider, William Schoening, German Schumacher, Megan E. Schwamb, Jacques Sebag, Brian Selvy, Glenn H. Sembroski, Lynn G. Seppala, Andrew Serio, Eduardo Serrano, Richard A. Shaw, Ian Shipsey, Jonathan Sick, Nicole Silvestri, Colin T. Slater, J. Allyn Smith, R. Chris Smith, Shahram Sobhani, Christine Soldahl, Lisa Storrie-Lombardi, Edward Stover, Michael A. Strauss, Rachel A. Street, Christopher W. Stubbs, Ian S. Sullivan, Donald Sweeney, John D. Swinbank, Alexander Szalay, Peter Takacs, Stephen A. Tether, Jon J. Thaler, John Gregg Thayer, Sandrine Thomas, Adam J. Thornton, Vaikunth Thukral, Jeffrey Tice, David E. Trilling, Max Turri, Richard Van Berg, Daniel Vanden Berk, Kurt Vetter, Françoise Virieux, Tomislav Vucina, William Wahl, Lucianne Walkowicz, Brian Walsh, Christopher W. Walter, Daniel L. Wang, Shin-Yawn Wang, Michael Warner, Oliver Wiecha, Beth Willman, Scott E. Winters, David Wittman, Sidney C. Wolff, W. Michael Wood-Vasey, Xiuqin Wu, Bo Xin, Peter Yoachim, and Hu Zhan. LSST: From Science Drivers to Reference Design and Anticipated Data Products. *The Astrophysical Journal*, 873(2):111, March 2019c. doi: 10.3847/1538-4357/ab042c.

- Elise Jennings, Rachel Wolf, and Masao Sako. A new approach for obtaining cosmological constraints from type ia supernovae using approximate bayesian computation, 2016.
- S. W. Jha. *Type Iax Supernovae*, page 375. 2017. doi: 10.1007/978-3-319-21846-5\_42.
- D. Heath Jones, Will Saunders, Matthew Colless, Mike A. Read, Quentin A. Parker, Fred G. Watson, Lachlan A. Campbell, Daniel Burkey, Thomas Mauch, Lesa Moore, Malcolm Hartley, Paul Cass, Dionne James, Ken Russell, Kristin Fiegert, John Dawe, John Huchra, Tom Jarrett, Ofer Lahav, John Lucey, Gary A. Mamon, Dominique Proust, Elaine M. Sadler, and Ken-ichi Wakamatsu. The 6dF Galaxy Survey: samples, observational techniques and the first data release. *MNRAS*, 355(3):747–763, December 2004. doi: 10.1111/j.1365-2966.2004.08353.x.
- D. O. Jones, D. M. Scolnic, A. G. Riess, R. Kessler, A. Rest, R. P. Kirshner, E. Berger, C. A. Ortega, R. J. Foley, R. Chornock, P. J. Challis, W. S. Burgett, K. C. Chambers, P. W. Draper, H. Flewelling, M. E. Huber, N. Kaiser, R. P. Kudritzki, N. Metcalfe, R. J. Wainscoat, and C. Waters. Measuring the Properties of Dark Energy with Photometrically Classified Pan-STARRS Supernovae. I. Systematic Uncertainty from Core-collapse Supernova Contamination. *ApJ*, 843(1):6, July 2017. doi: 10.3847/1538-4357/aa767b.
- Guoliang Kang, Lu Jiang, Yi Yang, and Alexander G Hauptmann. Contrastive adaptation network for unsupervised domain adaptation. In *Proceedings of the IEEE/CVF conference on computer vision and pattern recognition*, pages 4893–4902, 2019.
- N. V. Karpenka, F. Feroz, and M. P. Hobson. A simple and robust method for automated photometric classification of supernovae using neural networks. *MNRAS*, 429(2):1278–1285, February 2013. doi: 10.1093/mnras/sts412.
- D. Kasen and L. Bildsten. Supernova Light Curves Powered by Young Magnetars. *apj*, 717:245–249, July 2010. doi: 10.1088/0004-637X/717/1/245.
- Patrick L. Kelly, Malcolm Hicken, David L. Burke, Kaisey S. Mandel, and Robert P. Kirshner. Hubble Residuals of Nearby Type Ia Supernovae are Correlated with Host Galaxy Masses. *ApJ*, 715(2):743–756, June 2010. doi: 10.1088/0004-637X/715/2/743.
- L. Kelsey, M. Sullivan, M. Smith, P. Wiseman, D. Brout, T. M. Davis, C. Frohmaier, L. Galbany, M. Grayling, C. P. Gutiérrez, S. R. Hinton, R. Kessler, C. Lidman, A. Möller, M. Sako, D. Scolnic, S. A. Uddin, M. Vincenzi, T. M. C. Abbott, M. Agüena, S. Allam, J. Annis, S. Avila, D. Bacon, E. Bertin, D. Brooks, D. L. Burke, A. Carnero Rosell, M. Carrasco Kind, J. Carretero, F. J. Castander, M. Costanzi, L. N. da Costa, S. Desai, H. T. Diehl, P. Doel, S. Everett, I. Ferrero, A. Ferté, B. Flaugher, P. Fosalba, J. García-Bellido, D. W. Gerdes, D. Gruen, R. A. Gruendl, J. Gschwend, G. Gutierrez, D. L. Hollowood, K. Honscheid, D. J. James, A. G. Kim, K. Kuehn, N. Kuropatkin, O. Lahav, M. Lima, J. L. Marshall, P. Martini, F. Menanteau, R. Miquel, R. Morgan, R. L. C. Ogando, A. Palmese, F. Paz-Chinchón, A. A. Plazas, A. K. Romer, C. Sánchez, E. Sanchez, S. Serrano, I. Sevilla-Noarbe, E. Suchyta, G. Tarle, D. Thomas, C. To, T. N. Varga, A. R. Walker, R. D. Wilkinson, and DES Collaboration. The effect of environment on Type Ia supernovae in the Dark

- Energy Survey three-year cosmological sample. *MNRAS*, 501(4):4861–4876, March 2021. doi: 10.1093/mnras/staa3924.
- L. Kelsey, M. Sullivan, P. Wiseman, P. Armstrong, R. Chen, D. Brout, T. M. Davis, M. Dixon, C. Frohmaier, L. Galbany, O. Graur, R. Kessler, C. Lidman, A. Möller, B. Popovic, B. Rose, D. Scolnic, M. Smith, M. Vincenzi, T. M. C. Abbott, M. Agüena, S. Allam, O. Alves, J. Annis, D. Bacon, E. Bertin, S. Bocquet, D. Brooks, D. L. Burke, A. Carnero Rosell, M. Carrasco Kind, J. Carretero, M. Costanzi, L. N. da Costa, M. E. S. Pereira, S. Desai, H. T. Diehl, S. Everett, I. Ferrero, J. Frieman, J. García-Bellido, D. Gruen, R. A. Gruendl, J. Gschwend, G. Gutierrez, S. R. Hinton, D. L. Hollowood, K. Honscheid, D. J. James, K. Kuehn, N. Kuropatkin, G. F. Lewis, J. Mena-Fernández, R. Miquel, A. Palmese, F. Paz-Chinchón, A. Pieres, A. A. Plazas Malagón, M. Raveri, M. Rodríguez-Monroy, A. K. Romer, E. Sanchez, V. Scarpine, M. Schubnell, I. Sevilla-Noarbe, E. Suchyta, M. E. C. Swanson, G. Tarle, D. L. Tucker, N. Weaverdyck, and DES Collaboration. Concerning colour: The effect of environment on type Ia supernova colour in the dark energy survey. *MNRAS*, 519(2):3046–3063, February 2023. doi: 10.1093/mnras/stac3711.
- W. D. Kenworthy, D. O. Jones, M. Dai, R. Kessler, D. Scolnic, D. Brout, M. R. Siebert, J. D. R. Pierel, K. G. Dettman, G. Dimitriadis, R. J. Foley, S. W. Jha, Y.-C. Pan, A. Riess, S. Rodney, and C. Rojas-Bravo. SALT3: An improved type Ia supernova model for measuring cosmic distances. *The Astrophysical Journal*, 923(2):265, dec 2021. doi: 10.3847/1538-4357/ac30d8. URL <https://doi.org/10.3847/1538-4357/ac30d8>.
- R. Kessler and D. Scolnic. Correcting type Ia supernova distances for selection biases and contamination in photometrically identified samples. *The Astrophysical Journal*, 836(1):56, February 2017. ISSN 1538-4357. doi: 10.3847/1538-4357/836/1/56. URL <http://dx.doi.org/10.3847/1538-4357/836/1/56>.
- R. Kessler, B. Bassett, P. Belov, V. Bhatnagar, H. Campbell, A. Conley, J. A. Frieman, A. Glazov, S. González-Gaitán, R. Hlozek, S. Jha, S. Kuhlmann, M. Kunz, H. Lampeitl, A. Mahabal, J. Newling, R. C. Nichol, D. Parkinson, N. Sajeeth Philip, D. Poznanski, J. W. Richards, S. A. Rodney, M. Sako, D. P. Schneider, M. Smith, M. Stritzinger, and M. Varughese. Results from the Supernova Photometric Classification Challenge. *pasp*, 122:1415, December 2010a. doi: 10.1086/657607.
- R. Kessler, B. Bassett, P. Belov, V. Bhatnagar, H. Campbell, A. Conley, J. A. Frieman, A. Glazov, S. González-Gaitán, R. Hlozek, S. Jha, S. Kuhlmann, M. Kunz, H. Lampeitl, A. Mahabal, J. Newling, R. C. Nichol, D. Parkinson, N. Sajeeth Philip, D. Poznanski, J. W. Richards, S. A. Rodney, M. Sako, D. P. Schneider, M. Smith, M. Stritzinger, and M. Varughese. Results from the Supernova Photometric Classification Challenge. *pasp*, 122:1415, December 2010b. doi: 10.1086/657607.

- R. Kessler, J. Guy, J. Marriner, M. Betoule, J. Brinkmann, D. Cinabro, P. El-Hage, J. A. Frieman, S. Jha, J. Mosher, and D. P. Schneider. Testing Models of Intrinsic Brightness Variations in Type Ia Supernovae and Their Impact on Measuring Cosmological Parameters. *apj*, 764:48, February 2013a. doi: 10.1088/0004-637X/764/1/48.
- R. Kessler, J. Marriner, M. Childress, R. Covarrubias, C. B. D’Andrea, D. A. Finley, J. Fischer, R. J. Foley, D. Goldstein, R. R. Gupta, K. Kuehn, M. Marcha, R. C. Nichol, A. Papadopoulos, M. Sako, D. Scolnic, M. Smith, M. Sullivan, W. Wester, F. Yuan, T. Abbott, F. B. Abdalla, S. Allam, A. Benoit-Lévy, G. M. Bernstein, E. Bertin, D. Brooks, A. Carnero Rosell, M. Carrasco Kind, F. J. Castander, M. Crocce, L. N. da Costa, S. Desai, H. T. Diehl, T. F. Eifler, A. Fausti Neto, B. Flaugher, J. Frieman, D. W. Gerdes, D. Gruen, R. A. Gruendl, K. Honscheid, D. J. James, N. Kuropatkin, T. S. Li, M. A. G. Maia, J. L. Marshall, P. Martini, C. J. Miller, R. Miquel, B. Nord, R. Ogando, A. A. Plazas, K. Reil, A. K. Romer, A. Roodman, E. Sanchez, I. Sevilla-Noarbe, R. C. Smith, M. Soares-Santos, F. Sobreira, G. Tarle, J. Thaler, R. C. Thomas, D. Tucker, A. R. Walker, and DES Collaboration. The Difference Imaging Pipeline for the Transient Search in the Dark Energy Survey. *AJ*, 150(6): 172, December 2015. doi: 10.1088/0004-6256/150/6/172.
- R. Kessler, J. Marriner, M. Childress, R. Covarrubias, C. B. D’Andrea, D. A. Finley, J. Fischer, R. J. Foley, D. Goldstein, R. R. Gupta, K. Kuehn, M. Marcha, R. C. Nichol, A. Papadopoulos, M. Sako, D. Scolnic, M. Smith, M. Sullivan, W. Wester, F. Yuan, T. Abbott, F. B. Abdalla, S. Allam, A. Benoit-Lévy, G. M. Bernstein, E. Bertin, D. Brooks, A. Carnero Rosell, M. Carrasco Kind, F. J. Castander, M. Crocce, L. N. da Costa, S. Desai, H. T. Diehl, T. F. Eifler, A. Fausti Neto, B. Flaugher, J. Frieman, D. W. Gerdes, D. Gruen, R. A. Gruendl, K. Honscheid, D. J. James, N. Kuropatkin, T. S. Li, M. A. G. Maia, J. L. Marshall, P. Martini, C. J. Miller, R. Miquel, B. Nord, R. Ogando, A. A. Plazas, K. Reil, A. K. Romer, A. Roodman, E. Sanchez, I. Sevilla-Noarbe, R. C. Smith, M. Soares-Santos, F. Sobreira, G. Tarle, J. Thaler, R. C. Thomas, D. Tucker, and A. R. Walker. The difference imaging pipeline for the transient search in the dark energy survey. *The Astronomical Journal*, 150(6):172, November 2015. ISSN 1538-3881. doi: 10.1088/0004-6256/150/6/172. URL <http://dx.doi.org/10.1088/0004-6256/150/6/172>.
- R. Kessler, G. Narayan, A. Avelino, E. Bachelet, R. Biswas, P. J. Brown, D. F. Chernoff, A. J. Connolly, M. Dai, S. Daniel, R. Di Stefano, M. R. Drout, L. Galbany, S. González-Gaitán, M. L. Graham, R. Hložek, E. E. O. Ishida, J. Guillochon, S. W. Jha, D. O. Jones, K. S. Mandel, D. Muthukrishna, A. O’Grady, C. M. Peters, J. R. Pierel, K. A. Ponder, A. Prša, S. Rodney, and V. A. Villar. Models and Simulations for the Photometric LSST Astronomical Time Series Classification Challenge (PLAsTiCC). *arXiv e-prints*, art. arXiv:1903.11756, Mar 2019a.
- R. Kessler, G. Narayan, A. Avelino, E. Bachelet, R. Biswas, P. J. Brown, D. F. Chernoff, A. J. Connolly, M. Dai, S. Daniel, R. Di Stefano, M. R. Drout, L. Galbany, S. González-Gaitán, M. L. Graham, R. Hložek, E. E. O. Ishida, J. Guillochon, S. W. Jha, D. O. Jones, K. S. Mandel, D. Muthukrishna, A. O’Grady, C. M. Peters, J. R. Pierel, K. A. Ponder, A. Prša, S. Rodney, V. A. Villar, LSST Dark Energy Science Collaboration, and Transient and Variable Stars Science Collaboration. Models and Simulations for the Photometric LSST Astronomical Time Series Classification Challenge (PLAsTiCC). *PASP*, 131(1003):094501, September 2019b. doi: 10.1088/1538-3873/ab26f1.

- R. Kessler, G. Narayan, A. Avelino, E. Bachelet, R. Biswas, P. J. Brown, D. F. Chernoff, A. J. Connolly, M. Dai, S. Daniel, R. Di Stefano, M. R. Drout, L. Galbany, S. González-Gaitán, M. L. Graham, R. Hložek, E. E. O. Ishida, J. Guillochon, S. W. Jha, D. O. Jones, K. S. Mandel, D. Muthukrishna, A. O'Grady, C. M. Peters, J. R. Pierel, K. A. Ponder, A. Prša, S. Rodney, V. A. Villar, LSST Dark Energy Science Collaboration, and Transient and Variable Stars Science Collaboration. Models and Simulations for the Photometric LSST Astronomical Time Series Classification Challenge (PLAsTiCC). *PASP*, 131(1003):094501, September 2019c. doi: 10.1088/1538-3873/ab26f1.
- R. Kessler, G. Narayan, A. Avelino, E. Bachelet, R. Biswas, P. J. Brown, D. F. Chernoff, A. J. Connolly, M. Dai, S. Daniel, R. Di Stefano, M. R. Drout, L. Galbany, S. González-Gaitán, M. L. Graham, R. Hložek, E. E. O. Ishida, J. Guillochon, S. W. Jha, D. O. Jones, K. S. Mandel, D. Muthukrishna, A. O'Grady, C. M. Peters, J. R. Pierel, K. A. Ponder, A. Prša, S. Rodney, and V. A. Villar and. Models and simulations for the photometric LSST astronomical time series classification challenge (PLAsTiCC). *Publications of the Astronomical Society of the Pacific*, 131(1003):094501, jul 2019. doi: 10.1088/1538-3873/ab26f1. URL <https://doi.org/10.1088/1538-3873/ab26f1>.
- Richard Kessler, Andrew C. Becker, David Cinabro, Jake Vanderplas, Joshua A. Frieman, John Marriner, Tamara M. Davis, Benjamin Dilday, Jon Holtzman, Saurabh W. Jha, Hubert Lampeitl, Masao Sako, Mathew Smith, Chen Zheng, Robert C. Nichol, Bruce Bassett, Ralf Bender, Darren L. Depoy, Mamoru Doi, Ed Elson, Alexei V. Filippenko, Ryan J. Foley, Peter M. Garnavich, Ulrich Hopp, Yutaka Ihara, William Ketzeback, W. Kollatschny, Kohki Konishi, Jennifer L. Marshall, Russet J. McMillan, Gajus Miknaitis, Tomoki Morokuma, Edvard Mörtzell, Kaike Pan, Jose Luis Prieto, Michael W. Richmond, Adam G. Riess, Roger Romani, Donald P. Schneider, Jesper Sollerman, Naohiro Takanashi, Kouichi Tokita, Kurt van der Heyden, J. C. Wheeler, Naoki Yasuda, and Donald York. First-Year Sloan Digital Sky Survey-II Supernova Results: Hubble Diagram and Cosmological Parameters. *ApJS*, 185(1):32–84, November 2009a. doi: 10.1088/0067-0049/185/1/32.
- Richard Kessler, Joseph P. Bernstein, David Cinabro, Benjamin Dilday, Joshua A. Frieman, Saurabh Jha, Stephen Kuhlmann, Gajus Miknaitis, Masao Sako, Matt Taylor, and Jake Vanderplas. SNANA: A Public Software Package for Supernova Analysis. *Proceedings of the Astronomical Society of the Pacific*, 121(883):1028, September 2009b. doi: 10.1086/605984.
- Richard Kessler, Joseph P. Bernstein, David Cinabro, Benjamin Dilday, Joshua A. Frieman, Saurabh Jha, Stephen Kuhlmann, Gajus Miknaitis, Masao Sako, Matt Taylor, and Jake Vanderplas. SNANA: A Public Software Package for Supernova Analysis. *PASP*, 121(883):1028, September 2009c. doi: 10.1086/605984.
- Richard Kessler, Bruce Bassett, Pavel Belov, Vasudha Bhatnagar, Heather Campbell, Alex Conley, Joshua A. Frieman, Alexandre Glazov, Santiago González-Gaitán, Renée Hložek, Saurabh Jha, Stephen Kuhlmann, Martin Kunz, Hubert Lampeitl, Ashish Mahabal, James Newling, Robert C. Nichol, David Parkinson, Ninan Sajeeth Philip, Dovi Poznanski, Joseph W. Richards, Steven A. Rodney, Masao Sako, Donald P. Schneider, Mathew Smith, Maximilian Stritzinger, and Melvin Varughese. Results from the Supernova Photometric Classification Challenge. *PASP*, 122(898): 1415, December 2010c. doi: 10.1086/657607.

- Richard Kessler, David Cinabro, Bruce Bassett, Benjamin Dilday, Joshua A. Frieman, Peter M. Garnavich, Saurabh Jha, John Marriner, Robert C. Nichol, Masao Sako, Mathew Smith, Joseph P. Bernstein, Dmitry Bizyaev, Ariel Goobar, Stephen Kuhlmann, Donald P. Schneider, and Maximilian Stritzinger. PHOTOMETRIC ESTIMATES OF REDSHIFTS AND DISTANCE MODULI FOR TYPE Ia SUPERNOVAE. *The Astrophysical Journal*, 717(1):40–57, jun 2010a. doi: 10.1088/0004-637x/717/1/40. URL <https://doi.org/10.1088/0004-637x/717/1/40>.
- Richard Kessler, David Cinabro, Bruce Bassett, Benjamin Dilday, Joshua A. Frieman, Peter M. Garnavich, Saurabh Jha, John Marriner, Robert C. Nichol, Masao Sako, Mathew Smith, Joseph P. Bernstein, Dmitry Bizyaev, Ariel Goobar, Stephen Kuhlmann, Donald P. Schneider, and Maximilian Stritzinger. Photometric estimates of redshifts and distance moduli for type Ia supernovae. *The Astrophysical Journal*, 717(1):40–57, June 2010b. ISSN 1538-4357. doi: 10.1088/0004-637x/717/1/40. URL <http://dx.doi.org/10.1088/0004-637x/717/1/40>.
- Richard Kessler, Alex Conley, Saurabh Jha, and Stephen Kuhlmann. Supernova Photometric Classification Challenge. *arXiv e-prints*, art. arXiv:1001.5210, January 2010a.
- Richard Kessler, Alex Conley, Saurabh Jha, and Stephen Kuhlmann. Supernova Photometric Classification Challenge. *arXiv e-prints*, art. arXiv:1001.5210, January 2010b.
- Richard Kessler, Julien Guy, John Marriner, Marc Betoule, Jon Brinkmann, David Cinabro, Patrick El-Hage, Joshua A. Frieman, Saurabh Jha, Jennifer Mosher, and Donald P. Schneider. Testing Models of Intrinsic Brightness Variations in Type Ia Supernovae and Their Impact on Measuring Cosmological Parameters. *ApJ*, 764(1):48, February 2013b. doi: 10.1088/0004-637x/764/1/48.
- Richard Kessler, Julien Guy, John Marriner, Marc Betoule, Jon Brinkmann, David Cinabro, Patrick El-Hage, Joshua A. Frieman, Saurabh Jha, Jennifer Mosher, and Donald P. Schneider. Testing Models of Intrinsic Brightness Variations in Type Ia Supernovae and Their Impact on Measuring Cosmological Parameters. *ApJ*, 764(1):48, February 2013c. doi: 10.1088/0004-637x/764/1/48.
- Alex G. Kim and Ramon Miquel. Measuring type Ia supernova distances and redshifts from their multi-band light curves. *Astroparticle Physics*, 28(4-5):448–455, dec 2007. doi: 10.1016/j.astropartphys.2007.08.009. URL <https://doi.org/10.1016/j.astropartphys.2007.08.009>.
- Akisato Kimura, Ichiro Takahashi, Masaomi Tanaka, Naoki Yasuda, Naonori Ueda, and Naoki Yoshida. Single-epoch supernova classification with deep convolutional neural networks. *2017 IEEE 37th International Conference on Distributed Computing Systems Workshops (ICDCSW)*, Jun 2017. doi: 10.1109/icdcs.2017.47. URL <http://dx.doi.org/10.1109/ICDCSW.2017.47>.
- Diederik P. Kingma and Jimmy Ba. Adam: A Method for Stochastic Optimization. *arXiv e-prints*, art. arXiv:1412.6980, December 2014.
- Diederik P. Kingma and Jimmy Ba. Adam: A method for stochastic optimization, 2017.
- Doogesh Kodi Ramanah, Nikki Arendse, and Radosław Wojtak. AI-driven spatio-temporal engine

- for finding gravitationally lensed supernovae. *arXiv e-prints*, art. arXiv:2107.12399, July 2021.
- Pang Wei Koh, Shiori Sagawa, Henrik Marklund, Sang Michael Xie, Marvin Zhang, Akshay Balsubramani, Weihua Hu, Michihiro Yasunaga, Richard Lanus Phillips, Irena Gao, Tony Lee, Etienne David, Ian Stavness, Wei Guo, Berton A. Earnshaw, Imran S. Haque, Sara Beery, Jure Leskovec, Anshul Kundaje, Emma Pierson, Sergey Levine, Chelsea Finn, and Percy Liang. WILDS: A benchmark of in-the-wild distribution shifts. In *International Conference on Machine Learning (ICML)*, 2021.
- E. Komatsu et al. Five-Year Wilkinson Microwave Anisotropy Probe (WMAP) Observations: Cosmological Interpretation. *Astrophys. J. Suppl.*, 180:330–376, 2009. doi: 10.1088/0067-0049/180/2/330.
- Alex Krizhevsky, Ilya Sutskever, and Geoffrey E Hinton. Imagenet classification with deep convolutional neural networks. *Advances in neural information processing systems*, 25:1097–1105, 2012a.
- Alex Krizhevsky, Ilya Sutskever, and Geoffrey E Hinton. Imagenet classification with deep convolutional neural networks. In *Advances in Neural Information Processing Systems (NeurIPS)*, pages 1097–1105, 2012b.
- Alex Krizhevsky, Ilya Sutskever, and Geoffrey E Hinton. Imagenet classification with deep convolutional neural networks. *Communications of the ACM*, 60(6):84–90, 2017.
- Ananya Kumar, Aditi Raghunathan, Robbie Jones, Tengyu Ma, and Percy Liang. Fine-tuning can distort pretrained features and underperform out-of-distribution. In *International Conference on Learning Representations (ICLR)*, 2022.
- Martin Kunz, Bruce A. Bassett, and Renée A. Hlozek. Bayesian estimation applied to multiple species. *Phys. Rev. D*, 75:103508, May 2007. doi: 10.1103/PhysRevD.75.103508. URL <https://link.aps.org/doi/10.1103/PhysRevD.75.103508>.
- Hubert Lampeitl, Mathew Smith, Robert C. Nichol, Bruce Bassett, David Cinabro, Benjamin Dilday, Ryan J. Foley, Joshua A. Frieman, Peter M. Garnavich, Ariel Goobar, Myungshin Im, Saurabh W. Jha, John Marriner, Ramon Miquel, Jakob Nordin, Linda Östman, Adam G. Riess, Masao Sako, Donald P. Schneider, Jesper Sollerman, and Maximilian Stritzinger. The Effect of Host Galaxies on Type Ia Supernovae in the SDSS-II Supernova Survey. *ApJ*, 722(1):566–576, October 2010. doi: 10.1088/0004-637X/722/1/566.
- Le Fèvre, O., Vettolani, G., Garilli, B., Tresse, L., Bottini, D., Le Brun, V., Maccagni, D., Picat, J. P., Scaramella, R., Scodreggio, M., Zanichelli, A., Adami, C., Arnaboldi, M., Arnouts, S., Bardelli, S., Bolzonella, M., Cappi, A., Charlot, S., Ciliegi, P., Contini, T., Foucaud, S., Franzetti, P., Gavignaud, I., Guzzo, L., Ilbert, O., Iovino, A., McCracken, H. J., Marano, B., Marinoni, C., Mathez, G., Mazure, A., Meneux, B., Merighi, R., Paltani, S., Pellò, R., Pollo, A., Pozzetti, L., Radovich, M., Zamorani, G., Zucca, E., Bondi, M., Bongiorno, A., Busarello, G., Lamareille, F., Mellier, Y., Merluzzi, P., Ripepi, V., and Rizzo, D. The vimos vlt deep survey - first epoch vvds-deep



- survey: 11 spectra with and the redshift distribution over 0. *A&A*, 439(3):845–862, 2005. doi: 10.1051/0004-6361:20041960. URL <https://doi.org/10.1051/0004-6361:20041960>.
- Henrietta S. Leavitt. 1777 variables in the Magellanic Clouds. *Annals of Harvard College Observatory*, 60:87–108.3, January 1908.
- Y LeCun, B Boser, JS Denker, D Henderson, RE Howard, W Hubbard, and LD Jackel. Backpropagation applied to handwritten zip code recognition. *Neural computation*, 1(4):541–551, 1989a.
- Yann LeCun, Bernhard Boser, John S Denker, Donnie Henderson, Richard E Howard, Wayne Hubbard, and Lawrence D Jackel. Backpropagation applied to handwritten zip code recognition. *Neural computation*, 1(4):541–551, 1989b.
- Yann LeCun, Léon Bottou, Yoshua Bengio, and Patrick Haffner. Gradient-based learning applied to document recognition. *Proceedings of the IEEE*, 86(11):2278–2324, 1998.
- Claus Leitherer, I. Hui Li, Daniela Calzetti, and Timothy M. Heckman. Global Far-Ultraviolet (912–1800 Å) Properties of Star-forming Galaxies. *ApJS*, 140(2):303–329, June 2002. doi: 10.1086/342486.
- G. Lemaître. Un Univers homogène de masse constante et de rayon croissant rendant compte de la vitesse radiale des nébuleuses extra-galactiques. *Annales de la Société Scientifique de Bruxelles*, 47:49–59, January 1927.
- Mike Lewis, Yinhan Liu, Naman Goyal, Marjan Ghazvininejad, Abdelrahman Mohamed, Omer Levy, Ves Stoyanov, and Luke Zettlemoyer. Bart: Denoising sequence-to-sequence pre-training for natural language generation, translation, and comprehension. In *Association for Computational Linguistics (ACL)*, 2020.
- Yang Li, Si Si, Gang Li, Cho-Jui Hsieh, and Samy Bengio. Learnable fourier features for multi-dimensional spatial positional encoding. *Advances in Neural Information Processing Systems*, 34:15816–15829, 2021.
- Yubin Li, Xian Zhong Zheng, Qiu-Sheng Gu, Yi-Peng Wang, Zhang Zheng Wen, Kexin Guo, and Fang Xia An. Measuring structural parameters through stacking galaxy images. *The Astronomical Journal*, 152(6):201, dec 2016. doi: 10.3847/0004-6256/152/6/201. URL <https://dx.doi.org/10.3847/0004-6256/152/6/201>.
- C. Lidman, B. E. Tucker, T. M. Davis, S. A. Uddin, J. Asorey, K. Bolejko, D. Brout, J. Calcino, D. Carollo, A. Carr, M. Childress, J. K. Hoormann, R. J. Foley, L. Galbany, K. Glazebrook, S. R. Hinton, R. Kessler, A. G. Kim, A. King, A. Kremin, K. Kuehn, D. Lagattuta, G. F. Lewis, E. Macaulay, U. Malik, M. March, P. Martini, A. Möller, D. Mudd, R. C. Nichol, F. Panther, D. Parkinson, M. Pursiainen, M. Sako, E. Swann, R. Scalzo, D. Scolnic, R. Sharp, M. Smith, N. E. Sommer, M. Sullivan, S. Webb, P. Wiseman, Z. Yu, F. Yuan, B. Zhang, T. M. C. Abbott, M. Agüena, S. Allam, J. Annis, S. Avila, E. Bertin, S. Bhargava, D. Brooks, A. Carnero Rosell, M. Carrasco Kind, J. Car-

retero, F. J. Castander, M. Costanzi, L. N. da Costa, J. De Vicente, P. Doel, T. F. Eifler, S. Everett, P. Fosalba, J. Frieman, J. García-Bellido, E. Gaztanaga, D. Gruen, R. A. Gruendl, J. Gschwend, G. Gutierrez, W. G. Hartley, D. L. Hollowood, K. Honscheid, D. J. James, N. Kuropatkin, T. S. Li, M. Lima, H. Lin, M. A. G. Maia, J. L. Marshall, P. Melchior, F. Menanteau, R. Miquel, A. Palmese, F. Paz-Chinchón, A. A. Plazas, A. Roodman, E. S. Rykoff, E. Sanchez, B. Santiago, V. Scarpine, M. Schubnell, S. Serrano, I. Sevilla-Noarbe, E. Suchyta, M. E. C. Swanson, G. Tarle, D. L. Tucker, T. N. Varga, A. R. Walker, W. Wester, R. D. Wilkinson, and DES Collaboration. OzDES multi-object fibre spectroscopy for the Dark Energy Survey: results and second data release. *MNRAS*, 496(1):19–35, July 2020. doi: 10.1093/mnras/staa1341.

Hanxiao Liu, Zihang Dai, David R. So, and Quoc V. Le. Pay Attention to MLPs. *arXiv e-prints*, art. arXiv:2105.08050, May 2021.

Michelle Lochner, Jason D. McEwen, Hiranya V. Peiris, Ofer Lahav, and Max K. Winter. Photometric supernova classification with machine learning. *The Astrophysical Journal Supplement Series*, 225 (2):31, Aug 2016. ISSN 1538-4365. doi: 10.3847/0067-0049/225/2/31. URL <http://dx.doi.org/10.3847/0067-0049/225/2/31>.

LSST Science Collaboration, Paul A. Abell, Julius Allison, Scott F. Anderson, John R. Andrew, J. Roger P. Angel, Lee Armus, David Arnett, S. J. Asztalos, Tim S. Axelrod, Stephen Bailey, D. R. Ballantyne, Justin R. Bankert, Wayne A. Barkhouse, Jeffrey D. Barr, L. Felipe Barrientos, Aaron J. Barth, James G. Bartlett, Andrew C. Becker, Jacek Becla, Timothy C. Beers, Joseph P. Bernstein, Rahul Biswas, Michael R. Blanton, Joshua S. Bloom, John J. Bochanski, Pat Boeshaar, Kirk D. Borne, Marusa Bradac, W. N. Brandt, Carrie R. Bridge, Michael E. Brown, Robert J. Brunner, James S. Bullock, Adam J. Burgasser, James H. Burge, David L. Burke, Phillip A. Cargile, Srinivasan Chandrasekharan, George Chartas, Steven R. Chesley, You-Hua Chu, David Cinabro, Mark W. Claire, Charles F. Claver, Douglas Clowe, A. J. Connolly, Kem H. Cook, Jeff Cooke, Asantha Cooray, Kevin R. Covey, Christopher S. Culliton, Roelof de Jong, Willem H. de Vries, Victor P. Debattista, Francisco Delgado, Ian P. Dell’Antonio, Saurav Dhital, Rosanne Di Stefano, Mark Dickinson, Benjamin Dilday, S. G. Djorgovski, Gregory Dobler, Ciro Donalek, Gregory Dubois-Felsmann, Josef Durech, Ardis Eliasdottir, Michael Eracleous, Laurent Eyer, Emilio E. Falco, Xiaohui Fan, Christopher D. Fassnacht, Harry C. Ferguson, Yanga R. Fernandez, Brian D. Fields, Douglas Finkbeiner, Eduardo E. Figuera, Derek B. Fox, Harold Francke, James S. Frank, Josh Frieman, Sebastien Fromenteau, Muhammad Furqan, Gaspar Galaz, A. Gal-Yam, Peter Garnavich, Eric Gawiser, John Geary, Perry Gee, Robert R. Gibson, Kirk Gilmore, Emily A. Grace, Richard F. Green, William J. Gressler, Carl J. Grillmair, Salman Habib, J. S. Haggerty, Mario Hamuy, Alan W. Harris, Suzanne L. Hawley, Alan F. Heavens, Leslie Hebb, Todd J. Henry, Edward Hileman, Eric J. Hilton, Keri Hoadley, J. B. Holberg, Matt J. Holman, Steve B. Howell, Leopoldo Infante, Zeljko Ivezic, Suzanne H. Jacoby, Bhuvnesh Jain, R. Jedicke, M. James Jee, J. Garrett Jernigan, Saurabh W. Jha, Kathryn V. Johnston, R. Lynne Jones, Mario Juric, Mikko Kaasalainen, Styliani, Kafka, Steven M. Kahn, Nathan A. Kaib, Jason Kalirai, Jeff Kantor, Mansi M. Kasliwal, Charles R. Keeton, Richard Kessler, Zoran Knezevic, Adam Kowalski, Victor L. Krabbendam, K. Simon Krughoff, Shrinivas Kulkarni, Stephen Kuhlman, Mark Lacy, Sebastien Lepine, Ming Liang, Amy Lien, Paulina Lira, Knox S. Long, Suzanne Lorenz, Jennifer M. Lotz, R. H. Lupton, Julie Lutz, Lucas M. Macri, Ashish A. Mahabal, Rachel Mandelbaum, Phil Marshall, Mor-

gan May, Peregrine M. McGehee, Brian T. Meadows, Alan Meert, Andrea Milani, Christopher J. Miller, Michelle Miller, David Mills, Dante Minniti, David Monet, Anjum S. Mukadam, Ehud Nakar, Douglas R. Neill, Jeffrey A. Newman, Sergei Nikolaev, Martin Nordby, Paul O'Connor, Masamune Oguri, John Oliver, Scot S. Olivier, Julia K. Olsen, Knut Olsen, Edward W. Olszewski, Hakeem Oluseyi, Nelson D. Padilla, Alex Parker, Joshua Pepper, John R. Peterson, Catherine Petry, Philip A. Pinto, James L. Pizagno, Bogdan Popescu, Andrej Prsa, Veljko Radcka, M. Jordan Raddick, Andrew Rasmussen, Arne Rau, Jeonghee Rho, James E. Rhoads, Gordon T. Richards, Stephen T. Ridgway, Brant E. Robertson, Rok Roskar, Abhijit Saha, Ata Sarajedini, Evan Scannapieco, Terry Schalk, Rafe Schindler, Samuel Schmidt, Sarah Schmidt, Donald P. Schneider, German Schumacher, Ryan Scranton, Jacques Sebag, Lynn G. Seppala, Ohad Shemmer, Joshua D. Simon, M. Sivertz, Howard A. Smith, J. Allyn Smith, Nathan Smith, Anna H. Spitz, Adam Stanford, Keivan G. Stassun, Jay Strader, Michael A. Strauss, Christopher W. Stubbs, Donald W. Sweeney, Alex Szalay, Paula Szkody, Masahiro Takada, Paul Thorman, David E. Trilling, Virginia Trimble, Anthony Tyson, Richard Van Berg, Daniel Vanden Berk, Jake VanderPlas, Licia Verde, Bojan Vrsnak, Lucianne M. Walkowicz, Benjamin D. Wandelt, Sheng Wang, Yun Wang, Michael Warner, Risa H. Wechsler, Andrew A. West, Oliver Wiecha, Benjamin F. Williams, Beth Willman, David Wittman, Sidney C. Wolff, W. Michael Wood-Vasey, Przemek Wozniak, Patrick Young, Andrew Zentner, and Hu Zhan. *Lsst science book, version 2.0, 2009a.*

LSST Science Collaboration, Paul A. Abell, Julius Allison, Scott F. Anderson, John R. Andrew, J. Roger P. Angel, Lee Armus, David Arnett, S. J. Asztalos, Tim S. Axelrod, Stephen Bailey, D. R. Ballantyne, Justin R. Bankert, Wayne A. Barkhouse, Jeffrey D. Barr, L. Felipe Barrientos, Aaron J. Barth, James G. Bartlett, Andrew C. Becker, Jacek Becla, Timothy C. Beers, Joseph P. Bernstein, Rahul Biswas, Michael R. Blanton, Joshua S. Bloom, John J. Bochanski, Pat Boeshaar, Kirk D. Borne, Marusa Bradac, W. N. Brandt, Carrie R. Bridge, Michael E. Brown, Robert J. Brunner, James S. Bullock, Adam J. Burgasser, James H. Burge, David L. Burke, Phillip A. Cargile, Srinivasan Chandrasekharan, George Chartas, Steven R. Chesley, You-Hua Chu, David Cinabro, Mark W. Claire, Charles F. Claver, Douglas Clowe, A. J. Connolly, Kem H. Cook, Jeff Cooke, Asantha Cooray, Kevin R. Covey, Christopher S. Culliton, Roelof de Jong, Willem H. de Vries, Victor P. Debattista, Francisco Delgado, Ian P. Dell'Antonio, Saurav Dhital, Rosanne Di Stefano, Mark Dickinson, Benjamin Dilday, S. G. Djorgovski, Gregory Dobler, Ciro Donalek, Gregory Dubois-Felsmann, Josef Durech, Ardis Eliasdottir, Michael Eracleous, Laurent Eyer, Emilio E. Falco, Xiaohui Fan, Christopher D. Fassnacht, Harry C. Ferguson, Yanga R. Fernandez, Brian D. Fields, Douglas Finkbeiner, Eduardo E. Figuera, Derek B. Fox, Harold Francke, James S. Frank, Josh Frieman, Sebastien Fromenteau, Muhammad Furqan, Gaspar Galaz, A. Gal-Yam, Peter Garnavich, Eric Gawiser, John Geary, Perry Gee, Robert R. Gibson, Kirk Gilmore, Emily A. Grace, Richard F. Green, William J. Gressler, Carl J. Grillmair, Salman Habib, J. S. Haggerty, Mario Hamuy, Alan W. Harris, Suzanne L. Hawley, Alan F. Heavens, Leslie Hebb, Todd J. Henry, Edward Hileman, Eric J. Hilton, Keri Hoadley, J. B. Holberg, Matt J. Holman, Steve B. Howell, Leopoldo Infante, Zeljko Ivezic, Suzanne H. Jacoby, Bhuvnesh Jain, R. Jedicke, M. James Jee, J. Garrett Jernigan, Saurabh W. Jha, Kathryn V. Johnston, R. Lynne Jones, Mario Juric, Mikko Kaasalainen, Styliani, Kafka, Steven M. Kahn, Nathan A. Kaib, Jason Kalirai, Jeff Kantor, Mansi M. Kasliwal, Charles R. Keeton, Richard Kessler, Zoran Knezevic, Adam Kowalski, Victor L. Krabbendam, K. Simon Krughoff, Shrinivas Kulkarni, Stephen Kuhlman, Mark Lacy, Sebastien Lepine, Ming Liang, Amy Lien, Paulina Lira, Knox S. Long, Suzanne Lorenz, Jen-

nifer M. Lotz, R. H. Lupton, Julie Lutz, Lucas M. Macri, Ashish A. Mahabal, Rachel Mandelbaum, Phil Marshall, Morgan May, Peregrine M. McGehee, Brian T. Meadows, Alan Meert, Andrea Milani, Christopher J. Miller, Michelle Miller, David Mills, Dante Minniti, David Monet, Anjum S. Mukadam, Ehud Nakar, Douglas R. Neill, Jeffrey A. Newman, Sergei Nikolaev, Martin Nordby, Paul O'Connor, Masamune Oguri, John Oliver, Scot S. Olivier, Julia K. Olsen, Knut Olsen, Edward W. Olszewski, Hakeem Oluseyi, Nelson D. Padilla, Alex Parker, Joshua Pepper, John R. Peterson, Catherine Petry, Philip A. Pinto, James L. Pizagno, Bogdan Popescu, Andrej Prsa, Veljko Radcka, M. Jordan Raddick, Andrew Rasmussen, Arne Rau, Jeonghee Rho, James E. Rhoads, Gordon T. Richards, Stephen T. Ridgway, Brant E. Robertson, Rok Roskar, Abhijit Saha, Ata Sarajedini, Evan Scannapieco, Terry Schalk, Rafe Schindler, Samuel Schmidt, Sarah Schmidt, Donald P. Schneider, German Schumacher, Ryan Scranton, Jacques Sebag, Lynn G. Seppala, Ohad Shemmer, Joshua D. Simon, M. Sivertz, Howard A. Smith, J. Allyn Smith, Nathan Smith, Anna H. Spitz, Adam Stanford, Keivan G. Stassun, Jay Strader, Michael A. Strauss, Christopher W. Stubbs, Donald W. Sweeney, Alex Szalay, Paula Szkody, Masahiro Takada, Paul Thorman, David E. Trilling, Virginia Trimble, Anthony Tyson, Richard Van Berg, Daniel Vanden Berk, Jake VanderPlas, Licia Verde, Bojan Vrsnak, Lucianne M. Walkowicz, Benjamin D. Wandelt, Sheng Wang, Yun Wang, Michael Warner, Risa H. Wechsler, Andrew A. West, Oliver Wiecha, Benjamin F. Williams, Beth Willman, David Wittman, Sidney C. Wolff, W. Michael Wood-Vasey, Przemek Wozniak, Patrick Young, Andrew Zentner, and Hu Zhan. LSST Science Book, Version 2.0. *arXiv e-prints*, art. arXiv:0912.0201, December 2009b.

Knut Lundmark. The Motions and the Distances of Spiral Nebulæ. *MNRAS*, 85:865, June 1925. doi: 10.1093/mnras/85.8.865.

Piero Madau and Mark Dickinson. Cosmic Star-Formation History. *ARA&A*, 52:415–486, August 2014. doi: 10.1146/annurev-astro-081811-125615.

F. Mannucci, M. Della Valle, N. Panagia, E. Cappellaro, G. Cresci, R. Maiolino, A. Petrosian, and M. Turatto. The supernova rate per unit mass. *A&A*, 433(3):807–814, April 2005. doi: 10.1051/0004-6361:20041411.

R. J. McLure, L. Pentericci, A. Cimatti, J. S. Dunlop, D. Elbaz, A. Fontana, K. Nandra, R. Amorin, M. Bolzonella, A. Bongiorno, A. C. Carnall, M. Castellano, M. Cirasuolo, O. Cucciati, F. Cullen, S. De Barros, S. L. Finkelstein, F. Fontanot, P. Franzetti, M. Fumana, A. Gargiulo, B. Garilli, L. Guaita, W. G. Hartley, A. Iovino, M. J. Jarvis, S. Juneau, W. Karman, D. Maccagni, F. Marchi, E. Mármol-Queraltó, E. Pompei, L. Pozzetti, M. Scodreggio, V. Sommariva, M. Talia, O. Almaini, I. Balestra, S. Bardelli, E. F. Bell, N. Bourne, R. A. A. Bowler, M. Brusa, F. Buitrago, K. I. Caputi, P. Cassata, S. Charlot, A. Citro, G. Cresci, S. Cristiani, E. Curtis-Lake, M. Dickinson, G. G. Fazio, H. C. Ferguson, F. Fiore, M. Franco, J. P. U. Fynbo, A. Galametz, A. Georgakakis, M. Giavalisco, A. Grazian, N. P. Hathi, I. Jung, S. Kim, A. M. Koekemoer, Y. Khusanova, O. Le Fèvre, J. M. Lotz, F. Mannucci, D. T. Maltby, K. Matsuoka, D. J. McLeod, H. Mendez-Hernandez, J. Mendez-Abreu, M. Mignoli, M. Moresco, A. Mortlock, M. Nonino, M. Pannella, C. Papovich, P. Popesso, D. P. Rosario, M. Salvato, P. Santini, D. Schaerer, C. Schreiber, D. P. Stark, L. A. M. Tasca, R. Thomas, T. Treu, E. Vanzella, V. Wild, C. C. Williams, G. Zamorani, and E. Zucca. The VANDELSESO public spectroscopic survey. *MNRAS*, 479(1):25–42, September 2018. doi: 10.1093/mnras/sty1213.

- Ayan Mitra, Richard Kessler, Surhud More, Renee Hlozek, and The LSST Dark Energy Science Collaboration. Using host galaxy photometric redshifts to improve cosmological constraints with type ia supernova in the lsst era, 2022. URL <https://arxiv.org/abs/2210.07560>.
- M. Modjaz, S. Blondin, R. P. Kirshner, T. Matheson, P. Berlind, F. B. Bianco, M. L. Calkins, P. Challis, P. Garnavich, M. Hicken, S. Jha, Y. Q. Liu, and G. H. Marion. Optical Spectra of 73 Stripped-envelope Core-collapse Supernovae. *AJ*, 147(5):99, May 2014. doi: 10.1088/0004-6256/147/5/99.
- A. Möller and T. de Boissière. SuperNNova: an open-source framework for Bayesian, neural network-based supernova classification. *MNRAS*, 491(3):4277–4293, January 2020a. doi: 10.1093/mnras/stz3312.
- A. Möller and T. de Boissière. SuperNNova: an open-source framework for Bayesian, neural network-based supernova classification. *MNRAS*, 491(3):4277–4293, January 2020b. doi: 10.1093/mnras/stz3312.
- A. Möller, V. Ruhlmann-Kleider, C. Leloup, J. Neveu, N. Palanque-Delabrouille, J. Rich, R. Carlberg, C. Lidman, and C. Pritchett. Photometric classification of type ia supernovae in the supernova legacy survey with supervised learning. *Journal of Cosmology and Astroparticle Physics*, 2016(12):008–008, Dec 2016. ISSN 1475-7516. doi: 10.1088/1475-7516/2016/12/008. URL <http://dx.doi.org/10.1088/1475-7516/2016/12/008>.
- A. Möller, M. Smith, M. Sako, M. Sullivan, M. Vincenzi, P. Wiseman, P. Armstrong, J. Asorey, D. Brout, D. Carollo, T. M. Davis, C. Frohmaier, L. Galbany, K. Glazebrook, L. Kelsey, R. Kessler, G. F. Lewis, C. Lidman, U. Malik, R. C. Nichol, D. Scolnic, B. E. Tucker, T. M. C. Abbott, M. Agüena, S. Allam, J. Annis, E. Bertin, S. Bocquet, D. Brooks, D. L. Burke, A. Carnero Rosell, M. Carrasco Kind, J. Carretero, F. J. Castander, C. Conselice, M. Costanzi, M. Crocce, L. N. da Costa, J. De Vicente, S. Desai, H. T. Diehl, P. Doel, S. Everett, I. Ferrero, D. A. Finley, B. Flaugher, D. Friedel, J. Frieman, J. García-Bellido, D. W. Gerdes, D. Gruen, R. A. Gruendl, J. Gschwend, G. Gutierrez, K. Herner, S. R. Hinton, D. L. Hollowood, K. Honscheid, D. J. James, K. Kuehn, N. Kuropatkin, O. Lahav, M. March, J. L. Marshall, F. Menanteau, R. Miquel, R. Morgan, A. Palmese, F. Paz-Chinchón, A. Pieres, A. A. Plazas Malagón, A. K. Romer, A. Roodman, E. Sanchez, V. Scarpine, M. Schubnell, S. Serrano, I. Sevilla-Noarbe, E. Suchyta, G. Tarle, D. Thomas, C. To, and T. N. Varga. The dark energy survey 5-yr photometrically identified type Ia supernovae. *MNRAS*, 514(4):5159–5177, August 2022. doi: 10.1093/mnras/stac1691.
- E. Morganson, R. A. Gruendl, F. Menanteau, M. Carrasco Kind, Y. C. Chen, G. Daues, A. Drlica-Wagner, D. N. Friedel, M. Gower, M. W. G. Johnson, M. D. Johnson, R. Kessler, F. Paz-Chinchón, D. Petravick, C. Pond, B. Yanny, S. Allam, R. Armstrong, W. Barkhouse, K. Bechtol, A. Benoit-Lévy, G. M. Bernstein, E. Bertin, E. Buckley-Geer, R. Covarrubias, S. Desai, H. T. Diehl, D. A. Goldstein, D. Gruen, T. S. Li, H. Lin, J. Marriner, J. J. Mohr, E. Neilsen, C. C. Ngeow, K. Paech, E. S. Rykoff, M. Sako, I. Sevilla-Noarbe, E. Sheldon, F. Sobreira, D. L. Tucker, W. Wester, and DES Collaboration. The Dark Energy Survey Image Processing Pipeline. *PASP*, 130(989):074501, July 2018. doi: 10.1088/1538-3873/aab4ef.

Adam Moss. Improved Photometric Classification of Supernovae using Deep Learning. *arXiv e-prints*, art. arXiv:1810.06441, October 2018.

Daniel Muthukrishna, Gautham Narayan, Kaisey S. Mandel, Rahul Biswas, and Renée Hložek. Rapid: Early classification of explosive transients using deep learning. *Publications of the Astronomical Society of the Pacific*, 131(1005):118002, September 2019. ISSN 1538-3873. doi: 10.1088/1538-3873/ab1609. URL <http://dx.doi.org/10.1088/1538-3873/ab1609>.

J. Myles, A. Alarcon, A. Amon, C. Sánchez, S. Everett, J. DeRose, J. McCullough, D. Gruen, G. M. Bernstein, M. A. Troxel, S. Dodelson, A. Campos, N. MacCrann, B. Yin, M. Raveri, A. Amara, M. R. Becker, A. Choi, J. Cordero, K. Eckert, M. Gatti, G. Giannini, J. Gschwend, R. A. Gruendl, I. Harrison, W. G. Hartley, E. M. Huff, N. Kuropatkin, H. Lin, D. Masters, R. Miquel, J. Prat, A. Roodman, E. S. Rykoff, I. Sevilla-Noarbe, E. Sheldon, R. H. Wechsler, B. Yanny, T. M. C. Abbott, M. Aguena, S. Allam, J. Annis, D. Bacon, E. Bertin, S. Bhargava, S. L. Bridle, D. Brooks, D. L. Burke, A. Carnero Rosell, M. Carrasco Kind, J. Carretero, F. J. Castander, C. Conselice, M. Costanzi, M. Croce, L. N. da Costa, M. E. S. Pereira, S. Desai, H. T. Diehl, T. F. Eifler, J. Elvin-Poole, A. E. Evrard, I. Ferrero, A. Ferté, B. Flaugher, P. Fosalba, J. Frieman, J. García-Bellido, E. Gaztanaga, T. Giannantonio, S. R. Hinton, D. L. Hollowood, K. Honscheid, B. Hoyle, D. Huterer, D. J. James, E. Krause, K. Kuehn, O. Lahav, M. Lima, M. A. G. Maia, J. L. Marshall, P. Martini, P. Melchior, F. Menanteau, J. J. Mohr, R. Morgan, J. Muir, R. L. C. Ogando, A. Palmese, F. Paz-Chinchón, A. A. Plazas, M. Rodriguez-Monroy, S. Samuroff, E. Sanchez, V. Scarpine, L. F. Secco, S. Serrano, M. Smith, M. Soares-Santos, E. Suchyta, M. E. C. Swanson, G. Tarle, D. Thomas, C. To, T. N. Varga, J. Weller, and W. Wester. Dark Energy Survey Year 3 results: redshift calibration of the weak lensing source galaxies. *MNRAS*, 505(3):4249–4277, August 2021. doi: 10.1093/mnras/stab1515.

A Möller and T de Boissière. Supernnova: an open-source framework for bayesian, neural network-based supernova classification. *Monthly Notices of the Royal Astronomical Society*, 491(3):4277–4293, December 2019. ISSN 1365-2966. doi: 10.1093/mnras/stz3312. URL <http://dx.doi.org/10.1093/mnras/stz3312>.

Mahdi Pakdaman Naeini, Gregory F. Cooper, and Milos Hauskrecht. Obtaining well calibrated probabilities using bayesian binning. In *Proceedings of the Twenty-Ninth AAAI Conference on Artificial Intelligence*, AAAI'15, page 2901–2907. AAAI Press, 2015. ISBN 0262511290.

SJ Nakoneczny, M Bilicki, Agnieszka Pollo, M Asgari, A Dvornik, T Erben, B Giblin, C Heymans, H Hildebrandt, A Kannawadi, et al. Photometric selection and redshifts for quasars in the kilo-degree survey data release 4. *Astronomy & Astrophysics*, 649:A81, 2021.

Brett Naul, Joshua S. Bloom, Fernando Pérez, and Stéfan van der Walt. A recurrent neural network for classification of unevenly sampled variable stars. *Nature Astronomy*, 2:151–155, November 2018. doi: 10.1038/s41550-017-0321-z.

New York Times. Finds spiral nebulae are stellar systems; dr. hubbell confirms view that they are 'island universes' similar to our own. *New York Times*, 1924.

- Jeffrey A. Newman, Michael C. Cooper, Marc Davis, S. M. Faber, Alison L. Coil, Puragra Guhathakurta, David C. Koo, Andrew C. Phillips, Charlie Conroy, Aaron A. Dutton, Douglas P. Finkbeiner, Brian F. Gerke, David J. Rosario, Benjamin J. Weiner, C. N. A. Willmer, Renbin Yan, Justin J. Harker, Susan A. Kassin, N. P. Konidaris, Kamson Lai, Darren S. Madgwick, K. G. Noeske, Gregory D. Wirth, A. J. Connolly, N. Kaiser, Evan N. Kirby, Brian C. Lemaux, Lihwai Lin, Jennifer M. Lotz, G. A. Luppino, C. Marinoni, Daniel J. Matthews, Anne Metevier, and Ricardo P. Schiavon. THE DEEP2 GALAXY REDSHIFT SURVEY: DESIGN, OBSERVATIONS, DATA REDUCTION, AND REDSHIFTS. *The Astrophysical Journal Supplement Series*, 208(1):5, aug 2013. doi: 10.1088/0067-0049/208/1/5. URL <https://doi.org/10.1088/0067-0049/208/1/5>.
- Nathan Ng, Kyunghyun Cho, and Marzyeh Ghassemi. Ssmba: Self-supervised manifold based data augmentation for improving out-of-domain robustness. In *Proceedings of the 2020 Conference on Empirical Methods in Natural Language Processing (EMNLP)*, pages 1268–1283, 2020.
- M. Nicholl, J. Guillochon, and E. Berger. The Magnetar Model for Type I Superluminous Supernovae. I. Bayesian Analysis of the Full Multicolor Light-curve Sample with MOSFiT. *apj*, 850:55, November 2017. doi: 10.3847/1538-4357/aa9334.
- Alexandru Niculescu-Mizil and Rich Caruana. Predicting good probabilities with supervised learning. In *Proceedings of the 22nd International Conference on Machine Learning, ICML '05*, page 625–632, New York, NY, USA, 2005. Association for Computing Machinery. ISBN 1595931805. doi: 10.1145/1102351.1102430. URL <https://doi.org/10.1145/1102351.1102430>.
- N. Palanque-Delabrouille, V. Ruhlmann-Kleider, S. Pascal, J. Rich, J. Guy, G. Bazin, P. Astier, C. Balland, S. Basa, R. G. Carlberg, A. Conley, D. Fouchez, D. Hardin, I. M. Hook, D. A. Howell, R. Pain, K. Perrett, C. J. Pritchett, N. Regnault, and M. Sullivan. Photometric redshifts for type ia supernovae in the supernova legacy survey. *Astronomy and Astrophysics*, 514:A63, may 2010. doi: 10.1051/0004-6361/200913283. URL <https://doi.org/10.1051/0004-6361/200913283>.
- Johanna Pasquet, E. Bertin, M. Treyer, S. Arnouts, and D. Fouchez. Photometric redshifts from SDSS images using a convolutional neural network. *Astronomy & Astrophysics*, 621:A26, dec 2018. doi: 10.1051/0004-6361/201833617. URL <https://doi.org/10.1051/0004-6361/201833617>.
- Johanna Pasquet, Jérôme Pasquet, Marc Chaumont, and Dominique Fouchez. PELICAN: deep architecture for the Light Curve ANalysis. *A&A*, 627:A21, July 2019a. doi: 10.1051/0004-6361/201834473.
- Johanna Pasquet, Jérôme Pasquet, Marc Chaumont, and Dominique Fouchez. PELICAN: deep architecture for the Light Curve ANalysis. *A&A*, 627:A21, July 2019b. doi: 10.1051/0004-6361/201834473.
- H. B. Perets, A. Gal-Yam, P. A. Mazzali, D. Arnett, D. Kagan, A. V. Filippenko, W. Li, I. Arcavi, S. B. Cenko, D. B. Fox, D. C. Leonard, D. S. Moon, D. J. Sand, A. M. Soderberg, J. P. Anderson, P. A. James, R. J. Foley, M. Ganeshalingam, E. O. Ofek, L. Bildsten, G. Nelemans, K. J. Shen, N. N. Weinberg, B. D. Metzger, A. L. Piro, E. Quataert, M. Kiewe, and D. Poznanski. A faint type of

- supernova from a white dwarf with a helium-rich companion. *Nature*, 465(7296):322–325, May 2010. doi: 10.1038/nature09056.
- S. Perlmutter, S. Gabi, G. Goldhaber, A. Goobar, D. E. Groom, I. M. Hook, A. G. Kim, M. Y. Kim, J. C. Lee, R. Pain, C. R. Pennypacker, I. A. Small, R. S. Ellis, R. G. McMahon, B. J. Boyle, P. S. Bunclark, D. Carter, M. J. Irwin, K. Glazebrook, H. J. M. Newberg, A. V. Filippenko, T. Matheson, M. Dopita, and W. J. Couch. Measurements of the Cosmological Parameters  $\Omega$  and  $\Lambda$  from the First Seven Supernovae at  $z \geq 0.35$ . *ApJ*, 483(2):565–581, July 1997. doi: 10.1086/304265.
- S. Perlmutter, G. Aldering, G. Goldhaber, R. A. Knop, P. Nugent, P. G. Castro, S. Deustua, S. Fabbro, A. Goobar, D. E. Groom, I. M. Hook, A. G. Kim, M. Y. Kim, J. C. Lee, N. J. Nunes, R. Pain, C. R. Pennypacker, R. Quimby, C. Lidman, R. S. Ellis, M. Irwin, R. G. McMahon, P. Ruiz-Lapuente, N. Walton, B. Schaefer, B. J. Boyle, A. V. Filippenko, T. Matheson, A. S. Fruchter, N. Panagia, H. J. M. Newberg, W. J. Couch, and The Supernova Cosmology Project. Measurements of  $\omega$  and  $\lambda$  from 42 high-redshift supernovae. *The Astrophysical Journal*, 517(2):565–586, June 1999. ISSN 1538-4357. doi: 10.1086/307221. URL <http://dx.doi.org/10.1086/307221>.
- Saul Perlmutter. Nobel lecture: Measuring the acceleration of the cosmic expansion using supernovae. *Rev. Mod. Phys.*, 84:1127–1149, Aug 2012. doi: 10.1103/RevModPhys.84.1127. URL <https://link.aps.org/doi/10.1103/RevModPhys.84.1127>.
- K. Perrett, M. Sullivan, A. Conley, S. González-Gaitán, R. Carlberg, D. Fouchez, P. Ripoché, J. D. Neill, P. Astier, D. Balam, C. Balland, S. Basa, J. Guy, D. Hardin, I. M. Hook, D. A. Howell, R. Pain, N. Palanque-Delabrouille, C. Pritchett, N. Regnault, J. Rich, V. Ruhlmann-Kleider, S. Baumont, C. Lidman, S. Perlmutter, and E. S. Walker. Evolution in the Volumetric Type Ia Supernova Rate from the Supernova Legacy Survey. *AJ*, 144(2):59, August 2012. doi: 10.1088/0004-6256/144/2/59.
- M. M. Phillips. The Absolute Magnitudes of Type IA Supernovae. *ApJ*, 413:L105, August 1993. doi: 10.1086/186970.
- J. D. R. Pierel, S. Rodney, A. Avelino, F. Bianco, A. V. Filippenko, R. J. Foley, A. Friedman, M. Hicken, R. Hounsell, S. W. Jha, R. Kessler, R. P. Kirshner, K. Mandel, G. Narayan, D. Scolnic, and L. Strolger. Extending Supernova Spectral Templates for Next-generation Space Telescope Observations. *pasp*, 130(11):114504, November 2018a. doi: 10.1088/1538-3873/aadb7a.
- J. D. R. Pierel, S. Rodney, A. Avelino, F. Bianco, A. V. Filippenko, R. J. Foley, A. Friedman, M. Hicken, R. Hounsell, S. W. Jha, R. Kessler, R. P. Kirshner, K. Mandel, G. Narayan, D. Scolnic, and L. Strolger. Extending Supernova Spectral Templates for Next-generation Space Telescope Observations. *pasp*, 130(11):114504, November 2018b. doi: 10.1088/1538-3873/aadb7a.
- J. D. R. Pierel, S. Rodney, A. Avelino, F. Bianco, A. V. Filippenko, R. J. Foley, A. Friedman, M. Hicken, R. Hounsell, S. W. Jha, R. Kessler, R. P. Kirshner, K. Mandel, G. Narayan, D. Scolnic, and L. Strolger.



ger. Extending Supernova Spectral Templates for Next-generation Space Telescope Observations.

*pasp*, 130(11):114504, November 2018c. doi: 10.1088/1538-3873/aadb7a.

J. D. R. Pierel, S. Rodney, A. Avelino, F. Bianco, A. V. Filippenko, R. J. Foley, A. Friedman, M. Hicken, R. Hounsell, S. W. Jha, R. Kessler, R. P. Kirshner, K. Mandel, G. Narayan, D. Scolnic, and L. Strolger. Extending Supernova Spectral Templates for Next-generation Space Telescope Observations. *PASP*, 130(993):114504, November 2018d. doi: 10.1088/1538-3873/aadb7a.

Planck Collaboration, N. Aghanim, Y. Akrami, M. Ashdown, J. Aumont, C. Baccigalupi, M. Ballardini, A. J. Banday, R. B. Barreiro, N. Bartolo, S. Basak, R. Battye, K. Benabed, J. P. Bernard, M. Bersanelli, P. Bielewicz, J. J. Bock, J. R. Bond, J. Borrill, F. R. Bouchet, F. Boulanger, M. Bucher, C. Burigana, R. C. Butler, E. Calabrese, J. F. Cardoso, J. Carron, A. Challinor, H. C. Chiang, J. Chluba, L. P. L. Colombo, C. Combet, D. Contreras, B. P. Crill, F. Cuttaia, P. de Bernardis, G. de Zotti, J. Delabrouille, J. M. Delouis, E. Di Valentino, J. M. Diego, O. Doré, M. Douspis, A. Ducout, X. Dupac, S. Dusini, G. Efstathiou, F. Elsner, T. A. Enßlin, H. K. Eriksen, Y. Fantaye, M. Farhang, J. Fergusson, R. Fernandez-Cobos, F. Finelli, F. Forastieri, M. Frailis, A. A. Fraisse, E. Franceschi, A. Frolov, S. Galeotta, S. Galli, K. Ganga, R. T. Génova-Santos, M. Gerbino, T. Ghosh, J. González-Nuevo, K. M. Górski, S. Gratton, A. Gruppuso, J. E. Gudmundsson, J. Hamann, W. Handley, F. K. Hansen, D. Herranz, S. R. Hildebrandt, E. Hivon, Z. Huang, A. H. Jaffe, W. C. Jones, A. Karakci, E. Keihänen, R. Keskitalo, K. Kiiveri, J. Kim, T. S. Kisner, L. Knox, N. Krachmalnicoff, M. Kunz, H. Kurki-Suonio, G. Lagache, J. M. Lamarre, A. Lasenby, M. Lattanzi, C. R. Lawrence, M. Le Jeune, P. Lemos, J. Lesgourgues, F. Levrier, A. Lewis, M. Liguori, P. B. Lilje, M. Lilley, V. Lindholm, M. López-Cañiego, P. M. Lubin, Y. Z. Ma, J. F. Macías-Pérez, G. Maggio, D. Maino, N. Mandolesi, A. Mangilli, A. Marcos-Caballero, M. Maris, P. G. Martin, M. Martinelli, E. Martínez-González, S. Matarrese, N. Mauri, J. D. McEwen, P. R. Meinhold, A. Melchiorri, A. Mennella, M. Migliaccio, M. Millea, S. Mitra, M. A. Miville-Deschênes, D. Molinari, L. Montier, G. Morgante, A. Moss, P. Natoli, H. U. Nørgaard-Nielsen, L. Pagano, D. Paoletti, B. Partridge, G. Patanchon, H. V. Peiris, F. Perrotta, V. Pettorino, F. Piacentini, L. Polastri, G. Polenta, J. L. Puget, J. P. Rachen, M. Reinecke, M. Remazeilles, A. Renzi, G. Rocha, C. Rosset, G. Roudier, J. A. Rubiño-Martín, B. Ruiz-Granados, L. Salvati, M. Sandri, M. Savelainen, D. Scott, E. P. S. Shellard, C. Sirignano, G. Sirri, L. D. Spencer, R. Sunyaev, A. S. Suur-Uski, J. A. Tauber, D. Tavagnacco, M. Tenti, L. Toffolatti, M. Tomasi, T. Trombetti, L. Valenziano, J. Valiviita, B. Van Tent, L. Vibert, P. Vielva, F. Villa, N. Vittorio, B. D. Wandelt, I. K. Wehus, M. White, S. D. M. White, A. Zacchei, and A. Zonca. Planck 2018 results. VI. Cosmological parameters. *A&A*, 641:A6, September 2020. doi: 10.1051/0004-6361/201833910.

Brodie Popovic, Dan Scolnic, and Richard Kessler. Assessment of Systematic Uncertainties in the Cosmological Analysis of the SDSS Supernovae Photometric Sample. *ApJ*, 890(2):172, February 2020. doi: 10.3847/1538-4357/ab6deb.

Brodie Popovic, Dillon Brout, Richard Kessler, Dan Scolnic, and Lisa Lu. Improved Treatment of Host-galaxy Correlations in Cosmological Analyses with Type Ia Supernovae. *ApJ*, 913(1):49, May 2021. doi: 10.3847/1538-4357/abf14f.

- Dovi Poznanski, Dan Maoz, and Avishay Gal-Yam. Bayesian Single-Epoch Photometric Classification of Supernovae. *AJ*, 134(3):1285–1297, September 2007. doi: 10.1086/520956.
- M. Pursiainen, M. Childress, M. Smith, S. Prajs, M. Sullivan, T. M. Davis, R. J. Foley, J. Asorey, J. Calcinò, D. Carollo, C. Curtin, C. B. D’Andrea, K. Glazebrook, C. Gutierrez, S. R. Hinton, J. K. Hoormann, C. Inserra, R. Kessler, A. King, K. Kuehn, G. F. Lewis, C. Lidman, E. Macaulay, A. Möller, R. C. Nichol, M. Sako, N. E. Sommer, E. Swann, B. E. Tucker, S. A. Uddin, P. Wiseman, B. Zhang, T. M. C. Abbott, F. B. Abdalla, S. Allam, J. Annis, S. Avila, D. Brooks, E. Buckley-Geer, D. L. Burke, A. Carnero Rosell, M. Carrasco Kind, J. Carretero, F. J. Castander, C. E. Cunha, C. Davis, J. De Vicente, H. T. Diehl, P. Doel, T. F. Eifler, B. Flaugher, P. Fosalba, J. Frieman, J. García-Bellido, D. Gruen, R. A. Gruendl, G. Gutierrez, W. G. Hartley, D. L. Hollowood, K. Honscheid, D. J. James, T. Jeltema, N. Kuropatkin, T. S. Li, M. Lima, M. A. G. Maia, P. Martini, F. Menanteau, R. L. C. Ogando, A. A. Plazas, A. Roodman, E. Sanchez, V. Scarpine, R. Schindler, R. C. Smith, M. Soares-Santos, F. Sobreira, E. Suchyta, M. E. C. Swanson, G. Tarle, D. L. Tucker, A. R. Walker, and DES Collaboration. Rapidly evolving transients in the Dark Energy Survey. *MNRAS*, 481(1):894–917, November 2018. doi: 10.1093/mnras/sty2309.
- Helen Qu. helenqu/scone: first release, April 2021a. URL <https://doi.org/10.5281/zenodo.4660288>.
- Helen Qu. helenqu/scone: early lightcurve classification release, October 2021b. URL <https://doi.org/10.5281/zenodo.5602043>.
- Helen Qu and Masao Sako. Photo-zSNthesis: Converting Type Ia Supernova Lightcurves to Redshift Estimates via Deep Learning. *Astrophysical Journal*, 954(2):201, September 2023. doi: 10.3847/1538-4357/aceafa.
- Helen Qu, Masao Sako, Anais Möller, and Cyrille Doux. SCONE: Supernova Classification with a Convolutional Neural Network. *AJ*, 162(2):67, August 2021. doi: 10.3847/1538-3881/ac0824.
- Helen Qu, Masao Sako, Anais Möller, and Cyrille Doux. SCONE: Supernova classification with a convolutional neural network. *The Astronomical Journal*, 162(2):67, jul 2021. doi: 10.3847/1538-3881/ac0824. URL <https://doi.org/10.3847/1538-3881/ac0824>.
- Joaquin Quiñonero-Candela, Masashi Sugiyama, Anton Schwaighofer, and Neil D. Lawrence. *Dataset shift in machine learning*. The MIT Press, 2009.
- Alec Radford, Jong Wook Kim, Chris Hallacy, Aditya Ramesh, Gabriel Goh, Sandhini Agarwal, Girish Sastry, Amanda Askell, Pamela Mishkin, Jack Clark, Gretchen Krueger, and Ilya Sutskever. Learning transferable visual models from natural language supervision. In *International Conference on Machine Learning (ICML)*, volume 139, pages 8748–8763, 2021.
- Colin Raffel, Noam Shazeer, Adam Roberts, Katherine Lee, Sharan Narang, Michael Matena, Yanqi Zhou, Wei Li, and Peter J. Liu. Exploring the limits of transfer learning with a unified text-to-text transformer. *arXiv preprint arXiv:1910.10683*, 2019.

- Sylvestre-Alvise Rebuffi, Sven Gowal, Dan Andrei Calian, Florian Stimberg, Olivia Wiles, and Timothy A Mann. Data augmentation can improve robustness. *Advances in Neural Information Processing Systems*, 34:29935–29948, 2021.
- A. Rest, D. Scolnic, R. J. Foley, M. E. Huber, R. Chornock, G. Narayan, J. L. Tonry, E. Berger, A. M. Soderberg, C. W. Stubbs, A. Riess, R. P. Kirshner, S. J. Smartt, E. Schlafly, S. Rodney, M. T. Botticella, D. Brout, P. Challis, I. Czekala, M. Drout, M. J. Hudson, R. Kotak, C. Leibler, R. Lunnan, G. H. Marion, M. McCrum, D. Milisavljevic, A. Pastorello, N. E. Sanders, K. Smith, E. Stafford, D. Thilker, S. Valenti, W. M. Wood-Vasey, Z. Zheng, W. S. Burgett, K. C. Chambers, L. Denneau, P. W. Draper, H. Flewelling, K. W. Hodapp, N. Kaiser, R. P. Kudritzki, E. A. Magnier, N. Metcalfe, P. A. Price, W. Sweeney, R. Wainscoat, and C. Waters. Cosmological Constraints from Measurements of Type Ia Supernovae Discovered during the First 1.5 yr of the Pan-STARRS1 Survey. *ApJ*, 795(1):44, November 2014. doi: 10.1088/0004-637X/795/1/44.
- Michael D. Richard and Richard P. Lippmann. Neural Network Classifiers Estimate Bayesian a posteriori Probabilities. *Neural Computation*, 3(4):461–483, 12 1991. ISSN 0899-7667. doi: 10.1162/neco.1991.3.4.461. URL <https://doi.org/10.1162/neco.1991.3.4.461>.
- Joseph W. Richards, Darren Homrighausen, Peter E. Freeman, Chad M. Schafer, and Dovi Poznanski. Semi-supervised learning for photometric supernova classification. *MNRAS*, 419(2): 1121–1135, January 2012. doi: 10.1111/j.1365-2966.2011.19768.x.
- A. G. Riess. An Accelerating Universe and Other Cosmological Implications from SNe IA. In *American Astronomical Society Meeting Abstracts #192*, volume 192 of *American Astronomical Society Meeting Abstracts*, page 17.06, May 1998.
- Adam G. Riess, Stefano Casertano, Wenlong Yuan, Lucas M. Macri, and Dan Scolnic. Large Magellanic Cloud Cepheid Standards Provide a 1% Foundation for the Determination of the Hubble Constant and Stronger Evidence for Physics beyond  $\Lambda$ CDM. *ApJ*, 876(1):85, May 2019. doi: 10.3847/1538-4357/ab1422.
- M. Rigault, V. Brinnel, G. Aldering, P. Antilogus, C. Aragon, S. Bailey, C. Baltay, K. Barbary, S. Bongard, K. Boone, C. Buton, M. Childress, N. Chotard, Y. Copin, S. Dixon, P. Fagrelus, U. Feindt, D. Fouchez, E. Gangler, B. Hayden, W. Hillebrandt, D. A. Howell, A. Kim, M. Kowalski, D. Kuesters, P.-F. Leget, S. Lombardo, Q. Lin, J. Nordin, R. Pain, E. Pecontal, R. Pereira, S. Perlmutter, D. Rabinowitz, K. Runge, D. Rubin, C. Saunders, G. Smadja, C. Sofiatti, N. Suzuki, S. Taubenberger, C. Tao, and R. C. Thomas. Strong dependence of type ia supernova standardization on the local specific star formation rate. *Astronomy & Astrophysics*, 644:A176, dec 2020. doi: 10.1051/0004-6361/201730404. URL <https://doi.org/10.1051/0004-6361/201730404>.
- B. M. Rose, C. Baltay, R. Hounsell, P. Macias, D. Rubin, D. Scolnic, G. Aldering, R. Bohlin, M. Dai, S. E. Deustua, R. J. Foley, A. Fruchter, L. Galbany, S. W. Jha, D. O. Jones, B. A. Joshi, P. L. Kelly, R. Kessler, R. P. Kirshner, K. S. Mandel, S. Perlmutter, J. Pierel, H. Qu, D. Rabinowitz, A. Rest, A. G. Riess, S. Rodney, M. Sako, M. R. Siebert, L. Strolger, N. Suzuki, S. Thorp, S. D. Van Dyk, K. Wang, S. M. Ward, and W. M. Wood-Vasey. A reference survey for supernova cosmology with

the nancy grace roman space telescope, 2021.

Olga Russakovsky, Jia Deng, Hao Su, Jonathan Krause, Sanjeev Satheesh, Sean Ma, Zhiheng Huang, Andrej Karpathy, Aditya Khosla, Michael Bernstein, Alexander C. Berg, and Li Fei-Fei. ImageNet Large Scale Visual Recognition Challenge. *International Journal of Computer Vision (IJCV)*, 115(3):211–252, 2015. doi: 10.1007/s11263-015-0816-y.

Kate Saenko, Brian Kulis, Mario Fritz, and Trevor Darrell. Adapting visual category models to new domains. In *European conference on computer vision*, pages 213–226, 2010.

Shiori Sagawa, Pang Wei Koh, Tony Lee, Irena Gao, Sang Michael Xie, Kendrick Shen, Ananya Kumar, Weihua Hu, Michihiro Yasunaga, H. Marklund, Sara Beery, E. David, I. Stavness, Wei Guo, J. Leskovec, Kate Saenko, Tatsunori B. Hashimoto, S. Levine, Chelsea Finn, and Percy Liang. Extending the WILDS benchmark for unsupervised adaptation. In *International Conference on Learning Representations (ICLR)*, 2022.

Masao Sako, Bruce Bassett, Andrew Becker, David Cinabro, Fritz DeJongh, D. L. Depoy, Ben Dilday, Mamoru Doi, Joshua A. Frieman, Peter M. Garnavich, Craig J. Hogan, Jon Holtzman, Saurabh Jha, Richard Kessler, Kohki Konishi, Hubert Lampeitl, John Marriner, Gajus Miknaitis, Robert C. Nichol, Jose Luis Prieto, Adam G. Riess, Michael W. Richmond, Roger Romani, Donald P. Schneider, Mathew Smith, Mark SubbaRao, Naohiro Takanashi, Kouichi Tokita, Kurt van der Heyden, Naoki Yasuda, Chen Zheng, John Barentine, Howard Brewington, Changsu Choi, Jack Dembicky, Michael Harnavek, Yutaka Ihara, Myungshin Im, William Ketzeback, Scott J. Kleinman, Jurek Krzesiński, Daniel C. Long, Elena Malanushenko, Viktor Malanushenko, Russet J. McMillan, Tomoki Morokuma, Atsuko Nitta, Kaike Pan, Gabrelle Saurage, and Stephanie A. Snedden. The Sloan Digital Sky Survey-II Supernova Survey: Search Algorithm and Follow-up Observations. *AJ*, 135(1):348–373, January 2008a. doi: 10.1088/0004-6256/135/1/348.

Masao Sako, Bruce Bassett, Andrew Becker, David Cinabro, Fritz DeJongh, D. L. Depoy, Ben Dilday, Mamoru Doi, Joshua A. Frieman, Peter M. Garnavich, Craig J. Hogan, Jon Holtzman, Saurabh Jha, Richard Kessler, Kohki Konishi, Hubert Lampeitl, John Marriner, Gajus Miknaitis, Robert C. Nichol, Jose Luis Prieto, Adam G. Riess, Michael W. Richmond, Roger Romani, Donald P. Schneider, Mathew Smith, Mark SubbaRao, Naohiro Takanashi, Kouichi Tokita, Kurt van der Heyden, Naoki Yasuda, Chen Zheng, John Barentine, Howard Brewington, Changsu Choi, Jack Dembicky, Michael Harnavek, Yutaka Ihara, Myungshin Im, William Ketzeback, Scott J. Kleinman, Jurek Krzesiński, Daniel C. Long, Elena Malanushenko, Viktor Malanushenko, Russet J. McMillan, Tomoki Morokuma, Atsuko Nitta, Kaike Pan, Gabrelle Saurage, and Stephanie A. Snedden. The Sloan Digital Sky Survey-II Supernova Survey: Search Algorithm and Follow-up Observations. *AJ*, 135(1):348–373, January 2008b. doi: 10.1088/0004-6256/135/1/348.

Masao Sako, Bruce Bassett, Brian Connolly, Benjamin Dilday, Heather Cambell, Joshua A. Frieman, Larry Gladney, Richard Kessler, Hubert Lampeitl, John Marriner, Ramon Miquel, Robert C. Nichol, Donald P. Schneider, Mathew Smith, and Jesper Sollerman. Photometric type ia supernova candidates from the three-year sdss-ii sn survey data. *The Astrophysical Journal*, 738(2):162, August 2011. ISSN 1538-4357. doi: 10.1088/0004-637x/738/2/162. URL <http://dx.doi.org/10.1088/0004-637x/738/2/162>.

1088/0004-637X/738/2/162.

Masao Sako, Bruce Bassett, Brian Connolly, Benjamin Dilday, Heather Cambell, Joshua A. Frieman, Larry Gladney, Richard Kessler, Hubert Lampeitl, John Marriner, Ramon Miquel, Robert C. Nichol, Donald P. Schneider, Mathew Smith, and Jesper Sollerman. Photometric Type Ia Supernova Candidates from the Three-year SDSS-II SN Survey Data. *ApJ*, 738(2):162, September 2011a. doi: 10.1088/0004-637X/738/2/162.

Masao Sako, Bruce Bassett, Brian Connolly, Benjamin Dilday, Heather Cambell, Joshua A. Frieman, Larry Gladney, Richard Kessler, Hubert Lampeitl, John Marriner, Ramon Miquel, Robert C. Nichol, Donald P. Schneider, Mathew Smith, and Jesper Sollerman. Photometric Type Ia Supernova Candidates from the Three-year SDSS-II SN Survey Data. *ApJ*, 738(2):162, September 2011b. doi: 10.1088/0004-637X/738/2/162.

Masao Sako, Bruce Bassett, Andrew C. Becker, Peter J. Brown, Heather Campbell, Rachel Wolf, David Cinabro, Chris B. D'Andrea, Kyle S. Dawson, Fritz DeJongh, Darren L. Depoy, Ben Dilday, Mamoru Doi, Alexei V. Filippenko, John A. Fischer, Ryan J. Foley, Joshua A. Frieman, Lluís Galbany, Peter M. Garnavich, Ariel Goobar, Ravi R. Gupta, Gary J. Hill, Brian T. Hayden, Renée Hlozek, Jon A. Holtzman, Ulrich Hopp, Saurabh W. Jha, Richard Kessler, Wolfram Kollatschny, Giorgos Leloudas, John Marriner, Jennifer L. Marshall, Ramon Miquel, Tomoki Morokuma, Jennifer Mosher, Robert C. Nichol, Jakob Nordin, Matthew D. Olmstead, Linda Östman, Jose L. Prieto, Michael Richmond, Roger W. Romani, Jesper Sollerman, Max Stritzinger, Donald P. Schneider, Mathew Smith, J. Craig Wheeler, Naoki Yasuda, and Chen Zheng. The Data Release of the Sloan Digital Sky Survey-II Supernova Survey. *PASP*, 130(988):064002, June 2018a. doi: 10.1088/1538-3873/aab4e0.

Masao Sako, Bruce Bassett, Andrew C. Becker, Peter J. Brown, Heather Campbell, Rachel Wolf, David Cinabro, Chris B. D'Andrea, Kyle S. Dawson, Fritz DeJongh, Darren L. Depoy, Ben Dilday, Mamoru Doi, Alexei V. Filippenko, John A. Fischer, Ryan J. Foley, Joshua A. Frieman, Lluís Galbany, Peter M. Garnavich, Ariel Goobar, Ravi R. Gupta, Gary J. Hill, Brian T. Hayden, Renée Hlozek, Jon A. Holtzman, Ulrich Hopp, Saurabh W. Jha, Richard Kessler, Wolfram Kollatschny, Giorgos Leloudas, John Marriner, Jennifer L. Marshall, Ramon Miquel, Tomoki Morokuma, Jennifer Mosher, Robert C. Nichol, Jakob Nordin, Matthew D. Olmstead, Linda Östman, Jose L. Prieto, Michael Richmond, Roger W. Romani, Jesper Sollerman, Max Stritzinger, Donald P. Schneider, Mathew Smith, J. Craig Wheeler, Naoki Yasuda, and Chen Zheng. The Data Release of the Sloan Digital Sky Survey-II Supernova Survey. *PASP*, 130(988):064002, June 2018b. doi: 10.1088/1538-3873/aab4e0.

Masao Sako, Bruce Bassett, Andrew C. Becker, Peter J. Brown, Heather Campbell, Rachel Wolf, David Cinabro, Chris B. D'Andrea, Kyle S. Dawson, Fritz DeJongh, Darren L. Depoy, Ben Dilday, Mamoru Doi, Alexei V. Filippenko, John A. Fischer, Ryan J. Foley, Joshua A. Frieman, Lluís Galbany, Peter M. Garnavich, Ariel Goobar, Ravi R. Gupta, Gary J. Hill, Brian T. Hayden, Renée Hlozek, Jon A. Holtzman, Ulrich Hopp, Saurabh W. Jha, Richard Kessler, Wolfram Kollatschny, Giorgos Leloudas, John Marriner, Jennifer L. Marshall, Ramon Miquel, Tomoki Morokuma, Jennifer Mosher, Robert C. Nichol, Jakob Nordin, Matthew D. Olmstead, Linda Östman, Jose L. Pri-

- eto, Michael Richmond, Roger W. Romani, Jesper Sollerman, Max Stritzinger, Donald P. Schneider, Mathew Smith, J. Craig Wheeler, Naoki Yasuda, and Chen Zheng. The data release of the sloan digital sky survey-ii supernova survey. *Publications of the Astronomical Society of the Pacific*, 130(988):064002, May 2018. ISSN 1538-3873. doi: 10.1088/1538-3873/aab4e0. URL <http://dx.doi.org/10.1088/1538-3873/aab4e0>.
- C. Sánchez, M. Carrasco Kind, H. Lin, R. Miquel, F. B. Abdalla, A. Amara, M. Banerji, C. Bonnett, R. Brunner, D. Capozzi, A. Carnero, F. J. Castander, L. A. N. da Costa, C. Cunha, A. Fausti, D. Gerdes, N. Greisel, J. Gschwend, W. Hartley, S. Jouvel, O. Lahav, M. Lima, M. A. G. Maia, P. Martí, R. L. C. Ogando, F. Ostrovski, P. Pellegrini, M. M. Rau, I. Sadeh, S. Seitz, I. Sevilla-Noarbe, A. Sypniewski, J. de Vicente, T. Abbot, S. S. Allam, D. Atlee, G. Bernstein, J. P. Bernstein, E. Buckley-Geer, D. Burke, M. J. Childress, T. Davis, D. L. DePoy, A. Dey, S. Desai, H. T. Diehl, P. Doel, J. Estrada, A. Evrard, E. Fernández, D. Finley, B. Flaugher, J. Frieman, E. Gaztanaga, K. Glazebrook, K. Honscheid, A. Kim, K. Kuehn, N. Kuropatkin, C. Lidman, M. Makler, J. L. Marshall, R. C. Nichol, A. Roodman, E. Sánchez, B. X. Santiago, M. Sako, R. Scalzo, R. C. Smith, M. E. C. Swanson, G. Tarle, D. Thomas, D. L. Tucker, S. A. Uddin, F. Valdés, A. Walker, F. Yuan, and J. Zuntz. Photometric redshift analysis in the Dark Energy Survey Science Verification data. *MNRAS*, 445(2):1482–1506, December 2014. doi: 10.1093/mnras/stu1836.
- Carles Sánchez, Marco Raveri, Alex Alarcon, and Gary M. Bernstein. Propagating sample variance uncertainties in redshift calibration: simulations, theory, and application to the COSMOS2015 data. *MNRAS*, 498(2):2984–2999, October 2020. doi: 10.1093/mnras/staa2542.
- P. Sánchez-Sáez, I. Reyes, C. Valenzuela, F. Förster, S. Eyheramendy, F. Elorrieta, F. E. Bauer, G. Cabrera-Vives, P. A. Estévez, M. Catelan, G. Pignata, P. Huijse, D. De Cicco, P. Arévalo, R. Carrasco-Davis, J. Abril, R. Kurtev, J. Borissova, J. Arredondo, E. Castillo-Navarrete, D. Rodríguez, D. Ruz-Mieres, A. Moya, L. Sabatini-Gacitúa, C. Sepúlveda-Cobo, and E. Camacho-Iñiguez. Alert Classification for the ALERCE Broker System: The Light Curve Classifier. *AJ*, 161(3):141, March 2021. doi: 10.3847/1538-3881/abd5c1.
- Edward F. Schlafly and Douglas P. Finkbeiner. Measuring Reddening with Sloan Digital Sky Survey Stellar Spectra and Recalibrating SFD. *ApJ*, 737(2):103, August 2011. doi: 10.1088/0004-637X/737/2/103.
- David J. Schlegel, Douglas P. Finkbeiner, and Marc Davis. Maps of Dust Infrared Emission for Use in Estimation of Reddening and Cosmic Microwave Background Radiation Foregrounds. *ApJ*, 500(2):525–553, June 1998. doi: 10.1086/305772.
- D. Scolnic and R. Kessler. Measuring Type Ia Supernova Populations of Stretch and Color and Predicting Distance Biases. *ApJ*, 822(2):L35, May 2016. doi: 10.3847/2041-8205/822/2/L35.
- D. M. Scolnic, D. O. Jones, A. Rest, Y. C. Pan, R. Chornock, R. J. Foley, M. E. Huber, R. Kessler, G. Narayan, A. G. Riess, S. Rodney, E. Berger, D. J. Brout, P. J. Challis, M. Drout, D. Finkbeiner, R. Lunnan, R. P. Kirshner, N. E. Sanders, E. Schlafly, S. Smartt, C. W. Stubbs, J. Tonry, W. M. Wood-Vasey, M. Foley, J. Hand, E. Johnson, W. S. Burgett, K. C. Chambers, P. W. Draper, K. W.

- Hodapp, N. Kaiser, R. P. Kudritzki, E. A. Magnier, N. Metcalfe, F. Bresolin, E. Gall, R. Kotak, M. McCrum, and K. W. Smith. The Complete Light-curve Sample of Spectroscopically Confirmed SNe Ia from Pan-STARRS1 and Cosmological Constraints from the Combined Pantheon Sample. *ApJ*, 859(2):101, June 2018. doi: 10.3847/1538-4357/aab9bb.
- J. L. Sérsic. Influence of the atmospheric and instrumental dispersion on the brightness distribution in a galaxy. *Boletín de la Asociación Argentina de Astronomía La Plata Argentina*, 6:41–43, February 1963.
- Kendrick Shen, Robbie Jones, Ananya Kumar, Sang Michael Xie, Jeff Z. HaoChen, Tengyu Ma, and Percy Liang. Connect, not collapse: Explaining contrastive learning for unsupervised domain adaptation. In *International Conference on Machine Learning (ICML)*, 2022.
- Hidetoshi Shimodaira. Improving predictive inference under covariate shift by weighting the log-likelihood function. *Journal of Statistical Planning and Inference*, 90:227–244, 2000.
- Isaac Shivvers, Maryam Modjaz, WeiKang Zheng, Yuqian Liu, Alexei V. Filippenko, Jeffrey M. Silverman, Thomas Matheson, Andrea Pastorello, Or Graur, Ryan J. Foley, Ryan Chornock, Nathan Smith, Jesse Leaman, and Stefano Benetti. Revisiting the Lick Observatory Supernova Search Volume-limited Sample: Updated Classifications and Revised Stripped-envelope Supernova Fractions. *PASP*, 129(975):054201, May 2017. doi: 10.1088/1538-3873/aa54a6.
- Patrice Y. Simard, Dave Steinkraus, and John C. Platt. Best practices for convolutional neural networks applied to visual document analysis. *International Conference on Document Analysis and Recognition*, 2:958–964, 2003.
- Karen Simonyan and Andrew Zisserman. Very deep convolutional networks for large-scale image recognition. *CoRR*, abs/1409.1556, 2014a.
- Karen Simonyan and Andrew Zisserman. Very deep convolutional networks for large-scale image recognition. *arXiv preprint arXiv:1409.1556*, 2014b.
- V. M. Slipher. Nebulae. *Proceedings of the American Philosophical Society*, 56:403–409, January 1917.
- M. Smith, C. B. D’Andrea, M. Sullivan, A. Möller, R. C. Nichol, R. C. Thomas, A. G. Kim, M. Sako, F. J. Castander, A. V. Filippenko, R. J. Foley, L. Galbany, S. González-Gaitán, E. Kasai, R. P. Kirshner, C. Lidman, D. Scolnic, D. Brout, T. M. Davis, R. R. Gupta, S. R. Hinton, R. Kessler, J. Lasker, E. Macaulay, R. C. Wolf, B. Zhang, J. Asorey, A. Avelino, B. A. Bassett, J. Calcino, D. Carollo, R. Casas, P. Challis, M. Childress, A. Clocchiatti, S. Crawford, C. Frohmaier, K. Glazebrook, D. A. Goldstein, M. L. Graham, J. K. Hoormann, K. Kuehn, G. F. Lewis, K. S. Mandel, E. Morganson, D. Muthukrishna, P. Nugent, Y. C. Pan, M. Pursiainen, R. Sharp, N. E. Sommer, E. Swann, B. P. Thomas, B. E. Tucker, S. A. Uddin, P. Wiseman, W. Zheng, T. M. C. Abbott, J. Annis, S. Avila, K. Bechtol, G. M. Bernstein, E. Bertin, D. Brooks, D. L. Burke, A. Carnero Rosell, M. Carrasco Kind, J. Carretero, C. E. Cunha, L. N. da Costa, C. Davis, J. De Vicente, H. T. Diehl, T. F. Eifler, J. Estrada, J. Frieman, J. García-Bellido, E. Gaztanaga, D. W. Gerdes, D. Gruen, R. A. Gruendl,

- J. Gschwend, G. Gutierrez, W. G. Hartley, D. L. Hollowood, K. Honscheid, B. Hoyle, D. J. James, M. W. G. Johnson, M. D. Johnson, N. Kuropatkin, T. S. Li, M. Lima, M. A. G. Maia, M. March, J. L. Marshall, P. Martini, F. Menanteau, C. J. Miller, R. Miquel, E. Neilsen, R. L. C. Ogando, A. A. Plazas, A. K. Romer, E. Sanchez, V. Scarpine, M. Schubnell, S. Serrano, I. Sevilla-Noarbe, M. Soares-Santos, F. Sobreira, E. Suchyta, G. Tarle, D. L. Tucker, and W. Wester. First Cosmology Results using Supernovae Ia from the Dark Energy Survey: Survey Overview, Performance, and Supernova Spectroscopy. *AJ*, 160(6):267, December 2020a. doi: 10.3847/1538-3881/abc01b.
- M. Smith, M. Sullivan, P. Wiseman, R. Kessler, D. Scolnic, D. Brout, C. B. D’Andrea, T. M. Davis, R. J. Foley, C. Frohmaier, L. Galbany, R. R. Gupta, C. P. Gutiérrez, S. R. Hinton, L. Kelsey, C. Lidman, E. Macaulay, A. Möller, R. C. Nichol, P. Nugent, A. Palmese, M. Pursiainen, M. Sako, E. Swann, R. C. Thomas, B. E. Tucker, M. Vincenzi, D. Carollo, G. F. Lewis, N. E. Sommer, T. M. C. Abbott, M. Agüena, S. Allam, S. Avila, E. Bertin, S. Bhargava, D. Brooks, E. Buckley-Geer, D. L. Burke, A. Carnero Rosell, M. Carrasco Kind, M. Costanzi, L. N. da Costa, J. De Vicente, S. Desai, H. T. Diehl, P. Doel, T. F. Eifler, S. Everett, B. Flaugher, P. Fosalba, J. Frieman, J. García-Bellido, E. Gaztanaga, K. Glazebrook, D. Gruen, R. A. Gruendl, J. Gschwend, G. Gutierrez, W. G. Hartley, D. L. Hollowood, K. Honscheid, D. J. James, E. Krause, K. Kuehn, N. Kuropatkin, M. Lima, N. MacCrann, M. A. G. Maia, J. L. Marshall, P. Martini, P. Melchior, F. Menanteau, R. Miquel, F. Paz-Chinchón, A. A. Plazas, A. K. Romer, A. Roodman, E. S. Rykoff, E. Sanchez, V. Scarpine, M. Schubnell, S. Serrano, I. Sevilla-Noarbe, E. Suchyta, M. E. C. Swanson, G. Tarle, D. Thomas, D. L. Tucker, T. N. Varga, A. R. Walker, and DES Collaboration. First cosmology results using type Ia supernovae from the Dark Energy Survey: the effect of host galaxy properties on supernova luminosity. *MNRAS*, 494(3):4426–4447, May 2020b. doi: 10.1093/mnras/staa946.
- G. F. Smoot, C. L. Bennett, A. Kogut, J. Aymon, C. Backus, G. de Amici, K. Galuk, P. D. Jackson, P. Keegstra, L. Rokke, L. Tenorio, S. Torres, S. Gulkis, M. G. Hauser, M. A. Janssen, J. C. Mather, R. Weiss, D. T. Wilkinson, E. L. Wright, N. W. Boggess, E. S. Cheng, T. Kelsall, P. Lubin, S. Meyer, S. H. Moseley, T. L. Murdock, R. A. Shafer, and R. F. Silverberg. Preliminary Results from the COBE Differential Microwave Radiometers: Large Angular Scale Isotropy of the Cosmic Microwave Background. *ApJ*, 371:L1, April 1991. doi: 10.1086/185988.
- Kihyuk Sohn, David Berthelot, Chun-Liang Li, Zizhao Zhang, Nicholas Carlini, Ekin D. Cubuk, Alex Kurakin, Han Zhang, and Colin Raffel. Fixmatch: Simplifying semi-supervised learning with consistency and confidence. *arXiv*, 2020.
- J. Sollerman, S. Yang, S. Schulze, N. L. Strotjohann, A. Jerkstrand, S. D. Van Dyk, E. C. Kool, C. Barbarino, T. G. Brink, R. Bruch, K. De, A. V. Filippenko, C. Fremling, K. C. Patra, D. Perley, L. Yan, Y. Yang, I. Andreoni, R. Campbell, M. Coughlin, M. Kasliwal, Y. L. Kim, M. Rigault, K. Shin, A. Tzanidakis, M. C. B. Ashley, A. M. Moore, and T. Travouillon. Three Core-Collapse Supernovae with Nebular Hydrogen Emission. *arXiv e-prints*, art. arXiv:2107.14503, July 2021.
- Masashi Sugiyama, Matthias Krauledat, and Klaus-Robert Müller. Covariate shift adaptation by importance weighted cross validation. *Journal of Machine Learning Research (JMLR)*, 8:985–1005, 2007.



- M. Sullivan, D. A. Howell, K. Perrett, P. E. Nugent, P. Astier, E. Aubourg, D. Balam, S. Basa, R. G. Carlberg, A. Conley, S. Fabbro, D. Fouchez, J. Guy, I. Hook, H. Lafoux, J. D. Neill, R. Pain, N. Palanque-Delabrouille, C. J. Pritchett, N. Regnault, J. Rich, R. Taillet, G. Aldering, S. Baumont, J. Bronder, M. Filiol, R. A. Knop, S. Perlmutter, and C. Tao. Photometric Selection of High-Redshift Type Ia Supernova Candidates. *AJ*, 131(2):960–972, February 2006a. doi: 10.1086/499302.
- M. Sullivan, D. Le Borgne, C. J. Pritchett, A. Hodsman, J. D. Neill, D. A. Howell, R. G. Carlberg, P. Astier, E. Aubourg, D. Balam, S. Basa, A. Conley, S. Fabbro, D. Fouchez, J. Guy, I. Hook, R. Pain, N. Palanque-Delabrouille, K. Perrett, N. Regnault, J. Rich, R. Taillet, S. Baumont, J. Bronder, R. S. Ellis, M. Filiol, V. Lisset, S. Perlmutter, P. Ripoche, and C. Tao. Rates and Properties of Type Ia Supernovae as a Function of Mass and Star Formation in Their Host Galaxies. *ApJ*, 648(2): 868–883, September 2006b. doi: 10.1086/506137.
- M. Sullivan, D. Le Borgne, C. J. Pritchett, A. Hodsman, J. D. Neill, D. A. Howell, R. G. Carlberg, P. Astier, E. Aubourg, D. Balam, S. Basa, A. Conley, S. Fabbro, D. Fouchez, J. Guy, I. Hook, R. Pain, N. Palanque-Delabrouille, K. Perrett, N. Regnault, J. Rich, R. Taillet, S. Baumont, J. Bronder, R. S. Ellis, M. Filiol, V. Lisset, S. Perlmutter, P. Ripoche, and C. Tao. Rates and properties of type ia supernovae as a function of mass and star formation in their host galaxies. *The Astrophysical Journal*, 648(2):868–883, September 2006. ISSN 1538-4357. doi: 10.1086/506137. URL <http://dx.doi.org/10.1086/506137>.
- M. Sullivan, A. Conley, D. A. Howell, J. D. Neill, P. Astier, C. Balland, S. Basa, R. G. Carlberg, D. Fouchez, J. Guy, D. Hardin, I. M. Hook, R. Pain, N. Palanque-Delabrouille, K. M. Perrett, C. J. Pritchett, N. Regnault, J. Rich, V. Ruhlmann-Kleider, S. Baumont, E. Hsiao, T. Kronborg, C. Lidman, S. Perlmutter, and E. S. Walker. The dependence of Type Ia Supernovae luminosities on their host galaxies. *Monthly Notices of the Royal Astronomical Society*, 406(2):782–802, 07 2010. ISSN 0035-8711. doi: 10.1111/j.1365-2966.2010.16731.x. URL <https://doi.org/10.1111/j.1365-2966.2010.16731.x>.
- M. Sullivan, J. Guy, A. Conley, N. Regnault, P. Astier, C. Balland, S. Basa, R. G. Carlberg, D. Fouchez, D. Hardin, I. M. Hook, D. A. Howell, R. Pain, N. Palanque-Delabrouille, K. M. Perrett, C. J. Pritchett, J. Rich, V. Ruhlmann-Kleider, D. Balam, S. Baumont, R. S. Ellis, S. Fabbro, H. K. Fakhouri, N. Fourmanoit, S. González-Gaitán, M. L. Graham, M. J. Hudson, E. Hsiao, T. Kronborg, C. Lidman, A. M. Mourao, J. D. Neill, S. Perlmutter, P. Ripoche, N. Suzuki, and E. S. Walker. SNLS3: Constraints on Dark Energy Combining the Supernova Legacy Survey Three-year Data with Other Probes. *ApJ*, 737(2):102, August 2011. doi: 10.1088/0004-637X/737/2/102.
- Baochen Sun, Jiashi Feng, and Kate Saenko. Return of frustratingly easy domain adaptation. In *Association for the Advancement of Artificial Intelligence (AAAI)*, 2016.
- Casper Kaae Sønderby, Lasse Espeholt, Jonathan Heek, Mostafa Dehghani, Avital Oliver, Tim Salimans, Shreya Agrawal, Jason Hickey, and Nal Kalchbrenner. Metnet: A neural weather model for precipitation forecasting, 2020.

The PLAsTiCC team, Tarek Allam Jr. au2, Anita Bahmanyar, Rahul Biswas, Mi Dai, Lluís Galbany, Renée Hložek, Emille E. O. Ishida, Saurabh W. Jha, David O. Jones, Richard Kessler, Michelle Lochner, Ashish A. Mahabal, Alex I. Malz, Kaisey S. Mandel, Juan Rafael Martínez-Galarza, Jason D. McEwen, Daniel Muthukrishna, Gautham Narayan, Hiranya Peiris, Christina M. Peters, Kara Ponder, Christian N. Setzer, The LSST Dark Energy Science Collaboration, The LSST Transients, and Variable Stars Science Collaboration. The photometric lsst astronomical time-series classification challenge (plasticc): Data set, 2018.

David Tellez, Maschenka Balkenhol, Irene Otte-H

"oller, Rob van de Loo, Rob Vogels, Peter Bult, Carla Wauters, Willem Vreuls, Suzanne Mol, Nico Karssemeijer, et al. Whole-slide mitosis detection in h&e breast histology using phh3 as a reference to train distilled stain-invariant convolutional networks. *IEEE transactions on medical imaging*, 37(9):2126–2136, 2018.

The PLAsTiCC team, Jr. Allam, Tarek, Anita Bahmanyar, Rahul Biswas, Mi Dai, Lluís Galbany, Renée Hložek, Emille E. O. Ishida, Saurabh W. Jha, David O. Jones, Richard Kessler, Michelle Lochner, Ashish A. Mahabal, Alex I. Malz, Kaisey S. Mandel, Juan Rafael Martínez-Galarza, Jason D. McEwen, Daniel Muthukrishna, Gautham Narayan, Hiranya Peiris, Christina M. Peters, Kara Ponder, Christian N. Setzer, The LSST Dark Energy Science Collaboration, The LSST Transients, and Variable Stars Science Collaboration. The Photometric LSST Astronomical Time-series Classification Challenge (PLAsTiCC): Data set. *arXiv e-prints*, art. arXiv:1810.00001, September 2018a.

The PLAsTiCC team, Jr. Allam, Tarek, Anita Bahmanyar, Rahul Biswas, Mi Dai, Lluís Galbany, Renée Hložek, Emille E. O. Ishida, Saurabh W. Jha, David O. Jones, Richard Kessler, Michelle Lochner, Ashish A. Mahabal, Alex I. Malz, Kaisey S. Mandel, Juan Rafael Martínez-Galarza, Jason D. McEwen, Daniel Muthukrishna, Gautham Narayan, Hiranya Peiris, Christina M. Peters, Kara Ponder, Christian N. Setzer, The LSST Dark Energy Science Collaboration, The LSST Transients, and Variable Stars Science Collaboration. The Photometric LSST Astronomical Time-series Classification Challenge (PLAsTiCC): Data set. *arXiv e-prints*, art. arXiv:1810.00001, September 2018b.

Ilya Tolstikhin, Neil Houlsby, Alexander Kolesnikov, Lucas Beyer, Xiaohua Zhai, Thomas Unterthiner, Jessica Yung, Andreas Steiner, Daniel Keysers, Jakob Uszkoreit, Mario Lucic, and Alexey Dosovitskiy. MLP-Mixer: An all-MLP Architecture for Vision. *arXiv e-prints*, art. arXiv:2105.01601, May 2021.

Robert Tripp. A two-parameter luminosity correction for Type IA supernovae. *A&A*, 331:815–820, March 1998.

Eric Tzeng, Judy Hoffman, Kate Saenko, and Trevor Darrell. Adversarial discriminative domain adaptation. In *Computer Vision and Pattern Recognition (CVPR)*, 2017.

Aaron van den Oord, Nal Kalchbrenner, and Koray Kavukcuoglu. Pixel recurrent neural networks, 2016.

- Ashish Vaswani, Noam Shazeer, Niki Parmar, Jakob Uszkoreit, Llion Jones, Aidan N Gomez, Łukasz Kaiser, and Illia Polosukhin. Attention is all you need. *Advances in neural information processing systems*, 30, 2017.
- V. A. Villar, E. Berger, B. D. Metzger, and J. Guillochon. Theoretical Models of Optical Transients. I. A Broad Exploration of the Duration-Luminosity Phase Space. *apj*, 849:70, November 2017a. doi: 10.3847/1538-4357/aa8fcb.
- V. A. Villar, E. Berger, B. D. Metzger, and J. Guillochon. Theoretical Models of Optical Transients. I. A Broad Exploration of the Duration-Luminosity Phase Space. *apj*, 849:70, November 2017b. doi: 10.3847/1538-4357/aa8fcb.
- V. Ashley Villar, Miles Cranmer, Gabriella Contardo, Shirley Ho, and Joshua Yao-Yu Lin. Anomaly Detection for Multivariate Time Series of Exotic Supernovae. *arXiv e-prints*, art. arXiv:2010.11194, October 2020.
- V. Ashley Villar, Griffin Hosseinzadeh, Edo Berger, Michelle Ntampaka, David O. Jones, Peter Challis, Ryan Chornock, Maria R. Drout, Ryan J. Foley, Robert P. Kirshner, Ragnhild Lunnan, Raffaella Margutti, Dan Milisavljevic, Nathan Sanders, Yen-Chen Pan, Armin Rest, Daniel M. Scolnic, Eugene Magnier, Nigel Metcalfe, Richard Wainscoat, and Christopher Waters. Super-raenn: A semisupervised supernova photometric classification pipeline trained on pan-starrs1 medium-deep survey supernovae. *The Astrophysical Journal*, 905(2):94, December 2020. ISSN 1538-4357. doi: 10.3847/1538-4357/abc6fd. URL <http://dx.doi.org/10.3847/1538-4357/abc6fd>.
- V. Ashley Villar, Griffin Hosseinzadeh, Edo Berger, Michelle Ntampaka, David O. Jones, Peter Challis, Ryan Chornock, Maria R. Drout, Ryan J. Foley, Robert P. Kirshner, Ragnhild Lunnan, Raffaella Margutti, Dan Milisavljevic, Nathan Sanders, Yen-Chen Pan, Armin Rest, Daniel M. Scolnic, Eugene Magnier, Nigel Metcalfe, Richard Wainscoat, and Christopher Waters. SuperRAENN: A Semisupervised Supernova Photometric Classification Pipeline Trained on Pan-STARRS1 Medium-Deep Survey Supernovae. *ApJ*, 905(2):94, December 2020. doi: 10.3847/1538-4357/abc6fd.
- V. Ashley Villar, Kaylee de Soto, and Alex Gagliano. Hierarchical cross-entropy loss for classification of astrophysical transients, 2023.
- M. Vincenzi, M. Sullivan, R. E. Firth, C. P. Gutiérrez, C. Frohmaier, M. Smith, C. Angus, and R. C. Nichol. Spectrophotometric templates for core-collapse supernovae and their application in simulations of time-domain surveys. *MNRAS*, 489(4):5802–5821, November 2019. doi: 10.1093/mnras/stz2448.
- M. Vincenzi, M. Sullivan, O. Graur, D. Brout, T. M. Davis, C. Frohmaier, L. Galbany, C. P. Gutiérrez, S. R. Hinton, R. Hounsell, L. Kelsey, R. Kessler, E. Kovacs, S. Kuhlmann, J. Lasker, C. Lidman, A. Möller, R. C. Nichol, M. Sako, D. Scolnic, M. Smith, E. Swann, P. Wiseman, J. Asorey, G. F. Lewis, R. Sharp, B. E. Tucker, M. Agüena, S. Allam, S. Avila, E. Bertin, D. Brooks, D. L. Burke, A. Carnero Rosell, M. Carrasco Kind, J. Carretero, F. J. Castander, A. Choi, M. Costanzi, L. N.

- da Costa, M. E. S. Pereira, J. De Vicente, S. Desai, H. T. Diehl, P. Doel, S. Everett, I. Ferrero, P. Fosalba, J. Frieman, J. García-Bellido, E. Gaztanaga, D. W. Gerdes, D. Gruen, R. A. Gruendl, G. Gutierrez, D. L. Hollowood, K. Honscheid, B. Hoyle, D. J. James, K. Kuehn, N. Kuropatkin, M. A. G. Maia, P. Martini, F. Menanteau, R. Miquel, R. Morgan, A. Palmese, F. Paz-Chinchón, A. A. Plazas, A. K. Romer, E. Sanchez, V. Scarpine, S. Serrano, I. Sevilla-Noarbe, M. Soares-Santos, E. Suchyta, G. Tarle, D. Thomas, C. To, T. N. Varga, A. R. Walker, R. D. Wilkinson, and DES Collaboration. The Dark Energy Survey supernova programme: modelling selection efficiency and observed core-collapse supernova contamination. *MNRAS*, 505(2):2819–2839, August 2021. doi: 10.1093/mnras/stab1353.
- M Vincenzi, M Sullivan, A Möller, P Armstrong, B A Bassett, D Brout, D Carollo, A Carr, T M Davis, C Frohmaier, L Galbany, K Glazebrook, O Graur, L Kelsey, R Kessler, E Kovacs, G F Lewis, C Lidman, U Malik, R C Nichol, B Popovic, M Sako, D Scolnic, M Smith, G Taylor, B E Tucker, P Wiseman, M Agüena, S Allam, J Annis, J Asorey, D Bacon, E Bertin, D Brooks, D L Burke, A Carnero Rosell, J Carretero, F J Castander, M Costanzi, L N da Costa, M E S Pereira, J De Vicente, S Desai, H T Diehl, P Doel, S Everett, I Ferrero, B Flaugher, P Fosalba, J Frieman, J García-Bellido, D W Gerdes, D Gruen, G Gutierrez, S R Hinton, D L Hollowood, K Honscheid, D J James, K Kuehn, N Kuropatkin, O Lahav, T S Li, M Lima, M A G Maia, J L Marshall, R Miquel, R Morgan, R L C Ogando, A Palmese, F Paz-Chinchón, A Pieres, A A Plazas Malagón, K Reil, A Roodman, E Sanchez, M Schubnell, S Serrano, I Sevilla-Noarbe, E Suchyta, G Tarle, C To, T N Varga, J Weller, and R D Wilkinson. The dark energy survey supernova program: Cosmological biases from supernova photometric classification. *MNRAS*, jun 2022. doi: 10.1093/mnras/stac1404. URL <https://doi.org/10.1093/mnras/stac1404>.
- M. Vincenzi, M. Sullivan, A. Möller, P. Armstrong, B. A. Bassett, D. Brout, D. Carollo, A. Carr, T. M. Davis, C. Frohmaier, L. Galbany, K. Glazebrook, O. Graur, L. Kelsey, R. Kessler, E. Kovacs, G. F. Lewis, C. Lidman, U. Malik, R. C. Nichol, B. Popovic, M. Sako, D. Scolnic, M. Smith, G. Taylor, B. E. Tucker, P. Wiseman, M. Agüena, S. Allam, J. Annis, J. Asorey, D. Bacon, E. Bertin, D. Brooks, D. L. Burke, A. Carnero Rosell, J. Carretero, F. J. Castander, M. Costanzi, L. N. da Costa, M. E. S. Pereira, J. De Vicente, S. Desai, H. T. Diehl, P. Doel, S. Everett, I. Ferrero, B. Flaugher, P. Fosalba, J. Frieman, J. García-Bellido, D. W. Gerdes, D. Gruen, G. Gutierrez, S. R. Hinton, D. L. Hollowood, K. Honscheid, D. J. James, K. Kuehn, N. Kuropatkin, O. Lahav, T. S. Li, M. Lima, M. A. G. Maia, J. L. Marshall, R. Miquel, R. Morgan, R. L. C. Ogando, A. Palmese, F. Paz-Chinchón, A. Pieres, A. A. Plazas Malagón, K. Reil, A. Roodman, E. Sanchez, M. Schubnell, S. Serrano, I. Sevilla-Noarbe, E. Suchyta, G. Tarle, C. To, T. N. Varga, J. Weller, R. D. Wilkinson, and DES Collaboration. The Dark Energy Survey supernova program: cosmological biases from supernova photometric classification. *MNRAS*, 518(1):1106–1127, January 2023. doi: 10.1093/mnras/stac1404.
- Bo Wang and Zhanwen Han. Progenitors of type Ia supernovae. *New A Rev.*, 56(4):122–141, June 2012. doi: 10.1016/j.newar.2012.04.001.
- Yun Wang, E. Gjergo, and S. Kuhlmann. Analytic photometric redshift estimator for Type Ia supernovae from the Large Synoptic Survey Telescope. *MNRAS*, 451(2):1955–1963, August 2015. doi: 10.1093/mnras/stv1090.

- P. Wiseman, M. Smith, M. Childress, L. Kelsey, A. Möller, R. R. Gupta, E. Swann, C. R. Angus, D. Brout, T. M. Davis, R. J. Foley, C. Frohmaier, L. Galbany, C. P. Gutiérrez, C. Inserra, R. Kessler, G. F. Lewis, C. Lidman, E. Macaulay, R. C. Nichol, M. Pursiainen, M. Sako, D. Scolnic, N. E. Sommer, M. Sullivan, B. E. Tucker, T. M. C. Abbott, M. Agüena, S. Allam, S. Avila, E. Bertin, D. Brooks, E. Buckley-Geer, D. L. Burke, A. Carnero Rosell, D. Carollo, M. Carrasco Kind, L. N. da Costa, J. De Vicente, S. Desai, H. T. Diehl, P. Doel, T. F. Eifler, S. Everett, P. Fosalba, J. Frieman, J. García-Bellido, E. Gaztanaga, D. W. Gerdes, M. S. S. Gill, K. Glazebrook, R. A. Gruendl, J. Gschwend, W. G. Hartley, S. R. Hinton, D. L. Hollowood, K. Honscheid, D. J. James, K. Kuehn, N. Kuropatkin, M. Lima, M. A. G. Maia, M. March, P. Martini, P. Melchior, F. Menanteau, R. Miquel, R. L. C. Ogando, F. Paz-Chinchón, A. A. Plazas, A. K. Romer, A. Roodman, E. Sanchez, V. Scarpine, S. Serrano, E. Suchyta, M. E. C. Swanson, G. Tarle, D. Thomas, D. L. Tucker, T. N. Varga, A. R. Walker, R. D. Wilkinson, and (DES Collaboration). Supernova host galaxies in the dark energy survey: I. Deep coadds, photometry, and stellar masses. *MNRAS*, 495(4):4040–4060, July 2020. doi: 10.1093/mnras/staa1302.
- P. Wiseman, M. Sullivan, M. Smith, C. Frohmaier, M. Vincenzi, O. Graur, B. Popovic, P. Armstrong, D. Brout, T. M. Davis, L. Galbany, S. R. Hinton, L. Kelsey, R. Kessler, C. Lidman, A. Möller, R. C. Nichol, B. Rose, D. Scolnic, M. Toy, Z. Zontou, J. Asorey, D. Carollo, K. Glazebrook, G. F. Lewis, B. E. Tucker, T. M. C. Abbott, M. Agüena, S. Allam, F. Andrade-Oliveira, J. Annis, D. Bacon, E. Bertin, D. Brooks, E. Buckley-Geer, D. L. Burke, A. Carnero Rosell, M. Carrasco Kind, J. Carretero, M. Costanzi, L. N. da Costa, M. E. S. Pereira, S. Desai, H. T. Diehl, P. Doel, S. Everett, I. Ferrero, B. Flaugher, P. Fosalba, J. Frieman, J. García-Bellido, E. Gaztanaga, T. Giannantonio, D. Gruen, R. A. Gruendl, J. Gschwend, G. Gutierrez, D. L. Hollowood, K. Honscheid, B. Hoyle, D. J. James, E. Krause, K. Kuehn, N. Kuropatkin, M. A. G. Maia, J. L. Marshall, P. Martini, F. Menanteau, R. Miquel, R. Morgan, R. L. C. Ogando, A. Palmese, F. Paz-Chinchón, D. Petravick, A. Pieres, A. A. Plazas Malagón, A. K. Romer, E. Sanchez, V. Scarpine, M. Schubnell, S. Serrano, I. Sevilla-Noarbe, M. Soares-Santos, E. Suchyta, M. E. C. Swanson, G. Tarle, D. Thomas, C. To, T. N. Varga, A. R. Walker, and DES Collaboration. Rates and delay times of Type Ia supernovae in the Dark Energy Survey. *MNRAS*, 506(3):3330–3348, September 2021. doi: 10.1093/mnras/stab1943.
- S. E. Woosley, P. A. Pinto, P. G. Martin, and Thomas A. Weaver. Supernova 1987A in the Large Magellanic Cloud: The Explosion of a approximately  $20 M_{sun}$  Star Which Has Experienced Mass Loss? *ApJ*, 318:664, July 1987. doi: 10.1086/165402.
- Qizhe Xie, Zihang Dai, Eduard Hovy, Minh-Thang Luong, and Quoc V Le. Unsupervised data augmentation for consistency training. In *Advances in Neural Information Processing Systems (NeurIPS)*, 2020a.
- Qizhe Xie, Minh-Thang Luong, Eduard Hovy, and Quoc V. Le. Self-training with noisy student improves imagenet classification. *arXiv*, 2020b.
- Qize Yang, Xihan Wei, Biao Wang, Xian-Sheng Hua, and Lei Zhang. Interactive self-training with mean teachers for semi-supervised object detection. In *2021 IEEE/CVF Conference on Computer Vision and Pattern Recognition (CVPR)*, pages 5937–5946, 2021. doi: 10.1109/CVPR46437.2021.

00588.

Matthew D Zeiler and Rob Fergus. Visualizing and understanding convolutional networks. In *European conference on computer vision*, pages 818–833. Springer, 2014.

Hongyi Zhang, Moustapha Cissé, Yann N. Dauphin, and David Lopez-Paz. mixup: Beyond empirical risk minimization. *ICLR*, 2017.

Qi Zhang, Yifei Wang, and Yisen Wang. How mask matters: Towards theoretical understandings of masked autoencoders. *Advances in Neural Information Processing Systems*, 35:27127–27139, 2022.

Haoyi Zhou, Shanghang Zhang, Jieqi Peng, Shuai Zhang, Jianxin Li, Hui Xiong, and Wancai Zhang. Informer: Beyond efficient transformer for long sequence time-series forecasting. In *Proceedings of the AAAI conference on artificial intelligence*, volume 35, pages 11106–11115, 2021.